

# Semiconducting two dimensional transition metal dichalcogenides *via* solution-processable routes

Présentée le 1<sup>er</sup> juillet 2022

Faculté des sciences de base  
Laboratoire d'ingénierie moléculaire des nanomatériaux optoélectroniques  
Programme doctoral en chimie et génie chimique

pour l'obtention du grade de Docteur ès Sciences

par

## Rebekah Anne WELLS

Acceptée sur proposition du jury

Prof. V. Hatzimanikatis, président du jury  
Prof. K. Sivula, directeur de thèse  
Prof. P. Samorì, rapporteur  
Prof. C. Mattevi, rapporteuse  
Prof. K. Agrawal, rapporteur



# Acknowledgements

I want to first extend my sincerest gratitude to the members of my thesis jury, Professors Kevin Sivula, Vassily Hatzimanikatis, Kumar Agrawal, Paolo Samori, Cecilia Mattevi. Not only did they indeed read and carefully consider my thesis, but they also offered additional insights and posed thoughtful questions. I feel lucky to say that I actually enjoyed my thesis defense experience and I wish a similar one to others. A special thanks to Prof. Hatzimanikatis for remaining calm in the face of last-minute issues and helping me to feel confident during my presentation (not to mention sharing his tea and coffee supplies with me these past five years).

To Professor Kevin Sivula, my thesis advisor and mentor, I cannot say how grateful I am to have been able to pursue my academic interests in LIMNO under your guidance. After all that I have seen at EPFL I know how rare it is to find a boss who is available anytime you need them yet doesn't (over) micromanage and, on top of that, with whom you are compatible with. One of my biggest hurdles to moving beyond the thesis is recognizing that you are really a one-of-a-kind boss. You let me pursue the projects that interested me, even if they weren't exactly what was planned. You listened to all of my ideas: the good, the bad, and the crazy. While you let me work at my own rhythm, you never let me fall behind when the road was tough and progress felt impossible. The LIMNO lab environment is also exceptional. There is so much sharing, collaboration, and diversity, which are a testament of your curating and leadership abilities. And of course, I learnt so much from you as a scientist – how to ask better questions, how to make cohesive stories, and to be skeptical of everything and optimistic at the same time. Thank you so much for your support, counsel, and patience above all.

A special thanks to Professor Scott Warren, who is a big reason that I am here today. During my years in his lab, you trusted me to be a contributing member of the team and gave me independence to pursue my own projects, even as an undergraduate. Of course, I learned so much in terms of research and science; but more than anything, you supported me when I didn't believe in myself. You encouraged me when I wanted to study abroad but was afraid of how it would look on my transcripts. When I wanted to go abroad for the PhD you were overwhelmingly in favor, despite others who would have told me otherwise. And when it came time to apply for awards at the end of my studies, you pushed me to apply for things I was sure I was "unqualified" for. Now when I doubt myself, I remember that day in your office when you told me to apply because you had "already written the recommendation letter" in anticipation. These little things made all the difference. Thank you for believing in me and, importantly, for telling me so.

Now, to my LIMNO family, thank you all for being the best and most supportive team anyone could ask for. Despite varying age, backgrounds, experience, and mother tongues, there has always been a strong feeling of comradeship and equality. I've learned so much from every one of you, either by directly asking or by simply observing. To Charles and Florent, the electrochemical experts and 3D printing gurus: you were the ones that showed me how rigorous you have to be to do good, solid science. On top of that you answered all of my questions, helped me with my 3D designs, and somehow never got annoyed with me. A special shout out to Charles and his green thumb for helping to make the balcony garden a success. To the notorious Florian Le Formel who kept the atmosphere light and fun and the group meetings very honest: thank you also for being my emergency emergency contact back in the day. To Liza who reminded me that there is strength in numbers: Thank you for your patience and for not giving up on me even when I was difficult to work with. To Han Hee, the best chef ever: thank you for your constant positivity and support. You were always around for advice and to lend a helping hand (or polymer). To my first office mates Liang and Nestor: thank you for the warm welcome. Liang, I always sought your advice as it was thoughtful and honest. Even though our subjects were so different it didn't stop you from helping me try to understand and progress. Nestor, your presence was vital to my early days at EPFL. Your constructive criticism, honesty, and knowledge about everything there is worth knowing made you a great colleague, but your humor, kindness, and selflessness made you a great friend. And to Jun Ho with whom I shared my work home, thank you for always keeping your "door open" even though I was already in the office. Your advice has always been spot on ranging from academic to career to personal. I will miss being able to turn to you when my data doesn't make sense or I need reassurance for my figure or I'm nervous about the future. Thanks for putting up with me.

To the next level of LIMNO folk, my fellow PhD wannabes, it's been so cool to work with you all and watch you grow in both your work and personal lives. Ardvindh with your directness and good humor, thanks for all your advice over the years. YP, king of IMPS/IMVS, thanks for always lending a hand and helping me try my best (and worst) ideas. Barbara, the automation queen, thanks for your kindness and positivity. Nukorn, keeper of the reference potential and champion group cleaning fellow, thanks for your kindness and for all the small maintenance tasks you do that seemingly go unnoticed. A big thank you to Colin who always helps with me my swiss problems and is up for adventure. Simon and Conor, the most unlikely officemates, thanks for always rallying and keeping LIMNO's social life alive. Simon, thanks for all the XRD work and especially for explaining it, never stop being you. Connor, thank you for the positive energy you bring in and outside of the lab and for always going above and beyond your role. And a big one to Nicolas, for joining me in this last stage of my thesis and dealing with all of my eccentric, end-of-thesis behavior. No doubt that you'll find your path and that it will be an exciting one, keep up the good work and don't be afraid to fail from time to time. It's been an absolute pleasure to work with you all, keep doing what you do and I wish you all the best and more.

Enfin, to Marina Caretti, thank you for never giving up on me and never giving up on yourself. You were one of my first friends in Lausanne and a rock for me in my low points. I knew I could always come to you and you would make time. You even made me part of your family. We survived a lot together from failing experiments to relationships to family dramas to health and everything in between. I'm so proud of the work you did in your thesis; I never ever doubted you and yet you still exceeded expectations. You're a brilliant and thorough scientist and I'm so glad you stuck around for a few more years. I hope our paths will continue to cross and overlap in life.

To my work wife and partner in crime, I am still bitter that you left me to live the California dream. Alice Gillen, you're an absolute powerhouse. No matter what you do it's with intensity and passion. I always admired this about you and this is what got me through that final push of third year woes – I mean if you can plan a wedding and submit a thesis I guess I can finishing treating my data. Our midnight experiments, holy cow runs, and tipsy experiment planning from our kitchen table reminded me that being serious about science and having fun don't have to be mutually exclusive.

But my LIMNO team was not my only team. A huge shoutout to the EDCH PhD committee who helped me to manage my tasks and intentions as the EDCH PhD representative. A special thanks to Pauline for her hard work and dedication to improving mental health at EPFL. And to Phil Ly, without whom no social event would ever have made from idea table to the actual physical event, thanks for being a great support, friend, and overall great human being. Wishing you a speedy and fruitful thesis journey.

To my collaborators, thanks for supporting my efforts and being willing to go along with my crazy ideas. Especially to Miao and Bart for letting me convince you spend your time and energy on a new type of sample. To Marta for fruitful discussion and support during the thesis. To Yanfei et Zhenyu for giving your all to my difficult requests. To Hannah Johnson for supporting me financially (in a way) and following my projects with enthusiasm and care and for throwing me some projects to join in on as well. Always a pleasure to have you in the lab. To Pascal for excellent XRD data and explanations and for introducing me to the synchrotron. To Mounir for all of my million questions you've answered – not just about XPS, but career and Switzerland and sports; we're very lucky to have you. And finally to Victor, for all of his work to help me get my beloved STEM images and for quality assurance. You were willing to give my samples a try when no one else would bother. I learned so much from you and always really enjoyed working with you. The best compliment will always be your asking to keep my samples.

As for my non-academic teams, the Lausanne Invitational! Olivier and Mike, thanks for keeping it rad and getting me into trouble – and usually helping me out of it as well. I'm so lucky to have stumbled onto your friendship. All the riding, chilling, and steezing would not have been possible without such a solid crew. Olivier, thanks for always being up for a good time and showing me the best freeride spots – and for getting me to push my limits. Mike, man what a time we have had. Not only skiing, but surfing and climbing and good times at the chateau. Everything was more fun with you – even the worst parts of the thesis. Thanks for making me a mate, giving me a Czech family, and for riding the same wave. Thanks also to Tereza for putting Mike in his place so the rest of us don't have to! Thanks to both of you for all the memories shared and for always letting me third wheel.



Speaking of surf and snowboard, shout out to Vlad for being an all-around amazing friend and teaching me to surf and plant my poles. We shared some great times on the mountain, great meals, hard workouts, and, most importantly, great ice cream. Despite coming from opposite sides of the world and EPFL, we're always on the same page.

To my other adventure buddies over the years, Giorgios, Pierre Y, Pierre L, Elodie, Flo, Chris, Olivia, and Leo, thanks for keeping me alive. Big shout out to Giorgos for being down to try anything and for never accepting mediocrity. I still hope we will work together one day. Special thanks to Leo for all of the good memories made across Europe: Nice, Rhodes, Zinal, Lausanne, Zurich, and those to come. You're one of a kind. Thanks for never letting me undersell myself, nor take myself too seriously. Looking forward to future adventures.

To Sofie, thank you for helping me live in adventure and luxury simultaneously and for giving me a Danish family. I can't believe our unlikely meeting 10 years ago turned into such a beautiful friendship. Opposite in so many ways, we compliment each other so well. Whether it's trying new food, new sports, or new locations, together we push ourselves to experience more and enjoy life to the fullest. Can't wait for our next expedition.

To my penthouse peeps, thanks for being my Swiss family. To Gabby for always keeping it clean and real. To Martin and Sonia for joining me on my many adventures and being absolute mates. For Swiss and Scottish Christmas celebrations and ski days and trampolining and all the rest. To Austin for being the little brother I never wanted and for being so go-with-the-flow. For rescuing me from would-be-terrible dates and letting me rescue you on mountains so I have a nice story to tell. To Maria for amazing cakes, moussaka, and exotic plants. To Edgar and Laura for the absolute best ski days imaginable, movie nights, family dinners, yoga sessions, bouldering nights, night ski touring, stressing about jobs and theses, windsurfing in April, and now even some mountain biking. Y'all are seriously the best and no one will ever live up to this. Thanks for everything and more.

To the friends far away who didn't forget about me, Shan, Jess, and Ray, thank you just for being you. Jessie, for your incredibly kind soul and understanding. For your support and hype even when life is falling apart. Shannon, for your compassion and humor. For always making time in your busy schedule and knowing the right thing to say. Ray, for the surprise friendship I never expected. Your bluntness and support never let me get away with anything and it's usually exactly what I need. You always make time for me and you're the one I call in a crisis – you get me better than anyone whether it's work or personal or just a random life crisis. Not to mention that you're an incredible scientist and scholar. Still not sorry about stealing your lab partner though.

To Corentin, the best adventure partner of all, thank you for making literally everything better. From adventures like climbing and camping and splitboarding and surfing to menial tasks like cooking and going to work and finishing my thesis. Thank you for always double checking my knot and making sure I get home safe. Thank you for battling the hell that is formatting in Microsoft Word. Your support in the final leg of my thesis was vital to my happiness and well-being. One day we might even be able to pronounce one another's name.

And finally, to my family. To my foundation and never ending supply of support, a simple thank you will never be enough. Dad, you always believed in me and pushed me to be my best. You spent your entire life providing for me to have the best and be able to go after my dreams, when I wasn't exactly sure what they were. To my sibling who is the life of every party and got all the humor in the family, no matter how old you get you will always be my little one. Thank you for always making me laugh and for being there when I needed you. You give so much of your strength to others, don't forget to save some for yourself. You can do anything. And to my mom and best friend. Without you there would be no me in any sense of the phrase. You have nurtured me in every possible way no matter the cost to you. I can never express enough gratitude for all that you have done. I hope just that you know how much you mean to me and how much you inspired me to always be my true self. Thank you a million times over.



# Abstract

Two-dimensional (2D) transition metal dichalcogenides (TMDs) possess remarkable optoelectronic properties which are unique and tunable based on composition and thickness. These materials are poised to revolutionize ultrathin devices across many fields including transistors, light emitting diodes, solar cells, and photoelectrodes, to name a few. In particular, single-flake devices for solar energy conversion have achieved promising performances using high-quality TMD nanosheets. However, a major obstacle to realizing these devices outside of the lab continues to be the large-scale production of pristine 2D TMD nanomaterial. To this end the following work aims to overcome the issue of scalability to produce thin films of semiconducting 2D TMD nanosheets without sacrificing material quality nor device performance. The first chapter lays a road map of how to reach this goal and highlights issues that will be addressed. The second chapter details the development of a novel powder-based electrochemical pellet intercalation (ECPI) technique which allows for scalable production of solution-processable 2D TMDs. Using this technique to prepare 2D MoS<sub>2</sub> yields extremely thin semiconducting nanosheets (predominantly monolayers) with large lateral dimensions (> 1 μm) and impressive absorbed photon-to-current conversion efficiencies (APCE) up to 90%, suggesting high quantum yield. Notably this method can be used to make a range of 2D TMDs including MoS<sub>2</sub>, WS<sub>2</sub>, and WSe<sub>2</sub>. In the third chapter the ECPI method is further extended to produce alloyed 2D TMD nanosheets, which allows for continuous tuning of their optoelectronic properties. In addition to compositional tuning, five alloys, four ternary (Mo<sub>0.5</sub>W<sub>0.5</sub>S<sub>2</sub>, Mo<sub>0.5</sub>W<sub>0.5</sub>Se<sub>2</sub>, MoSSe, WSSe) and one quaternary (Mo<sub>0.5</sub>W<sub>0.5</sub>SSe), are demonstrated. This demonstration greatly expands the range of optoelectronic properties that can be obtained *via* economic and solution-processable means and leads the way to large-area 2D TMD devices. Finally, chapter four describes a method for processing large volumes of TMD nanosheets into large-area films without compromising favorable film morphology. The method is developed into a continuous roll-to-roll (R2R) film system, capable of printing ultrathin TMD films at the meters-squared scale. In addition to being applicable to different 2D TMDs (MoS<sub>2</sub> and WSe<sub>2</sub>), it is also viable for the production of large-area heterojunction thin films. Together these chapters address multiple key challenges in the field and present a holistic approach to overcoming them.

## Keywords

Transition metal dichalcogenide; MoS<sub>2</sub>; Mo<sub>0.5</sub>W<sub>0.5</sub>S<sub>2</sub>; electrochemical intercalation; photoelectrode; thin film; alloy; solar energy conversion; quantum yield; large-area; solution-processable; defect; iodide oxidation, high resolution scanning transmission electron microscopy, roll-to-roll

# Résumé

Les matériaux bidimensionnels (2D) composant les dichalcogénures de métaux de transition (TMD) possèdent des propriétés uniques qui peuvent être ajustées en fonction de leur composition et de leur épaisseur. Ces matériaux sont bien placés pour révolutionner les appareils fins dans de nombreux domaines, notamment les transistors, les diodes électroluminescentes, les cellules solaires, les photoélectrodes, etc... En particulier, les appareils qui se composent d'une seule nanofeuillette TMD (monocouche) ont obtenu des performances prometteuses lorsque des nanofeuillets TMD de très haute qualité sont utilisés. Cependant, un obstacle majeur pour la réalisation d'appareils hors laboratoire est la fabrication de ces matériaux immaculés en grande quantité. Cette thèse a pour but de surmonter ce problème d'évolutivité pour produire des films fins en composant les TMD 2D semi-conducteurs sans sacrifier, ni la qualité du matériau, ni les performances de l'appareil. Dans une première partie, un plan est présenté et suggère des solutions pour atteindre cet objectif. Il décrit aussi les problèmes qui seront abordés dans la suite du manuscrit. Une seconde partie détaille le développement d'une nouvelle technique, utilisant des poudres commerciales, pour la production de matériaux TMD 2D de manière évolutive en utilisant l'intercalation de pastilles électrochimiques (ECPI). L'utilisation de cette technique pour préparer du MoS<sub>2</sub> 2D produit des nanofeuillets très fines (principalement monocouche) avec de grandes dimensions latérales (> 1 µm). Ces nanofeuillets possèdent une efficacité de conversion photon-courant électrique (APCE) allant jusqu'à 90 %, suggérant un rendement de quantique élevé. Notamment, avec cette méthode, il est possible de produire de nombreux types de TMD 2D, par exemple, MoS<sub>2</sub>, WS<sub>2</sub> et WSe<sub>2</sub>. Dans une troisième partie, la technique ECPI est avancée aux TMD 2D alliés qui permettent un réglage continu des propriétés optoélectroniques. En plus du réglage lié à la composition, cinq alliages, quatre ternaires (Mo<sub>0.5</sub>W<sub>0.5</sub>S<sub>2</sub>, Mo<sub>0.5</sub>W<sub>0.5</sub>Se<sub>2</sub>, MoSSe, WSSe) et un quaternaire (Mo<sub>0.5</sub>W<sub>0.5</sub>SSe), sont présentés. Cette démonstration augmente la gamme de propriétés optoélectroniques accessibles par des voies économiques et fait en solution, ouvrant la voie à des appareils de grande échelle basés sur des matériaux TMD 2D. Enfin, une quatrième partie décrit une méthode de traitement de grands volumes de nanofeuillets en films fins de grande surface, sans sacrifier la morphologie favorable du film. Cette méthode est développée dans un système continu rouleau-à-rouleau (R2R) capable d'imprimer des films très fins de l'ordre du mètre carré. En plus d'être applicable pour différents TMD 2D (MoS<sub>2</sub> and WSe<sub>2</sub>), il convient également à la production de films à hétérojonction. Ensemble, ces chapitres abordent plusieurs défis clés dans le domaine des 2D TMD et présentent une approche pour les surmonter.

## Mots-clés

Dichalcogénures de métaux de transition; MoS<sub>2</sub>; Mo<sub>0.5</sub>W<sub>0.5</sub>S<sub>2</sub>; intercalation électrochimique; photoélectrodes; films fins; alliages; conversion de l'énergie solaire; rendement de quantique; grande échelle; transformable en solution; défaut; oxydation de l'iodure; microscope électronique en transmission à balayage de résolution haute; rouleau-à-rouleau

# Table of Contents

<b>Semiconducting two-dimensional transition metal dichalcogenides <i>via</i> solution-processable routes.....</b>	<b>i</b>
<b>Acknowledgements .....</b>	<b>iii</b>
<b>Abstract .....</b>	<b>vii</b>
<b>Keywords .....</b>	<b>vii</b>
<b>Résumé .....</b>	<b>viii</b>
<b>Mots-clés .....</b>	<b>viii</b>
<b>List of Figures .....</b>	<b>xii</b>
<b>List of Tables .....</b>	<b>xiv</b>
<b>List of Equations .....</b>	<b>xiv</b>
<b>List of Annex Items .....</b>	<b>xiv</b>
<b>Chapter 1     State-of-the-art, challenges, and motivation .....</b>	<b>1</b>
1.1     Introduction.....	2
1.2     Bulk TMD crystal structure .....	3
1.3     Intrinsic semiconducting properties of 2D TMDs .....	4
1.4     Tuning the semiconducting properties of 2D TMD nanoflakes .....	5
1.4.1     Heterojunctions .....	5
1.4.2     Doping.....	5
1.4.3     Defect engineering.....	5
1.4.4     Alloying.....	6
1.5     Solution-processable routes towards thin films of 2D TMDs .....	7
1.6     Liquid phase exfoliation methods.....	9
1.6.1     Ultrasonication.....	9
1.6.2     Shear-mixing .....	10
1.6.3     Ion intercalation .....	10
1.7     Nanomaterial size selection.....	11
1.7.1     Centrifugation .....	11
1.7.2     Density gradient ultracentrifugation.....	12
1.7.3     Sieve filtration .....	12
1.8     Solution-processable film formation .....	14
1.8.1     Drop casting and related techniques .....	14
1.8.2     Dip coating .....	15
1.8.3     Liquid-air interfacial self-assembly.....	16
1.8.4     Liquid-liquid interfacial self-assembly.....	16
1.9     Fine tuning thin films of 2D TMDs .....	18
1.9.1     Van der Waals heterojunctions.....	18

1.9.2	Hybrid organic-inorganic heterojunctions.....	18
1.9.3	Defect mitigation .....	19
1.10	Motivation .....	22
<b>Chapter 2</b>	<b>High performance semiconducting nanosheets <i>via</i> a scalable powder-based electrochemical exfoliation technique .....</b>	<b>23</b>
2.1	Introduction.....	24
2.2	Results and discussion .....	25
2.2.1	Electrochemical intercalation/exfoliation of pressed powder pellets.....	25
2.2.2	Nanosheet characterization .....	29
2.2.3	Defect mapping of EPI-made and ultrasonicated nanosheets .....	32
2.2.4	Nanosheet optoelectronic and photoelectrochemical performance.....	36
2.2.5	Applications to other layered TMD materials .....	41
2.3	Conclusions.....	42
2.4	Methods .....	44
<b>Chapter 3</b>	<b>Facile production of two-dimensional transition metal dichalcogenide alloys <i>via</i> a powder-based, solution-processable approach .....</b>	<b>49</b>
3.1	Introduction.....	50
3.2	Results and discussion .....	51
3.2.1	Bulk alloyed TMD pellet fabrication .....	51
3.2.2	Nanosheet characterization .....	53
3.2.3	Composition-tuned $\text{Mo}_{(1-x)}\text{W}_x\text{S}_2$ alloyed nanosheets.....	55
3.2.4	Other ternary TMD alloys.....	57
3.2.5	Quaternary TMD alloy formation .....	59
3.2.6	Overview of the electronic structures of the 2D TMDs made <i>via</i> ECPI-exfoliation .....	62
3.3	Conclusions.....	63
3.4	Methods .....	64
<b>Chapter 4</b>	<b>Roll-to-roll deposition of semiconducting 2D nanoflake films of transition metal dichalcogenides for optoelectronic applications.....</b>	<b>67</b>
4.1	Introduction.....	69
4.2	Results and discussion .....	70
4.3	Conclusions.....	81
4.4	Methods .....	82
<b>Chapter 5</b>	<b>Conclusions and outlook .....</b>	<b>85</b>
5.1	Summary of findings.....	85
5.2	Future work .....	87
5.2.1	Future work related to this thesis .....	87
5.2.2	2D TMDs for solar energy conversion on a global scale.....	89
<b>Annex</b>	<b>.....</b>	<b>90</b>

## Table of Contents

---

References .....	96
CV Rebekah Wells.....	105

## List of Figures

Figure 1.1. Schematic representations of TMD atomic structure and polymorphs. ....	3
Figure 1.2. Band structure of TMDs based on thickness and composition. ....	4
Figure 1.3. Influence of defects and alloying on TMD band structure. ....	6
Figure 1.4. Examples of single flake PV and PEC devices. ....	7
Figure 1.5. Schematic representations of popular LPE methods. ....	9
Figure 1.6. Depictions of three common techniques used to separate nanoflakes by size. ....	11
Figure 1.7. Relationship of nanoflake dimension to internal quantum yield. ....	13
Figure 1.8. Examples of different film formation techniques. ....	15
Figure 1.9. Description of LLISA film formation method. ....	17
Figure 1.10. Examples of TMD based heterojunctions. ....	19
Figure 1.11. Examples of defect mitigation techniques. ....	20
Figure 2.1. Schematic of the electrochemical pellet intercalation (ECPI) exfoliation method. ....	25
Figure 2.2. Scanning electron microscope images of annealed and unannealed pressed MoS <sub>2</sub> pellets. ....	26
Figure 2.3. The stages of pellet intercalation. ....	26
Figure 2.4. Evidence of intercalation of THA <sup>+</sup> into the MoS <sub>2</sub> layered structure. ....	27
Figure 2.5. UV-Vis of fresh and sonicated NMP. ECPI-made MoS <sub>2</sub> dispersions. ....	28
Figure 2.6. Structural and morphological characterization of ECPI made-MoS <sub>2</sub> nanosheets. ....	29
Figure 2.7. Size-thickness analysis for ECPI-made MoS <sub>2</sub> nanosheets. ....	30
Figure 2.8. Chemical characterization of ECPI-made MoS <sub>2</sub> nanosheets. ....	31
Figure 2.9. STEM and high-resolution STEM for ECPI-made and ultrasonicated MoS <sub>2</sub> nanoflakes. ....	32
Figure 2.10. Statistical and UV-Vis analysis of ultrasonicated MoS <sub>2</sub> nanoflakes. ....	33
Figure 2.11. Results of 2D-PAINT method for mapping defects on films. ....	34
Figure 2.12. Optoelectronic properties for thin films of ECPI-made nanosheets and sonicated nanoflakes. ....	36
Figure 2.13. Photoluminescence spectra for ECPI-made MoS <sub>2</sub> nanosheets of different sizes. ....	37
Figure 2.14. Photoluminescence for thin ECPI-made MoS <sub>2</sub> nanoflakes. ....	37
Figure 2.15. Bottom gate / bottom contact transistors from ECPI-made and ultrasonicated MoS <sub>2</sub> nanoflakes. ....	38
Figure 2.16. Photoelectrochemical (PEC) properties for films of ECPI-made nanosheets and sonicated nanoflakes. ....	39
Figure 2.17. ECPI-made nanosheets of other layered materials. ....	41
Figure 2.18. Optoelectronic and PEC properties of ECPI-made WSe <sub>2</sub> and WS <sub>2</sub> nanosheets. ....	41
Figure 3.1. Schematic of the modified electrochemical pellet intercalation (ECPI) exfoliation for formation of 2D TMD alloys. ....	51
Figure 3.2. Characterization of alloyed TMD pellet. ....	52



---

Figure 3.3. STEM and high-resolution STEM of $\text{Mo}_{0.5}\text{W}_{0.5}\text{S}_2$ nanosheets. ....	53
Figure 3.4. Optoelectronic characterization of $\text{Mo}_{(1-x)}\text{W}_x\text{S}_2$ nanosheets. ....	55
Figure 3.5. XPS for films of alloyed TMD nanosheets. ....	57
Figure 3.6. Characterization of ternary alloyed nanosheets made from combinations of Mo, W, S, and Se. ....	58
Figure 3.7. Characterization of quaternary alloy $\text{Mo}_{0.5}\text{W}_{0.5}\text{SSe}$ . ....	59
Figure 3.8. STEM EDX and high-resolution STEM of 2D $\text{Mo}_{0.5}\text{W}_{0.5}\text{SSe}$ nanosheets.....	60
Figure 3.9. Summary of electronic structures of the ECPI-made 2D TMDs.....	62
Figure 4.1. Roll-to-roll (R2R) apparatus. ....	70
Figure 4.2. Ultraviolet-visible spectroscopy for the R2R solvent system. ....	71
Figure 4.3. Comparison of number of dispersion injection sites.....	72
Figure 4.4. Optimization of $\text{MoS}_2$ nanoflake film loading. ....	73
Figure 4.5. Optimizing substrate pre-treatment. ....	74
Figure 4.6. Reproducibility of R2R-made films.....	75
Figure 4.7. Characterization of R2R deposited nanoflake films. ....	76
Figure 4.8. Characterization of R2R nanoflake films. ....	76
Figure 4.9. PEC characterization of R2R nanoflake films.....	77
Figure 4.10. Comparison of substrate roughness and conductivity.....	78
Figure 4.11. Characterization of batch scale $\text{WSe}_2/\text{MoS}_2$ heterojunction film. ....	79
Figure 4.12. Characterization of a R2R $\text{MoS}_2/\text{WSe}_2$ heterojunction film. ....	80

## List of Tables

Table 1. Reference table comparing the performance of ECPI-made nanosheets to other relevant works. ....	43
Table 2. Summary of parameters used in the semi-continuous deposition injection rate study. ....	73
Table 3. Substrate sheet-resistivity as measured by a four-point probe. ....	78

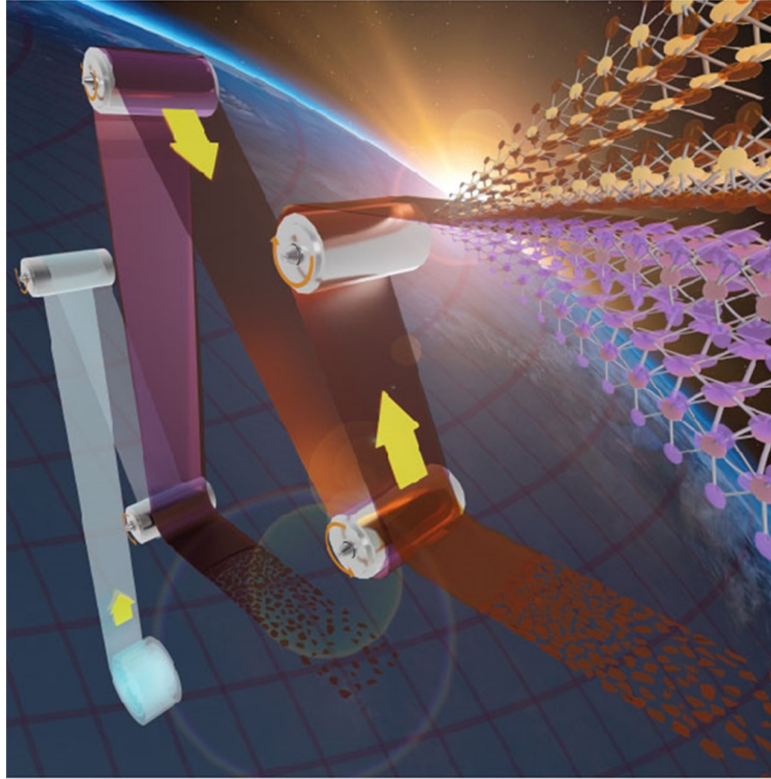
## List of Equations

Equation 1.1. Bowing parameters.....	6
Equation 2.1. Absorptance of MoS <sub>2</sub> film on FTO-glass.....	45
Equation 2.2. Extracted absorptance of MoS <sub>2</sub> . ....	45
Equation 2.3. Charge carrier mobility. ....	46

## List of Annex Items

Annex Item 1. Additional high-resolution STEM images for ECPI-made and ultrasonicated MoS <sub>2</sub> .....	90
Annex Item 2. Raw images from optical defect mapping experiment (2D PAINT) for sonicated and ECPI-made MoS <sub>2</sub> . ....	90
Annex Item 3. Raw LSV for "champion" performing device for ECPI-made MoS <sub>2</sub> nanosheets. ....	91
Annex Item 4. Typical batch-scale nanoflake films made <i>via</i> LLISA deposition. ....	91
Annex Item 5. STEM EDX of exfoliated nanosheets made from alloyed powders which were not mechanically ground.....	92
Annex Item 6. iDPC image of a Mo <sub>0.5</sub> W <sub>0.5</sub> S <sub>2</sub> nanosheet. ....	92
Annex Item 7. Detailed fittings of W4f spectra.....	93
Annex Item 8. Detailed fittings of Mo3d spectra. ....	93
Annex Item 9. Composite of Raman spectra for pure, ternary, and quaternary TMD materials. ....	94
Annex Item 10. PL of a glass slide. ....	94
Annex Item 11. Electron microscopy of batch-scale LLISA films of ultrasonicated TMD nanoflakes. ..	95
Annex Item 12. Additional PEC characterization of R2R films. ....	95

# Chapter 1 State-of-the-art, challenges, and motivation



Imagining global-scale implementation of 2D TMDs for solar energy conversion.

Two-dimensional (2D) transition metal dichalcogenides (TMDs) are an exciting and important emerging class of materials; however, to date promising devices made from these materials have remained at the laboratory scale. The purpose of this thesis is to contribute to the development of techniques to prepare and process 2D TMDs that can enable high performance while being amenable to large scale fabrication. Accordingly, this first chapter presents an overview of the background, concepts, and challenges addressed in this thesis. First, a basic introduction into TMDs and 2D TMDs is given including their intrinsic semiconducting properties and general strategies for modifying them (sections 1.2-1.4). The next section (section 1.5) introduces solution processable routes for thin films of 2D TMDs. This is followed by sections detailing each stage of the fabrication process including: exfoliation (section 1.6), size selection (section 1.7), film formation (section 1.8), and post processing techniques (section 1.9). In addition to current and past works these sections highlight ongoing challenges that need to be overcome. Finally, the last section (section 1.10) provides the motivation for this thesis and gives an overview of the following chapters.

## 1.1 Introduction

In recent years the world has seen shortages in semiconductor-based devices as a result of climate change, a global pandemic, and geopolitical tensions.<sup>1,2</sup> A key issue is the dominance of silicon in the semiconducting market and the world's heavy dependence on it, creating a supply-demand crisis. In particular, silicon-based photovoltaic materials, which represent a key part of renewable energy technologies, made up 95% of the market in 2020.<sup>3</sup> However, as a result of dangling bond terminated surfaces, silicon is susceptible to both photocorrosion in ambient environments and photochemical corrosion in electrolyte.<sup>4–8</sup> Likewise, would-be alternative III-V compound semiconductors such as GaAs suffer from photochemical instability for similar reasons.<sup>4,5,7,9</sup> This presents a major barrier towards their use in photoelectrochemical (PEC) applications in particular. Indeed, the best chance of halting climate change is a switch to renewable energy where solar represents the most abundant and promising source, making the development of stable, high-performing photovoltaic (PV) and PEC devices crucial. Thus, there is a critical need to diversify our sourcing of semiconductors to include non-traditional materials that can withstand extreme environments. Such materials should be made of earth-abundant components, be stable under harsh conditions, possess high absorption coefficients, and be facile to process via scalable and economical routes. Considering these numerous restrictions, an emerging class of semiconducting materials promises to present a solution: two-dimensional (2D) transition metal dichalcogenides (TMDs).

Bulk TMDs are earth abundant, cheap, and extremely robust. They exist as layered structures such that their basal planes are dangling bond-free, making them resistant to destructive process like oxidation or photocorrosion.<sup>10</sup> Additionally, they possess promising optoelectronic properties which can be tuned based on thickness and elemental composition.<sup>10,11</sup> For these reasons bulk TMDs have long attracted interest in a range of applications including solar energy conversion,<sup>12,13</sup> energy storage,<sup>14,15</sup> and electronics.<sup>16,17</sup> More recently the ability to produce, identify, and manipulate 2D versions of these materials has greatly expanded their application reach and improved their device performance. Their atomically-thin nature has even been shown useful in circumventing long-standing challenges faced by thicker devices, such as those based on silicon.<sup>18–20</sup> When considering 2D TMDs, materials such as MoS<sub>2</sub>, WSe<sub>2</sub>, WS<sub>2</sub>, and MoSe<sub>2</sub> demonstrate improved semiconducting properties compared to their bulk counterparts. This represents a path towards ultrathin devices which give higher performances while using less material. As such, 2D TMDs are ideal candidates to become the foundation of next-generation optoelectronic devices.

## 1.2 Bulk TMD crystal structure

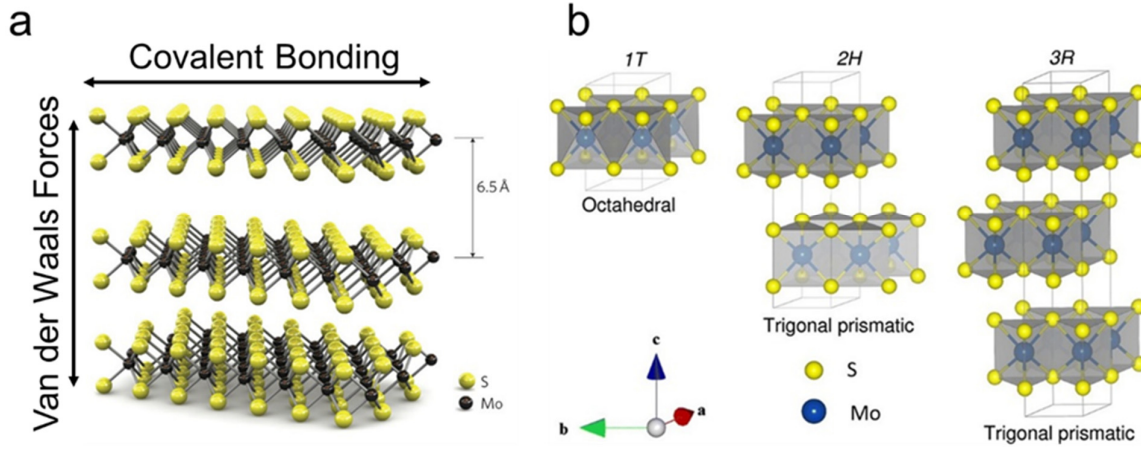


Figure 1.1. Schematic representations of TMD atomic structure and polymorphs.

(a) Depiction of layered TMD structure depicting van der Waals interlayer forces and covalent intralayer bonding. (b) Schematic of TMD polymorphs depicting the semi-metallic 1T phase (left) and the semiconducting hexagonal 2H (middle) and rhombohedral 3R (right) phases. Figures reproduced from references <sup>21</sup> (a) and <sup>22</sup> (b).

Atomically, TMDs are composed of X-M-X layers, where M is the transition metal (Mo, W, Re, Nb, etc.) and X are the chalcogen atoms (S, Se, Te).<sup>10</sup> Covalent bonding is experienced in-plane, while weak van der Waals (vdW) forces hold the layers together (Figure 1.1a.).<sup>10</sup> The surfaces of these layers are terminated with the lone pairs of the sulfur atoms which makes for dangling bond-free surfaces and inert basal planes.<sup>10</sup> In contrast the edges of the material are highly reactive due to the termination of the crystal.<sup>10,23</sup> Given the possible number of combinations, around 40 unique layered TMD compounds have been realized, exhibiting the full range of behaviors from metal to semimetal to semiconductor to superconductor.<sup>10</sup> Of the possibilities, M=Mo, W and X= S, Se are among the most studied for their intrinsic semiconducting behavior and are thus the combinations that will be further discussed in this thesis.

For these four combinations the most stable atomic configuration is the semiconducting 2H phase wherein the chalcogen atoms are stacked vertically in a trigonal prismatic geometry (Figure 1.1b).<sup>10</sup> This is in contrast to the semi-metallic 1T phase where the chalcogen atoms are rotated 90° to form an octahedral configuration.<sup>10</sup> Furthermore, the preferred stacking is the AbA BaB hexagonal form (2H), compared to the AbA CaC BcB rhombohedral unit cell (3R) (Figure 1.1b), where upper- and lowercase represent the chalcogen and metal atoms, respectively.<sup>10,22</sup>

### 1.3 Intrinsic semiconducting properties of 2D TMDs

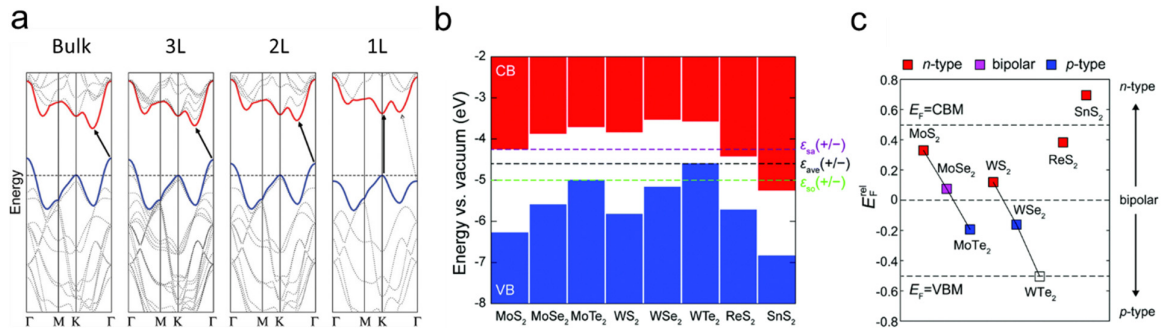


Figure 1.2. Band structure of TMDs based on thickness and composition.

(a) Calculated band diagram for MoS<sub>2</sub> from bulk (left) to monolayer (right). The red and blue lines highlight the CB minimum the VB maximum, respectively, across the Brillouin zone. The black arrows represent the allowed bandgap for the different thicknesses which increases as the material is thinned and transitions from indirect to direct. (b) Reported CB minima, VB maxima, and bandgaps for a range of 2D TMDs. (c) Reported Fermi levels and resulting semiconducting behavior for a range of 2D TMDs. Figures reproduced from references <sup>11</sup> (a) and <sup>24</sup> (b, c).

Briefly, the electronic structure of inorganic semiconductors is made up of electronic states that can be occupied by electrons, and which make up two “continuous” allowed energy bands: valence and conduction, displayed in Figure 1.2a in blue and red, respectively. The valence band (VB) edge (or maximum) is the highest occupied band while the conduction band (CB) edge (or minimum) is the lowest unoccupied band. The space between these two entities is known as the band gap, wherein no state can exist. To promote an electron from the VB to the CB photons can be used as an energy source, creating photogenerated charges that can be harnessed to drive electrical, chemical, and electrochemical processes.<sup>25</sup>

Each feature of the band structure greatly effects the way the semiconductor interacts with its surroundings including reactivity and light absorption. For example, a large bandgap material will only absorb high energy photons and is generally more photostable. Additionally, the location of the VB maximum and CB minimum will determine if a photogenerated charge (hole or electron, respectively) has enough potential energy to drive a chemical reaction.<sup>25</sup> Thus, it is of great interest to be able to exert control over a material’s electronic structure and therefore semiconducting behavior.

Naturally, the elemental composition of the TMD is the first consideration. For example, MoS<sub>2</sub> and WS<sub>2</sub> typically display n-type dominant behavior, where electrons are the majority carrier, while WSe<sub>2</sub> behaves inversely as a p-type material with hole majority carriers (Figure 1.2c).<sup>17,24–26</sup> MoSe<sub>2</sub> is generally considered to be ambipolar, displaying both behaviors facily.<sup>24</sup> Another example, MoS<sub>2</sub> and WS<sub>2</sub> have larger bandgaps compared to the selenides, affording them more stability and resistance to degradation (Figure 1.2b).<sup>24,25,27</sup> Furthermore, the energy level of the conduction band in WSe<sub>2</sub> is such that a photogenerated electron can perform the water reduction reaction while the same cannot be said for MoS<sub>2</sub> (Figure 1.2b).<sup>26</sup>

In addition to elemental composition (MX<sub>2</sub>) and atomic configuration (e.g., 2H, 1T, or 3R phase), the semiconducting properties of 2D TMDs are dependent on the number of layers. In fact, quantum confinement caused by the thinning of these materials from bulk to atomic thickness leads to new and often improved optical, electronic, and mechanical properties.<sup>11,28,29</sup> For example, bulk MoS<sub>2</sub> possesses an indirect bandgap of around 1 eV.<sup>11,12,30</sup> By thinning the material the bandgap is widened, eventually transitioning to a direct bandgap of around 1.9 eV in the monolayer case (Figure 1.2a).<sup>11,30</sup> This leads to the emergence of phenomena such as photoluminescence and ambipolar behavior in the presence of an electric field. Similar trends are observed for WS<sub>2</sub>, WSe<sub>2</sub>, and MoSe<sub>2</sub>.<sup>27</sup>

## 1.4 Tuning the semiconducting properties of 2D TMD nanoflakes

While choice of TMD composition and thickness already offers a certain degree of tunability, the optoelectronic properties of 2D nanoflakes can be further tuned via heterojunctions, doping, defect engineering, and alloying. These concepts are briefly introduced here but will be discussed in more detail in later sections.

### 1.4.1 Heterojunctions

A heterojunction occurs when two materials with different bandgaps are interfaced. The electronic communication is a direct result of the band alignments, which create an interfacial dipole.<sup>31</sup> For example,  $\text{MoSe}_2$ - $\text{MoS}_2$  forms a type II staggered junction where electrons are funneled from  $\text{MoSe}_2$  to  $\text{MoS}_2$  and holes are transported in the opposite direction (Figure 1.2b). As such, a type II heterojunction is a reasonable strategy to increase photogenerated charge separation and avoid recombination. When considering inorganic combinations, vdW heterojunctions (ex.,  $\text{MoSe}_2$ - $\text{MoS}_2$ ) present a particular advantage because they are not subject to problems caused by lattice mismatch in chemically bonded junctions.<sup>31</sup> Hybrid heterojunctions can also be made by interfacing an inorganic and organic material. Here the tunability of organic material can be leveraged; however, stability of the organic layer can be an issue.<sup>32</sup>

### 1.4.2 Doping

Doping provides another means of modifying the carrier concentration of a semiconductor from its intrinsic levels. As intrinsic carriers are already low it only takes a very small amount of doping to produce drastic changes in the optoelectronic behavior of the material.<sup>25</sup> Doping with a comparatively rich electron species leads to n-type doping, while doping with electron deficient species yields p-type doping.<sup>25</sup> Classically this was done by introducing an impurity atom into the crystal lattice of the material.<sup>25</sup> Mo- and W-based TMDs can experience n-type doping by the addition of transition metals in columns further right (Re, Rh, etc.) on the periodic table and p-type doping from columns further left (Nb, Zr, etc.). Another strategy uses molecular chemistry to modulate charge carrier concentration. Molecular doping can be split into two groups: non-covalent and covalent interactions.<sup>33</sup> Briefly, non-covalent molecular doping (ex., physisorption) can be based on (1) redox couples which donate either electrons or holes based on the band alignment of the TMD,<sup>34</sup> or (2) permanent dipoles which generate an electric field at the surface of the TMD.<sup>33</sup> This approach has the advantage of leaving the TMD crystal lattice unaltered, but the disadvantage of being an unstable interaction.<sup>33</sup> On the other hand, covalent molecular doping involves creating a stable chemical bond between the TMD layer and the molecular dopant.<sup>33</sup> Typically this takes place by taking advantage of point defects (ex., chalcogenide vacancies) or phase engineering (semi-metallic 1T phase). Notably this requires starting with defective material in order to obtain these interactions.

### 1.4.3 Defect engineering

Often considered a form of doping, defect engineering can be a viable route for tuning the semiconducting properties of TMDs in of itself. It is well-known that defects are naturally present in TMDs and take the form of point defects, grain boundaries, dislocations, phase impurities, and so on (Figure 1.3a).<sup>10,33,35–41</sup> Indeed defects, especially point defects, lead to a density of states within the bandgap, which causes the observations of p- and n-type behavior (Figure 1.3b).<sup>35,40</sup> One of the simplest examples is seen in  $\text{MoS}_2$  where sulfur vacancies cause n-type doping by introducing lone pairs to the lattice, while excess sulfur causes p-type doping (Figure 1.3b).<sup>35</sup> Interestingly, “defect engineering” can involve creating or healing defects to push the behavior in one direction or the other as desired and it is not uncommon for scientists to exert control by first creating defects (i.e. sulfur vacancies) and then healing (i.e. chemical treatment, annealing) them incrementally.<sup>33,41,42</sup> To create these defects they can be done in-situ (during synthesis) by adjusting growth or exfoliation conditions or ex-situ (post-synthesis) via numerous methods including but not limited to: electron beam radiation, ion beam radiation, plasma treatment, thermal treatment, and so on.<sup>35,42</sup>

### 1.4.4 Alloying

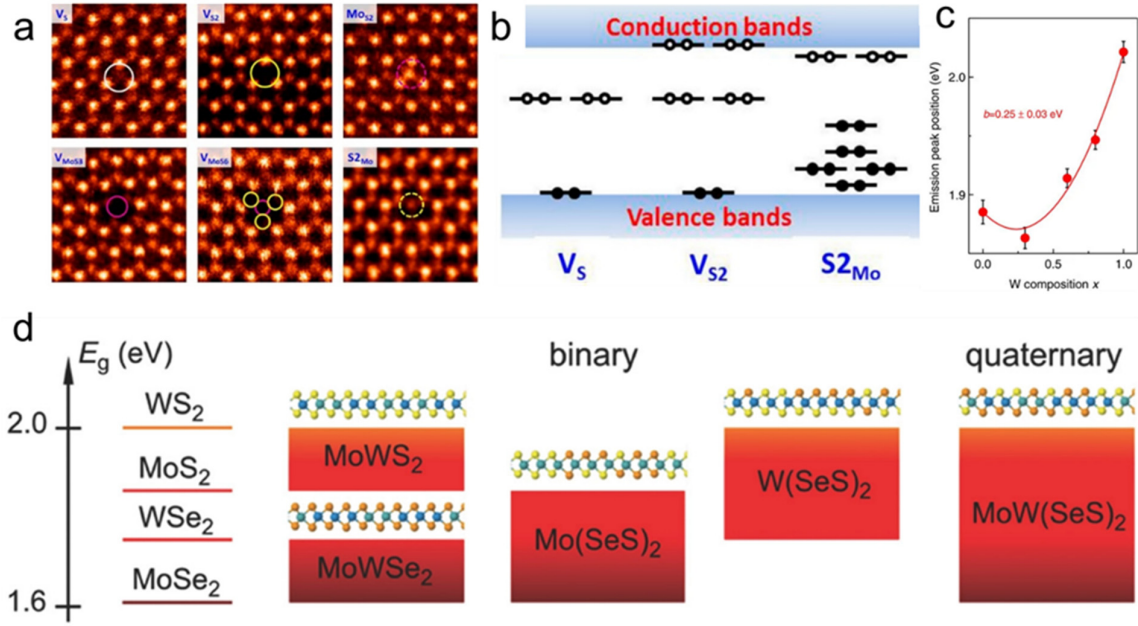


Figure 1.3. Influence of defects and alloying on TMD band structure.

(a) Atomic resolution of intrinsic defects in monolayer MoS<sub>2</sub>. From left to right: S monovacancy, S double vacancy, S replaced by Mo atom, vacancy complex of Mo and three S pairs, vacancy complex of Mo and six S pairs, and Mo are placed by S column. (b) Schematic representation of the energy levels of the defects identified in (a) leading to inter bandgap states. (c) Example of the band bowing phenomenon observed in alloyed TMDs. (d) Schematic showing the band gaps of pure monolayer TMDs and the potential band gap range for ternary TMDs and quaternary TMDs from Mo, W, S, and Se. Figures reproduced from references <sup>43</sup> (a,b), <sup>44</sup> (c), and <sup>45</sup> (d).

Finally, alloying allows for continuously tunable bandgaps, where the optoelectronic properties can be precisely controlled based on the alloy combination and composition. The formation of these alloys is energetically favorable and complete miscibility is attainable.<sup>46,47</sup> Indeed, all possible combinations involving Mo, W, S, and Se, including ternary and quaternary alloys have been predicted theoretically and demonstrated experimentally (Figure 1.3d).<sup>44–52</sup> As is the case for the pure materials, monolayer TMD alloys possess direct bandgaps because the same orbitals participate in the conduction and valence band of the alloys as the pure materials.<sup>46,47</sup> However, the location point of the alloyed bandgap in the Brillouin zone may differ from the pure case and the bandgap energy varies parabolically as a function of alloy composition (Figure 1.3c).<sup>44–47</sup> This is due a phenomenon known as bandgap bowing and can be described by Equation 1.1, where MX<sub>2</sub> and MX<sub>2</sub>' represent the two alloys, E<sub>g</sub> is the bandgap energy, x is the concentration of the MX<sub>2</sub>' alloy, and b is the bowing parameter.<sup>45,47</sup>

$$E_{E_g, MX_2 - MX'_2} = (1 - x)E_{E_g, MX_2} + (x)E_{E_g, MX'_2} - bx(1 - x)$$

Equation 1.1. Bowing parameters.

This relationship can be broadly explained by intra-band coupling within the bands and inter-band coupling between them.<sup>47</sup> Intra-band coupling raises the VB and lowers the CB (i.e., smaller bandgap) while inter-band coupling has the reverse effects (i.e., larger bandgap).<sup>47</sup> Thus, the composition of the alloys, which controls the contributions from each set of orbitals, dictates which band interaction is dominate and to what degree.<sup>46,47</sup> The vast number of possible TMD combinations in conjunction with composition tuning allow for unprecedented optoelectronic opportunities for these materials.



## 1.5 Solution-processable routes towards thin films of 2D TMDs

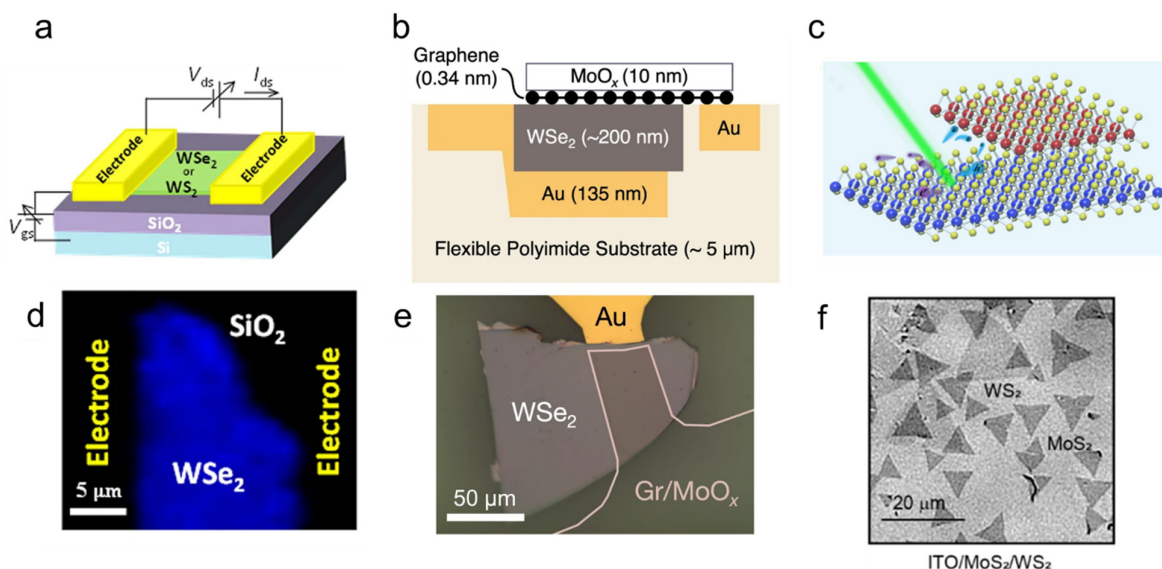


Figure 1.4. Examples of single flake PV and PEC devices.

Schematics of (a) rigid solar cell device based on a single flake of mechanically exfoliated WSe<sub>2</sub> or WS<sub>2</sub>, (b) flexible solar cell device based on a single flake of mechanically exfoliated WSe<sub>2</sub>, and (c) PEC system based on single flake and heterojunctions of MoS<sub>2</sub> and WSe<sub>2</sub>. (d) Raman mapping of single flake device depicted in (a). (e) Optical image of single flake device depicted in (c). (f) Optical transmission images of the CVD grown flakes depicted in (c). Figures reproduced from references <sup>53</sup> (a,d), <sup>3</sup> (b,e), and <sup>54</sup> (c,f).

For most applications using semiconducting devices (electrical, photovoltaic (PV), photoelectrochemical (PEC), etc.) thin films represent a large majority of the device configuration. However, to date the vast majority of research on TMD based solar energy conversion devices has been based on single flake or single crystal devices (Figure 1.4).<sup>3,26,30,54–60</sup> While these devices have uncovered the potential of TMDs for solar energy conversion, they are typically fabricated using methods which are challenging to upscale such as mechanical exfoliation (Figure 1.4a-d) or chemical vapor deposition (CVD) (Figure 1.4e,f) and are therefore not viable for large scale energy conversion.<sup>61</sup>

When considering solar energy conversion at a global scale, for example, large-area films represent the most promising approach.<sup>61</sup> Thus, to realize the goal of introducing semiconducting 2D TMDs to the global market, it is vital to be able to produce high-performing, large-area 2D TMD films in a facile and economic manner.<sup>61</sup> Due to challenges in scale-up this thesis will not consider bottom-up approaches (CVD, physical vapor deposition (PVD), molecular beam epitaxy (MBE), etc.), but will instead focus on top-down methods for thin film fabrication.

Of the numerous possibilities, liquid-phase exfoliation (LPE) is promising owing to the mild conditions used and ease of production which readily facilitates upscaling. LPE of 2D materials was first demonstrated by transforming bulk graphite powder into graphene nanosheets via ultrasonication.<sup>62</sup> Soon after similar methods were used to demonstrate LPE on TMDs, namely MoS<sub>2</sub>, which afforded still more opportunity for tunability.<sup>63,64</sup> Thus, the notion of solution-processable 2D materials became a reality.

Accordingly, the next challenge was how to further process these materials including size selection and assembly into ultrathin films for devices. Once again, a number of methods have been proposed, some already existing such as spin coating, drop casting, or dip coating, while other techniques were specifically developed for the unique chemistry and geometry of these materials, i.e.: liquid-liquid interfacial self-assembly (LLISA).<sup>65</sup>

Finally, as with all thin films, these ultrathin films are subject to defects present in their structure which eventually hinder device performance.<sup>66–68</sup> This is especially detrimental for PV and PEC devices where defects act as recombination centers, competing with the desired mechanism and lowering the efficiency of the device.<sup>66,67</sup> For 2D TMD nanomaterials the defects present within the nanoflakes present a particularly difficult problem and ongoing challenge in the field.

In this next section, the different possible paths to process 2D TMDs from bulk powders to ultrathin films of semiconducting nanomaterials are discussed and compared. Focus is placed on the importance of choosing a suitable exfoliation method to produce pristine, thin nanosheets with large lateral dimensions and the ongoing need for alternative methods. Next discussed is the importance of careful film preparation including nanoflake size-selection and how to maximize nanoflake-substrate communication. Finally, potential defect mitigation strategies to cope with defects within the nanoflakes are explored. Special emphasis is placed on pathways which are fully scalable while offering pristine TMD nanoflake films.

## 1.6 Liquid phase exfoliation methods

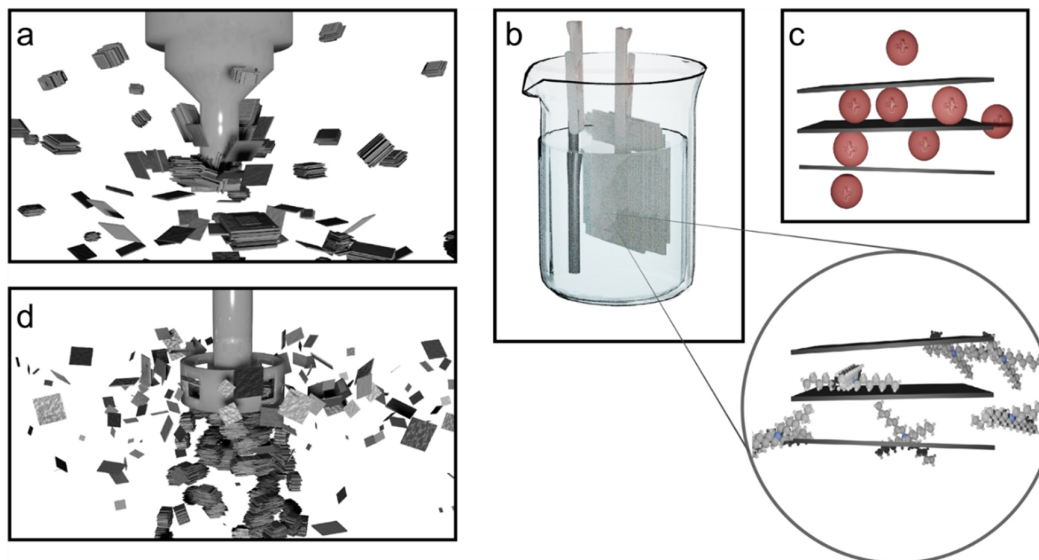


Figure 1.5. Schematic representations of popular LPE methods.

(a) Ultrasonication of bulk TMD nanosheets (black) using a horn probe (gray). (b) Electrochemical intercalation of a single crystal TMD (right) with large molecule cation THA<sup>+</sup> (inset). (c) Small ion (pink) intercalation of bulk TMD structure (black). (d) Shear mixing bulk TMD (black) using a high-speed rotor (gray).

The first step in the bulk-to-2D thin film process is exfoliating the bulk material into 2D material which can be later used for processing. As previously discussed, solution-processable methods offer the most flexibility in terms of scalability and processability. When considering scalable methods, commercially available, micron-sized powder is preferred over single crystals as starting material. With this in mind, there are three techniques which dominate the literature: ultrasonication, shear mixing, and ion intercalation.

### 1.6.1 Ultrasonication

As discussed in the introduction, solvent-assisted exfoliation via ultrasonication was one of the first routes developed for LPE of layered materials (Figure 1.5a). Briefly, the method works by introducing ultrasonic waves to a solvent, whose surface tension should match closely that of the surface energy of the layered material.<sup>69</sup> The ultrasonic waves generate cavitation bubbles at the edges and in between the layers of the material.<sup>69</sup> When these bubbles collapse high-energy microjets form which can overcome the interlayer forces of the (vdW) material, breaking them apart.<sup>69</sup> Notably these forces cause breaks in the *z* direction to separate the layers, but also in the *x-y* plane inducing scission across the crystal structure.<sup>64</sup> This second feature leads to two main drawbacks: poor nanoflake morphology in the form of small lateral dimensions and uneven layers and high defect densities particularly on the edges but also across the planes of the flakes.<sup>64</sup> Indeed, it has been well-documented, especially for MoS<sub>2</sub>, that nanoflakes suffer from a size-thickness dependency wherein thin flakes have small lateral dimensions and only thicker flakes possess larger dimensions.<sup>64,67</sup> It has also been shown that high quantum yields in TMD nanoflakes can only be achieved with thin flakes possessing large lateral dimensions, presenting an intrinsic limitation for devices made from ultrasonicated nanoflakes.<sup>67</sup> Additionally, it has been well-documented that the uneven layers lead to step edges across the basal plane of the flakes, effectively creating edge-defects across the basal plane.<sup>64,66,67</sup> Because of these drawbacks, 2D TMD nanoflakes made via ultrasonication tend to give poor device performance and require additional treatment methods to mitigate the defects.<sup>66,67</sup> For these reasons more attention has been directed towards finding alternative LPE methods to ultrasonication.<sup>70,71</sup>

### 1.6.2 Shear-mixing

In an effort to avoid the drawbacks of ultrasonication, scientists sought to employ shear-mixing (Figure 1.5d), a technique already widely used for dispersing nanoparticles.<sup>72,73</sup> Using a high speed rotor, fluid shear is created when the velocity of the fluid at the center of the rotor differs from that at the outside diameter. While being much gentler, this technique relies on similar principles to ultrasonication such as choosing an appropriate solvent and inputting energy to overcome the van der Waals forces between the layers.<sup>72</sup> However, these energy densities are orders of magnitude lower for shear-mixing and the mechanism involves shear-induced interlayer sliding.<sup>72</sup> Despite this method being more gentle, studies showed that the nanoflakes produced were indistinguishable compared to ultrasonicated nanomaterial.<sup>72</sup> That is, that the size-thickness dependency continues to be an issue with thin nanoflakes possessing small lateral dimensions.<sup>73</sup> Thus, while shear-mixing provides additional options for scalability it does not provide any clear advantages in terms of nanoflake morphology. Indeed, in-house attempts to exfoliate MoS<sub>2</sub> with shear mixing yielded high volumes of nanomaterial, but with poor device performance in PEC applications, even compared to sonicated samples.

### 1.6.3 Ion intercalation

Still another method for LPE is ion-intercalation, wherein a cation is inserted in between the layers of a van der Waals material, thereby expanding the interlayer spacing (Figure 1.5c).<sup>69,74</sup> As this weakens the interlayer forces agitation can then be used to exfoliate the materials.<sup>69,74</sup>

The most commonly used is the lithium ion. In this case the agitation is caused by exposing the intercalated material to water which reacts with the metal cation, producing hydrogen and breaking apart the layers.<sup>75</sup> While this method produces high yields of material, the process leads to a phase transition from the semiconducting 2H phase to the semi-metallic 1T phase.<sup>74–76</sup> The resulting material is also small, fragmented, and riddled with defects.<sup>75,76</sup> For catalytic applications these properties are desirable,<sup>75–77</sup> but for semiconducting and PEC applications they are disastrous.<sup>74,78,79</sup>

Recently a few groups found a way to take advantage of the high yields offered by ion-intercalation, while maintaining the semiconducting behavior of the TMD nanoflakes.<sup>78,80</sup> Rather than small, highly reducing cations, these works use large molecule cations whose effects are benign.<sup>78,80</sup> As the molecules are much larger than the interlayer spacing of the materials, scientists used electrochemical intercalation to drive these molecules in between the layers of single crystal TMDs (Figure 1.5b), which are intrinsically conductive.<sup>78,80</sup> The size of the molecules is such that only gentle agitation is required to exfoliate the materials from their intercalated state to 2D nanoflakes.<sup>78,80</sup> In fact, they show that this method gives extremely thin nanoflakes with (1-3 layers) with remarkably large lateral dimensions.<sup>78,80</sup> Furthermore, the gentle nature of the exfoliation yields sheets with uniform basal planes, notably absent of the step edges observed in ultrasonication.<sup>80,80</sup> Despite the major advance in solution-processable techniques, the scalability of this method is limited owing to its use of large single crystals as starting material.

As such there remains a need in the field for an LPE method which can produce thin, large-area nanoflakes using a fully scalable approach.

## 1.7 Nanomaterial size selection

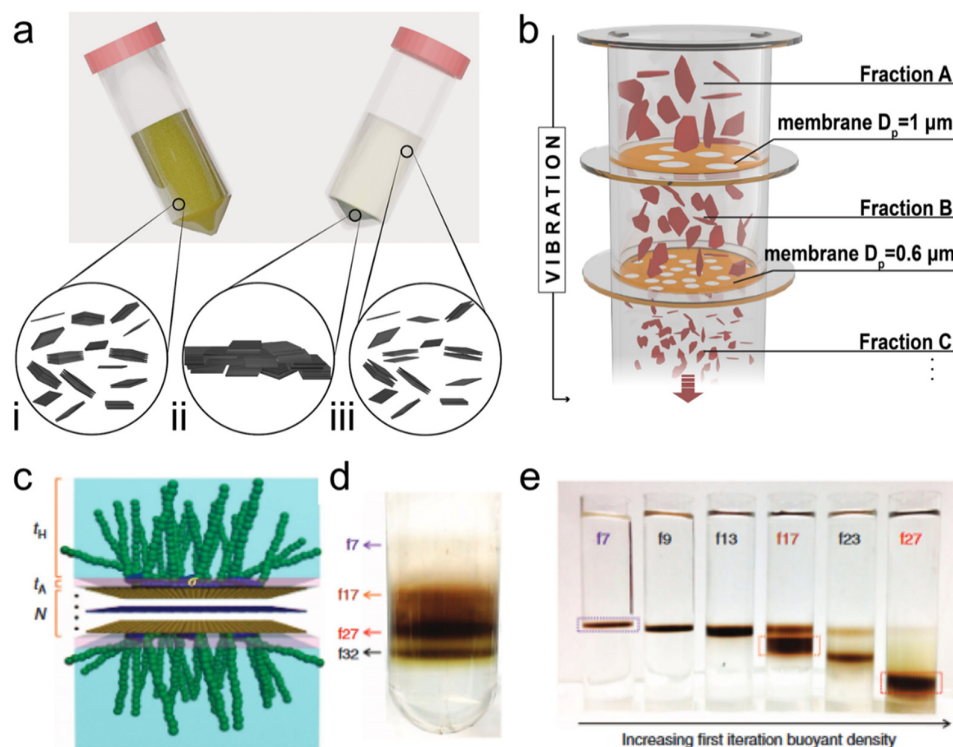


Figure 1.6. Depictions of three common techniques used to separate nanoflakes by size.

(a) Schematic of centrifugation. The starting dispersion (left) is made up of a polydisperse mix of nanoflakes both thick and thin (i). After centrifugation a new dispersion is obtained (right) where large material has been sedimented (ii) leaving thinner material in the supernatant (iii). (b) Schematic of sieve-based filtration. A raw dispersion is introduced to the top compartment and is sequentially filtered as the solution moves down the column through the membranes. Pore size of the membrane decreases at each stage effectively separating the nanoflakes into groups with different lateral dimensions. (c) Schematic depicting surfactant (green) altering the buoyancy of the nanoflake (yellow and purple) in solution. (d) Example of DGU performed on a dispersion of  $\text{MoS}_2$ . The observed bands are a result of nanoflakes of different buoyancies settling along the induced gradient; heavier flakes settle at the bottom (f32) while lighter flakes remain higher (f7). (e) Additional DGU performed on the extracted bands shown in (b) where additional band formation is observed, indicative of further size separation. Figures reproduced from references <sup>67</sup> (b) and <sup>81</sup> (c-e).

Nanoflake size selection directly follows exfoliation. As with LPE there are many techniques for size selection in the liquid phase and the choice of method will change based on the needs of the desired final product. In terms of scalability centrifugation, density gradient ultracentrifugation, and filtration are among the most feasible and therefore the most popular. The advantages and drawbacks of each are briefly discussed in the following sections.

### 1.7.1 Centrifugation

Beginning with the simplest, centrifugation involves rotating samples at high speeds around an axis, taking advantage of the centrifugal force to separate particles from the solution based on size, shape, and density (Figure 1.6a). Generally speaking, the heaviest particles will collect in the bottom of the solution to form a pellet (Figure 1.6a-ii), while lighter particles remain in the supernatant of the solution (Figure 1.6a-iii). Depending on the application the user may wish to collect the heavier material in the pellet or the lighter material in the supernatant. The supernatant can also be further processed for additional size selection or purification.<sup>82</sup> For example, ultrasonication exfoliation of  $\text{MoS}_2$  or  $\text{WSe}_2$  often requires an initial low speed centrifugation to remove unexfoliated bulk material.<sup>65,66,82,83</sup> The supernatant is collected and centrifuged again at a higher speed, this time collecting the medium sized material in the pellet, leaving the smallest, fragmented parts in the supernatant to be discarded.<sup>65,66,83</sup>

The advantages of centrifugation are that it is simple and easy to perform and can be readily scaled up to process large volumes of material. Furthermore, yield can be easily tuned based on processing conditions.<sup>64</sup> However, the main disadvantage is the lack of control that can be exercised in the case of very polydisperse solutions, where acquisition of monodisperse thickness samples is nearly impossible.<sup>67</sup> Consider the case of a very large, thin flake and a very small, thick flake; the effects of the centrifugal force will act similarly on these two particles, causing them to exist in the same fraction.<sup>64,67</sup> Thus, it is challenging to separate the two populations and also implies that very large, thin flakes may be lost to the “bulk” fraction while extremely small, thick flakes may never be pulled out of the solution. As a result, centrifugation should be used in the case of applications requiring high-yield dispersions and where some flexibility in terms of nanoflake dimension can be afforded.

### 1.7.2 Density gradient ultracentrifugation

To overcome the issue of precise control, an iteration of centrifugation known as density gradient ultracentrifugation (DGU) can be used (Figure 1.6c-e). This technique, while similar to basic centrifugation, additionally exploits the differences in the buoyancy of the nanoparticles which is a function of their size.<sup>81,84,85</sup> Briefly, a solution is prepared such that it possesses a linear gradient, *i.e.* denser at the bottom than at the top. The nanoparticle dispersion is introduced to this density gradient solution and centrifuged, usually at high speeds (20-40 krpm) for long periods of time (> 40 hours).<sup>81,84,85</sup> During this time the nanoparticles move through the density gradient until they arrive at a region whose density matches their own; in some cases the nanoparticle is modified with a surfactant to tune its buoyancy (Figure 1.6c).<sup>81,84</sup> In this way an equilibrium is reached, and different “bands” can be observed as result of the well-separated fractions (Figure 1.6d).<sup>81,84,85</sup> The fractions can be used as they are or further processed for additional separation (Figure 1.6e). In this way dispersions with narrow size-distributions have been obtained for carbon nanotubes,<sup>84</sup> graphene,<sup>85</sup> and finally MoS<sub>2</sub>,<sup>81</sup> with application for other layered materials.

Naturally the clear advantage is a solution-processable route for extremely precise control over nanoflake lateral dimensions and thickness. The disadvantages are then that the method is rather cumbersome and easily botched, requires a special centrifuge, requires long processing times, and produces relatively low yields. The scalability of this complex method, while necessary and even more so due to low yields, is thus less accessible than other separation methods. However, for applications where only certain nanoflakes of unique dimension can be used (ex: monolayer with 1.5  $\mu\text{m}^2$  area) DGU is an appropriate choice.

### 1.7.3 Sieve filtration

Finally, there exists a third possibility which offers a compromise between size-selection, yield, and scalability yet relies on different principles of separation: sieve-based filtration (Figure 1.6b). This solution is a way to access different size classes of nanoflakes including the largest populations.<sup>67</sup> The size distributions are notably less precise than DGU, but still more narrow than centrifugation alone.<sup>64,67,81</sup> Similarly, yield is lower than for centrifugation, but higher than for DGU.<sup>64,67,81</sup> The filtration works by setting up a pressure-driven liquid column with multiple stages composed of membranes of decreasing pore size (Figure 1.6b). The crude dispersion is introduced at the top of the column. At the first stage large diameter flakes are blocked while small and intermediate flakes continue down the column. With decreasing pore size, nanoflakes of decreasing lateral dimensions are passed through. It was demonstrated that it was possible to obtain narrow distributions of flake lateral dimensions by using this method (Figure 1.7a-d). To further separate by flake thickness a simple centrifugation cycle can be applied as the weight of the flakes is then dominated by thickness rather than lateral dimensions. Overall yield here remains high as no nanoflakes are purposely discarded in the process and scale-up is achieved by simply increasing the filter area.

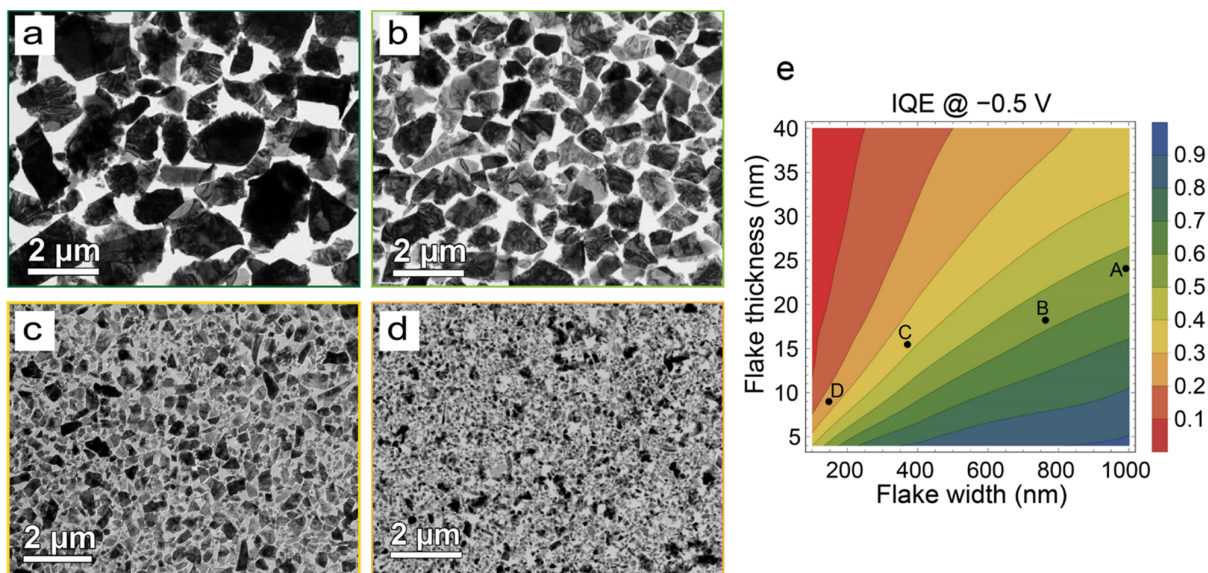


Figure 1.7. Relationship of nanoflake dimension to internal quantum yield.

(a-d) Transmission electron microscopy images of films of filtered nanoflake dispersions from largest (a) to smallest (d). (e) Estimated internal quantum efficiency (IQE) of  $\text{WSe}_2$  nanoflakes as a function of lateral dimensions and thickness based on simulated charge carrier transport. The marked regions labelled A-D represent the experimental results of the films depicted in a-d, respectively. Figures reproduced from reference <sup>67</sup> (a-e).

Once again, the advantages here are the ease of scalability, ease of operation, and a fairly narrow distribution of flake lateral dimensions. One can imagine that more and more filters could be added to narrow these distributions further, but that flow rate would eventually suffer as a result slowing the process. The column also requires constant agitation to prevent pore cake-up which can still be an issue. These factors along with the need for an additional step to separate by thickness represent the drawbacks for this method. This method is therefore an ideal compromise for situations where both good yield and narrow distribution are required.

Most importantly this study highlighted a clear relationship between nanoflake dimension and the quantum efficiency of the nanoflake (Figure 1.7e).<sup>67</sup> Essentially, flakes with small lateral dimensions, even if thin, and thick flakes, even with large lateral dimensions, suffer from low internal quantum yields and are intrinsically limited by this. However, large-area, thin flakes are predicted to show high internal quantum yields. This size-dependent performance highlights importance of careful nanoflake size separation and selection and reinforces the necessity to choose an exfoliation method which allows for production of the desired nanoflake morphology.

## 1.8 Solution-processable film formation

Once the nanoflakes have been produced and selected with care, they can be assembled into a thin film device. As with the previous sections, there are many ways to do this, but not all routes to film formation are created equally and much depends on the requirements of the final device. For most applications using thin films of TMD nanoflakes with good connectivity and free of nanoflake aggregates is necessary and preferential orientation may be required. With this in mind the next section presents brief overviews of some of the most popular methods: drop casting, doctor blading, spray coating, spin-coating, dip coating, and liquid-liquid interfacial self-assembly techniques.

### 1.8.1 Drop casting and related techniques

Beginning with the ubiquitous, drop casting is by far the simplest method to coat a surface and can be used in nearly any situation. As its name suggests, liquid containing the desired material is literally dropped onto the target substrate and allowed to dry. Naturally, the method can be tuned by the concentration of the dispersion, volume of the droplet, temperature of the substrate, and so on. However, it is challenging to obtain a homogeneous coating using this method owing to the “coffee ring” effect (Figure 1.8a).<sup>86,87</sup> That is to say that the material, which is initially distributed evenly over the drop and therefore surface, concentrates into the outer edges of the drop creating rings. A type of capillary flow is to blame for this behavior, wherein the edges in contact with the surface dry faster and are replenished with liquid from the interior, thereby confining a large portion of the material to the outer ring.<sup>86</sup> For some analyses where a uniform coating is not required this can be an acceptable trade: uniformity for simplicity; however, for many applications the nonuniformity as seen in Figure 1.8d poses major problems (aggregation, discontinuity, random orientation, etc.).<sup>87</sup>

Some groups have proposed ways to mitigate the ring effect by modifying the substrate (i.e., nanopatterning), modifying the dispersion (i.e., using ellipsoidal particles), or by changing the liquid-substrate environment during the drying process (i.e., applying a temperature gradient, applying bias, or applying surface acoustic waves).<sup>87</sup> Unfortunately, while the suggested methods prove effective, they severely complicate the process, eliminating the advantage of simplicity in the drop casting method. Furthermore, it is impossible to control particle orientation. While this is not an issue for spherical particles, the anisotropic nature of nanoflakes necessitates control over the orientation with respect to one another and to the substrate in order to achieve high-performing devices. This is discussed in more detail in section 1.8.4 (Liquid-liquid interfacial self-assembly).



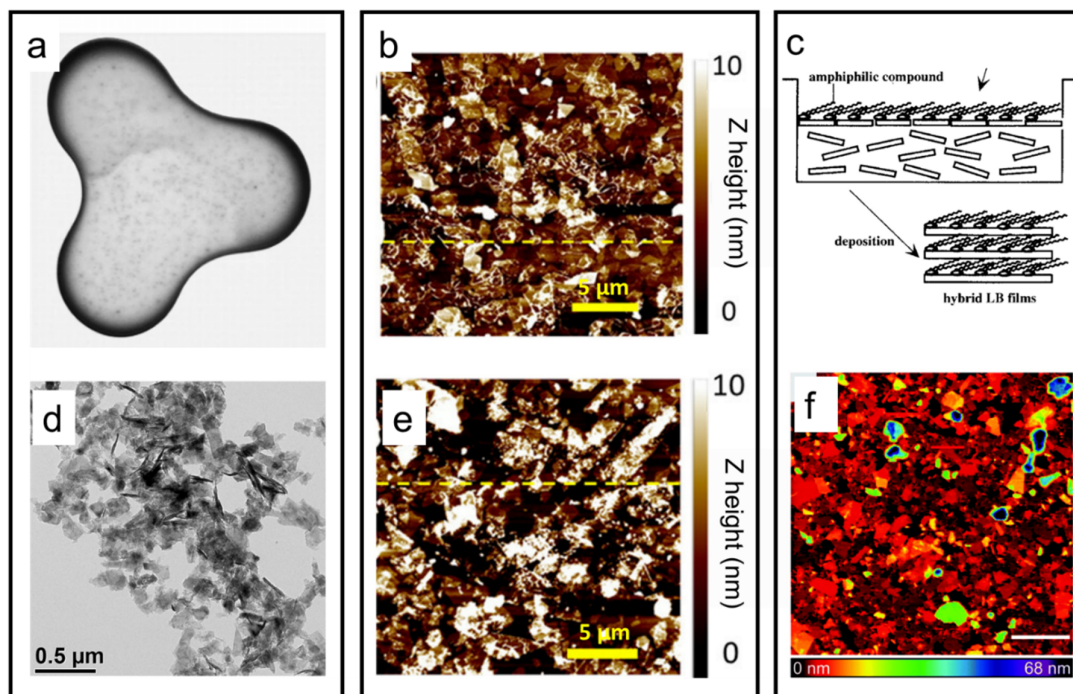


Figure 1.8. Examples of different film formation techniques.

These techniques include drop casting (left), spin coating (middle, top), spray coating (middle, bottom), and Langmuir-Blodgett (LB). (a) Optical image of the “coffee ring” effect as demonstrated by a drop of coffee. (d) transmission electron microscopy image of drop casted MoS<sub>2</sub> nanoflakes. Atomic force microscopy images of (b) spin coated, (e) spray coated MoS<sub>2</sub>. (c) Schematic of the Langmuir-Blodgett technique. (f) Atomic force microscopy image film made using LB film formation. Figures reproduced from references <sup>86</sup> (a), <sup>88</sup> (b, e), <sup>89</sup> (c), <sup>82</sup> (d), and <sup>90</sup> (f).

Two other methods which can be considered upgraded versions of drop casting are doctor blading and spray coating. The first involves dragging a blade over the drop casted dispersion and substrate to create a more uniformly thick film. The latter uses a nozzle to spray a heated solution into a substrate (Figure 1.8e). Both methods can be used to avoid the “coffee ring” effect, but still suffer from other nonuniformities that arise during drying. Additionally, like with their parent method, no control over particle orientation can be exercised.<sup>88</sup> Therefore, these methods may be suitable for depositing organic molecules and polymers but are still inadequate to form high-quality TMD nanoflake films.

Still another method based on the drop casting technique is spin-coating. In this case the dispersion is once again dropped on the substrate, however rather than leaving the droplet to dry as is, the substrate is spun around the z-axis, evenly distributing the solution across the substrate (Figure 1.8b).<sup>88</sup> This method control film thickness reliably and reproducibly and can be tuned again via droplet volume and concentration as well as by spin speed and time. However, the issue continues to be the lack of control over flake orientation and flake-flake overlap.<sup>88</sup> Furthermore, spin coating is not considered a scalable technique when considering industrial applications and production.

## 1.8.2 Dip coating

An alternative to drop casting and its variants, dip coating is carried out by emerging and slowly withdrawing the substrate from the dispersion. Briefly, the nanoparticles are drawn into the meniscus created by the emerging substrate and deposited as the thin liquid layer dries. This generally leads to uniformly thick films with close particle packing; however, to achieve this the method needs to be optimized according to particle, dispersion solvent, and substrate. Additional factors to optimize and tune the final film include dispersion concentration and withdrawal speed. While this represents an easily scalable technique for homogenous film deposition, there is still no control over flake orientation or overlap.

Up to this point the film deposition techniques discussed have all suffered from a lack of control over the orientation of the particles with respect to the substrate and to one another. For nanoflakes this represents a serious challenge for high-performing devices. Still another challenge with the previous methods present itself in the case of multiple layer deposition. Essentially a good solvent which prevents aggregate formation in the dispersion can also dissolve a deposited nanoflake films. Therefore, each of the previous methods which require contact between the dispersion solvent and the substrate will also disturb the previously deposited film. One solution is to choose a poor solvent for the dispersion so as to not disturb the film, but then the risk of aggregates and inhomogeneous film formation is greater. It is therefore necessary to consider an entirely different kind of film deposition technique if one wants to make homogeneous, oriented thin films of TMD nanoflakes

### 1.8.3 Liquid-air interfacial self-assembly

To this end Langmuir-Blodgett (LB) techniques are considered as means of controlling nanoflake orientation via self-assembly. Originally the method was developed with surfactants which form a monolayer at the liquid-air interface, typically with water which is a poor solvent for organic molecules.<sup>91</sup> The monolayer of molecules could be transferred by simply moving a hydrophobic substrate through the interface.<sup>91</sup> The molecules, being more attracted to the substrate than the water, are transferred in the same orientation in which they self-assembled at the interface.<sup>91</sup> Notably this represents a relatively facile method with demonstrated control over particle orientation. Furthermore, because the particles are forced to the interface by choosing a poor solvent, multiple layer depositions are possible as the solvent will not disturb the already deposited film.

As with organic molecules, water is a poor solvent for untreated TMD nanoflakes; however rather than float to the surface the flakes will slowly form restacked aggregates and eventually crash out of solution. In an attempt to pull the flakes to the liquid-air surface early works employed amphiphilic compounds, which have both a hydrophilic part to attract the TMD nanoflake and a hydrophilic part that migrates to the surface.<sup>89,92</sup> Like this nanoflakes could be pulled from the dispersion to the liquid-air interface and deposited in the LB fashion.<sup>89,92</sup> In this way closely packed, oriented films are obtained. However, there is still a lack of control over nanoflake overlap and good contact between the basal planes of the flakes and the substrate is not guaranteed. Furthermore, these amphiphilic compounds are insulating and removing them post film deposition can be challenging.<sup>82</sup>

A version of this technique uses the water-air interface, dripping the nanoflake dispersion on the surface rather than try to pull them from the water.<sup>90</sup> As with previous demonstrations this creates tightly packed films (Figure 1.8f), however there is still no mechanism to control nanoflake overlap and ensure a flat surface. Thus, while these self-assembly methods represent important advances, some additional modifications are required in order to achieve the goal of well-oriented, non-aggregated thin films of TMD nanoflakes.

### 1.8.4 Liquid-liquid interfacial self-assembly

Taking inspiration from the LB techniques a space-confined liquid-liquid interfacial self-assembly (LLISA) film deposition technique was developed (Figure 1.9a).<sup>65</sup> In place of a liquid-air interface, this technique uses an interface between two immiscible liquids which are both poor solvents for TMDs, for example water and hexane. Rather than try to extract the nanoflakes from one of the poor solvents, a dispersion of nanoflakes in a good solvent (i.e., NMP) is injected directly at the interface between the two solvents. In the case of a water-hexane-NMP system, the NMP dispersion is injected just above the interface, the flakes settle at the water-heptane interface, and NMP, which is miscible with water, sinks into the water phase leaving only a single layer of flakes. As such the flakes are confined to the interface and forced to orient horizontally along the interfacial plane. Not only do the flakes self-orient, but they assemble such that overlap between flakes is minimized as long as injection stops once a complete film is formed. This creates a puzzle-like morphology of 2D TMD flakes as depicted in Figure 1.9b.

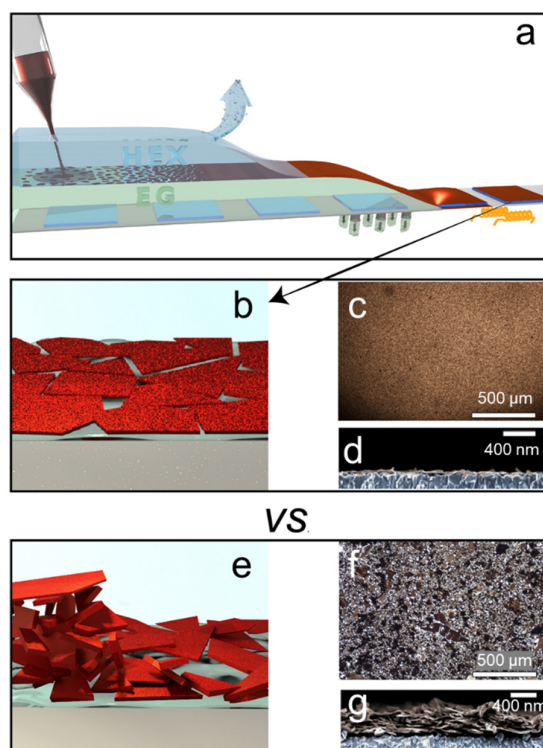


Figure 1.9. Description of LLISA film formation method.

(a) Schematic of LLISA method where the nanoflake dispersion (red) is injected at a hexane (blue)-ethylene glycol (green) interface until a complete film is formed after which the hexane layer is aspirated off and the ethylene layer removed to deposit the undisturbed film. (b) Illustration of LLISA film. (c) Top and (d) cross-section view of LLISA film. (e) Illustration of a film formed at an air-liquid interface. (f) Top and (g) cross-section view of air-liquid film. Figures reproduced from reference <sup>65</sup> (a-g).

After film formation at the interface, the top layer (hexane, for example) is removed via vacuum (or syringe) leaving the single layer of self-assembled nanoflakes on the surface of the water. The film can then be transferred to the desired substrate either from above, via stamping, or below, by placing the substrate in the water layer and slowly removing the water thereby lowering the film onto the substrate. Importantly both methods afford the user to maintain the same morphology created at the liquid interface in the final film (Figure 1.9b,c)

In the same work where this method was presented, it was shown that the LLISA film exhibited more desirable morphology than a film created at the liquid air interface (Figure 1.9e-g).<sup>65</sup> Notably no aggregates were formed (Figure 1.9c), and a single layer of flakes could be seen to clearly lie flat along the substrate (Figure 1.9d), neither of which was true for the air-liquid film (Figure 1.9e-g). The improved nanoflake-substrate contact led to improved film conductivity and superior performance as a photocathode for water reduction. Indeed, the film had higher photocurrents yet lower light absorption indicating superior incident photon-to-chemical conversion efficiency (IPCE). Importantly film thickness could be tuned by adding additional layers without disturbing previous layers all while maintaining the puzzle-like structure.

Since its realization the LLISA technique has been used frequently when dealing with 2D TMD nanoflakes as it delivers optoelectronic and electrochemical performances superior to previous works where any of the previously discussed methods were employed (drop casting, spin coating, etc.).<sup>66,67,82,93,94</sup> This allowed for the exploration of fundamental principles related to 2D TMD films without the convolution of poor substrate contact or faulty flake-to-flake charge transfer.<sup>67,72,94</sup> For example, the realization that optimal solar-to-chemical energy conversion takes place in large, thin flakes thereby motivating much of the work presented in this thesis.<sup>67</sup>

## 1.9 Fine tuning thin films of 2D TMDs

At this stage, after preparing, selecting, and depositing the TMD nanoflakes along the needs of the device, the process may be complete. However, as is often the case, additional modification may still be needed to enhance or adjust certain aspects of the film. In this final section a few of the many ways to do this, namely via heterojunctions and defect mitigation techniques, are considered.

### 1.9.1 Van der Waals heterojunctions

As briefly discussed in section 1.4.1, van der Waals heterojunctions (vdWHJ) can be an effective way both to tune the final properties of the film and enhance photogenerated charge separation, particularly in TMDs. The vdW interactions between the two materials help the two materials to restack with some degree of orientation and communicate electronically.<sup>60</sup> Of the three possible types, type II heterojunctions with staggered band alignment are the most promising for PEC applications.<sup>60</sup> Indeed, many works have focused on TMD vdWHJs with  $\text{WS}_2\text{-MoS}_2$ ,  $\text{WSe}_2\text{-WS}_2$ , and  $\text{WSe}_2\text{-MoS}_2$  being the most popular (Figure 1.10a-c).<sup>59,60,83,95-97</sup> As the CB minimum and VB maximum are found in separate materials, photogenerated charges prefer to migrate and reside in separate locations (Figure 1.10b).<sup>60,95,97</sup> This enhances charge separation and facilitates eventual charge transfer by reducing charge recombination.<sup>60,95,97</sup> Indeed, groups have shown photoluminescence quenching in monolayer vdWHJs suggesting efficient charge transfer and reduced charge recombination.<sup>60,95</sup> This is important for solid-state devices and crucial for PEC devices where transferring photogenerated charges out of the material to perform the desired chemical reaction can be challenging. Notably enhanced PEC performance has also been shown in  $\text{MoS}_2\text{-WS}_2$  vdWHJs.<sup>95,96</sup> Given the ease of creating high-quality TMD vdWHJs using the previously discussed LLISA method (Figure 1.10c), it is a powerful route towards enhancing the performance of TMD-based devices and one that is solution-processable.

### 1.9.2 Hybrid organic-inorganic heterojunctions

Beyond inorganic heterojunctions, combinations of organic and inorganic materials can be used to create type II junctions as well.<sup>93,98</sup> As the organic layer can be easily tuned it may even offer a greater range of possibilities compared to purely inorganic combinations. The feasibility of a hybrid organic/inorganic heterojunction was demonstrated using perylene-diimide functionalized with dihexanoic acid (DHA-PDI) and  $\text{MoS}_2$  (Figure 1.10d,e).<sup>93</sup> The hybrid system, used as a photoanode, produced photocurrents 6 to 10 times higher than either individual material (Figure 1.10f) and IPCE values up to 8 times higher. The behavior was explained by improved photogenerated charge carrier separation which is similar to that seen in the type II TMD vdWHJs (Figure 1.10f-inset). This simple demonstration suggests even more opportunity for tunability in solution-processable TMD-based devices.

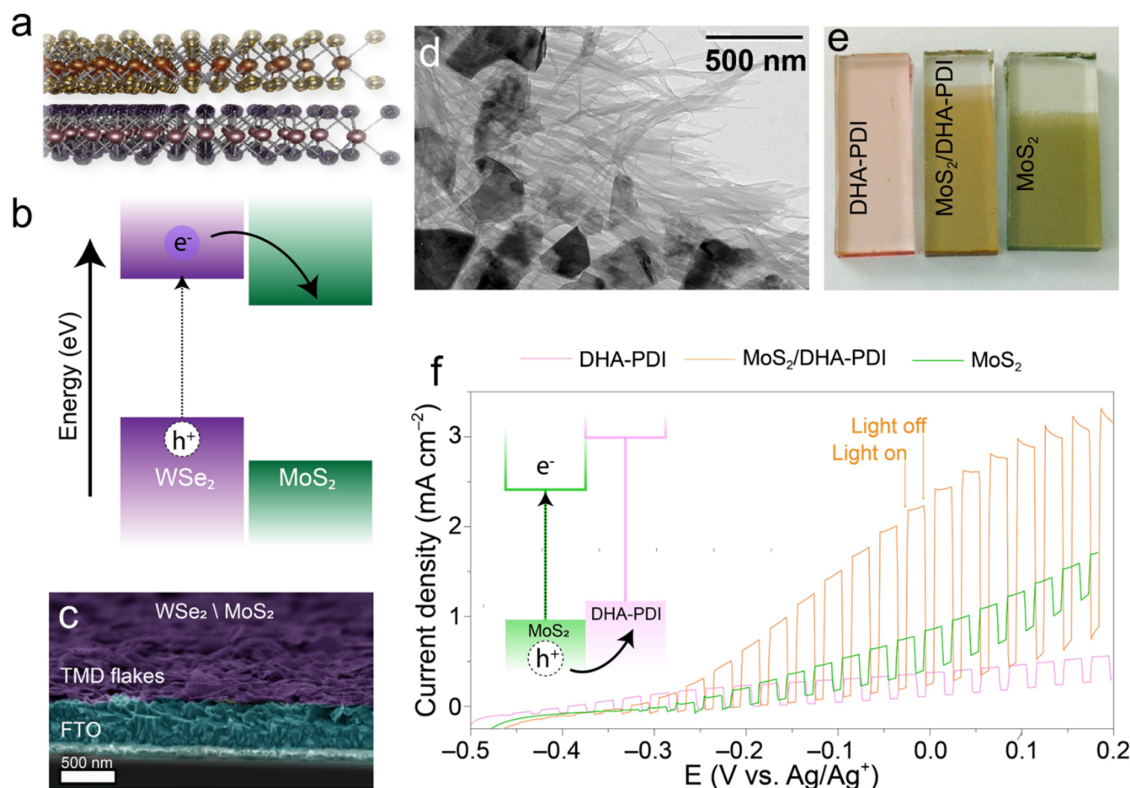


Figure 1.10. Examples of TMD based heterojunctions.

(a) Illustration of vdWHJ based on WSe<sub>2</sub> (purple) and MoS<sub>2</sub> (yellow) and (b) schematic of the resulting band alignment and charge separation mechanism. (c) Experimental demonstration of (a,b) using sequential LLISA film depositions. (d) transmission electron microscopy image of hybrid MoS<sub>2</sub>/DHA-PDI film. (e) Photograph of pure and hybrid films. (f) J-V curves of pure and hybrid films under intermittent lighting and an I<sup>-</sup>/I<sub>3</sub><sup>-</sup> redox couple (inset shows predicted band alignment and charge transfer mechanism). Figures reproduced from references <sup>83</sup> (c) and <sup>93</sup> (d-f).

### 1.9.3 Defect mitigation

Another way to reduce charge recombination and improve PEC performance is defect mitigation. This step typically takes place post film formation and there exists a myriad of techniques to achieve this. Like always the choice of defect mitigation technique (DMT) largely depends on the final use of the device, with some DMTs only being suitable for certain applications. This section discusses defect healing via thermal annealing and defect passivation via atomic layer deposition (ALD) and surfactant treatment.

#### 1.9.3.1 Low temperature annealing

Under the right conditions, thermal annealing is a simple, scalable option for defect healing in thin films. And while the effects can be difficult to attribute to one sole factor (i.e., defect healing, removal of contaminants, improved flake-substrate contact, etc.), the beneficial effects have been well demonstrated.<sup>78,79,99</sup> In extreme cases it has even been shown that it is possible to partially recover the semiconducting (2H) properties of chemically exfoliated semimetal (1T) MoS<sub>2</sub> nanoflakes by annealing at 300 °C.<sup>79</sup> While full recovery is not possible,<sup>79</sup> it suggests that post film annealing step are beneficial regardless of the state of the starting material. Indeed, several groups, have demonstrated increased performance after annealing at 200-300 °C for a variety of devices: photoelectrodes, transistors,<sup>78</sup> light emitters,<sup>79,99</sup> etc. Thus, thermal annealing represents an easy and reliable method for improving the performance of TMD devices. However, it should be noted that thermal annealing can also lead to defects depending on the parameters (i.e. temperature, vacuum, chalcogen-rich environment, substrate) selected.<sup>35</sup>

### 1.9.3.2 Defect passivation

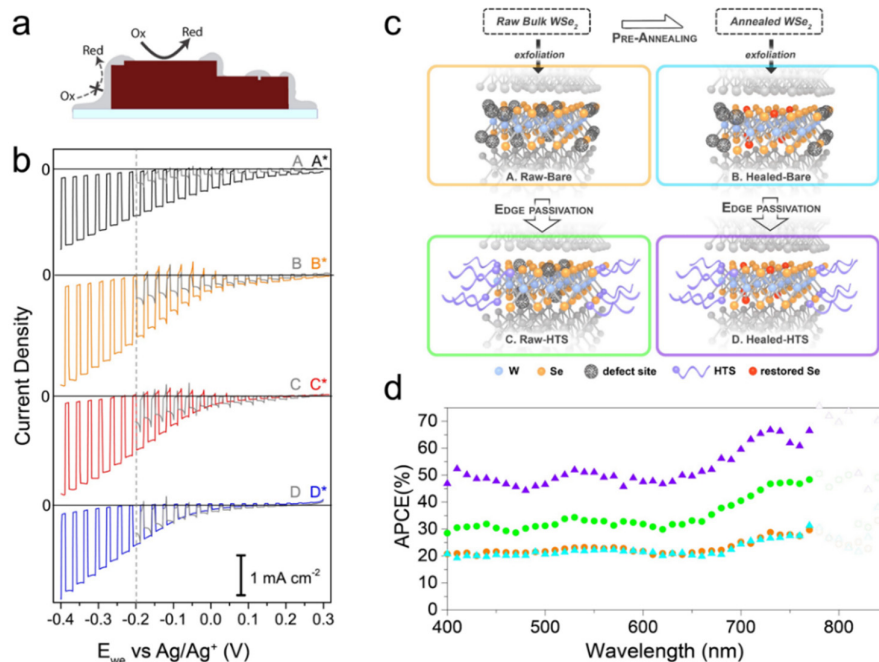


Figure 1.11. Examples of defect mitigation techniques.

(a) Schematic of edge defect passivation on the edges and step edges of a TMD nanoflake via ALD. (b) J-V curves of ALD deposition on different WSe<sub>2</sub> nanoflake films under intermittent light using organic redox chloranil. Gray lines show photocurrent ( $J_{ph}$ ) of the bare electrodes and colored lines show  $J_{ph}$  after ALD deposition. Flake size decreases from A to D. (c) Schematic of defect healing in WSe<sub>2</sub>. As-received powder (yellow) is pre-annealed (blue) or processed directly in to a nanosheet film. Both films are then treated with a silane group to give “raw-HTS” and “healed-HTS” films. (d) The absorbed-photon-to-chemical-energy (APCE) efficiency is shown for the resulting films described in (c) for hydrogen evolution in acidic conditions. Figures reproduced from references <sup>67</sup> (a,b) and <sup>66</sup> (c,d).

On the other hand, the effects of ALD and surfactant treatments are well-understood to be the result of defect passivation.<sup>66–68,100–102</sup> In short, ALD is a thin film deposition technique which works by reacting precursors in the gas phase, each one reacting sequentially with the surface and typically with preference to surface defects.<sup>67,101</sup> The process is self-limiting allowing very thin films to be deposited in a controllable fashion. Less controllable, chemical treatments work by introducing the thin film to a molecule which possesses one moiety that is attracted to dangling surface bonds (defects) in semiconductors.<sup>66,68,100</sup> This is usually done by submerging the film in a solution containing the surfactant, the most common being silane-based surfactants. The benefits and drawbacks of both treatments are considered next.

ALD of Al<sub>2</sub>O<sub>3</sub> has been frequently used to passivate edge defects, particularly in PEC devices for water oxidation.<sup>101</sup> For example, attempts to passivate WSe<sub>2</sub> with Al<sub>2</sub>O<sub>3</sub> yielded improved photocurrent and decreased dark current (Figure 1.11b).<sup>67</sup> However, the improvement scaled as a function of the nanoflake lateral dimensions with larger flakes benefitting the most.<sup>67</sup> It was shown that ALD took place preferentially at the edge sites, leaving the basal planes relatively untouched (Figure 1.11a).<sup>67</sup> Open-circuit potential measurements confirmed that photogenerated charge carrier recombination was largely suppressed, thus improving photovoltage.<sup>67</sup> However, because ALD had little interaction with the basal plane, step-edge defects located at these sites were not passivated. Thus, to bring the discussion full circle, sonicated flakes, which are smaller and possess many step-edge defects, would benefit less from this treatment compared to the single-crystal electrochemically intercalated nanoflakes (section 1.6.3), which have larger lateral dimensions and step-edge free basal planes. In contrast, ALD of Al<sub>2</sub>O<sub>3</sub> is not suitable applications that take place in aqueous solutions of H<sub>2</sub>SO<sub>4</sub>, namely PEC hydrogen production, owing to its instability in acid. Thus, DMT must be chosen according to nanoflake morphology as well as desired implementation.

In contrast, chemical treatments have been shown to work well in acidic conditions.<sup>66</sup> Silane groups represent the most commonly used molecules, with bis(trifluoromethane)sulfonimide (TFSI) being a popular choice. Though the mechanism of defect passivation is not well-understood, TFSI has been used to improve photoluminescence to near unity and improve charge mobility in MoS<sub>2</sub> nanosheets.<sup>68,82,100</sup> Indeed, treating MoS<sub>2</sub> nanoflakes with trichlorosilane groups can be used to improve the conductivity and charge mobility of multilayer devices; however, the length of the attached alkyl chains has a nontrivial effect.<sup>82</sup> Notably hexyltrichlorosilane (HTS) has been shown to outperform butyl- or octyltrichlorosilanes.<sup>82</sup> Accordingly, in another work, this finding was applied to single-layer nanoflake films of WSe<sub>2</sub> for water reduction in H<sub>2</sub>SO<sub>4</sub>.<sup>66</sup> Treating the WSe<sub>2</sub> photocathode with HTS effectively doubled the photocurrent compared to untreated samples (Figure 1.11d). In fact, when employed with a pre-treatment strategy (Figure 1.11c), HTS-treated samples nearly quadrupled the measured photocurrent and more than doubled the IPCE compared to untreated samples. This represents a facile DMT suitable for various materials and device applications.

Thus, as with each step in the film formation process, final device configuration (ex: vdWHJ) and DMT must be chosen based on the nature of the nanoflakes selected, the morphology of the deposited thin film, and the intended use of the entire system. For example, more aggressive DMTs are required for chemically exfoliated than for sonicated than for single-crystal electrochemically intercalated nanoflakes. This represents the final step in assembling a photochemically active 2D puzzle.



## 1.10 Motivation

The previous sections have highlighted the exceptional semiconducting properties of 2D materials and the numerous ways to produce, process, and tune them. Despite the large volume of existing work, there remain certain gaps which prevent the use of semiconducting TMDs on a globally relevant scale. In particular there exist many methods to make high-quality single-flake devices, but these approaches are not economically feasible for scale-up. In contrast, methods which have been identified as scalable produce nanoflakes with undesirable morphology and high defect densities, thereby diminishing their semiconducting properties. Thus, there remains a need for a scalable route to produce 2D TMD nanosheets without sacrificing quality. Furthermore, while much progress has been made towards fabricating films on the centimeter-squared scale, commercialization of 2D TMD-based devices for applications like solar energy conversion will require  $\text{m}^2$  fabrication capabilities. Once again this will require a system which is easily up scaled while maintaining desirable film morphology.

Without these missing pieces, TMD devices will never make the transition from laboratory to real-world devices in large-area applications. To this end, the goals of this thesis work are to (1) present a novel technique to produce high-performing, semiconducting nanosheets from commercially available powders and (2) design a thin film fabrication system capable of roll-to-roll 2D TMD film production.

Accordingly, *Chapter 2* tackles the issue of scalable production of high performance, semiconducting TMD nanosheets. A novel LPE method is presented which gives high yields of thin TMD nanosheets with large lateral dimensions and super semiconducting properties, especially when compared to traditional LPE techniques. Importantly this method uses commercially available powder, making it both economic and effective.

*Chapter 3* follows this up by expanding this method beyond pure 2D TMDs to include alloyed materials. It is demonstrated that a range of alloy compositions and concentrations can be made to fine tune the optoelectronic behavior of these materials. In addition to scalability, this method provides an avenue for making multilayer alloyed nanoflakes, both of which have generally been inaccessible to bottom-up approaches.

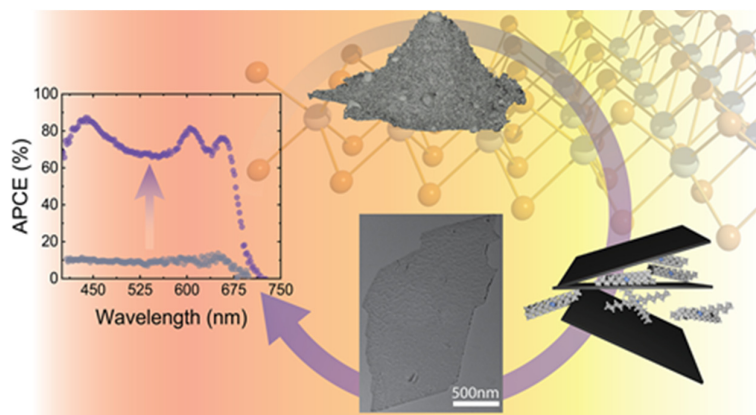
Therefore, *Chapter 4* addresses the second goal by presenting an upscaled LLISA film deposition capable of continuous, roll-to-roll 2D TMD film deposition. It is shown that this system can be applied for a range of layered materials and that multiple depositions are possible, opening the door for thin film tuning at the large scale.

Finally, *Chapter 5* provides conclusionary remarks and perspective on the future of this rapidly developing field. In addition to summing up the work presented in this thesis, remarks are made concerning ongoing questions and avenues for future work.

When used in combination the chapters of this thesis map a path towards large-area films of high-performing TMD nanosheets that can be precisely tuned according to the specific need of an application. It is hoped that this roadmap will assist in enabling the transition of 2D TMD-based devices out of the laboratory and into the real world.



## Chapter 2 High performance semiconducting nanosheets *via* a scalable powder-based electrochemical exfoliation technique<sup>†</sup>



A powder-based approach for the production of high-performance, semiconducting TMD nanosheets.

The previous chapter highlighted the exceptional semiconducting properties of two-dimensional (2D) transition metal dichalcogenides (TMDs) and motivated their incorporation into photovoltaic (PV) and photoelectrochemical (PEC) devices. However, it was also made clear that there lacks a suitable method for producing these materials in a scalable fashion without sacrificing quality. This is a major issue for their commercialization and will be addressed in the forthcoming chapter.

The liquid-phase exfoliation of semiconducting TMD powders into 2D nanosheets represents a promising route towards the scalable production of ultrathin high-performance optoelectronic devices. However, the harsh conditions required negatively affect semiconducting properties leading to poor device performance. Herein a gentle exfoliation method is demonstrated which employs standard bulk MoS<sub>2</sub> powder (pressed into pellets) together with the electrochemical intercalation of a quaternary alkyl ammonium. Resulting nanosheets are produced in high yield (32%) and are remarkably thin (mono-, bi-, tri-atomic layers) with large lateral dimensions (>1  $\mu\text{m}$ ), while retaining the semiconducting polymorph. Exceptional optoelectronic performance of nanosheet thin-films is observed such as enhanced photoluminescence, charge carrier mobility (up to  $0.2 \text{ cm}^2 \text{ V}^{-1} \text{ s}^{-1}$  in a multi-sheet device), and photon-to-current efficiency while maintaining high transparency (>80%). Specifically, as a photoanode for iodide oxidation, an internal quantum efficiency up to 90% (at +0.3 V vs Pt) is achieved (compared to only 12% for MoS<sub>2</sub> nanosheets produced *via* ultrasonication). Further using a combination of fluorescence microscopy and high-resolution scanning transmission electron microscopy (STEM) it is shown that the gently exfoliated nanosheets possess a defect density ( $2.33 \times 10^{13} \text{ cm}^{-2}$ ) comparable to monolayer MoS<sub>2</sub> prepared by vacuum-based techniques and at least four times less than ultrasonicated MoS<sub>2</sub> nanoflakes. Finally, the method is expanded towards other TMDs (WS<sub>2</sub>, WSe<sub>2</sub>) to demonstrate its versatility and open a path towards high-performance and fully scalable van der Waals heterojunction devices.

<sup>†</sup> This chapter is adapted from a peer-reviewed article published in ACS Nano: Rebekah A. Wells, Miao Zhang, Tzu-Heng Chen, Victor Boureau, Marina Caretti, Yongpeng Liu, Jun-Ho Yum, Hannah Johnson, Sachin Kinge, Aleksandra Radenovic, and Kevin Sivula. High Performance Semiconducting Nanosheets via a Scalable Powder-Based Electrochemical Exfoliation Technique. *ACS Nano*. **2022**.

## 2.1 Introduction

Ultrathin “two-dimensional” (2D) nanosheets of semiconducting transition metal dichalcogenides (2D TMDs) with the chemical formula  $MX_2$  ( $X = S, Se, \text{etc.}$   $M = W, Mo, \text{etc.}$ ) are promising materials for next-generation optoelectronic devices including transistors, light emitting diodes, and sensors, thanks to their exceptional semiconducting properties and intrinsic stability.<sup>103–106</sup> These attractive properties together with the earth abundance of their atomic components also makes them particularly attractive for large-scale applications requiring robust semiconductors such as photovoltaic, photoelectrochemical, or photocatalytic energy conversion at a globally-relevant scale.<sup>65,107–109</sup> Towards this goal, significant research efforts have been directed towards the fabrication of large-area, low-cost 2D TMD films.<sup>61,78,83,110</sup>

When considering the scalability and cost-effectiveness of 2D TMD film fabrication, liquid-phase exfoliation techniques that employ bulk powders of micrometer-sized TMD particles<sup>69</sup> have a clear advantage over techniques that employ high-vacuum processes (such as chemical vapor deposition (CVD)<sup>111,112</sup> and molecular beam epitaxy (MBE)<sup>113</sup>), or exfoliation methods that require large single crystals as starting material (*e.g.* mechanical exfoliation<sup>114</sup>). Indeed micron-sized crystalline powders of TMDs can be readily synthesized at large scales<sup>115</sup> and can be easily exfoliated into optoelectronically active 2D nanoflakes or nanosheets dispersed in solution using ultrasonication,<sup>63,69,116,117</sup> shear,<sup>118</sup> or chemical exfoliation (*via* Li ion intercalation).<sup>79,119</sup> The resulting 2D nanomaterial dispersions can then be easily processed into thin films using scalable roll-to-roll techniques.<sup>83</sup>

However, despite the versatility of the current liquid phase exfoliation approaches, the semiconducting performance of the produced nanosheets are drastically decreased by the harsh nature of these exfoliation methods.<sup>64,67,70,71,79</sup> Indeed, ultrasonication or shear methods break  $MX$  bonds within the 2D layers leading to nanoflakes with small lateral dimensions as well as a high concentration of chalcogenide vacancies,<sup>64,70,116</sup> and chemical exfoliation techniques lead to a conversion of the semiconducting 2H crystal phase of the TMD sheets to the semi-metallic 1T form, thus destroying the semiconducting properties.<sup>77,79,120,121</sup> While significant efforts have been directed to healing defects and repairing the semiconducting properties of liquid-phase exfoliated 2D TMDs,<sup>66,67,74,77,79,82,102,122</sup> most reported procedures require aggressive chemical, heating, or laser treatments in the solid state, which limits the versatility and scalability of the overall process. Moreover, the performance of defect-treated 2D nanoflakes generally remains poor<sup>79</sup> compared to nanosheet preparation methods that maintain the pristine 2H-phase throughout processing, or that produce it directly (*e.g.* CVD or MBE). Thus, despite significant efforts developing approaches for the liquid phase exfoliation of bulk TMD powders, there remains a clear need to realize a procedure that can yield high quality semiconducting TMD nanosheets directly *via* a scalable exfoliation procedure.

Electrochemically-driven intercalation techniques have the potential to offer scalable production of TMD nanosheets,<sup>77,123–125</sup> and moreover recent reports using bulk single crystals<sup>78,80</sup> of TMDs have suggested that high-quality semiconducting 2D nanosheets can be produced with an electrochemical intercalation technique employing bulky organic cations. While promising, these processes are fundamentally limited by the difficulty of producing large-sized bulk single crystal TMDs. The following work leverages the electrochemical intercalation approach using a bulky organic cation and presents a versatile method for the gentle exfoliation of TMDs starting with commercially available TMD powders. It is shown that  $MoS_2$  nanosheet thin films produced from this method exhibit exceptional optoelectronic performance and further demonstrated that the technique is suitable for exfoliating a range of TMD materials including  $MoS_2$ ,  $WSe_2$ , and  $WS_2$ .

## 2.2 Results and discussion

### 2.2.1 Electrochemical intercalation/exfoliation of pressed powder pellets

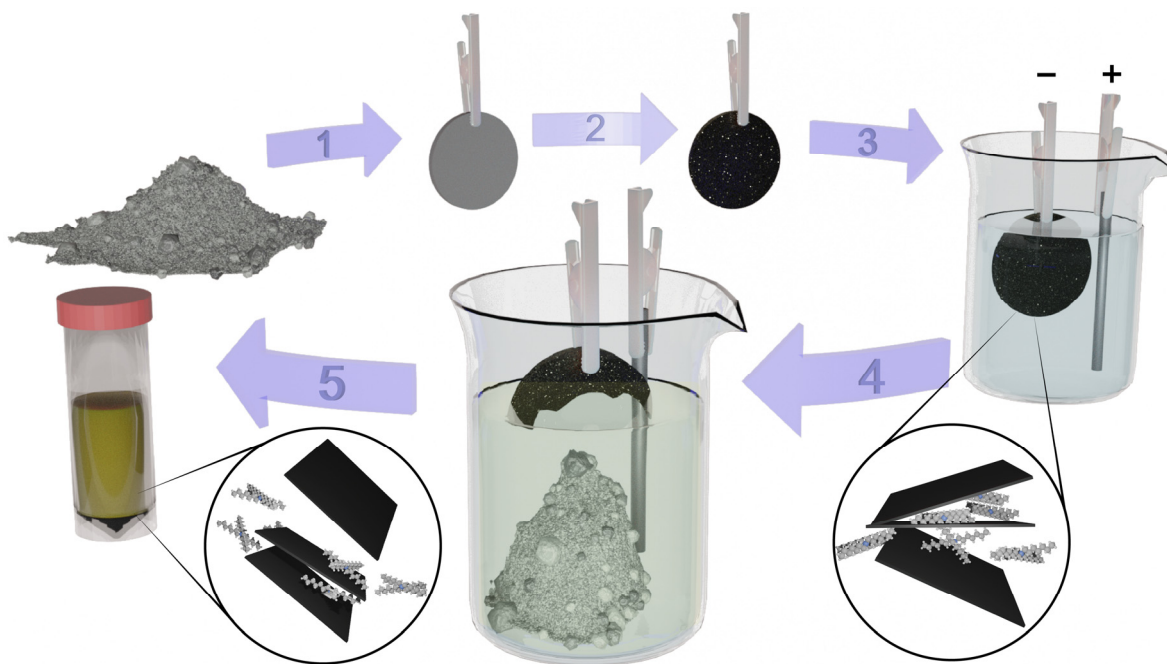


Figure 2.1. Schematic of the electrochemical pellet intercalation (ECPI) exfoliation method.

(1) As-received  $\text{MoS}_2$  powder is pressed into a pellet. (2) The pellet is annealed at  $1100^\circ\text{C}$  for 48 hours with excess S vapor. (3) The pellet is immersed in a solution of tetraheptylammonium bromide ( $\text{THA}^+\text{Br}^-$ ) with a glassy carbon rod counter electrode. (4) Operating the pellet as a cathode causes  $\text{THA}^+$  intercalation and the sloughing of intercalated  $\text{MoS}_2$ . (5) The intercalated powder is collected, rinsed, agitated, and finally centrifuged at low speed to remove remaining bulk material. The result is a viscous, green-brown solution of exfoliated  $\text{MoS}_2$  nanosheets.

To demonstrate the powder-based intercalation-exfoliation technique  $\text{MoS}_2$  is used as a model TMD material due to its well-documented challenges with the 1T-phase transition as well as its promising application for solar-energy conversion devices.<sup>56,96</sup> Figure 2.1 illustrates the full process of the electrochemical pellet intercalation (ECPI) exfoliation method. First, commercially available micrometer-sized powder (Figure 2.2a,d) is pressed into a pellet using a standard hydraulic press. The pellet is then annealed ( $1100^\circ\text{C}$  for 48 hours) under the presence of excess sulfur (3:1 molar ratio  $\text{MoS}_2:\text{S}$ ) to increase the mechanical robustness and electrical conductivity of the pellet. Indeed, larger crystalline domains are observed by scanning electron microscopy of the annealed pellet (Figure 2.2b,c,e,f) compared to the unannealed case and qualitative investigation of the pellet electronic conductivity shows little resistance across the annealed pellet compared to unannealed pellet.

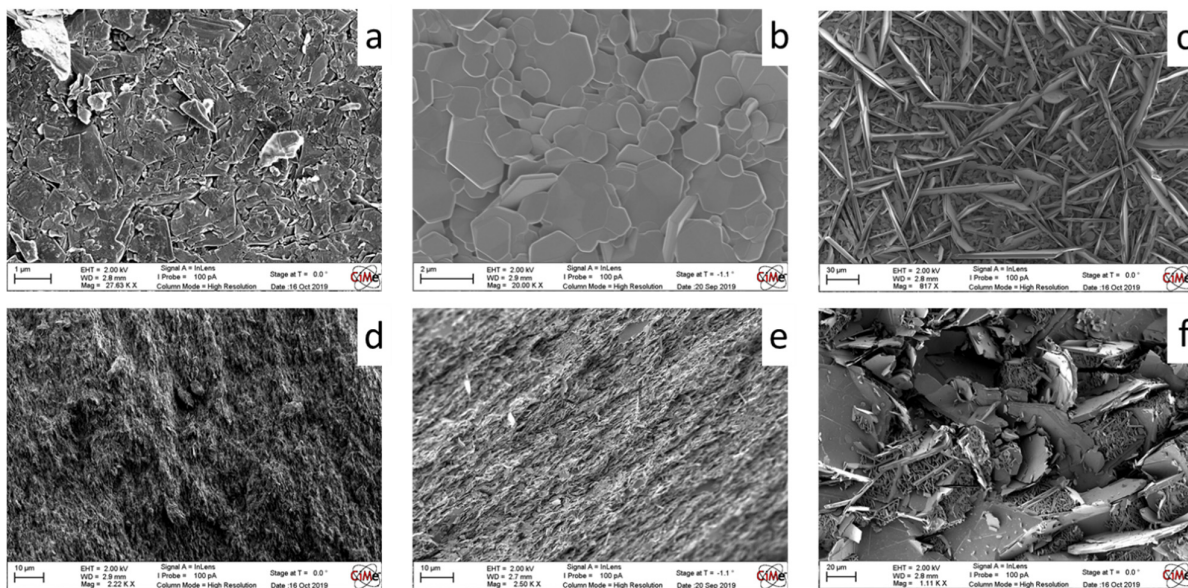


Figure 2.2. Scanning electron microscope images of annealed and unannealed pressed MoS<sub>2</sub> pellets.

Top view (a) and cross-section (d) of as-received MoS<sub>2</sub> powder pressed into a pellet without annealing. Only small domains up to 1 micron can be distinguished. Top view (b) and cross-section (e) of as-received MoS<sub>2</sub> powder pressed into a pellet and annealed at 1000 °C for 8 h with excess sulfur vapor. Some crystal growth and fusing is observed but domain size remains relatively small (< 2 μm). Top view (c) and cross-section (f) of as-received MoS<sub>2</sub> powder pressed into a pellet and annealed at 1100 °C for 48 h in excess sulfur. Large crystal domains and extensive fusing can be observed in the 50+ micron range in both top and cross-section view.

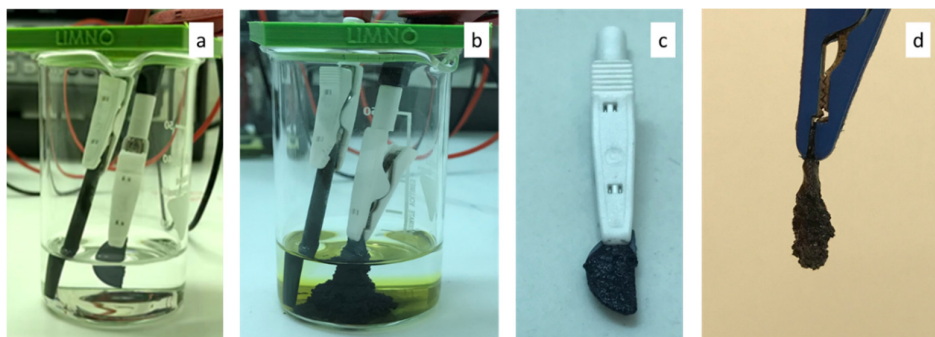


Figure 2.3. The stages of pellet intercalation.

First (a) the annealed MoS<sub>2</sub> pellet (white alligator clip) is submerged in solution containing THA<sup>+</sup> and 10V is applied. The pellet begins to intercalate slowly, resulting in the expansion of the pellet and some initial powder breaking free. After some time has passed more pellet material has intercalated and broken away leaving the fluffy black powder seen in (b). The yellow solution is the result of bromide oxidized to bromine by the glassy carbon electrode (rod). At the end of the intercalation process the majority of the pellet has broken away and remains at the bottom of the beaker. The remaining pellet has expanded as a result of the intercalated, but not departed, MoS<sub>2</sub>. A close up of the remaining intercalated pellet after one hour (c) and 24 hours (d).

The annealed pellet is then connected to a potentiostat as the working electrode using a metal clip and submerged into an acetonitrile-based electrolyte containing tetraheptylammonium (THA<sup>+</sup>) bromide, so chosen for its large size (20 Å) compared to the interlayer spacing of MoS<sub>2</sub> (6.1 Å), and to avoid phase-changes as a result of electron injection.<sup>78</sup> A glassy carbon rod is used as the counter electrode, placed roughly 1 cm from the MoS<sub>2</sub> pellet, and a bias of 10 V is applied causing THA<sup>+</sup> intercalation in the MoS<sub>2</sub> pellet cathode and bromide oxidization to bromine on the anode. As intercalation proceeds, the electrolyte turns yellow due to bromine formation while areas of the pellet in contact with the solution can be seen to visibly expand (Figure 2.3; a video demonstration can be found in the supporting information of reference<sup>126</sup>).

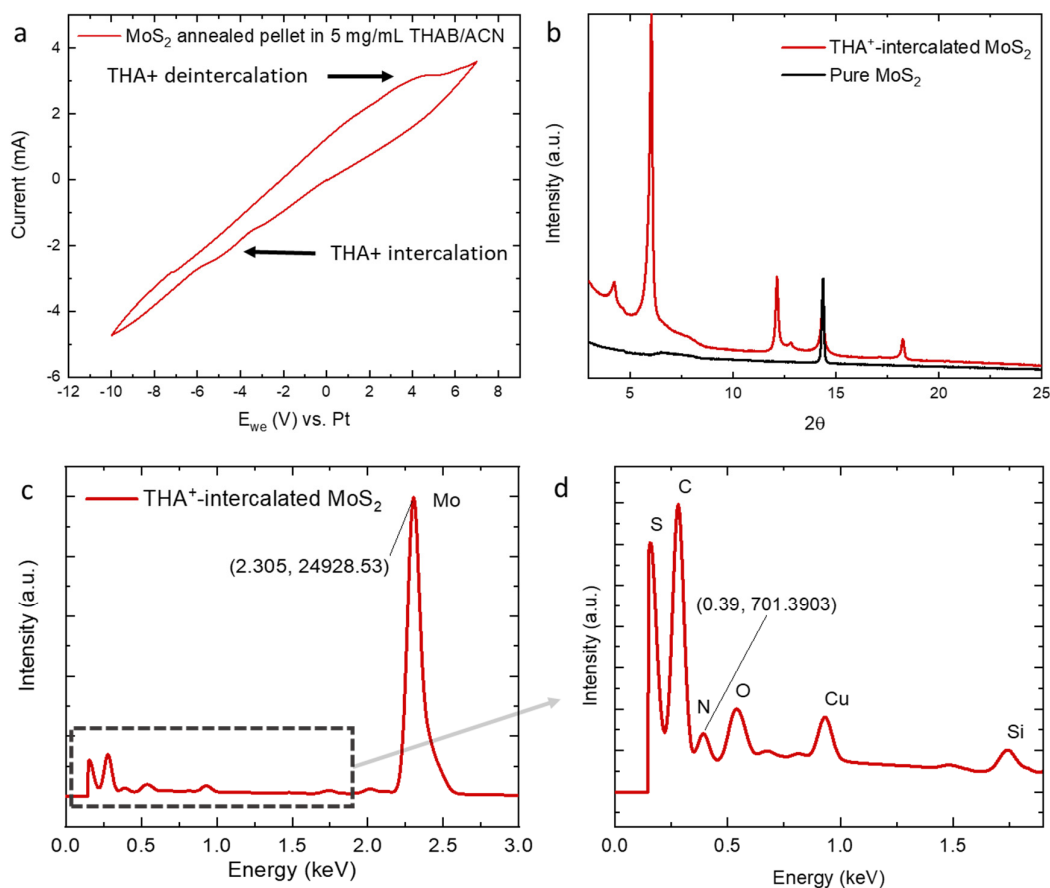


Figure 2.4. Evidence of intercalation of THA<sup>+</sup> into the MoS<sub>2</sub> layered structure.

(a) Cyclic voltammogram for the MoS<sub>2</sub> pellet in 5mg/mL THAB in acetonitrile with glassy carbon counter electrode and Pt wire reference electrode. Potential was swept between 8.0 and −10.0 V at 20 mV s<sup>−1</sup>. (b) X-ray diffraction for pure MoS<sub>2</sub> powder and THA-intercalated MoS<sub>2</sub> powder. (c,d) Energy dispersive X-ray spectroscopy of THA-intercalated MoS<sub>2</sub> powder. The N:Mo is calculated to be ~3%. Indicated region in (c) is shown magnified in panel (d).

Intercalation of MoS<sub>2</sub> with THA<sup>+</sup> is confirmed with cyclic voltammetry (CV), X-ray diffraction spectroscopy (XRD), and energy dispersive X-ray spectroscopy (EDS) (Figure 2.4). Periodically, these intercalated, expanded parts detach from the pellet exposing new area of the pellet for intercalation. In principle, this sloughing feature is an advantage over methods employing bulk single crystals where the single crystal cathode remains intact throughout the intercalation process. Additionally, since the detached material is both intercalated and partially exfoliated, complete exfoliation into nanosheets requires only gentle agitation (bath sonication in N-Methylpyrrolidone (NMP)), compared to the high-powered tip-probe sonication as described in single crystal demonstrations.<sup>78,80</sup>



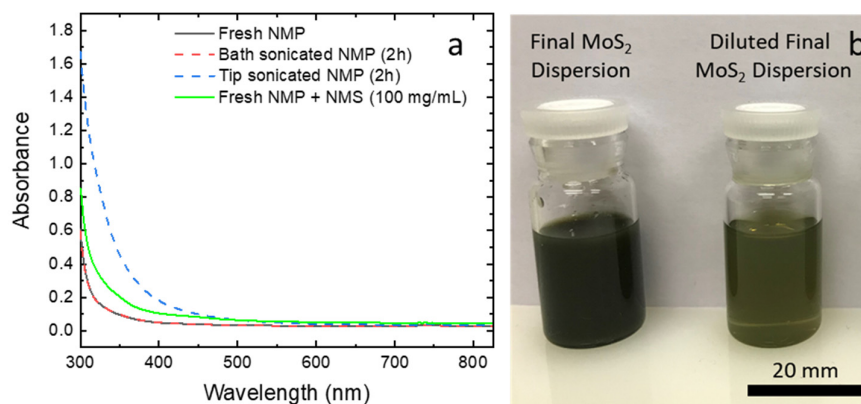


Figure 2.5. UV-Vis of fresh and sonicated NMP. ECPI-made MoS<sub>2</sub> dispersions.

(a) UV-Vis absorption of fresh NMP (black), bath sonicated NMP [Ultrasonic bath USC T, VWR, 45 kHz] (red dotted), tip sonicated NMP [800 W 50% - 10s on - 10s off - 0.4°C] (blue dotted), and fresh NMP with NMS dissolved up to 100 mg/mL (green). Because of the high energy input of tip sonication NMP degrades during exfoliation using ultrasonication. This can be seen by the increase of absorbance of the blue line in the lower visible region compared to the fresh NMP. This increase can be reproduced by dissolving NMS, a side product of NMP degradation, in fresh NMP. In contrast, the bath sonicated NMP is identical to the fresh NMP, suggesting the low energy input does not lead to degradation. (b) Final dispersion of ECPI-made MoS<sub>2</sub> nanosheets in NMP. The raw dispersion (left) is a viscous, greenish-brown solution in contrast to the black starting powder. The color change is better observed in a diluted (at random) dispersion (right).

Notably the presence of N-Methylsuccinimide (NMS), a side product of the high-power ultrasonication of NMP,<sup>71</sup> is absent in this bath agitation approach (Figure 2.5 a) confirming the gentler nature of the process and eliminating the problem of NMS contamination. After exfoliation, low-speed centrifugation is carried out to remove any unexfoliated bulk powder, leaving a viscous greenish-brown solution (Figure 2.5 b). It is notable that no further nanosheet size selection is performed to isolate monolayers, or remove the smallest, optoelectronically inactive nanoparticles, like is typically performed with ultrasonication approaches.<sup>67</sup> Though the ECPI exfoliation method can be easily adjusted (see Methods section), the typical process starts with 500 mg of as-received MoS<sub>2</sub> powder and ends with 8 mL of a dispersion with a concentration of around 20 mg mL<sup>-1</sup> corresponding to a single pass yield of 32%. While yield is subject to numerous adjustable processing parameters, namely centrifugation time and speed, this yield is similar to reports for high-power ultrasonication and higher than studies on shear or hybrid chemical intercalation-ultrasonication methods (See Table 1).<sup>64,70,118,119</sup>

## 2.2.2 Nanosheet characterization

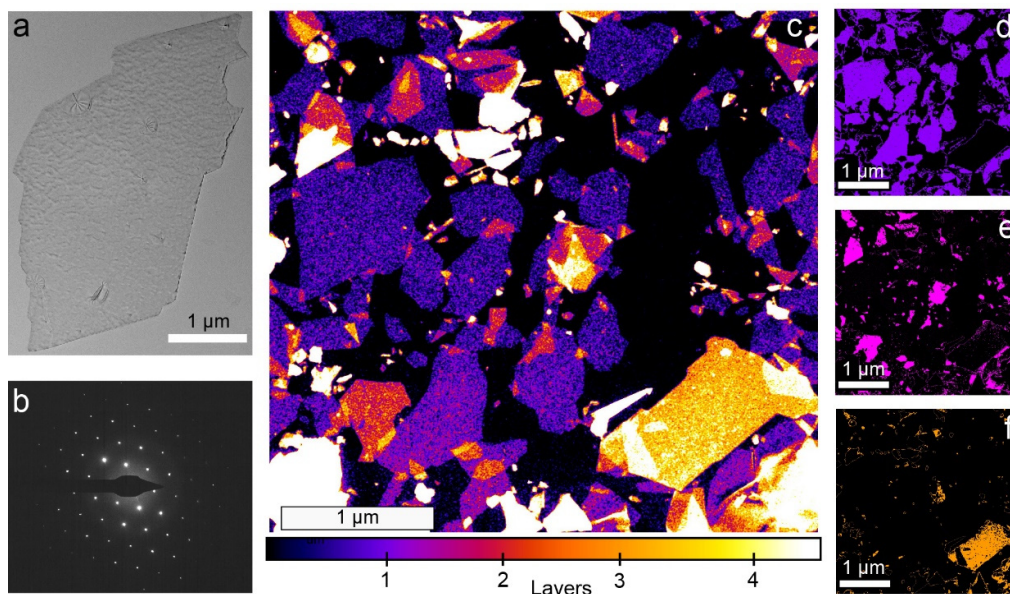


Figure 2.6. Structural and morphological characterization of ECPI made-MoS<sub>2</sub> nanosheets.

(a) TEM image and (b) selected area electron diffraction pattern of an ECPI-made MoS<sub>2</sub> nanosheet. (c) HAADF STEM image of a thin film of ECPI-made MoS<sub>2</sub> nanosheets. The color-scale highlights thickness differences in the flakes: purple for monolayer, pink for bilayer or overlapping monolayers, yellow for trilayers of overlapping mono/bi-layers, and white (saturated contrast) for regions greater than three layers. For better visualization the flakes have been separated according to thicknesses and are shown with the same color scale in (d), (e), and (f).

To verify the success of the ECPI exfoliation method, the resulting MoS<sub>2</sub> nanosheets are extensively characterized next. Transmission electron microscopy (TEM) was first used to examine drop-casted nanosheet dispersions. This revealed the presence of pristine, thin MoS<sub>2</sub> nanosheets with lateral dimensions greater than 1 μm, as seen in Figure 2.6a, that have selected area electron diffraction (SAED) patterns confirming the semiconducting 2H-MoS<sub>2</sub> structure (Figure 2.6b). In order to understand the relative abundance of such large, thin sheets (compared to smaller fragments) the MoS<sub>2</sub> dispersion was processed into a thin film using a liquid-liquid interfacial self-assembly (LLISA) technique as described previously,<sup>65,83</sup> which produces a single layer of MoS<sub>2</sub> nanosheets on a desired substrate and allows hundreds of individual flakes to be characterized simultaneously. The number of atomic layers in each nanosheet was investigated using high-angle annular dark field (HAADF) scanning TEM (STEM), a technique sensitive to the thickness of thin samples,<sup>127</sup> and the presence of monolayer nanosheets was further verified by atomic force microscopy (Figure 2.7b,c). The HAADF STEM image in Figure 2.6c was color-coded with respect to the number of atomic layers. Images showing isolated mono-, bi-, and trilayers, were extracted from the HAADF-STEM image (Figure 2.6c) and are displayed in Figure 2.6d,e, and f, respectively. These images facilitated the estimation of the nanosheet area distributions for each nanosheet layer population. Statistical results of the size estimation of over 150 nanosheets are displayed in the form of a histogram in Figure 2.7a. Notably, unlike previous observations with nanoflakes exfoliated by ultrasonication<sup>65–67,70,82</sup>, the ECPI exfoliation method produces a majority of monolayer sheets over the entire nanosheet area range observed.

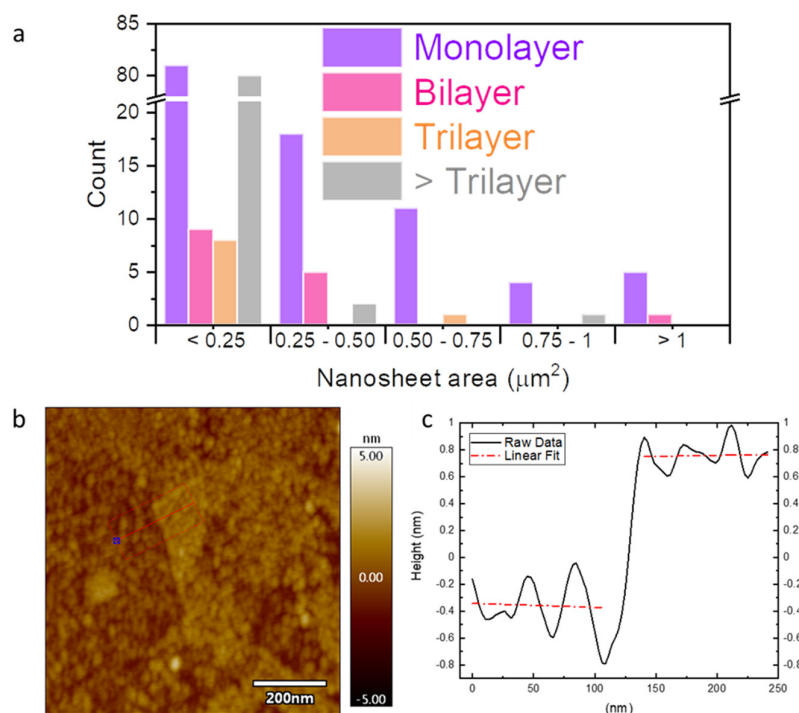


Figure 2.7. Size-thickness analysis for ECPI-made  $\text{MoS}_2$  nanosheets.

(a) Histogram of the nanosheet populations as a function of nanosheet area. Flakes thicker than 3 layers are less common than monolayers and tend to occupy the smallest area range. This is in direct contrast to the expected size-thickness dependency where big flakes are normally thick and small flakes are thin. (b) Atomic force microscopy (AFM) topography image of ECPI-made  $\text{MoS}_2$  nanosheets. (c) Height analysis of monolayer marked red in (b).

More specifically, previous descriptions of the liquid phase exfoliation of TMDs have consistently reported a similar relationship between nanoflake lateral size and number of atomic layers (nanoflake thickness) where monolayers have smallest dimensions and larger dimensions are only possible with thicker flakes.<sup>64,67,70,81</sup> This has been explicitly discussed for nanoflakes produced by ultrasonication exfoliation,<sup>64</sup> and it is likely linked to the anisotropic mechanical properties of the layered TMDs (stemming from the layered crystal structure). In stark contrast, the ECPI exfoliation method is capable of producing very thin flakes (mono-, bi-, trilayers) with large lateral dimensions ( $> 1 \mu\text{m}^2$ ) while nanosheets with more than three atomic layers mostly occupy the smallest area range ( $< 0.25 \mu\text{m}^2$ , see Figure 2.7a). It is reasonable to conclude that, since the ECPI exfoliation method does not rely on mechanical forces to exfoliate the TMD layers,<sup>78</sup> the resulting nanosheet size distribution does not have the same limitations as other powder-based exfoliation methods (See Table 1).



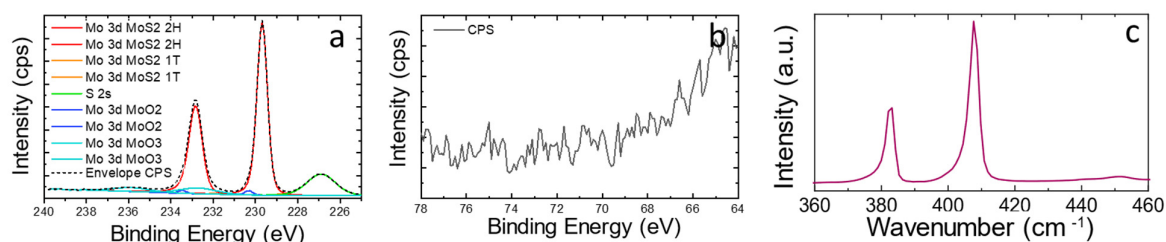


Figure 2.8. Chemical characterization of ECPI-made MoS<sub>2</sub> nanosheets.

The pristine nature of the nanosheets is confirmed by (a) Mo3d core level and (b) Br3d XPS and (a) Raman spectroscopy (see main text for references).

To further verify the quality of the ECPI exfoliated MoS<sub>2</sub> nanosheets, molybdenum and bromine core level X-ray photoelectron spectroscopy (XPS) and Raman spectroscopy of the LLISA-deposited nanosheet films were performed, and the results are shown in Figure 2.8. The XPS spectrum displays peaks from the Mo3d level at 229.7 eV and 232.7 eV and one peak from the S2s orbital at 227.2 eV, which are in good agreement with the accepted references for pristine material.<sup>128</sup> Moreover, the deconvolution and fitting of the spectrum showed no trace of 1T-phase MoS<sub>2</sub> (see Figure 2.8a), and no contribution from Br is recorded, suggesting that there is no detectable contamination from the THA<sup>+</sup> bromide (Figure 2.8b). Lastly, the Raman spectra displays two peaks corresponding to the in-plane E<sub>2g</sub> and out-of-plane A<sub>1g</sub> modes at 384 cm<sup>-1</sup> and 409 cm<sup>-1</sup>, respectively (Figure 2.8c). No peaks corresponding to the 1T-phase (154 cm<sup>-1</sup>, 219 cm<sup>-1</sup>, or 327 cm<sup>-1</sup>)<sup>129</sup> were observed. These values confirm the pristine nature of the film despite the mix of the nanosheet dimensions *Methods* section

### 2.2.3 Defect mapping of EPI-made and ultrasonicated nanosheets

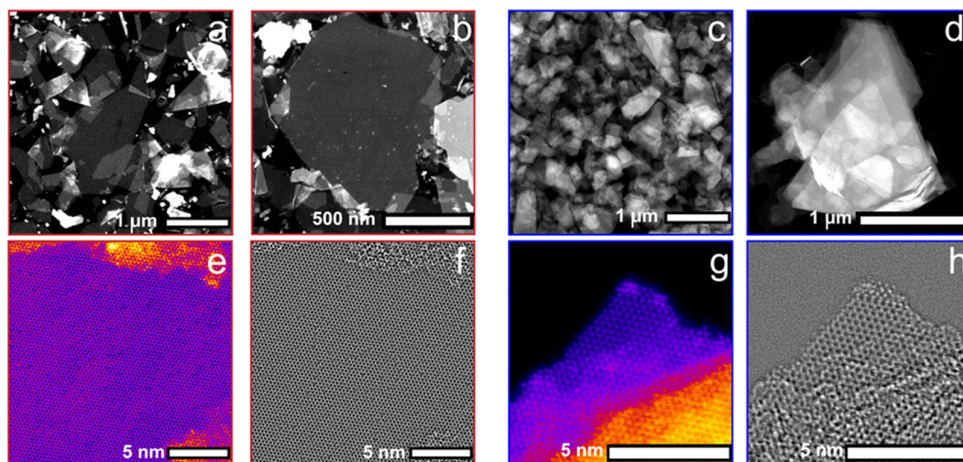


Figure 2.9. STEM and high-resolution STEM for ECPI-made and ultrasonicated MoS<sub>2</sub> nanoflakes.

HAADF STEM images for ECPI-made nanosheets (a, b) and sonicated (c, d) nanoflakes. High Resolution (HR) STEM images for ECPI-made nanosheets (e, f) and sonicated (g, h) nanoflakes. Brighter regions suggest thicker material that interacts more strongly with the electron beam causing more diffraction. (e, g) are HAADF detector images which have been falsely colored to highlight thickness differences. (f, h) are integrated differential phase contrast detector (IDPC) images which allow clearer visualization of crystal defects and adatom contamination.

It is well understood that preserving the 2H semiconducting phase in MoS<sub>2</sub> is crucial for optoelectronic applications. Compared to chemical intercalation, which induces the semimetal 1T phase, the ECPI method is clearly superior as a scalable method for producing semiconducting nanomaterials. However, it is less clear if this gentle exfoliation technique holds a clear advantage over other 2H-preserving exfoliation methods, namely ultrasonication. To ascertain this, dispersions of ultrasonicated MoS<sub>2</sub> nanoflakes using a procedure previously optimized for producing material with high photoelectrochemical activity<sup>83</sup> were prepared and compared to the ECPI-made nanosheets *via* a set of imaging techniques performed on thin films of nanoflakes deposited by the LLISA technique. Resulting images are shown in Figure 2.9.

HAADF STEM images for ECPI-produced nanosheet films and sonicated nanoflake films are shown in Figure 2.9a and Figure 2.9c, respectively. Both the ECPI and ultrasonicated nanoparticle thin films show the nearly close-packed morphology that is typical of the LLISA deposition technique.<sup>65–67,83</sup> However, the ECPI-made nanosheet film appears nearly transparent against the background compared to the ultrasonicated nanoflakes, which appear generally brighter. This is because the ECPI-made nanosheets are very thin, interacting minimally with the electron beam while the ultrasonicated nanoflakes are thicker and therefore diffract the beam more strongly. Thus, despite each film being made up of a single layer of nanosheets or nanoflakes, the ultrasonicated nanoflakes contain more atomic layers than the ECPI-made nanosheets. This is further supported by analysis of UV-Vis absorbance spectra of the nanoflake dispersions used to make the films (Figure 2.10b) where a shift in the exciton peak location confirms a difference in average atomic layer numbers of the exfoliated nanoflakes/sheets. In addition to thickness differences, the ultrasonicated flakes have smaller lateral dimensions which is expected according to the previous reports discussed above. Indeed, a statistical distribution of the nanoflake size (Figure 2.10a) shows that the vast majority (96%) of the ultrasonicated flakes are below 0.25 μm<sup>2</sup> in area. At higher magnifications (Figure 2.9b and Figure 2.9d for ECPI and ultrasonicated nanomaterials, respectively) a clear difference is also noted with respect to the presence of step-edge defects. While the ECPI-made nanosheets appear flat with minimal edge steps, the ultrasonicated nanoflakes seem to consist of stacked atomic layers with different lateral dimensions creating a large number of step-edges. Importantly, the presence of step-edge defects is well-known to have a detrimental effect on the semiconducting properties of TMDs.<sup>130</sup>

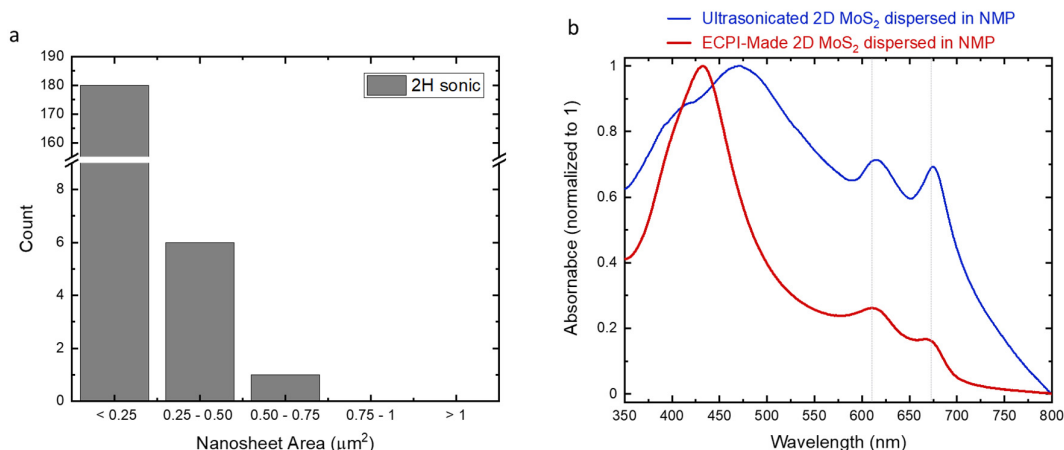


Figure 2.10. Statistical and UV-Vis analysis of ultrasonicated MoS<sub>2</sub> nanoflakes.

(a) Statistical analysis of lateral dimensions of the ultra-sonicated MoS<sub>2</sub> nanoflakes shown in Figure 2.9c in the main text. (b) UV-Vis absorption of the ECPI-made (red) and ultrasonicated (blue) MoS<sub>2</sub> dispersions. Exciton peaks A and B (around 670 nm and 612 nm, respectively) are blue shifted for the ECPI-made nanosheet dispersion compared to the ultrasonicated, suggesting thinner nanomaterial. A peak around 420 nm, often referred to as the “C peak” appears much sharper and in higher relative intensity to the A and B excitonic peaks in the ECPI-made dispersion compared to the ultrasonicated dispersion. This observation has been attributed to both thinner<sup>131–133</sup> and less defective<sup>79</sup> 2D MoS<sub>2</sub>.

Differences in the defect concentration of the nanomaterials produced by the two methods are further highlighted by high-resolution STEM imaging. Annular dark-field (ADF) images shown in Figure 2.9e and Figure 2.9g (color highlights the thickness differences) were acquired simultaneously with integrated differential phase contrast (iDPC)<sup>134</sup> images shown Figure 2.9f and Figure 2.9h for the ECPI-made and ultrasonicated MoS<sub>2</sub>, respectively (additional images can be found in Annex Item 1, for a more thorough comparison). Notably the iDPC technique is very sensitive to changes in height and contamination including adatoms.<sup>134</sup> From these images it is concluded that ECPI-made nanosheets do indeed possess flat basal planes as well as clean lattices. As with CVD or PVD grown and mechanically exfoliated nanoflakes,<sup>37,39,40,43,135</sup> sulfur monovacancy point defects can be observed; however, it is important to note that it is challenging to differentiate intrinsic defects from those induced during imaging.<sup>37,39</sup> However, visual inspection of several flakes gives an average defect density of  $2.3 \pm 0.6 \times 10^{13} \text{ cm}^{-2}$ , which is comparable to—and in some cases less than—defect densities reported for CVD or PVD grown and mechanically exfoliated flakes.<sup>39,40,136</sup> In contrast, given the irregular topography of the ultrasonicated nanoflakes, it is nearly impossible to find any large-area of flat basal plane of a few atomic layers thickness for high-resolution STEM imaging (Figure 2.9g and Figure 2.9h, see Annex Item 1 for additional images). Moreover, the iDPC technique highlights high amounts of adatom contamination which appears worse (blurrier) at the step-edges. These two factors make identifying point defects challenging and quantifying them unfeasible on the ultrasonicated nanoflakes.

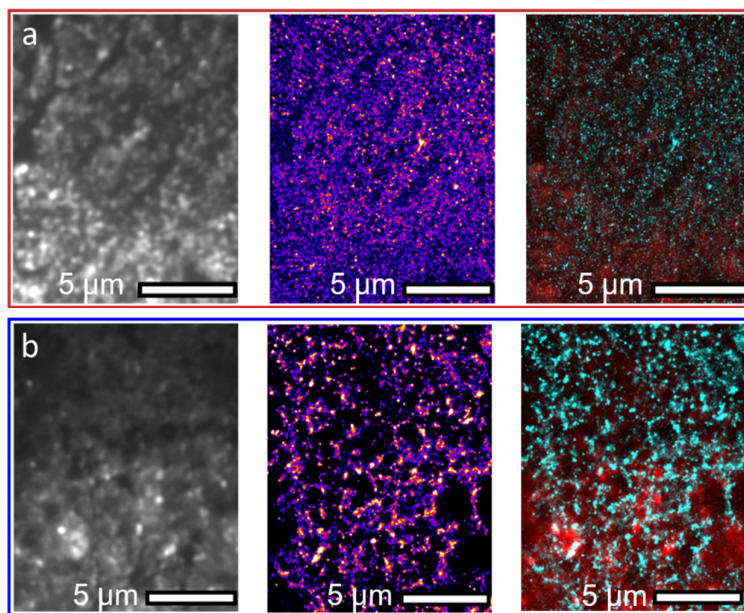


Figure 2.11. Results of 2D-PAINT method for mapping defects on films.

(a) ECPI-made nanosheets and (b) sonicated nanoflakes. Grayscale images show the PL for the 2D MoS<sub>2</sub> (left), heatmap images show the number of the detected probe-defect binding events (center), and cyan-red maps show the probe-defect binding events (cyan) overlaid on the 2D MoS<sub>2</sub> PL (red) to show probe location with respect to MoS<sub>2</sub> (right).

Given the difficulty to quantify the defect density difference between the MoS<sub>2</sub> nanomaterials produced with the two different exfoliation methods using electron microscopy imaging alone, the next characterization employs a recently-reported non-destructive technique for the large-area mapping of defects in 2D TMDs using fluorescent molecular probes.<sup>37</sup> This method, called 2D-PAINT, is a variation of Points Accumulation for Imaging in Nanoscale Topography (PAINT) and relies on the specific interaction between a thiol functionality on the molecular probe and defects (sulfur vacancies and edge defects) in the nanosheets. Also on the probe, opposite of the thiol group, is a dye whose intermittent fluorescence is detected and imaged in an optical microscope. Applying the 2D-PAINT protocol to the solution-processed 2D MoS<sub>2</sub> nanosheets herein affords the relative quantification of the defect densities on an ensemble of nanoparticles. The results are shown for thin films of ECPI-produced (Figure 2.11a) and ultrasonicated nanoflakes (Figure 2.11b). The first panel (grayscale image) shows the normalized photoluminescence (PL) of the MoS<sub>2</sub> nanosheets themselves (not the molecular probe PL) observed in the 675-725 nm wavelength range (unnormalized images are shown in Annex Item 2). The second panel (colored heatmap) displays the number of detected probes (509-530 nm wavelength range) that have bound to defect sites on the MoS<sub>2</sub> nanosheets over the acquisition of 1000 frames. As observed in the heatmaps, a higher concentration of probe-defect binding events is observed for the sonicated nanoflake films. An overlap of the PL of the MoS<sub>2</sub> flakes and the heatmap of the probe-defect binding events is shown in the third panel to better visualize the location of the probes with respect to the nanoflakes. To quantify the observed differences in probe-defect binding events, the event density rates were extracted for multiple areas of each film leading to an average probe-defect binding event density of 0.814  $\mu\text{m}^{-1} \text{ frame}^{-1}$  for the ultrasonicated flakes and 0.283  $\mu\text{m}^{-1} \text{ frame}^{-1}$  for ECPI-made sheets. Such an event density rate is proportional to the total defect density on the nanosheets. Thus, by using the 2D-PAINT method it can be estimated that ultrasonicated nanoflakes have roughly three times more defects compared to the ECPI-made nanosheets. However, due to the poorer dispersibility of the ultrasonicated nanoflakes, more aggregation was observed in the thin film, which likely leads to an underestimation of the defect density.

In fact, spatial autocorrelation of the probe-defect binding event heatmaps, allows us to quantitatively describe the distribution of the probes *via* Moran's Index.<sup>137</sup> For a Moran's I value = 0 the events are considered a random spatial distribution while increasing values are associated with grouping or clumping.<sup>137</sup> A Moran's I value of 0.22 was recorded for the ECPI-made nanosheets and 0.44 for the ultrasonicated nanoflakes,<sup>138</sup> which is consistent with a more even distribution for the ECPI-made samples and more concentrated probe binding events for the sonicated samples. It should be noted that the clumping experienced by the ultrasonicated flakes can potentially lead to over-crowded probe binding events that cannot be distinguished by 2D-PAINT, resulting in an underestimation of defects.

## 2.2.4 Nanosheet optoelectronic and photoelectrochemical performance

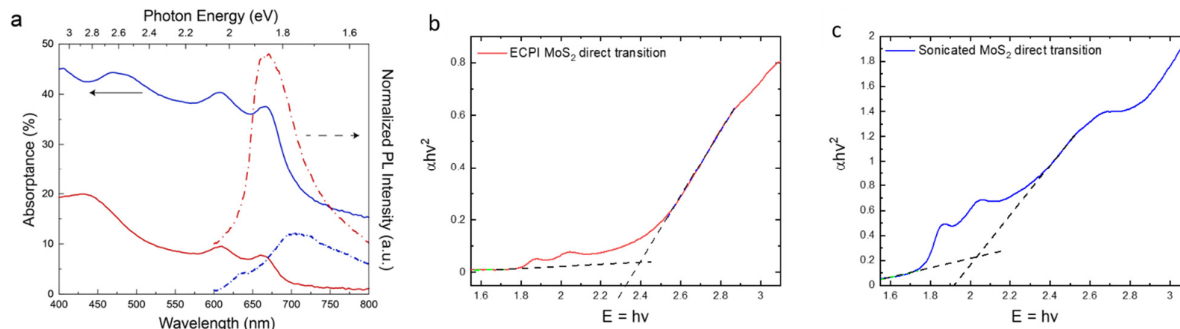


Figure 2.12. Optoelectronic properties for thin films of ECPI-made nanosheets and sonicated nanoflakes.

(a) UV-Visible (solid lines) and normalized PL (broken lines) spectra. Tauc plot analysis for the ECPI-made (b) and ultrasonicated (c) nanoflakes. By fitting the linear regions (blue and green dashed lines), extrapolating (black dashed lines), and finding the intersection gives the intercept at 2.39 eV for the ECPI-made nanosheets and 2.17 eV for the sonicated nanoflakes.

Having distinguished the ECPI-exfoliated nanosheets from the traditionally-produced ultrasonicated nanoflakes in terms of morphology and defects, it is necessary to establish how these differences affect the optoelectronic performance of the semiconducting nanomaterial. Firstly, the UV-Visible and PL spectra of the ECPI-prepared (red) and ultrasonicated (blue) nanosheet thin films are displayed in Figure 2.12a. In terms of light absorption, despite both films being made up of a single layer (one LLISA deposition) of nanosheets or nanoflakes with similar coverage ( $\sim 80\%$ ), the ultrasonicated nanoflake film absorbs 30-45% of the incident photons with energy above the excitonic peak (ca. 1.88 eV) while the ECPI-produced nanosheet film absorbs  $< 20\%$ . This is consistent with the observations made using STEM (Figure 2.9) wherein the thicker ultrasonicated nanoflakes interact more strongly with the electron beam and thus are expected to absorb more light. Additionally, blue shifts are observed in exciton peaks A and C of the ECPI film, found at 663 nm and 433 nm, respectively, compared to 668 nm and 477 nm in the ultrasonicated film, consistent with blue shifts observed in the nanoflake dispersions (Figure 2.10). These blue shifts suggest larger optoelectronic bandgaps as a result of fewer atomic layers in the produced nanomaterial<sup>11,139</sup>. Tauc plot analysis<sup>140</sup> confirms this hypothesis with estimated direct-transition band gap energies of  $\sim 2.4$  eV for ECPI-made nanosheets and  $\sim 2.0$  eV for ultrasonicated nanoflakes (Figure 2.12). Indeed, the optical properties of these films are in direct agreement with the trends observed in STEM (Figure 2.9).

Using laser excitation at a wavelength of 532 nm, PL can be detected for both types of MoS<sub>2</sub> nanosheets and is shown in Figure 2.12a (broken lines). The ECPI-produced nanosheets display strong PL; five-fold more than the ultrasonicated nanoflakes, when normalizing the response. In accordance with the UV-Visible, the PL displayed by the ECPI film is also blue shifted compared to the ultrasonicated film. It should be highlighted that the strong PL observed for the ECPI-made nanosheet films is achieved without any complex post-film treatments which are typically employed (*i.e.* via laser annealing,<sup>79,141</sup> chemical treatment,<sup>68,100,102</sup> *etc.*). In addition to the established lower defect density (which should reduce non-radiative recombination<sup>142</sup>) the higher PL can be attributed to morphology of the ECPI-made MoS<sub>2</sub> as thin, large-area TMD nanosheets have longer exciton lifetimes.<sup>67</sup>



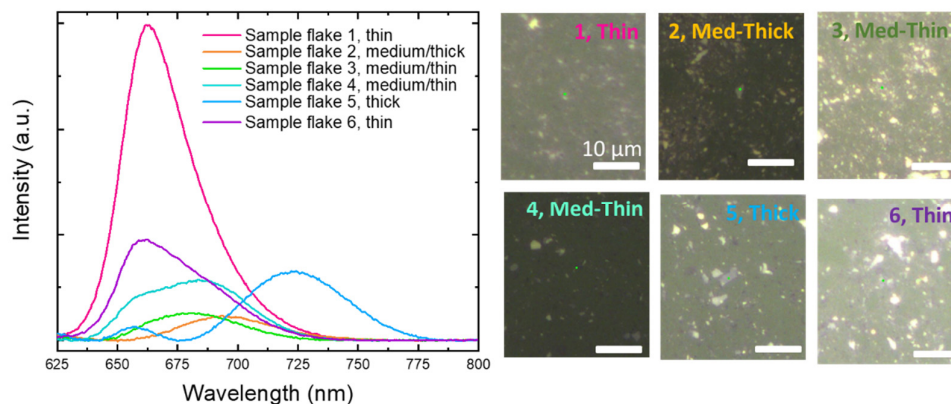


Figure 2.13. Photoluminescence spectra for ECPI-made  $\text{MoS}_2$  nanosheets of different sizes.

Photoluminescence was collected using a Raman laser and 100x objective lens. Spectra were taken for several different random points surveying a range of flakes thick and thin. All nanosheets display PL; however, the peak intensity and location shifts. Thus, PL is modulated as a function of flake size.

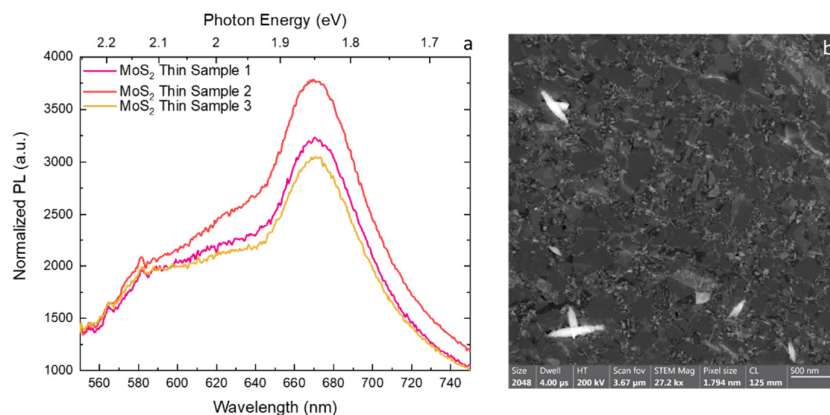


Figure 2.14. Photoluminescence for thin ECPI-made  $\text{MoS}_2$  nanoflakes.

A typical ECPI-made dispersion was further processed at 16670 rcf to select the smallest and thinnest ECPI-made flakes. The flakes are shown *via* HAADF STEM in (b). These flakes have much narrower size and thickness distributions. The lateral sizes, less than 500 nm across, are more similar to those seen in the ultrasonicated nanosheets. Despite having smaller lateral dimensions, the flakes still display photoluminescence (a).

Additionally, it is notable that PL is observed for all ECPI-produced nanosheets regardless of size and can even be modulated as a function of nanosheet thickness (Figure 2.13). In fact, further processing of ECPI exfoliated dispersions at high centrifuge speeds, to isolate nanosheets with smaller lateral size range (< 500 nm, more similar to that of the ultrasonicated flakes), resulted in nanoflake thin films showing a sharp PL peak response (Figure 2.14). In contrast, the ultrasonicated nanoflakes suffer from both small lateral dimensions (which limits exciton lifetime), and higher defect densities (which increases the probability of non-radiative recombination). Together these aspects lead to fast recombination rates and renders PL difficult to detect for ultrasonicated nanoflakes.<sup>68,94</sup>

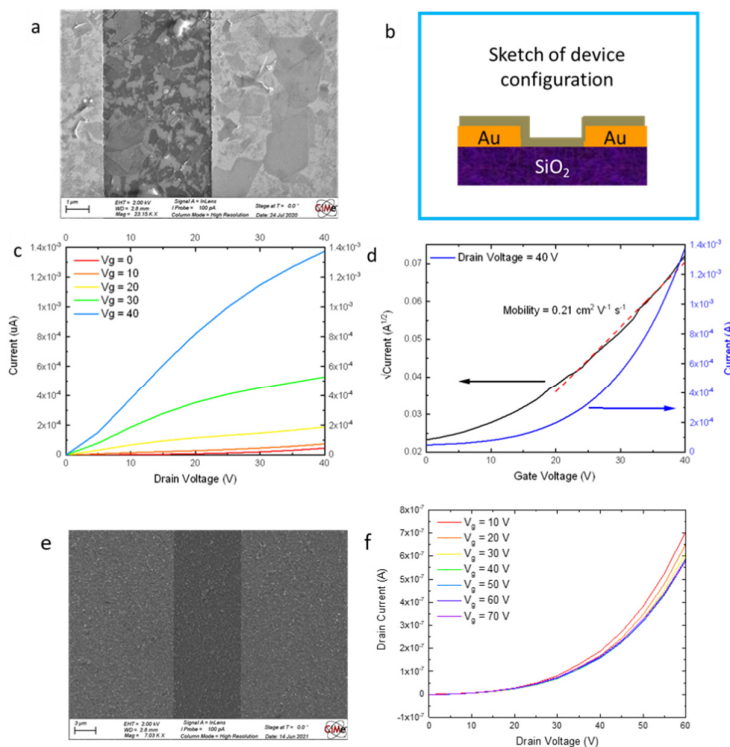


Figure 2.15. Bottom gate / bottom contact transistors from ECPI-made and ultrasonicated MoS<sub>2</sub> nanoflakes.

(a) Shows a SEM image of the channel, (b) shows a sketch of the device, (c) is the output curves for LLISA deposited ECPI-made MoS<sub>2</sub> nanosheets and (d) the transfer curve for a drain voltage of 40 V. (e) shows a SEM image of the channel, (f) displays the output curves for ultrasonicated MoS<sub>2</sub> nanoflakes.

To compare the electron charge carrier mobility,  $\mu_e$ , of thin films prepared using the ECPI exfoliation method to the standard ultrasonication, bottom gate/bottom contact field effect transistors (FETs) were fabricated by LLISA deposition of ECPI-made MoS<sub>2</sub> onto gold patterned SiO<sub>2</sub> substrates. These simple devices (Figure 2.15a-d) show promising electron mobilities (saturation region) up to  $\mu_{e,sat} = 0.2 \text{ cm}^2 \text{ V}^{-1} \text{ s}^{-1}$  (and an average  $\mu_{e,sat} = 0.11 \text{ cm}^2 \text{ V}^{-1} \text{ s}^{-1}$  over eight devices). Notably, this was achieved without any complex treatments, additives, or device configurations and represents a 10-fold improvement over previous work using top-contact FETs made from ultrasonication exfoliated MoS<sub>2</sub><sup>82</sup> even outperforming reports made from CVD grown MoS<sub>2</sub> films.<sup>143–145</sup> In contrast, devices prepared by the same method but with the ultrasonicated MoS<sub>2</sub> nanoflakes do not exhibit a gating effect (Figure 2.15e,f). This can be attributed to both the small lateral nanoflake size that reduces connectivity across the transistor channel as well as defect-driven charge recombination.

The impressive UV-Visible, PL, and FET behavior of the ECPI-made nanosheets suggest that this material should exhibit superior performance in solar energy conversion applications. To demonstrate this, simple photoelectrochemical (PEC) devices were made by depositing a single layer of the exfoliated MoS<sub>2</sub> nanosheets onto fluorine-doped tin oxide (FTO) coated glass substrates and evaluated the photo-driven oxidation of iodide (I<sup>-</sup>) to triiodide (I<sub>3</sub><sup>-</sup>) under simulated solar irradiation. The iodide/triiodide reaction (Figure 2.16c, inset) was chosen for its simple nature and well-studied mechanism<sup>146</sup> compared to other potential redox couples. Moreover, iodine (I<sub>2</sub>) can be isolated as a potentially useful product.<sup>147</sup> For comparison, ultrasonicated MoS<sub>2</sub> nanoflake film devices were fabricated and tested under the same conditions. The raw voltammetry data showing light and dark response can be seen in Figure 2.16a. The extracted photocurrent densities for the ECPI-made MoS<sub>2</sub> (red) and ultrasonicated MoS<sub>2</sub> (blue) are shown in Figure 2.16b as a function of the applied potential.



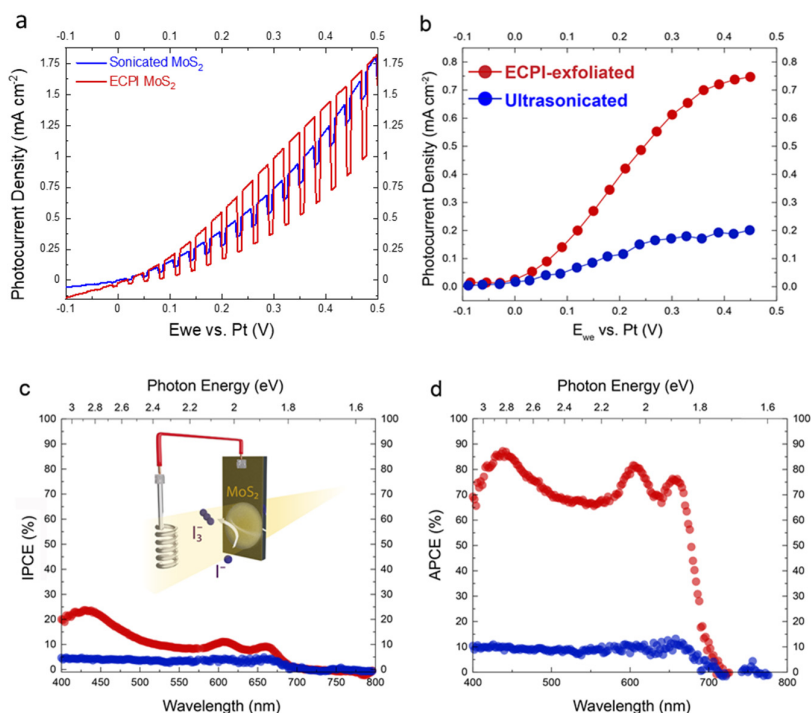


Figure 2.16. Photoelectrochemical (PEC) properties for films of ECPI-made nanosheets and sonicated nanoflakes.

(a) Raw linear scanning voltammetry (LSV) under intermittent 1-Sun solar illumination in 50 mM LiI, acetonitrile (a) Extracted photocurrent densities for the I<sup>-</sup>/I<sub>3</sub><sup>-</sup>. (c) Incident photon-to-current conversion efficiencies (IPCEs) for the I<sup>-</sup>/I<sub>3</sub><sup>-</sup> reaction at 0.3 V vs Pt reference electrode from 400-800 nm. Inset: schematic of PEC set-up and I<sup>-</sup>/I<sub>3</sub><sup>-</sup> reaction. (d) Absorbed photon-to-current conversion efficiencies (APCEs) correct IPCE for the percentage of photons absorbed by each film.

Films made from ECPI-exfoliated MoS<sub>2</sub> achieve impressive photocurrents (average of 0.9 mA cm<sup>-2</sup> at +0.45 V vs. Pt in 50 mM LiI in acetonitrile over 12 photoanodes tested), with champion devices surpassing 1.25 mA cm<sup>-2</sup> (Annex Item 3). Compared to ultrasonicated nanoflake films, ECPI-prepared nanosheet films absorb less light (Figure 2.12) yet have higher photocurrents (Figure 2.16a,b) and lower dark currents (see Figure 2.16a). Indeed at +0.3 V vs Pt, the ECPI-produced nanosheets shown in Figure 2.16b achieves three times more photocurrent (0.6 mA cm<sup>-2</sup>) than the sonicated nanoflakes (0.2 mA cm<sup>-2</sup>). Note<sup>38</sup> and (Figure 2.9 and Figure 2.11, respectively)

Considering the lower light absorption of the ECPI-made nanosheets compared to the ultrasonicated ones suggests a large difference in the internal quantum yield between the two preparation methods. To confirm this, the photon-to-current quantum yields were examined using monochromatic illumination between 400 and 800 nm at a photoanode bias of +0.3 V vs Pt (chosen in order to fairly compare the sonicated and ECPI-made nanoflakes since the high dark current of the ultrasonicated flakes at high voltages made extracting photocurrents unreliable). The extracted incident photon-to-current conversion efficiency (IPCE) for both exfoliation methods is shown in Figure 2.16c. In both cases the IPCE trace follows the absorbance spectrum of MoS<sub>2</sub>, with exciton peaks A and B around 660 nm and 606 nm, respectively. However, the maximum IPCE of the ultrasonicated nanoflake photoanode (blue) is around 5% while ECPI-made nanosheet photoanode (red) shows sharp features reaching 10% near the exciton peaks A and B and nearly 25% near excitonic peak C (430 nm).

The differences in the IPCE spectra are magnified when the photoanode light absorption is considered. Doing so gives the absorbed photon-to-current conversion efficiency (APCE) shown in Figure 2.16d. Here the superiority of the ECPI-made nanosheet film is clearly evident as it reaches 80% at 606 nm and 90% at 420 nm. Compared to sonicated films, having a maximum APCE of 10%, this is 9-fold increase. Qualitatively this agrees well with the previous observations that the ECPI-based nanosheet thin films absorb one third of the light on average (Figure 2.12a) yet produce three times the photocurrent (Figure 2.16b). Note that applying a more positive voltage to the ECPI-made nanosheet photoanodes would lead to slightly higher IPCE and APCE values since the saturation photocurrent density of the photoanode tested was 20% higher than at the conditions tested (+0.3 V).

Compared to CVD-grown TMD monolayers tested in similar or more elaborate systems,<sup>54,148–151</sup> the powder-processed ECPI-exfoliated perform equally or better (Table 1). For example, Wang *et al.* reported a CVD grown MoS<sub>2</sub> monolayer with external and internal quantum efficiencies of 3.69% and 44.2%, respectively, for the iodide/triiodide redox couple at +0.5 vs Ag/AgI in 1 M NaI (~0.57 vs Pt).<sup>54</sup> Thus, the ECPI-made nanosheets reported herein represent benchmark solar energy conversion performance for solution processed 2D MoS<sub>2</sub>.

## 2.2.5 Applications to other layered TMD materials

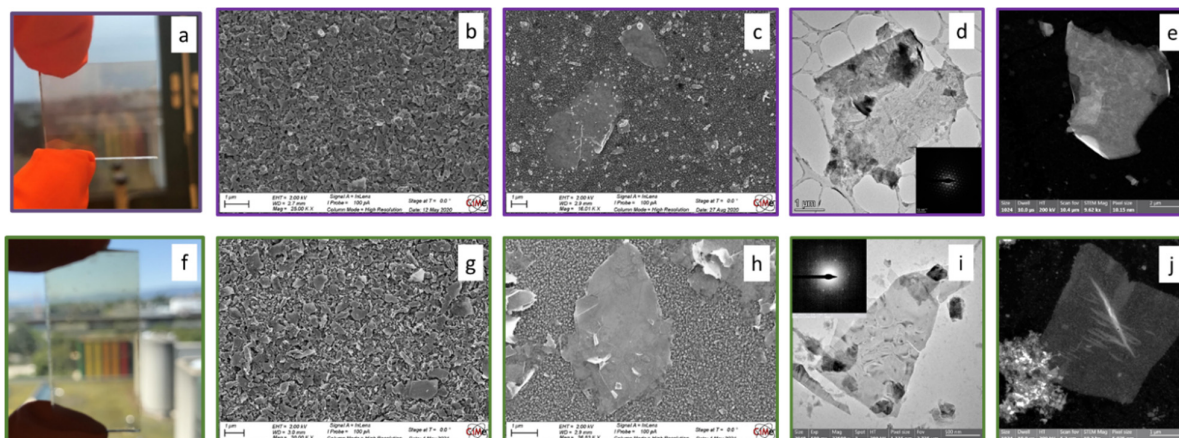


Figure 2.17. ECPI-made nanosheets of other layered materials.

Figures (a) and (f) show thin films of the ECPI-made 2D TMDs *via* LLISA deposition onto FTO for WSe<sub>2</sub> and WS<sub>2</sub>, respectively. Figures (b) and (g) show SEM images for sonicated nanoflakes of WSe<sub>2</sub> and WS<sub>2</sub>, respectively. Figures (c) and (h) show SEM images of ECPI-made nanosheets for WSe<sub>2</sub> and WS<sub>2</sub>, respectively. Figures (d) and (i) show bright-field TEM images for WSe<sub>2</sub> and WS<sub>2</sub>, respectively. Insets: selected area diffraction patterns. Figures (e) and (j) show HAADF STEM images for WSe<sub>2</sub> and WS<sub>2</sub>, respectively.

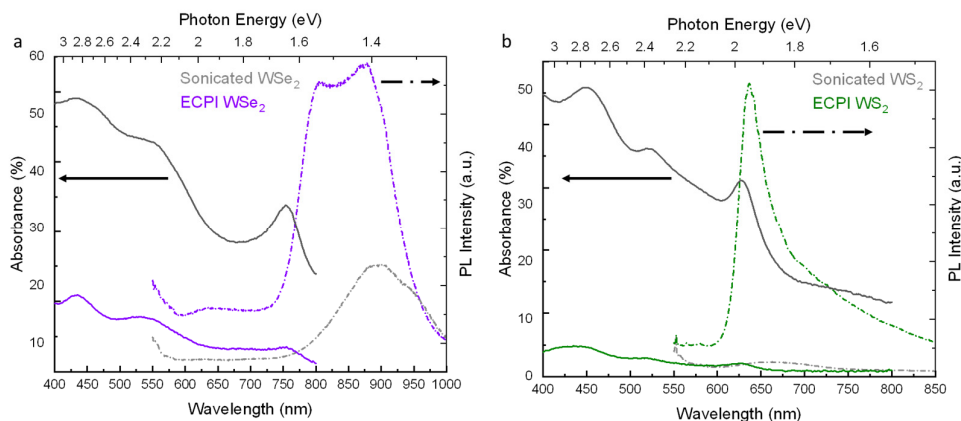


Figure 2.18. Optoelectronic and PEC properties of ECPI-made WSe<sub>2</sub> and WS<sub>2</sub> nanosheets.

UV-visible spectra (solid lines) and photoluminescence spectra (broken lines) for WSe<sub>2</sub> (a) and WS<sub>2</sub> (b). Colored lines represent ECPI made TMD while the gray lines show the sonicated material. As with MoS<sub>2</sub>, sonicated material counterabsorbs (solid lines) more photons than the ECPI-made nanosheet films. As expected ECPI-made nanosheets display more PL than their sonicated counterparts, three times as much in the case of WSe<sub>2</sub> and more than ten times as much for WS<sub>2</sub>.

As a final note, expanding the scope of the ECPI exfoliation method was demonstrated by employing it to prepare nanosheets of other TMDs such as *n*-type WS<sub>2</sub> and *p*-type WSe<sub>2</sub>. In these cases, only small adjustments (including, for example, the mass of powder for the pellet and the annealing conditions) were needed to afford the successful exfoliation. Large-area and thin nanosheets were observed for the W-based TMDs without any additional treatments (Figure 2.17). Comparing the UV-Visible and PL spectra of these ECPI exfoliated WS<sub>2</sub> and WSe<sub>2</sub> to their ultrasonicated counterparts shows similar improvements as was observed for MoS<sub>2</sub> (Figure S19, SI). These results underline the effectiveness of the scalable exfoliation technique reported herein and, since many 2D TMD-based devices employ van der Waals heterojunctions of more than one TMD, this showcases the feasibility of fully solution-processed high-performance heterojunction 2D TMD devices.

## 2.3 Conclusions

In summary, this chapter presented a versatile and scalable approach for the gentle exfoliation of layered TMDs into 2D nanosheets. By processing commercially-available TMD powders into annealed pellets, the intrinsic conductivity of the material was leveraged to electrochemically intercalate them with large molecule cations. In doing so size-thickness limitations experienced by other solution processable exfoliation techniques are overcome to produce very thin flakes with large lateral dimensions. While the traditionally-produced ultrasonicated nanoflakes are thick, small, and plagued by edge-steps, the ECPI-produced nanoflakes show more desirable morphology being thin, large, and with pristine, flat basal planes. These factors lead to improved optoelectronic properties including enhanced PL, exceptional charge carrier mobility, and high photocurrent density while absorbing less than 20% of the incident light. These last properties manifest as high internal quantum yields reaching 90% for the ECPI-made nanosheet photoanodes compared to just 12% for the ultrasonicated nanoflake photoanodes. Surprisingly the ECPI-made nanoflakes films even outperform CVD made flakes under similar testing conditions. Finally, the adaptability of this method is demonstrated by exfoliating W-based TMDs  $\text{WS}_2$  and  $\text{WSe}_2$ . Like  $\text{MoS}_2$ , these materials experience improved morphology and optoelectronic properties compared to their sonication counterparts. This greatly expands the range of configurations for high-performing 2D TMD devices. Thus, this work provides an advance for the scalable production of 2D materials ideally engineered for solar-energy conversion applications.

Table 1. Reference table comparing the performance of ECPI-made nanosheets to other relevant works.

Reference table comparing the properties, yield, photon conversion efficiency, intended use, and method of fabrication of TMD nanoflakes from 14 different works, including this one. The table includes both CVD and solution processable methods give the reader an overview of the field.

	TMD	Photoactive?	Nanoflake lateral size range	Yield	IPCE / APCE	Application	Device Structure	Procedure
Ref <sup>148</sup>	MoS <sub>2</sub>	Yes	NR	NA	2.5%/65% (1L), 0.4%/7% (7L)	Photodetector / photovoltaic	Graphene/MoS <sub>2</sub> single flake/graphene	CVD
Ref <sup>54</sup>	MoS <sub>2</sub> WS <sub>2</sub>	Yes	NR	NA	10%/NR (MoS <sub>2</sub> ), 30%/NR (WS <sub>2</sub> ), 80%/NR (MoS <sub>2</sub> /WS <sub>2</sub> )	Photoelectrode (I/I3)	Bare flake Bare flake Heterostructure	CVD
Ref <sup>151</sup>	MoSe <sub>2</sub>	Yes	NR	NA	0.6% (untreated)/NR 0.8% (laser annealed) /NR	Photoelectrode (I/I3)	Bare flake	CVD
Ref <sup>78</sup>	MoS <sub>2</sub>	Yes	500-2000 nm	NR	NR	Logic gates (transistors)	NA	Single crystal-based solution processed
Ref <sup>80</sup>	NbSe <sub>2</sub>	NR	100 – 10000 nm	NR	NR	Superconductors	Unmodified dispersion	Single crystal-based solution processed
Ref <sup>96</sup>	MoS <sub>2</sub>	Yes (w/ annealing)	NR	NR	0.01% / 0.02%	Photoelectrode (H <sub>2</sub> O/O <sub>2</sub> )	Bare film	Powder-based solution processed
Ref <sup>121</sup>	MoS <sub>2</sub>	No	NR	<20%	NR	Surface-enhanced Raman scattering (bio-sensing)	Bare film	Powder-based solution processed
Ref <sup>77</sup>	MoS <sub>2</sub>	No	300 - 500 nm	60%	NR	Electrocatalyst, supercapacitor	NA	Powder-based solution processed
Ref <sup>123</sup>	MoS <sub>2</sub>	NR	1000 – 3000 nm	NR	NR	Supercapacitor	Nanoflakes + carbon black + PVF on nickel foam	Powder-based solution processed
Ref <sup>118</sup>	MoS <sub>2</sub>	Yes	25-200 nm	1%	NR	HER catalyst	Bare film	Powder-based solution processed
Ref <sup>64</sup>	MoS <sub>2</sub>	Yes	300 – 2000 nm (thick)	40%	NR	Polymer reinforcement	MoS <sub>2</sub> embedded PVA	Powder-based solution processed
Ref <sup>65</sup>	WSe <sub>2</sub>	Yes	200 – 1000 nm	NR	.15%/NR	Photoelectrode (H <sub>2</sub> O/H <sub>2</sub> )	Bare film	Powder-based solution processed
Ref <sup>82</sup>	MoS <sub>2</sub>	Yes	50-250 nm	NR	NR	Transistor	TiO <sub>2</sub> under-layer, surface modified nanoflakes	Powder-based solution processed
Ref <sup>66</sup>	WSe <sub>2</sub>	Yes	198 ± 112 nm	NR	15%/70%	Photoelectrode (H <sub>2</sub> O/H <sub>2</sub> )	PVP under-layer, co-catalyst, silane treatment	Powder-based solution processed
This work <sup>126</sup>	MoS <sub>2</sub>	Yes	500 – 5000 nm	32%	25%/90%	Photoelectrode (I/I3)	Bare film	Powder-based solution processed

## 2.4 Methods

### *Pellet Pressing + Annealing*

500 mg of as-received  $\text{MoS}_2$  powder (Sigma-Aldrich; powder  $< 2 \mu\text{m}$ , 99%) was pressed using a manual Beckman hydraulic pellet press, 12.5 mm diameter die, up to 10 tons and held for 5 s. It is noted that this is a standard KCl pellet press (as used for FTIR spectroscopy sample preparation) which operates by filling the die (polished plate, powder, polished plate), compressing the sandwiched powder in the die with a pushing rod, and applying the pressure *via* the press to the pressing rod to compact the pellet. The polished plates and pressed pellet are then gently removed from the die using the pushing rod.

Up to three 500 mg pellets are vacuum sealed in a fused quartz glass tube (see Figure S20, SI) with 100 mg S powder (3:1 molar ratio  $\text{MoS}_2$ :S) ensuring the pellets are not touching to avoid fusing. The pellets are heated from room temperature to 1100 °C over 8 hours, held at 1100 °C for 48 hours, then allowed to cool naturally. Similar conditions were used for  $\text{WS}_2$ . For  $\text{WSe}_2$  better annealing results were obtained using 750 mg pellets and heating from room temperature to 1000 °C over 8 hours, holding for 12 hours, and cooling naturally. See Supporting Information, Method note 1 for additional information concerning starting mass, die diameter, and annealing conditions.

### *Electrochemical Pellet Intercalation and Exfoliation*

The annealed pellet was clipped with an alligator clip and placed in a 50 mL beaker with a glassy carbon counter electrode. Both electrodes were connected to a potentiostat with the  $\text{MoS}_2$  pellet as the working electrode, WE. The two electrodes are placed roughly 1 cm apart. A solution of 5 mg  $\text{mL}^{-1}$  tetraheptylammonium bromide (Acros Organics, 99%) in acetonitrile (Merck Millipore) was added until the pellet is submerged without liquid touching the alligator clip, and with sufficient space between electrodes to avoid contact as the WE expands. A voltage of 10 V was applied for 24 h (WE as cathode), during which the solution begins to turn yellow at the anode, and the pellet begins to slowly expand and slough off. After the pellet has become a fluffy powder at the bottom of the beaker, the powder and remaining pellet was carefully collected and washed thoroughly with ethanol *via* vacuum filtration with a nylon filter (pore size 0.45  $\mu\text{m}$ ). The solid material is transferred to a 50 mL centrifuge tube with 10 mL of NMP (Acros Organics; 99+% for spectroscopy) before and bath sonication (Ultrasonic bath USC T, VWR, 45 kHz) in water at 25 °C for 1-2 hours. Finally, the solution was centrifuged for 30 min at 120 rcf using an Eppendorf centrifuge 5810 equipped with a FA-45-6-30 rotor. The top 8 mL of supernatant is collected and transferred to a new container. See Supporting Information Method notes 2 - 6 for additional information concerning salt choice, applied voltage, intercalation time, exfoliation time, and centrifuge speed.

### *Ultrasonication Exfoliation*

For  $\text{MoS}_2$ , 500 mg of as-received powder (Sigma-Aldrich; powder  $< 2 \mu\text{m}$ , 99%) was sonicated in 50 mL of NMP (Acros Organics; 99+% for spectroscopy) by using a Qsonica Model Q700 probe sonicator for 2h at 50% amplitude (10 s on, 2 s off) while keeping the solution at 0.4 °C with a recirculating chiller. The resulting dispersion was first centrifuged for 30 min at 120 using an Eppendorf centrifuge 5810 equipped with a FA-45-6-30 rotor. The supernatant was collected and centrifuged at 7750 rcf for 30 min. The pellet was collected and redispersed in 10 mL (10:1 by volume) of tert-butanol:n-butanol (Sigma-Aldrich; ACS reagent >99.7%) *via* bath sonication for 30 min in ice water.

### *Thin Film Formation*

Thin films were made *via* a liquid/liquid interface created between deionized water and hexane (Sigma-Aldrich; >99%) using a previously-described approach.<sup>67</sup> Transfer to substrate was accomplished by aspirating the organic phase and then either aspirating the water phase to descend the film onto a pre-positioned substrate (for FTO glass) or *via* a stamping method (for FET substrates) wherein the substrate is manipulated with a suction pen and pressed into the film, transferring the material onto the substrate. FET substrates were cleaned by  $\text{UV/O}_3$  for 10 min prior to deposition. Films were then annealed at 200 °C for 120 min in a vacuum oven to remove excess solvent.

*UV-Visible / Raman / PL Spectroscopy / XPS / XRD*

UV-Vis spectra were acquired using a Shimadzu UV 3600 spectrometer from 800-300 nm using an integrating sphere with step size 1 nm and slit width of 5 nm. Measurements of solutions were taken using a quartz cuvette and films were analyzed directly in transmission mode. Dispersions of nanosheets in NMP were diluted in water. The same quantity of NMP was placed in water and used for a blank. Films were measured first in transmission mode then in reflectance mode using an air blank. Inverse mode was used to collect total reflectance and double beam mode was used to avoid fluctuations within the machine. All films were measured substrate-side towards the light source to mimic PEC testing conditions. The absorption of FTO was measured and calculated separately. Absorptance was calculated as shown in Equation 2.1 and Equation 2.2:

$$\text{Absorptance (A\%)} = 100 - \%T - \%R$$

Equation 2.1. Absorptance of MoS<sub>2</sub> film on FTO-glass.

$$\text{Absorptance(MoS}_2\text{)} = \text{Absorptance(MoS}_2\text{ + FTO)} - \text{Absorptance(FTO)}$$

Equation 2.2. Extracted absorptance of MoS<sub>2</sub>.

Where %T and %R are the percent transmission and reflection, respectively. Raman spectra and PL spectra were obtained using a Horiba Xplora Plus Raman microscope with 532 nm radiation (40 mW). Raman spectra were acquired from 100-1800 cm<sup>-1</sup> using a 100x objective, slit of 200 μm, hole of 500 μm, a grating with 2400 gr/mm, 10% filter, 10 s of acquisition, and 5 accumulations. The PL spectra were obtained from 550-950 nm using a 100x objective, a grating with 600gr/mm, slit of 200 μm, hole of 500 μm, 255 filter, 4s of acquisition, and 4 accumulations. PL spectra were normalized according to Raman signals appearing around 580 nm. XPS spectra were acquired using a PHI Versa Probe II (Physical Instruments AG, Germany). Analysis was performed using a monochromatic Al Kα X-ray source operated at 50 W. The spherical mirror analyzer was set at 45° take-off angle with respect to the sample surface. The pass energy was 46.95 eV yielding a full width at half maximum of 0.91 eV for the Ag 3d 5/2 peak. Curve fitting was performed using CasaXPS software. X-ray diffraction measurements were taken in Debye-Scherrer geometry (scanning mode) using Cu-K-alpha radiation on a Bruker D8 Discover Plus instrument equipped with a rotating anode and a Dectris Eiger2 500K detector. Samples were loaded into 0.5 mm borosilicate capillaries and spun during data acquisition.

*SEM / TEM / HAADF STEM / HR STEM*

SEM images were acquired using a Zeiss Merlin operated at 2 kV with probe current of 100 pA, a working distance of about 2.8 mm, and using an in-lens detector. HAADF STEM images and SAED were acquired on a FEI Talos F200S microscope operated at 200 kV. HAADF STEM images were obtained using a probe current of 100 pA, a camera length of 77 mm (collection angle > 75 mrad) and a dwell of 1-2 μs. High-resolution STEM images were acquired on a FEI Titan Themis microscope operated at 80 kV and equipped with a field emission gun (X-FEG). The aberrations of the probe were corrected with a CEOS DCOR system up to the 3rd order. ADF and iDPC imaging were acquired simultaneously using a probe current of 30 pA, a camera length of 230 mm (collection angle for ADF > 35 mrad) and a dwell time of 8 μs.

## 2D-PAINT

Defect mapping of MoS<sub>2</sub> was performed by the 2D-PAINT method that has been described in detail previously.<sup>37</sup> Imaging was performed on a custom-built total internal reflection fluorescence microscope with a dual-channel view optical system (DV2, Photometrics) and an EMCCD camera (iXon DU-897, Andor) that allows simultaneous recording of the specimen in the split wavelength windows of 509-530 nm and 675-725 nm. During imaging, liquid-exfoliated MoS<sub>2</sub> nanosheets on a coverslip are mounted in a reservoir on top of the high-NA oil-immersion objective lens (UApo Nx100, NA 1.49, Olympus). The probe, consisting of a 70 base pairs DNA oligomer with a thiol tail and an Atto 488 labeling dye is used in all experiments. The probe concentration was 1.0 nM. Illumination from a 488 nm laser (Sapphire, Coherent) was used to excite the sample and the probes. Exposure time is set as 50 ms with 500 ms sampling rate. For each experiment, 1000 frames are recorded. Post-processing of the images to localize the centroids of the defect-bound fluorophores is done by FIJI plugin ThunderStrom using integrated Gaussian PSF without multi-emitter fitting.<sup>152</sup> Reconstructed images were plotted using averaged shifted histograms rendering. Spatial autocorrelation analysis of the reconstructed images is performed with a MATLAB code<sup>153</sup> to extract Global Moran's I value with the weight matrix set as 9-by-9 pixels (equivalent to 20-by-20 nm, close to the localization uncertainty).

## FET Testing

FET measurements were carried out in a nitrogen atmosphere using a custom-built probe station and a Keithley 2612A dual-channel source measure unit. Au coated SiO<sub>2</sub> transistor substrates (Fraunhofer ISE) were used with 10 mm channel widths ( $W$ ) and an insulator capacitance ( $C_i$ ) of  $1.8 \cdot 10^{-8}$  F. Channel lengths ( $L$ ) of 5 or 10  $\mu\text{m}$  were used. Two LLISA nanosheet depositions on the substrate were used to ensure continuous nanosheet coverage. Drain voltage was scanned from 0-40 V with gate voltages from 0-40 V. The slope ( $m$ ) was extracted from the device transfer curve and the charge carrier mobility,  $\mu_{\text{sat}}$ , was calculated according to Equation 2.3:

$$\mu_{\text{sat}} = \frac{2Lm^2}{WC_i}$$

Equation 2.3. Charge carrier mobility.

## Photoelectrochemical Testing

Single-layer (one LLISA deposition) nanosheet films deposited on FTO-coated glass were used as photoelectrodes directly. Linear scanning voltammetry (LSV) measurements were obtained using a three-electrode (BioLogic SP-200 potentiostat) system with the TMD thin film as the working electrode a glassy carbon counter electrode and a Pt pseudoreference electrode. The active area of the electrode was 0.26 cm<sup>2</sup>. The electrolyte was 50 mM LiI and 25 mM TBAFP (Sigma-Aldrich, 99%) in acetonitrile (Merck Millipore). Voltage was applied from -0.3 V to +0.5 V (vs Pt) at a scan rate of 10 mV s<sup>-1</sup>. A 1000W Xe light source with water and KG2 filter (Schott) was used and calibrated to 1-sun intensity. Illumination was intermittent during LSV measurement ; on for 2s, off for 2s. All samples were measured substrate-side towards the light source. To estimate the IPCE, photoelectrodes were measured under illumination from a Tunable PowerArc monochromator. Incident photon power was recorded *via* a silicon photodiode. The illumination was scanned from 650 nm to 400 nm with 2 nm steps and 2s light on and 2s light off between wavelengths while the photocurrent was recorded at +0.3 V vs Pt.

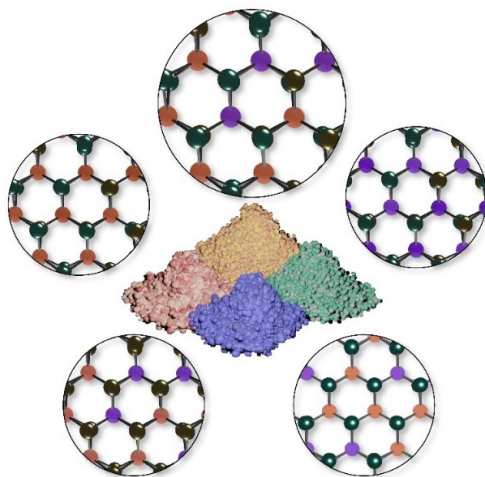


*Methods Notes:*

1. The starting mass of TMD powder and the die diameter can be adjusted as needed. It is also possible that annealing times and temperatures can be adjusted; however, it is important to observe enough crystal grown and fusing such that the pellet is electrically conductive. When using THAB a strong yellowing of the solution indicates successful intercalation while weak or non-yellowing solutions may suggest the pellet is not well-connected.
  - a. Typically annealing takes place in a quartz tube with an inner diameter of 15 mm and outer wall of 19 mm (2 mm thick walls). The final tube length is normally 12-15 cm after sealing. Note that with 100 mg of S powder the estimated pressure inside the tube can reach 16.5 bar and only certain quartz tubes are able to withstand this pressure as small defects in the quartz tubes walls can lead to explosions. To avoid this, the quartz must be of high quality with no defects.
2. It is expected that other ternary ammonium salts will perform with similar success (i.e. tetraethylammonium bromide, tetrapropylammonium bromide, tetrabutylammonium bromide, tetrabutyl ammonium tetrafluoroborate, etc.). To avoid producing bromine, tetraheptylammonium iodide or tetraheptylammonium hexa-/tetrafluoroborate may be used.
3. A lower or higher voltage may be used to achieve similar results. In the case of lower voltage, the intercalation will take place more slowly and will therefore require more time. Conversely, higher voltages will induce faster intercalation rates, but may have negative side effects with respect to oxidizing the counter electrode. A potential of 10 V was chosen as the acceptable compromise between voltage applied and intercalation time.
4. Intercalation can be carried out for more or less time as desired. Generally, less time means less intercalation and therefore less exfoliated material and more time produces the opposite trend to an extent. In the work shown here 24 hours was the appropriate compromise between yield and time. Note that that the unexfoliated, intact pellet can be retrieved after centrifugation, dried, and intercalated-exfoliated a second (or third, fourth, etc.) time without negative consequences. The amount of NMP added after washing can also be adjusted to tune final solution concentration as needed.
5. Bath exfoliation can also be extended as needed. If the solution does not appear viscous (clinging to the wall) and/or has not undergone a color change (from black to greenish for  $\text{MoS}_2$ ), the solution needs more sonication time. Figure S20b-e (see below) compares a well-exfoliated dispersion to a poorly exfoliated dispersion with photographs and microscope images. Since different bath ultrasonicators have different powers and often possess "hot spots", attention to this detail is important to ensure proper exfoliation.
6. Centrifuge speed can be adjusted to select for smaller or larger nanosheets as desired. For the purpose of this work 120 rcf was suitable for removing bulk material while maintaining good yield.



## Chapter 3 Facile production of two-dimensional transition metal dichalcogenide alloys *via* a powder-based, solution-processable approach



Commercially available powders transformed into alloyed TMD nanosheets.

The previous chapter described a novel powder-based route for making high-performance transition metal dichalcogenide (TMDs) nanosheets using an electrochemical pellet intercalation (ECPI) technique to assist exfoliation in a gentle manner. This method not only worked well for model material  $\text{MoS}_2$ , but could also be extended to other common TMDs ( $\text{WSe}_2$  and  $\text{WS}_2$ ). To further extend this method, this next chapter extends the technique beyond pure materials to include alloyed TMD nanosheets.

The alloying of two-dimensional (2D) TMDs represents a promising route towards inexpensive, robust, and scalable semiconductors with continuously tunable optoelectronic properties. However, to date all methods presented for fabricating alloyed TMD nanosheets involve complex fabrication processes, which are not suitable for the scalable production of large-area devices. Herein this chapter describes a powder-based, solution-processable route for the formation of 2D TMD alloyed nanosheets. This method builds upon the previously discussed ECPI technique by simply mechanically mixing two TMD powders prior to pellet formation. Beginning with the much-studied  $\text{Mo}_{0.5}\text{W}_{0.5}\text{S}_2$  alloy, it is shown that it is possible to achieve alloyed nanosheets wherein the metals are distributed over the nanosheets, as shown by high resolution scanning transmission microscopy (STEM) and that the composition can be reliably controlled during the pellet forming step as a result of ratio of the starting TMD powders. Accordingly, the optoelectronic properties of these TMD nanosheets are tuned as a function of composition. For another degree of tunability it is shown that this method can be used to form both metal-alloyed ( $\text{Mo}_{0.5}\text{W}_{0.5}\text{S}$  and  $\text{Mo}_{0.5}\text{W}_{0.5}\text{Se}$ ) and chalcogenide-alloyed ( $\text{MoSSe}$  and  $\text{WSSe}$ ) nanosheets. Finally, this method is employed to make quaternary ( $\text{Mo}_{0.5}\text{W}_{0.5}\text{SSe}$ ) nanosheets. Using STEM with the help of an integrated Differential Phase Contrast (iDPC) detector it is possible to differentiate the metal columns from the chalcogenide columns, confirming the distribution of the atoms and the formation of the alloy. As a final note ultraviolet photoelectron spectroscopy (UPS) is used to map the relative work functions of thin films of the nine (four pure, four ternary alloyed, one quaternary alloyed) 2D materials presented in this work. This demonstrates the ability of this powder-based, solution-processable approach to produce 2D TMDs with a broad range of optoelectronic properties in large quantities.

### 3.1 Introduction

Van der Waals layered materials are a promising class of materials owing to their thickness-dependent properties and the ease at which they can exfoliated. Transition metal dichalcogenides (TMDs) represent an important subset of this class of materials with nearly 40 different  $\text{MX}_2$  ( $\text{M}$  = metal,  $\text{X}$  = chalcogenide) combinations to choose from<sup>10</sup>. These combinations span the full range of materials from semimetal to semiconductor to superconductor<sup>10</sup>. Of the possibilities,  $\text{M}$  = Mo, W and  $\text{X}$  = S, Se have garnered much attention for their exceptional semiconducting properties, particularly in their two-dimensional (2D) form<sup>11,21,154,155</sup>. Accordingly, exciting advances have been made with these materials including photovoltaic, photoelectrochemical, catalysis, electronics, super-computing, and biomedical applications<sup>65,78,155–160</sup>.

More recently it has been shown that an additional degree of tunability can be obtained by making ternary and quaternary monolayer TMD alloys<sup>44,45,48,161–163</sup>. Alloying allows for continuously tunable bandgaps, where the optoelectronic properties can be precisely controlled based on the alloy combination and composition. The formation of these TMD alloys is energetically favorable and complete miscibility is attainable<sup>46,47</sup>. Indeed, all possible combinations involving Mo, W, S, and Se, including ternary and quaternary alloys have been predicted theoretically and demonstrated experimentally. As is the case for the pure materials, monolayer TMD alloys possess direct bandgaps because the same orbitals participate in the conduction and valence band of the alloys as the pure materials<sup>46,47</sup>. However, the location point of the alloyed bandgap in the Brillouin zone may differ from the pure case and the bandgap energy varies parabolically as a function of alloy composition due to a phenomenon known as band bowing<sup>44–47,163</sup>. The vast number of possible TMD combinations in conjunction with composition tuning allow for unprecedented optoelectronic opportunities for these materials.

However, it should be noted that all demonstrations to date have been made via energy intensive approaches including chemical vapor deposition (CVD), atomic layer deposition (ALD), molecular beam epitaxy (MBE), etc.<sup>161</sup> While these methods have provided the necessary results to demonstrate and characterize these 2D TMD alloys, they are not suitable for scaled-up production.<sup>61</sup> Additionally, studies have generally been limited to monolayers as growth conditions are such that large-area multi-layer flakes are challenging to obtain.<sup>45</sup>

This chapter address this limitation by presenting a solution-processable route for producing 2D TMD alloys. The method begins with inexpensive, commercially-available starting materials and leverages the method reported in chapter two, electrochemical pellet intercalation (ECPI), which has been shown to produce high-performing TMD nanosheets.<sup>126</sup> It is demonstrated that this method can be used to make a range of TMD alloys ( $\text{M}$  = Mo, W, Sn;  $\text{X}$  = S, Se), including ternary and quaternary, and that control over composition can be exerted. Importantly similar behaviors are observed in these solution-processed nanosheets as in those made via CVD and MBE thus paving the way for large-scale alloyed TMD devices.

## 3.2 Results and discussion

### 3.2.1 Bulk alloyed TMD pellet fabrication

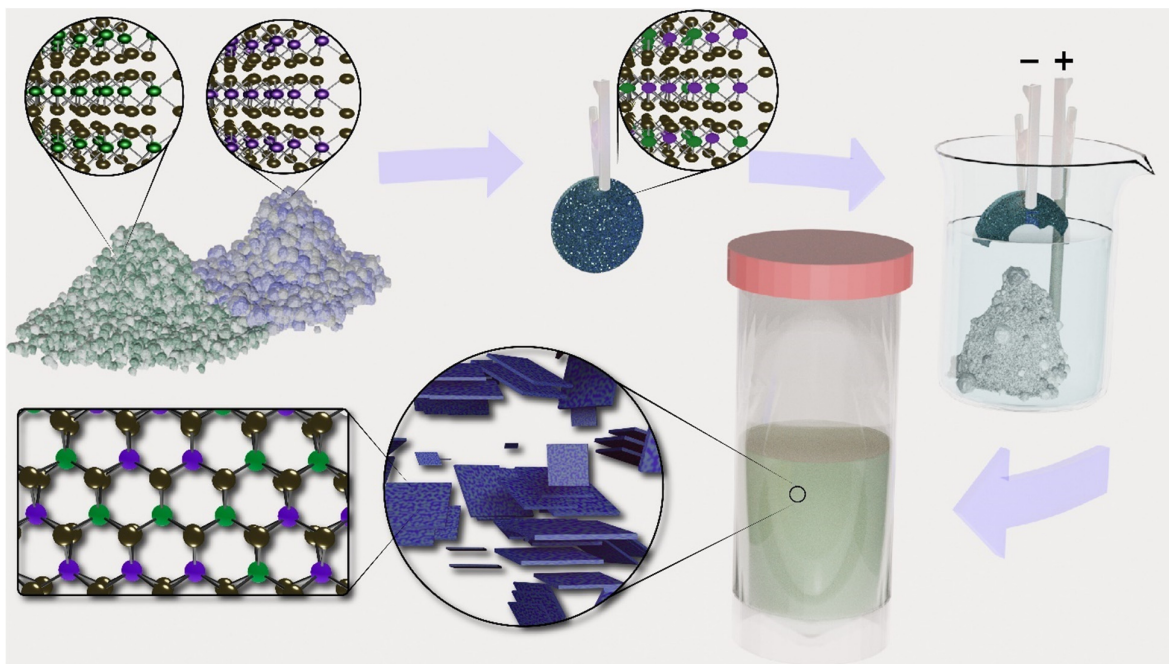


Figure 3.1. Schematic of the modified electrochemical pellet intercalation (ECPI) exfoliation for formation of 2D TMD alloys.

(1) As-received TMD (ex.,  $\text{MoS}_2$  and  $\text{WS}_2$ ) powders are ground together using mortar and pestle, pressed into a pellet, and annealed at  $1100^\circ\text{C}$  for 48 h with excess chalcogenide vapor. (2) The annealed pellet is immersed in a solution of tetraheptylammonium bromide ( $\text{THA}^+\text{Br}^-$ ) with a glassy carbon electrode. Applying a bias with the TMD pellet as a cathode causes the  $\text{THA}^+$  intercalation into the pellet and eventual detachment of the intercalated material. (3) The intercalated powder is collected, rinsed, gently agitated, and centrifuged at low speed to remove remaining bulk material. The result is a concentrated solution of exfoliated, alloyed TMD nanosheets.

The ECPI method, as presented in *Chapter 2*, is easily adjusted to make alloyed TMD nanosheets by simply mixing the two pure TMD powders prior to pellet formation as depicted in Figure 3.1. The two TMD powders are mechanically mixed in the desired concentration, for example equimolar amounts of  $\text{MoS}_2$  and  $\text{WS}_2$  to make  $\text{Mo}_{0.5}\text{W}_{0.5}\text{S}_2$ . Annealing times and temperatures can be tailored based on the chalcogen species; for example higher temperatures for S-based TMDs compared to Se.<sup>17</sup> After annealing the pellet has sufficient electronic conductivity and can be electrochemically intercalated with the large molecule cation  $\text{THA}^+$ . After exfoliation using ECPI, low-speed centrifugation is performed to remove the unexfoliated bulk, leaving a dispersion of TMD nanosheets. Note that this dispersion contains a range of flake thickness from mono- to few-layer and different flake sizes can be selected according to the needs of the intended application. If successful, this presents a promising approach when considering the difficulty of scaling up CVD techniques and, in particular, growing multilayer alloyed flakes.

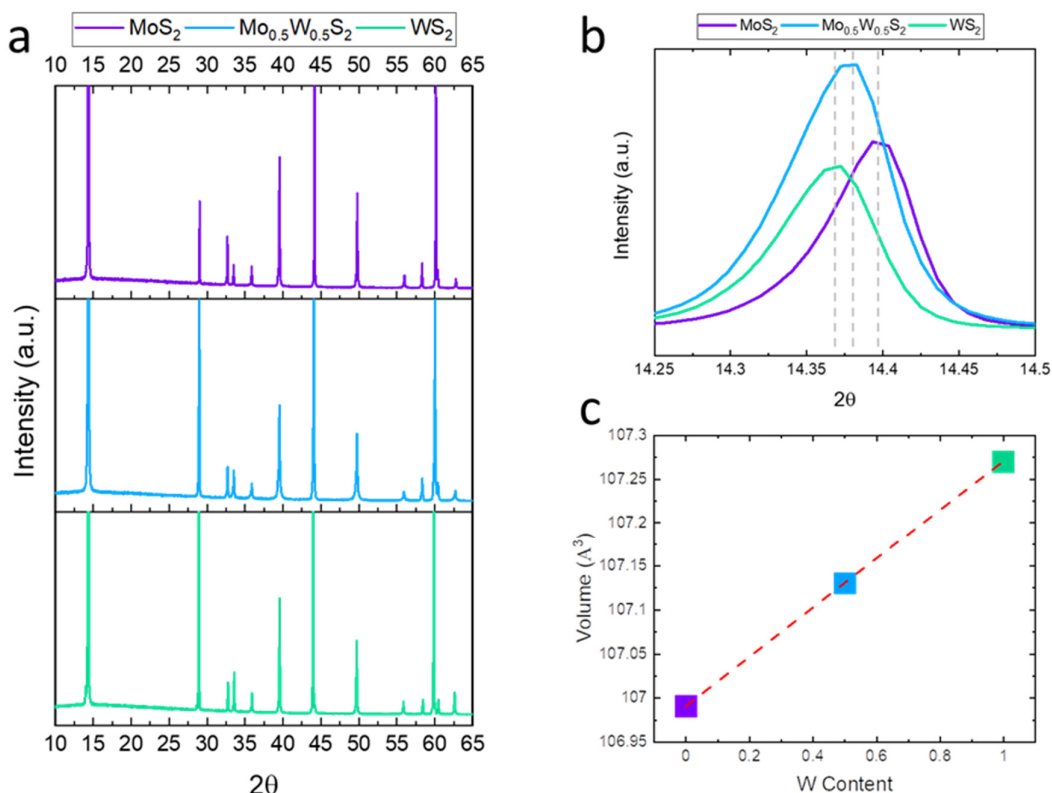


Figure 3.2. Characterization of alloyed TMD pellet.

Powder XRD patterns from pellets made of pure  $\text{MoS}_2$  (purple), pure  $\text{WS}_2$  (green), and 1:1  $\text{MoS}_2$ : $\text{WS}_2$  (blue). (a) Wide view shows sharp, high-intensity peaks confirming the crystallinity of the three pellets. (b) Close up of the (002) reflection shows systematic peak shifting consistent with changed lattice parameters. (c) Calculated lattice parameters for pure  $\text{MoS}_2$  (purple), pure  $\text{WS}_2$  (green), and 1:1  $\text{MoS}_2$ : $\text{WS}_2$  (blue) show a perfectly linear correlation consistent with Vegard's law.

As one of the most well-studied ternary alloys to date<sup>45–48,161,162,164–166</sup>,  $\text{Mo}_{(1-x)}\text{W}_x\text{S}_2$  was chosen as a model system to showcase this powder-based technique and demonstrate control over composition. A mixed pellet of 1:1 atomic ratio  $\text{MoS}_2$ : $\text{WS}_2$  was made by grinding together equimolar amounts of  $\text{MoS}_2$  and  $\text{WS}_2$  powder. In an effort to achieve a more homogenous mixture the two powders were manually ground in a mortar and pestle for 2–3 minutes before they were pressed into a pellet. The pellet was annealed at 1100 °C for 48 hours: the same conditions as for pure  $\text{MoS}_2$ / $\text{WS}_2$  pellets. X-ray diffraction (XRD) of the pure and mixed pellets shows well defined peaks consistent with successful formation of crystalline domains (Figure 3.2a). A closer look at the (1 0 2) peaks at 14.35–14.40 shows a systematic shift to higher  $2\theta$  from  $\text{WS}_2$  to  $\text{Mo}_{0.5}\text{W}_{0.5}\text{S}_2$  to  $\text{MoS}_2$  (Figure 3.2b). This is consistent with a change in lattice parameters with the incorporation of the W atom. By fitting the intensities show in Figure 3.2a it is possible to calculate the unit cell volume for each parameter, as shown in Figure 3.2c. The change in volume is perfectly linear and appears to follow Vegard's law for alloyed materials, which empirically states that combining two materials with the same crystal structure should yield a linear combination of their lattice parameters according to the composition.<sup>47</sup> This initial observation supports the notion that the 1:1  $\text{MoS}_2$ : $\text{WS}_2$  mixed pellet has been successfully transformed to form the  $\text{Mo}_{0.5}\text{W}_{0.5}\text{S}_2$  bulk alloy.

### 3.2.2 Nanosheet characterization

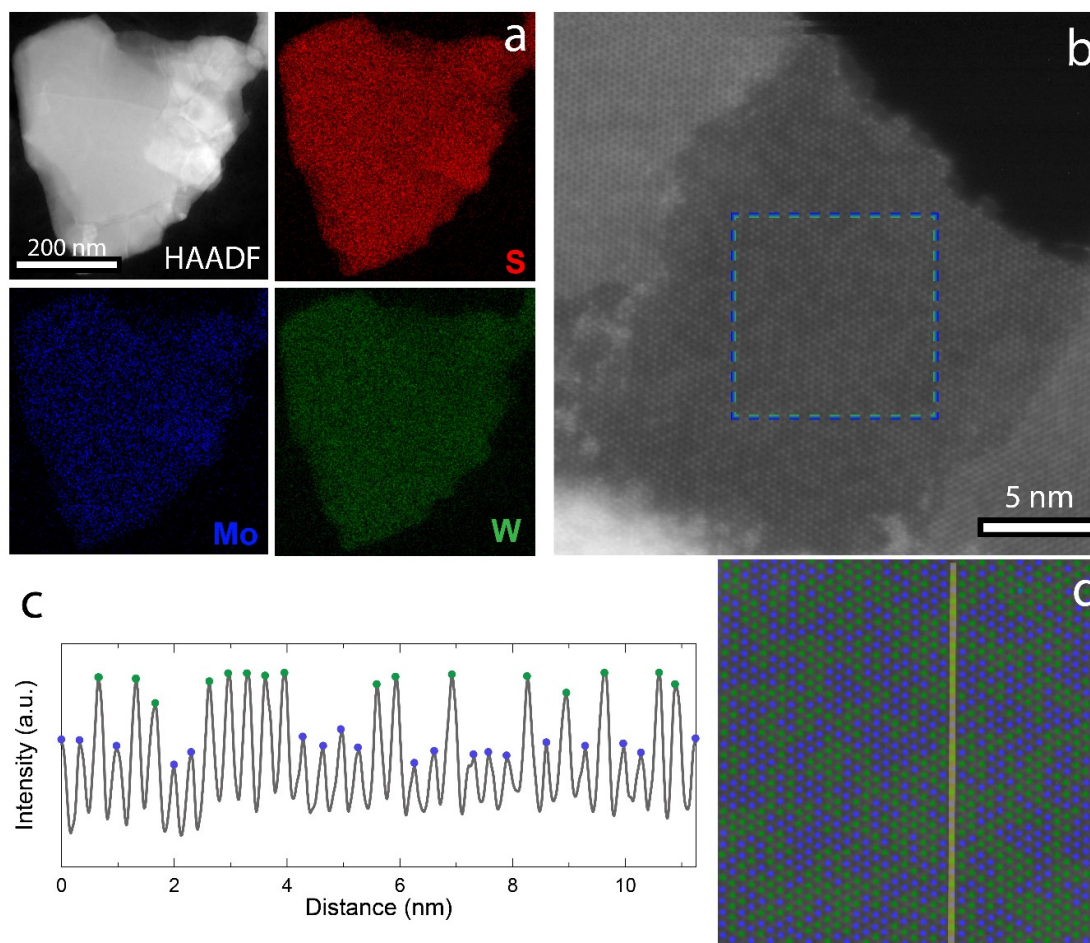


Figure 3.3. STEM and high-resolution STEM of  $\text{Mo}_{0.5}\text{W}_{0.5}\text{S}_2$  nanosheets.

(a) STEM EDX of a typical nanosheet shows presence of S (top right), Mo (bottom left), and W (bottom right) distributed across the flake. STEM operated at 200 kV. (b) High-resolution STEM HAADF image of monolayer region of a  $\text{Mo}_{0.5}\text{W}_{0.5}\text{S}_2$  nanosheet. Brighter atoms correspond to W; darker atoms to Mo. STEM operated at 80 kV. (d) Cropped and enlarged region highlighted in (b). Image falsely colored for clarity, W in green and Mo in blue. (c) Line intensity profile of grayscale image as indicated in (d). The maxima correspond to metal atoms and minima to  $\text{S}_2$  columns. W is assigned to the higher intensity maxima and Mo to the lower maxima. Quantitative analysis finds a 53:47 ratio for W:Mo.

After confirming the formation of the  $\text{Mo}_{0.5}\text{W}_{0.5}\text{S}_2$  alloy in the bulk phase, the pellet was electrochemically intercalated, as described in *Chapter 2*,<sup>126</sup> to give a viscous dispersion of exfoliated nanosheets. The dispersion was then characterized in the liquid phase or as thin films made by a previously described liquid-liquid interfacial self-assembly (LLISA) method.<sup>65</sup> Note that the thin films are approximately  $5 \text{ cm}^2$  (Annex Item 4), but have the potential to be easily scaled to meters-squared films.<sup>83</sup>

Given the alloyed nature of the pellet, the TMD nanosheets produced from the pellet are expected to be alloyed as well and with the same atomic concentration that was used to make the pellet. To confirm successful formation of the  $\text{Mo}_{0.5}\text{W}_{0.5}\text{S}_2$  alloyed nanosheets, scanning transmission electron microscopy (STEM) and energy dispersive X-ray (EDX) spectroscopy were used to observe the elemental mapping of the nanosheet (Figure 3.3a). From this image of a ca. 500 nm nanosheet it is possible to observe the presence of both the sulfur (red) and metal (blue and green) atoms, of which the latter appear to be homogeneously spread across the nanosheet, suggesting the successful formation of the 2D

$\text{Mo}_{0.5}\text{W}_{0.5}\text{S}_2$  alloy. Note that phase pure, i.e.,  $\text{MoS}_2$  and  $\text{WS}_2$ , nanosheets were observed if the starting powder was not mechanically ground prior to pellet formation (Annex Item 5).

As EDX cannot achieve atomic resolution, high resolution STEM was performed to confirm the atomic mixing of the Mo and W atoms. A high-resolution STEM high-angle annular dark field (HAADF) image of a monolayer region of a  $\text{Mo}_{0.5}\text{W}_{0.5}\text{S}_2$  nanosheet is shown in Figure 3.3b. The HAADF detector can be used to identify atoms of different Z values as the intensity of the signal, or brightness, scales according to  $Z^2$ .<sup>44</sup> Given that Mo and W have very different Z values, they can be reliably differentiated from one another as well as the S atoms (Figure 3.3c,d). W is the largest atom and thus interacts most strongly with the electron beam, appearing brighter, followed by Mo and then S. Figure 3.3d maps out the W and Mo atoms as green and blue, respectively, for clarity. By mapping the intensity as highlighted in Figure 3.3d, a periodic pattern is observed where the maxima represent a metal atom, and the minima is vacuum (Figure 3.3c). Two different maxima species can be seen where the higher maxima correspond to W and the lower correspond to Mo. The variation in the minima is explained by the different chemical species surrounding the vacuum space, which causes fluctuations in the beam.

An integrated differential phase contrast (iDPC) detector was used to observe both the metal (Mo, W) and chalcogen (S) sites simultaneously (Annex Item 6). In this case the intensity of the atoms follows a linear relationship of Z, allowing them to be differentiated;<sup>134</sup> here the brightest spots will once again be W, followed, by Mo, and then by S, and finally S. This last case can be observed as occasional light spots in the form of S vacancies. This is consistent with the previous work using this imaging technique (*Chapter 2*) as well as with CVD and mechanically exfoliated monolayers.<sup>39,44</sup>

While preliminary computational works had suggested that the most energetically favorable atomic configurations are those in which Mo-S-W bonds are maximized (an ordered W/Mo/W pattern),<sup>46</sup> experimental works, including this one, exclusively show a disordered phase, or clustering of atoms.<sup>44,162–164</sup> Indeed, Tan and coworkers reexamined this phenomena and found that the disordered phase becomes increasingly favorable with increasing temperature.<sup>167</sup> Therefore, given the annealing conditions used in this work (1100° C), the disordered phase is expected and consistent with both recent computational and previous experimental works.

Finally, the Mo:W atomic ratio is considered. As the atomic ratio of the pellet was made 1:1, the same is expected from the exfoliated nanosheets. Indeed, of the 1352 atoms displayed, 710 are W atoms and 642 are Mo atoms, yielding a W-to-Mo ratio of 53% to 47%. This initial result is a good indication that some compositional control can be exerted over the alloyed nanosheets via the starting mixture; however, additional compositions should be examined to confirm this.



### 3.2.3 Composition-tuned $\text{Mo}_{(1-x)}\text{W}_x\text{S}_2$ alloyed nanosheets

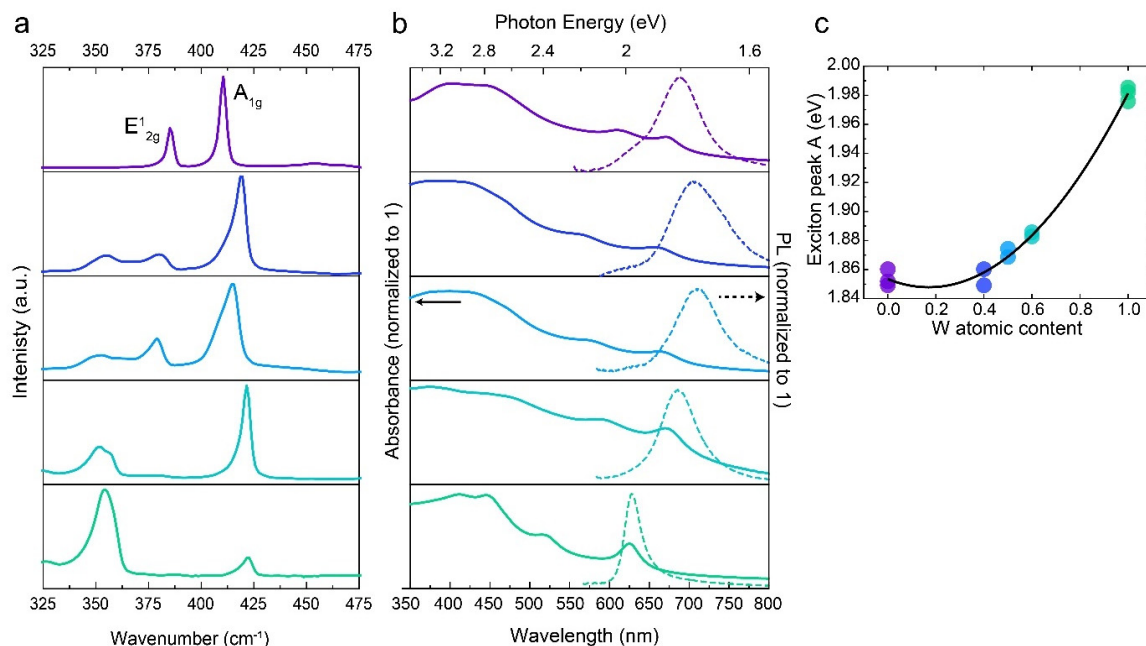


Figure 3.4. Optoelectronic characterization of  $\text{Mo}_{(1-x)}\text{W}_x\text{S}_2$  nanosheets.

Investigation of  $\text{Mo}_{(1-x)}\text{W}_x\text{S}_2$  nanosheets for  $x = 0$  (purple, top),  $x = 0.4$  (blue),  $x = 0.5$  (light blue),  $x = 0.6$  (teal), and  $x = 1$  (green, bottom). (a) Raman spectroscopy of a LLISA deposited thin film of 2D  $\text{Mo}_{(1-x)}\text{W}_x\text{S}_2$ . (b) Normalized UV-Vis absorbance spectra (solid lines) for  $\text{Mo}_{(1-x)}\text{W}_x\text{S}_2$  nanosheet dispersions and normalized PL (broken lines) for thin films. (c) Extracted A excitonic peaks from the UV-Vis spectra and plotted as a function of  $x$  (W atomic content). The black solid curve is the quadratic fit for the extracted data points and describes the bowing effect observed.

To ascertain whether some general control over nanosheet composition is feasible, the properties of these nanosheets are studied as a function of composition. It has been theoretically predicted that the most energetically favorable  $\text{Mo}_{(1-x)}\text{W}_x\text{S}_2$  alloys are in the range of  $x = 0.44$ - $0.66$ .<sup>46,47</sup> For this reason, alloyed TMD pellets with compositions  $x = 0.4$ - $0.6$  were chosen for exfoliation into nanosheets. Figure 3.4a shows the Raman spectra for LLISA films made of  $\text{MoS}_2$ ,  $\text{Mo}_{0.6}\text{W}_{0.4}\text{S}_2$ ,  $\text{Mo}_{0.5}\text{W}_{0.5}\text{S}_2$ ,  $\text{Mo}_{0.4}\text{W}_{0.6}\text{S}_2$ , and  $\text{WS}_2$  from top to bottom, respectively. Pure  $\text{MoS}_2$  displays the expected peaks at  $385\text{ cm}^{-1}$  ( $E_{2g}^1$ ) and  $410$  ( $A_{1g}$ ) consistent with few-layer  $\text{MoS}_2$ . With increasing W content, the  $A_{1g}$  mode shifts to lower frequencies (higher wavenumbers), eventually reaching  $422\text{ cm}^{-1}$ , consistent with pure, few layer  $\text{WS}_2$ . In contrast the  $E_{2g}^1$  peaks from the pure  $\text{MoS}_2$  shifts to higher frequencies (lower wavenumbers) and decreases in relative intensity with increasing W content, eventually disappearing. Additionally, a second  $E_{2g}^1$  peak is observed with the addition of  $\text{WS}_2$ , increasing in frequency as W content increases. These trends are consistent with those observed in CVD and ALD made  $\text{Mo}_{(1-x)}\text{W}_x\text{S}_2$  nanosheets,<sup>45,162,168,169</sup> demonstrating compositional control in the thin films presented here.

After confirming the composition of the flakes, the resulting optoelectronic properties can be evaluated. Figure 3.4b shows the normalized ultraviolet visible (UV-Vis) absorbance spectra for the  $\text{Mo}_{(1-x)}\text{W}_x\text{S}_2$  dispersions (solid lines) and the photoluminescence (PL) of the films (broken lines) studied in Figure 3.4a. It should be noted that the absorbance gives an overview of all the flakes present in solution while the PL focuses on a small region of a single film. Once again, the pure materials display the expected excitonic peaks at 671 nm (A) and 609 nm (B) for  $\text{MoS}_2$  (top) and 625 nm (A) for  $\text{WS}_2$  (bottom). Importantly distinct excitonic peaks are present in the alloyed nanosheet dispersions, as opposed to a mix of the  $\text{MoS}_2$  and  $\text{WS}_2$  signals. Indeed, as  $\text{WS}_2$  content increases the A excitonic peak shifts first to lower energy before shifting back to higher energies. This phenomenon is known as “band bowing” and it has been well-studied for alloyed TMDs.<sup>44–47,163,168–170</sup> To better observe this behavior the A exciton peaks for several samples have been extracted and plotted in Figure 3.4c. The bowing effect can be described by Equation 1.1,

$$E_{A_{\text{ext}},\text{Mo}_{(1-x)}\text{W}_x\text{S}_2} = (1 - x)E_{A_{\text{ext}},\text{MoS}_2} + xE_{A_{\text{ext}},\text{WS}_2} - bx(1 - x),$$

Equation 1.1. Bowing parameters.

where  $x$  is the W content,  $A_{\text{ext}}$  is the location of the excitonic peak, and  $b$  is the bowing parameter. Fitting the extracted points in Figure 3.4c yields a bowing parameter of  $0.19 \pm 0.01$  which is in excellent agreement with studies based on CVD and ALD-made monolayers.<sup>45,162,163</sup>

In accordance with the absorbance spectra, band bowing can be seen in the PL spectra of the thin films (Figure 3.4b, broken lines). Notably PL can be recorded for each alloy mixture, though intensity, Stokes shift, and peak sharpness can be variable as a result of the flake morphology in the region of interest as discussed in Chapter 2,<sup>126</sup> indeed additional tuning is possible by controlling layer number, which can be tuned during the centrifugation step and is an advantage over CVD methods as noted in the introduction. Despite possible variabilities the general trend holds: the PL peak shifts first to lower energy, then to higher energy. These results indicate that both absorbance and emission can be fine-tuned using this method.

### 3.2.4 Other ternary TMD alloys

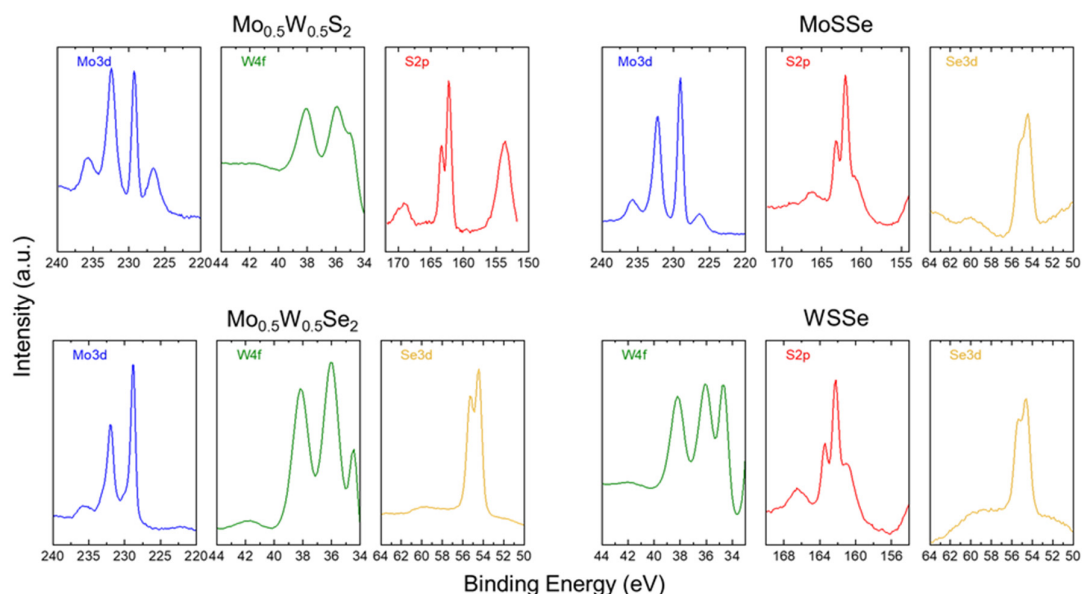


Figure 3.5. XPS for films of alloyed TMD nanosheets.

Mo3d (blue), W4f (green), S2p (red), and Se3d (yellow) core level spectra for the ternary alloyed TMD nanosheets confirms the presence of the expected elements for each combination.

It has been clearly shown that the ECPI method can be used to make alloyed  $\text{Mo}_{(1-x)}\text{W}_x\text{S}_2$  TMD nanosheets and that their optoelectronic properties can be accordingly controlled. To further extend the application of the ECPI alloy formation, it is of interest to consider what other ternary alloys could be prepared. Thus, attention is now directed to other combinations comprised of Mo, W, S, and Se. In addition to  $\text{Mo}_{(1-x)}\text{W}_x\text{S}_2$ , other candidates include  $\text{Mo}_{(1-x)}\text{W}_x\text{Se}_2$ ,  $\text{MoS}_{(1-y)}\text{Se}_y$ , and  $\text{WS}_{(1-y)}\text{Se}_y$ . As with  $\text{Mo}_{(1-x)}\text{W}_x\text{S}_2$ , it has been generally predicted that the most favorable concentrations are when  $x, y = 0.5$ .<sup>46,47</sup> Therefore,  $\text{Mo}_{0.5}\text{W}_{0.5}\text{Se}_2$ ,  $\text{MoSSe}$ , and  $\text{WSSe}$  were selected for this demonstration, and dispersions of alloyed nanosheets were prepared using the established ECPI method.

X-ray photoelectron spectroscopy (XPS) confirms the presence of the expected elements according to the alloy composition (Figure 3.5). A more detailed fitting of the W4f and Mo3d orbitals can be found in Annex Item 7 and Annex Item 8, respectively. It should be noted, however that these XPS results do not differentiate between an alloy and a heterojunction of pure phases, for example. To concretely confirm alloy formation Raman spectroscopy is shown in Figure 3.6a. These results show vibration modes which are distinct from the pure phase (ex., Mo-S-W or S-Mo-Se) and consistent with monolayer CVD grown demonstrations.<sup>44,45,49,50,162,168</sup> Panel one and two (green and purple) show evidence for the typical group VI metal-alloyed TMDs,  $\text{Mo}_{0.5}\text{W}_{0.5}\text{S}_2$  and  $\text{Mo}_{0.5}\text{W}_{0.5}\text{Se}_2$ . Notably this means that both n-type and p-type alloys can be fabricated and tuned using this method. Additionally, panel three and four (cyan and blue) confirm that chalcogen-alloyed TMDs are also attainable, finishing off the possible combinations. These mixtures are important as semiconductors with different extrinsic behaviors, for example n-type  $\text{WS}_2$  and p-type  $\text{WSe}_2$ , can be merged to make materials with ambipolar behavior,<sup>49</sup> for example. Additionally, the incorporation of S into Se-based materials may help to improve their stability.<sup>47</sup> This greatly expands the number of blends and, therefore, range of properties that can be harnessed using this method.

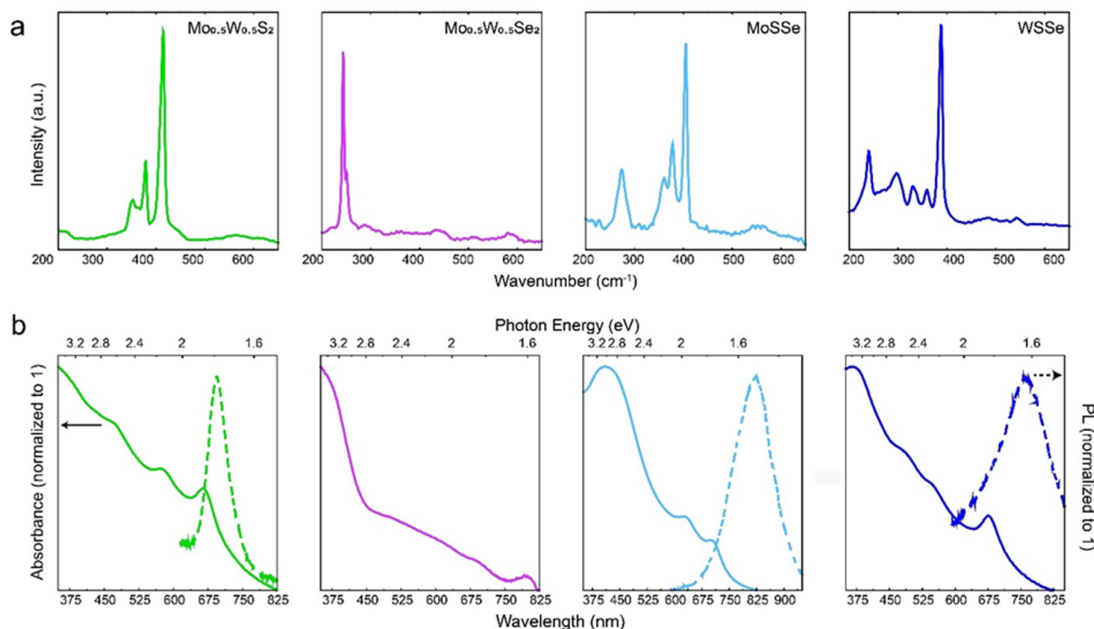


Figure 3.6. Characterization of ternary alloyed nanosheets made from combinations of Mo, W, S, and Se.

From left to right:  $\text{Mo}_{(1-x)}\text{W}_x\text{S}_2$  (green),  $\text{Mo}_{(1-x)}\text{W}_x\text{Se}_2$  (pink),  $\text{MoSSe}$  (cyan), and  $\text{WSSe}$  (blue). (a) Raman spectroscopy for thin films made of the four ternary alloys. (b) Normalized UV-Vis absorbance spectra of the nanosheet dispersions (solid lines) and normalized PL spectra of the thin films (broken lines) for the four ternary alloys.

Next, the optoelectronic properties are studied using UV-Vis (solid lines) and PL (broken lines) in Figure 3.6b. As with the Raman spectroscopy the UV-Vis spectra show unique absorption signals, displaying altered exciton peaks and regions of increased absorption compared to the pure TMDs. Accordingly, PL is also shifted compared to the pure materials and can be recorded for all combinations, with the exception of the  $\text{Mo}_{0.5}\text{W}_{0.5}\text{Se}_2$  alloy. Given the red-shifted nature (compared to  $\text{MoSe}_2$  and  $\text{WSe}_2$ ) of the excitonic peak and the expected Stokes shift of the PL signal, it is possible that PL is present but not detectable in the set-up used in this work. Another explanation could be the general instability of selenide-based materials.<sup>171</sup> Indeed, if too many defects are present charge recombination may occur too quickly to be detected in this very simple apparatus.

### 3.2.5 Quaternary TMD alloy formation

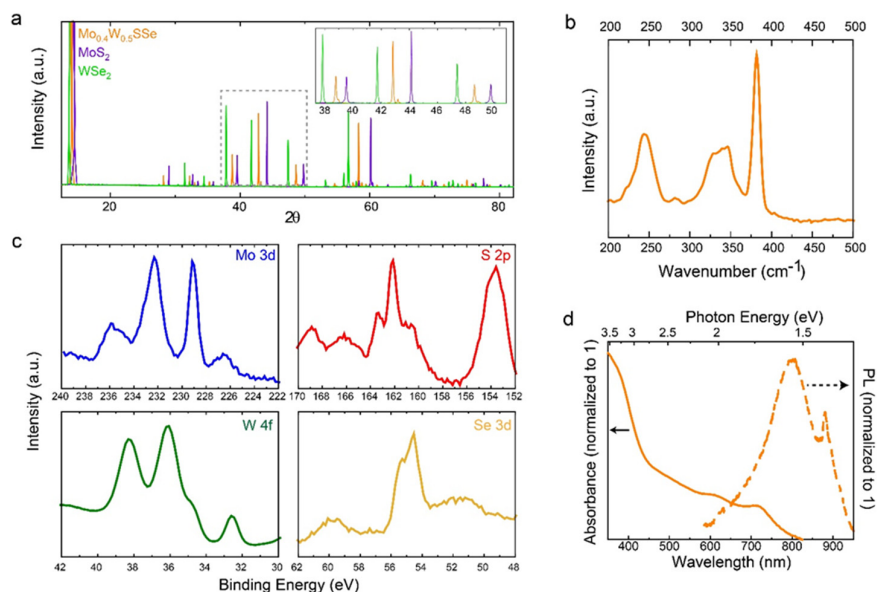


Figure 3.7. Characterization of quaternary alloy  $\text{Mo}_{0.5}\text{W}_{0.5}\text{SSe}$ .

(a) Powder XRD pattern for the alloyed pellet (orange) as well as the pure starting materials  $\text{MoS}_2$  (purple) and  $\text{WSe}_2$  (green). Inset gives a closer look at reflections (1 0 3), (0 0 6), and (1 0 5) from left to right, respectively. (b) Raman spectrum for a thin film of exfoliated  $\text{Mo}_{0.5}\text{W}_{0.5}\text{SSe}$ . (c) XPS spectra for a thin film of exfoliated  $\text{Mo}_{0.5}\text{W}_{0.5}\text{SSe}$  for core level Mo 3d (top left), W 4f (bottom left), S 2p (top right), and Se 3d (bottom right). (d) Normalized UV-Vis absorbance spectra of the nanosheet dispersions (solid lines) and normalized PL spectra of the thin films (broken lines) for the quaternary alloy. Sharp peak at 900 nm is assigned to fluorescing defects in the glass substrate.<sup>172</sup>

As all four of the common TMD components (Mo, W, S, Se) have been successfully incorporated into ternary alloys, it is reasonable to expect that the quaternary alloy  $\text{Mo}_{(1-x)}\text{W}_x\text{S}_{(2-y)}\text{Se}_y$  is attainable. This should be possible either by mixing all four binary TMDs  $\text{MoS}_2$ ,  $\text{WSe}_2$ ,  $\text{WS}_2$ ,  $\text{MoSe}_2$ , a combination of three, or the correct choice of two. Figure 3.7 shows the results of mixing  $\text{MoS}_2$  with  $\text{WSe}_2$  in equimolar amounts in hopes of obtaining  $\text{Mo}_{0.5}\text{W}_{0.5}\text{S}_1\text{Se}_1$  nanosheets using this method.

XRD analysis of the annealed  $\text{Mo}_{(0.5)}\text{W}_{0.5}\text{SSe}$  pellet is shown in Figure 3.7a, along with XRD for the pure materials that were mixed to form the pellet. From the wide view it can be seen that all three materials give sharp peaks, consistent with the formation of crystalline domains. The inset shows a close up of the (1 0 3), (0 0 6), and (1 0 5) peaks, respectively left to right. For each reflection the quaternary alloy lies directly in the middle of the two pure materials, seemingly following Vegard's law for alloyed materials.<sup>47</sup> As the lattice parameters for  $\text{MoS}_2$  and  $\text{WSe}_2$  are quite different,<sup>47</sup> a distinction is more clearly seen here than in the  $\text{Mo}_{0.5}\text{W}_{0.5}\text{S}_2$  pellet. Convinced of the successful alloying of the pellet, ECPI assisted exfoliation was performed to produce and analyze resulting nanosheets.

Once again XPS spectra confirms the presence of the four expected elements (Figure 3.7c, Annex Item 7, Annex Item 8), but this is not sufficient to assert alloy formation. For additional confirmation, the Raman spectrum for a  $\text{Mo}_{(0.5)}\text{W}_{0.5}\text{SSe}$  nanosheet film is shown in Figure 3.7b. This spectrum is complex as is expected for a material with many vibrational modes including: Mo-S-W, W-S, Mo-S, Mo-W-Se, W-S-Se, Mo-S-Se.<sup>44</sup> Importantly this spectra is not only distinct from either pure material, but also from all of the ternary alloys previously discussed (Annex Item 9).

The optoelectronic properties of these nanosheets are examined in Figure 3.7d. As with the previous alloys UV-Vis (solid line) shows a unique signature. The PL (broken line) is severely red shifted compared to the pure materials, thereby extending the range to the infrared edge of the spectrum. Note that the sharp peak seen around 900 nm is attributed to PL defects in the underlying glass substrate (Annex Item 10).

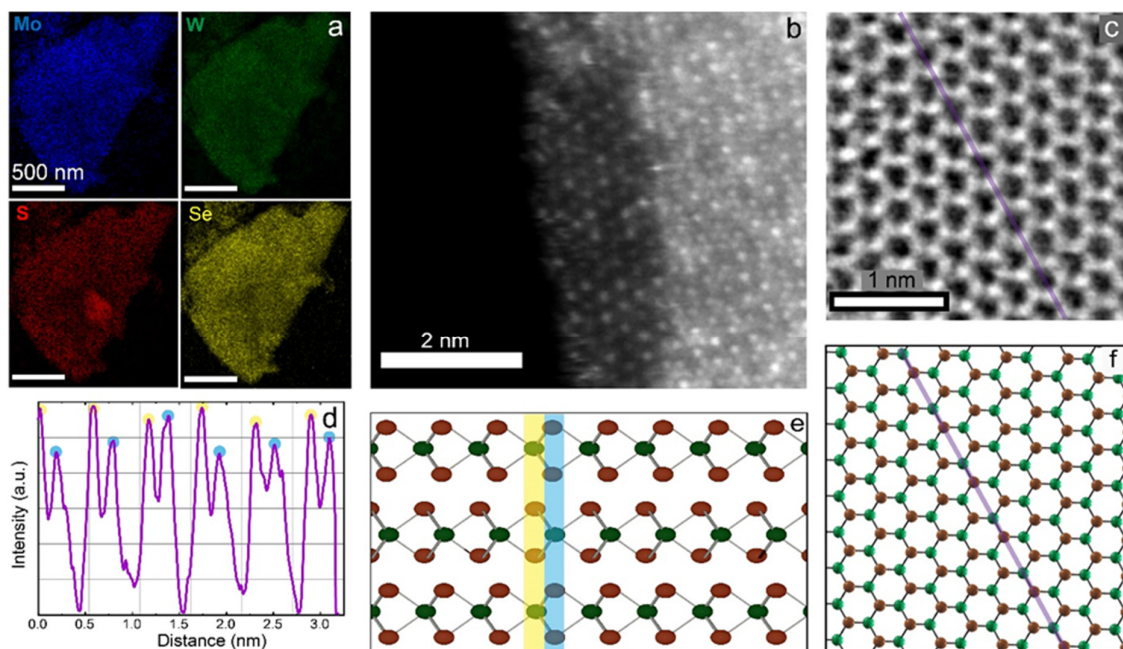


Figure 3.8. STEM EDX and high-resolution STEM of 2D  $\text{Mo}_{0.5}\text{W}_{0.5}\text{SSe}$  nanosheets.

(a) STEM EDX of a typical nanosheet shows presence of Mo (top left), W (top right), S (bottom left), and Se (bottom right) distributed across the flake. STEM operated at 200 kV. (b) High-resolution STEM HAADF image of a mono and bilayer region of a multilayer  $\text{Mo}_{0.5}\text{W}_{0.5}\text{SSe}$  nanosheet. On the monolayer area (left) brighter atoms correspond to W; darker atoms to Mo. On the bilayer area the brightest spots correspond to W/W columns, intermediary spots to Mo-W columns, and dimmest spots to Mo/Mo columns. STEM operated at 80 kV. (c) High-resolution STEM iDPC image of a multilayer flake where both metal and chalcogenide columns can be identified. (d) Line intensity profile for line highlighted in (c). Metal columns are assigned to the first maxima (green) and chalcogenides the second (red). (e) Schematic of predicted lattice recorded in (c) with the same line profile highlighted. Green atoms are assigned to metal columns and red to chalcogenide columns.

To examine the elemental mapping and atomic configuration of the quaternary alloyed nanosheets, STEM EDX and high-resolution STEM are shown in Figure 3.8. STEM EDX suggests the presence of all four elements with even spreading over the entire 2D nanosheet (Figure 3.8a). High-resolution STEM was performed in hopes of distinguishing atoms based on their Z values (Figure 3.8c-e); however, the lighter nature of the chalcogens atoms makes them more challenging to distinguish compared to the metal atoms. To overcome this an integrated differential phase contrast (iDPC) detector was used as it is more sensitive to small changes in Z, scaling linearly (Figure 3.8c).<sup>134,173</sup>

To reliably differentiate the atoms, a monolayer region is required to limit the possible number of chalcogenide atom combinations along the z-axis to five (i.e., S-S, S-Se, Se-Se, S-vacancy, Se-vacancy). Adding more layers quickly complicates the situation rendering quantitative analysis challenging. As the quaternary nanosheets were found to be more sensitive to oxidation and degradation, likely due to the selenium, only multilayer flakes could be examined (Figure 3.8b-e).

While it is not possible to identify the exact atomic nature of each item and therein quantify atomic ratios, Figure 3.8b-d still supports formation of the alloy and homogenous atom distribution. The edge of a nanosheet is shown in the HAADF image in Figure 3.8b with a small monolayer region on the bottom left and a bilayer on the right. Atoms of different intensities can be distinguished as result of the heavier W atoms and lighter Mo atoms. On the leftmost region the spots will be single Mo (dimmer) or W atoms (brighter), while the bilayer area will be metal columns (i.e., W/W (brightest), W/Mo (medium), Mo/Mo (dimmest)). Consistent with the STEM EDX, the two metal species are evenly distributed across the flake with some clustering as observed with the  $\text{Mo}_{0.5}\text{W}_{0.5}\text{S}_2$  case and consistent with ALD-grown monolayers.<sup>44</sup>

To observe the chalcogenide columns a thin region (tri-layer) of a flake is investigated with the iDPC detector (Figure 3.8c). From this grayscale image it is possible to observe the hexagonal lattice (illustrated in Figure 3.8f) of the nanosheet and to see that atom columns of varying intensities are present. A top-view schematic is shown in Figure 3.8f for clarity while Figure 3.8e shows the schematic of a cross section of a trilayer. Metal atoms ( $M = \text{Mo or W}$ ) are represented in green, chalcogen atoms ( $X = \text{S or Se}$ ) in red.

The line profile is shown in Figure 3.8d for the purple line highlighted in Figure 3.8c,f. A From this profile a periodic pattern is observed with two types of maxima corresponding to heavier columns (yellow) and lighter columns (blue). These maxima are a combination of metal and chalcogen atoms as depicted in Figure 3.8e. As the iDPC intensity scales linearly, the brightest spots correspond to  $M\text{-}X_2\text{-}M$  columns (yellow) and can therefore be attributed to the first maxima as it is, on average, the greater of the two. The second maxima species (marked in blue) is therefore attributed to the  $X_2\text{-}M\text{-}X_2$  columns (blue) and the minima is vacuum. Note that a flake with an even number of layers (2,4,6, etc.) would have two maxima which generally even out (i.e.,  $X_2\text{-}M\text{-}X_2\text{-}M$  or  $M\text{-}X_2\text{-}M\text{-}X_2$ ), while an odd number of layers will have one column that is typically greater than the other owing to the heavier metal atoms ( $M\text{-}X_2\text{-}M$  or  $X_2\text{-}M\text{-}X_2$ ). The latter case is observed here, supporting the tri-layer claim (observing a clear iDPC signal as shown here is challenging for flakes greater than 3 layers, eliminating 5-layers,7-layers, etc.).

Of critical importance, both the yellow and blue maxima vary along the line selection, indicating the presence of different chemical species. This indicates that different atomic combinations ( $M\text{-}X_2\text{-}M$  or  $X_2\text{-}M\text{-}X_2$  columns) are present and distributed over the nanosheet, further supporting the formation of the quaternary alloy. Thus, the 2D nanosheet quaternary alloy is formed with confidence.

### 3.2.6 Overview of the electronic structures of the 2D TMDs made *via* ECPI-exfoliation

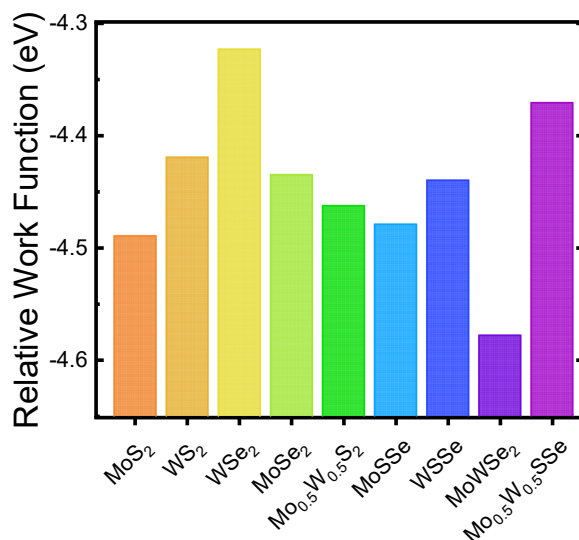


Figure 3.9. Summary of electronic structures of the ECPI-made 2D TMDs.

Relative work functions of all the thin films of 2D TMD materials explored in this work including: four pure materials, four ternary alloys, and one quaternary alloy.

Finally, ultraviolet photoelectron spectroscopy (UPS) was used to estimate changes in the band structure as a function of alloy composition. UPS was performed on the thin films made from each material. Taking the information provided by the secondary electron cut off (SECO) it is possible to estimate their work functions. Thus, the estimated relative work functions of the pure, ternary alloyed, and quaternary alloyed materials are depicted in Figure 3.8. The trends of the pure materials follow those reported in the literature,<sup>174</sup> allowing the trends of the alloyed materials to be considered as well. This display highlights the effectiveness of this ECPI-based approach and its ability to deliver TMD nanosheets with a broad range of optoelectronic properties.



### 3.3 Conclusions

In summary, this chapter presents a simple, solution-processable route for the scalable production of 2D TMD alloys. Using the previously described ECPI method, five different alloys were made and characterized, including four ternary and one quaternary combination. Concentrated dispersions were obtained wherein nanosheets films on the centimeter-squared scale were made and analyzed. Conveniently this method is applicable for metal ( $\text{Mo}_{(1-x)}\text{W}_x\text{X}_2$ ) and chalcogen ( $\text{MS}_{(2-y)}\text{Se}_y$ ) alloyed nanosheets or both ( $\text{Mo}_{(1-x)}\text{W}_x\text{S}_{(2-y)}\text{Se}_y$ ). Furthermore, it was shown that this method can be used to precisely tune the optoelectronic properties as a function of alloy composition. The trends observed are notably consistent with those reported for CVD and ALD-made monolayers. Not only does this represent a scalable alternative to such methods, but it also presents a solution to the limitation of CVD to grow large-area multilayer flake films. The work presented here is an important step forward in making large-area devices based on alloyed TMD nanosheets.

### 3.4 Methods

#### *Pellet Pressing + Annealing*

As-received TMD powder (Sigma-Aldrich; powder < 2  $\mu\text{m}$ , 99%) was pressed using a manual Beckman hydraulic pellet press, 12.5 mm diameter die, up to 10 tons and held for 5 s. It is noted that this is a standard KCl pellet press (as used for FTIR spectroscopy sample preparation) which operates by filling the die (polished plate, powder, polished plate), compressing the sandwiched powder in the die with a pushing rod, and applying the pressure *via* the press to the pressing rod to compact the pellet. The polished plates and pressed pellet are then gently removed from the die using the pushing rod.

For alloys the desired powder amounts were weighed based on desired atomic concentration and ground together with a mortar and pestle for 2-3 minutes. Typically batches of 3 or 6 pellets were weighed out simultaneously, grinded together, and then separated into portions for pellet pressing.

For S-based and S/Se materials (): Up to three 500 mg pellets are vacuum sealed in a fused quartz glass tube with 100 mg S powder (3:1 molar ratio  $\text{MoS}_2\text{:S}$ ) ensuring the pellets are not touching to avoid fusing. The pellets are heated from room temperature to 1100  $^\circ\text{C}$  over 8 hours, held at 1100  $^\circ\text{C}$  for 48 hours, then allowed to cool naturally.

For Se-based materials (): Up to three 750 mg pellets are vacuum sealed in a fused quartz glass tube with 100 mg Se powder () ensuring the pellets are not touching to avoid fusing. The pellets are heated from room temperature to 1000  $^\circ\text{C}$  over 8 hours, held at 1000  $^\circ\text{C}$  for 12 hours, then allowed to cool naturally.

For S/Se-based materials (): Up to three 500 mg pellets are vacuum sealed in a fused quartz glass tube with 50 mg of S powder and 50 mg of Se powder ensuring the pellets are not touching to avoid fusing. The pellets are heated from room temperature to 1100  $^\circ\text{C}$  over 8 hours, held at 1100  $^\circ\text{C}$  for 48 hours, then allowed to cool naturally.

See Methods section, Chapter 2, Method note 1 for additional information concerning starting mass, die diameter, and annealing conditions.

#### *Electrochemical Pellet Intercalation and Exfoliation*

The annealed pellet was clipped with an alligator clip and placed in a 50 mL beaker with a glassy carbon counter electrode. Both electrodes were connected to a potentiostat with the TMD pellet as the working electrode, WE. A solution of tetraheptylammonium bromide (Acros Organics, 99%) in acetonitrile (Merck Millipore) was added until the pellet is submerged without liquid touching the alligator clip, and with sufficient space between electrodes to avoid contact as the WE expands. For S and S/Se-based pellets 5  $\text{mg mL}^{-1}$  was used; for Se-based pellets 10  $\text{mg mL}^{-1}$  was used.

A voltage of 10 V was applied for 24 h (WE as cathode), during which the solution begins to turn yellow at the anode, and the pellet begins to slowly expand and slough off. After the pellet has become a fluffy powder at the bottom of the beaker, the powder and remaining pellet was carefully collected and washed thoroughly with ethanol *via* vacuum filtration with a nylon filter (pore size 0.45  $\mu\text{m}$ ). The solid material is transferred to a 50 mL centrifuge tube with 10 mL of NMP (Acros Organics; 99+% for spectroscopy) before and bath sonication (Ultrasonic bath USC T, VWR, 45 kHz) in water at 25 $^\circ\text{C}$  for 1-2 hours. Finally, the solution was centrifuged for 30 min at 120 rcf using an Eppendorf centrifuge 5810 equipped with a FA-45-6-30 rotor. The top 8 mL of supernatant is collected and transferred to a new container.

#### *Thin Film Formation*

Thin films were made *via* a liquid/liquid interface created between deionized water and hexane (Sigma-Aldrich; >99%) using a previously-described approach.<sup>67</sup> Transfer to substrate was accomplished by aspirating the organic phase and then either aspirating the water phase to descend the film onto a pre-positioned substrate (for FTO glass) or *via* a stamping method (for FET substrates) wherein the substrate is manipulated with a suction pen and pressed into the film, transferring the material onto the substrate. Films were then annealed at 200  $^\circ\text{C}$  for 120 min in a vacuum oven to remove excess solvent.

*UV-Visible / Raman / PL Spectroscopy / XPS / UPS / XRD*

UV-Vis spectra were acquired using a Shimadzu UV 3600 spectrometer from 825-300 nm using an integrating sphere with step size 1 nm and slit width of 5 nm. Measurements of solutions were taken using a quartz cuvette directly in transmission mode. Dispersions of nanosheets in NMP were diluted in NMP. NMP was used for a blank. Absorbance was calculated as shown in equation (1), where %T is percent transmission:

$$\text{Absorbance} = 2 - \log_{10}(\%T)$$

Raman spectra and PL spectra were obtained using a Horiba Xplora Plus Raman microscope with 532 nm radiation (40 mW). Raman spectra were acquired from 100-1800  $\text{cm}^{-1}$  using a 100x objective, slit of 200  $\mu\text{m}$ , hole of 500  $\mu\text{m}$ , a grating with 2400 gr/mm, 10% filter, 10 s of acquisition, and 5 accumulations.

PL spectra were obtained from 550-950 nm using a 100x objective, a grating with 600gr/mm, slit of 200  $\mu\text{m}$ , hole of 500  $\mu\text{m}$ , 255 filter, 4s of acquisition, and 4 accumulations. PL spectra were normalized according to Raman signals appearing around 580 nm to adjust for material content and then to [0,1] for display clarity.

XPS spectra were acquired using a PHI Versa Probe II (Physical Instruments AG, Germany). Analysis was performed using a monochromatic Al K $\alpha$  X-ray source operated at 50 W. The spherical mirror analyzer was set at 45° take-off angle with respect to the sample surface. The pass energy was 46.95 eV yielding a full width at half maximum of 0.91 eV for the Ag 3d 5/2 peak.

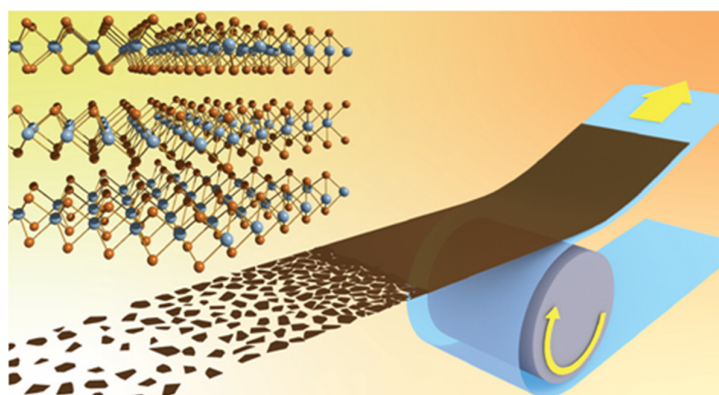
Powder XRD measurements were taken in Debye-Scherrer geometry (scanning mode) using Cu-K-alpha radiation on a Bruker D8 Discover Plus instrument equipped with a rotating anode and a Dectris Eiger2 500K detector. Samples were loaded into 0.5 mm borosilicate capillaries and spun during data acquisition. Lattice parameters were measured by fitting peak intensities. For thin films Bragg-Brentano XRD measurements were carried out using a Bruker D8 Vario diffractometer equipped with a Johansson K $\alpha$ 1 ( $\lambda = 1.5406 \text{ \AA}$ ).

*STEM EDX / HAADF STEM / HR STEM*

STEM EDX and HAADF STEM images were acquired on a FEI Talos F200S microscope operated at 200 kV. HAADF STEM images were obtained using a probe current of 100 pA, a camera length of 125 mm (collection angle > 75 mrad) and a dwell of 1-5  $\mu\text{s}$ . High-resolution STEM images were acquired on a FEI Titan Themis microscope operated at 80 kV and equipped with a field emission gun (X-FEG). The aberrations of the probe were corrected with a CEOS DCOR system up to the 3rd order. ADF and iDPC imaging were acquired simultaneously using a probe current of 30 pA, a camera length of 230 mm (collection angle for ADF > 35 mrad) and a dwell time of 8  $\mu\text{s}$ .



## Chapter 4 Roll-to-roll deposition of semiconducting 2D nanoflake films of transition metal dichalcogenides for optoelectronic applications<sup>‡</sup>



Roll-to-roll films of self-assembled TMD nanosheets.

The previous chapters have explored a novel approach for the scalable synthesis of two dimensional (2D) transitional metal dichalcogenides (TMDs) which promises large quantities of material without compromising the semiconducting properties of the nanosheets. When producing thin films of 2D TMDs, this requires a film production technique engineered to handle high volumes of material. Once again, the challenge is to do so without sacrificing the quality of the final film. This next chapter addresses this by describing an apparatus designed to deposit large-area films of 2D TMDs.

Exfoliated TMD nanomaterials possess remarkable and tunable semiconducting properties which make them competitive for use in ultrathin, flexible devices such as photodetectors, sensors, and photoelectrodes for solar energy conversion. Until now, the large-scale production of such devices has presented a challenge that limits their commercialization and broad application. This chapter demonstrates, for the first time, a procedure for the roll-to-roll (R2R) deposition of two-dimensional (2D) TMD nanoflake thin-films via a continuous liquid-liquid interfacial self-assembly method. Remarkably, no solvent removal is required during film deposition nor is there any nanoflake accumulation in the solvent bath, making continuous operation feasible. In this prototype deposition system described herein, TMD nanoflakes (9 nm average flake thickness, 50-500 nm long) are self-assembled into large-area films up to 100 mm in width that are reproducibly printed at  $10 \text{ mm s}^{-1}$  with nanoflake loadings of  $35 \text{ mg m}^{-2}$ . Optically uniform coverage on transparent conductive oxide coated flexible plastic substrates is shown and key printing parameters to afford the required single-flake-layer deposition are identified. Photoelectrochemical testing verifies optoelectronic activity of the  $\text{MoS}_2$  nanoflake films achieving photocurrent densities for iodide oxidation of  $40 \mu\text{A cm}^{-2}$  at  $+0.1 \text{ V}$  (vs. an  $\text{Ag}/\text{Ag}^+$  reference) under 1-sun illumination. In addition, it is shown that these R2R films are robust and that this method works for multiple (successive) flake layer depositions by preparing large area  $\text{MoS}_2/\text{WSe}_2$  heterojunction nanoflake films. This demonstration represents an important milestone in advancing large-scale production of 2D TMD films towards low-cost, high-performance optoelectronic devices.

<sup>‡</sup> This chapter is adapted from a peer-reviewed article published in ACS Applied Nano Materials: Rebekah A. Wells, Hannah Johnson, Charles R. Lhermitte, Sachin Kinge, and Kevin Sivula. *ACS Appl. Nano Mater.* **2019**, 2, 12, 7705–7712.

It should be noted that the exfoliated material used in the demonstrations of the R2R apparatus was prepared via ultrasonication. While the electrochemical pellet intercalation (ECPI) technique previously described is readily scaled up, laboratory demonstrations typically make 8-10 mL at a time. As the purpose of this demonstration was to show that large volumes of material could be efficiently processed into sheets, it was more reasonable to use ultrasonication, which typically makes 40 mL per batch.

## 4.1 Introduction

Mono- or few-layer semiconducting transition metal dichalcogenides (TMDs) from group 6 with the form  $MX_2$  ( $M = \text{Mo}, \text{W}$  and  $X = \text{S}, \text{Se}, \text{Te}$ ) have recently emerged as outstanding materials for many optoelectronic applications<sup>175,176</sup> due to their exceptional semiconducting properties and chemical robustness. These favorable properties arise from the TMD crystal structure of  $X-M-X$  layers held together with strong interlayer bonds and weak intralayer van der Waals forces that permit exfoliation into “two-dimensional” (2D) sheets or flakes.<sup>10</sup> Currently, 2D TMDs are under development as chemical and biological sensors,<sup>177,178</sup> light emitting diodes,<sup>179</sup> photodetectors,<sup>180,181</sup> and for solar energy conversion with photovoltaic and photoelectrochemical cells.<sup>109,182</sup>

The typically-employed mechanical exfoliation (adhesive tape) methods to prepare 2D TMDs yield micron-sized flakes isolated on a substrate; however, for many of the emerging applications—in particular for solar energy conversion—the need for the rapid production of large area (meters-squared) films of 2D TMDs is apparent.<sup>61</sup> While much effort has been dedicated to create large area films by gas phase deposition techniques such as chemical vapor deposition (CVD) or atomic layer deposition (ALD),<sup>183</sup> or using high temperature<sup>184</sup> or pressure conversion reactions (>500 °C *e.g.* using a carbonate melt<sup>185</sup>) these techniques are not ideally suited to fabricate solar energy conversion devices for global-scale implementation due to technical and economic limitations.<sup>61</sup> Indeed, due to the harsh conditions used CVD approaches require substrate transfer methods<sup>186</sup> or expensive noble metal substrates<sup>187</sup> to afford TMDs on conductive substrates. While plasma enhanced CVD may be able to overcome these limitations,<sup>188</sup> this process is energy intensive. ALD can also be compatible with lower temperatures, but requires exotic metal organic precursors to afford reproducible film formation and still suffers from difficulty controlling the cryptographic orientation of the resulting films.<sup>189</sup>

On the other hand, the liquid phase exfoliation (LPE) of bulk TMD powders can yield high-quality semiconducting mono- or few-layer nanoflakes dispersed in common solvents.<sup>69</sup> These dispersions can be prepared by various methods (*e.g.* ultrasonication,<sup>63</sup> shear mixing,<sup>72</sup> and electrochemical exfoliation<sup>190</sup>) and offer the potential for inexpensive, low-temperature solution-based processing of 2D TMD thin films.<sup>191,78,192</sup> Nevertheless, the use of typical solution processing techniques (*e.g.* spin coating, drop casting, inkjet printing, or spray coating) with 2D TMD dispersions is limited by the low dispersion concentrations of LPE semiconducting TMD nanoflakes and their rapid restacking/aggregation upon solvent evaporation.<sup>193,194,82</sup> To overcome this limitation, a self-assembly technique employing a liquid-liquid interface to suppress aggregation has been recently developed for 2D TMD nanoflake film deposition that yields single-flake layer films with good coverage and superior electronic contact to the deposition substrate compared to other solution processing methods.<sup>65</sup> This method has been demonstrated with  $\text{WSe}_2$ ,  $\text{MoS}_2$ ,  $\text{MoSe}_2$ , and over a range of different flake sizes.<sup>82,93</sup> Furthermore, the possibility to passivate defects introduced by the LPE process after film deposition has been demonstrated resulting in exceptional semiconducting properties for solar energy conversion (*i.e.* photoelectrochemical  $\text{H}_2$  production).<sup>66</sup>

While the liquid-liquid interfacial self-assembly deposition technique represents a viable route towards large area and high-performance solution processed 2D TMD films, the extension of this method to a true (*i.e.* fully continuous) roll-to-roll (R2R) process will be necessary for practical application.<sup>195</sup> However, in contrast to liquid-air self-assembly deposition techniques (*e.g.* Langmuir-Blodgett),<sup>196</sup> the extension of liquid-liquid interfacial self-assembly deposition techniques to R2R film processing of 2D TMDs has not been demonstrated to our knowledge. Herein a true R2R film deposition of 2D TMD nanoflake films is reported using a continuous liquid-liquid interfacial self-assembly method. This work identifies parameters critical to the homogeneous film formation, demonstrates the activity of resulting films toward solar energy conversion, and shows that R2R processing of van der Waals TMD heterojunctions via multilayer deposition is also possible.

## 4.2 Results and discussion

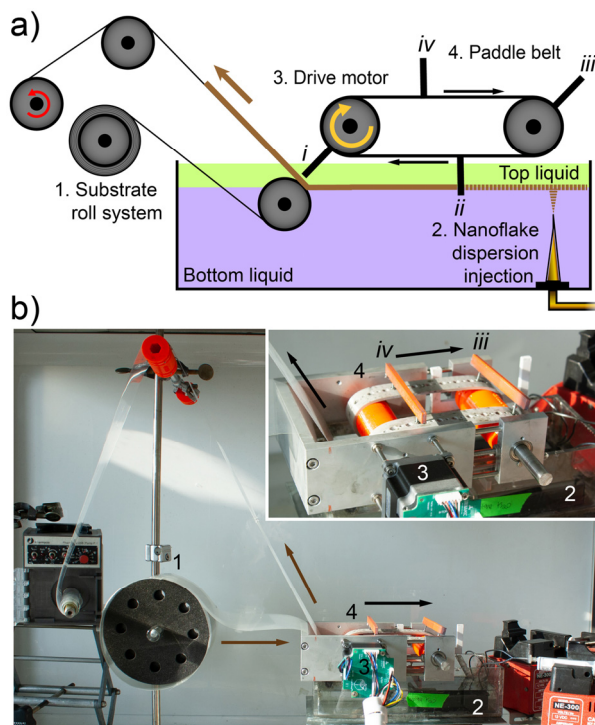


Figure 4.1. Roll-to-roll (R2R) apparatus.

A schematic side-view of the R2R deposition apparatus is shown in (a) and a photograph of the system is shown in (b) where the inset gives a close-up overhead view. The substrate is introduced via the substrate roll (1). An array of needles (2) connected to syringe pumps loads the nanoflake dispersion into the solvent bath. A computer-controlled drive motor (3) turns the paddle belt (4) and the attached pusher paddles (*i-iv*) that push the 2D TMD nanoflake film, which has self-assembled at the liquid-liquid interface between the top and bottom liquids, to the continuously moving substrate.

To demonstrate R2R 2D TMD film deposition the concept of the previously reported batch-mode liquid-liquid interfacial self-assembly method<sup>65</sup> was extended to a continuous-mode system. Briefly, the batch-mode operation begins by injecting a dispersion of TMD nanoflakes at the interface of two immiscible liquids (*i.e.* ethylene glycol and *n*-hexane), both of which are poor solvents for nanoflake dispersion. After loading the interface with an amount of nanoflakes sufficient to form a uniform single flake layer, the lower density liquid (*n*-hexane) forming the top layer is completely removed by aspiration *via* a pipette before the denser bottom liquid layer (ethylene glycol) is removed *via* vacuum through a glass frit to deposit a homogenous thin film on an awaiting substrate immersed in the bottom layer. Considering future industrial application, a first consideration was solvent modification to replace the solvents with more eco-friendly alternatives, using water and *n*-heptane as the bottom and top layers, respectively. The TMD nanoflakes produced via LPE (see Experimental Methods section) are re-dispersed in a 10:1 (v:v) *tert*-butanol:*n*-butanol mixture (the *n*-butanol is used to lower the melting point of the dispersion solvent). The dispersion solvent has a lower density than the bottom liquid phase (water), and this is important for the operation of the R2R system, which is shown schematically in Figure 4.1a and with a photograph in Figure 4.1b.



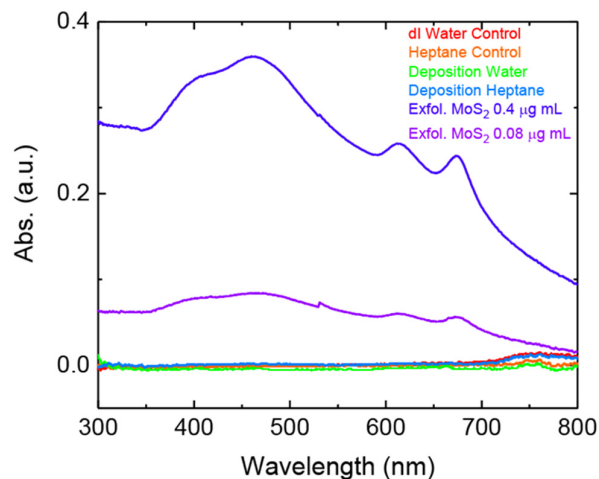


Figure 4.2. Ultraviolet-visible spectroscopy for the R2R solvent system.

The red and orange curves show controls for water and heptane, respectively. The blue and green curves show samples for heptane and water, respectively, which were taken after several consecutive film depositions had been performed in the same solvent bath. The violet and purple curves give the absorption spectra for trace amounts of MoS<sub>2</sub> dispersed in the 1:10 by volume tert-butanol/1-butanol mixture. Importantly, no trace of MoS<sub>2</sub> is observed in either of the solvents after the film deposition.

The R2R apparatus consists of a substrate roll system that guides a conductive, flexible plastic substrate (*e.g.* indium tin oxide (ITO) coated on polyethylene terephthalate (PET)) into and out of a bath containing the two liquids. Unlike the reported batch method, the TMD nanoflake dispersion in butanol can be injected from the bottom layer as shown in Figure 4.1a. The less dense butanol carries the TMD nanoflakes up through the water layer to the water-heptane interface, and the subsequent rapid dissolution of the butanol in the water layer leaves the nanoflakes at the interface. This bottom-positioned injection allows the dosing devices to be easily fixed to the bottom of the bath and also leaves the top of the bath free for the paddle-belt-pusher assembly, which is driven by a computer-controlled stepper motor. The paddles extend the width of the deposition bath and act as moveable barriers to push the nanoflake film, which has self-assembled at the liquid-liquid interface, to the substrate. Specifically, as the first paddle (*i*) advances out of the bath, the self-assembled TMD nanoflake layer behind it is pushed towards the receiving substrate by a second paddle (*ii*), as indicated in Figure 4.1a (a video demonstration can be found in the supporting information of reference <sup>83</sup>). Before paddle *ii* exits the bath, a third paddle (*iii*) enters the bath, and the formed nanoflake film in the region between paddles *ii* and *iii* is advanced towards the substrate. While a minimum of three paddles is necessary, in principle, four paddles was the optimal number for continuous operation based on the dimensions of this specifically designed system where the distance between the paddles is 85 mm.

It was first sought to demonstrate the R2R system with MoS<sub>2</sub> nanoflakes produced via LPE as these are the prototype 2D semiconducting TMD material. Remarkably, no solvent removal is required to produce a uniform film of MoS<sub>2</sub> nanoflakes on the desired substrate. This greatly simplifies the overall operating conditions and minimizes the amount of solvent needed. Furthermore, UV-Vis analysis of the solvents after a typical deposition run confirms the absence of detectable MoS<sub>2</sub> nanoflakes in either top or bottom layer (Figure 4.2), suggesting that the system can be operated continuously without the accumulation of nanoflakes in the bath. However, it should be noted that a technique to remove butanol from the bottom layer (*e.g.* by continuously adding fresh water and removing the butanol:water mixture), would be needed for continuous operation for extended duration, and was not implemented in this proof-of-concept system.

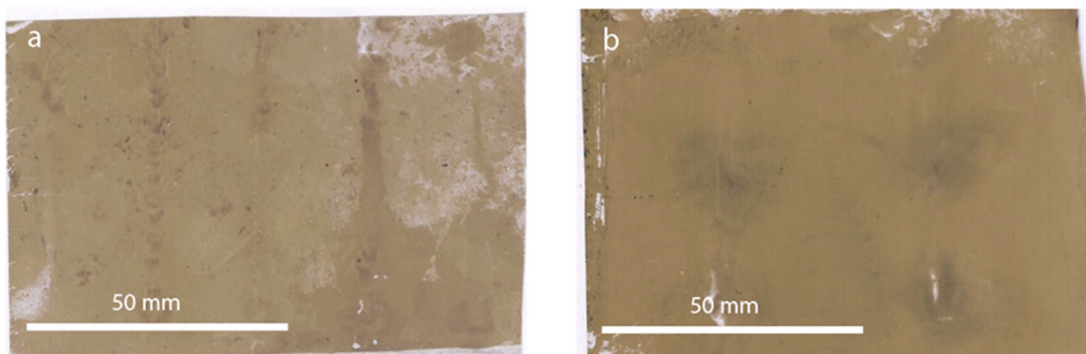


Figure 4.3. Comparison of number of dispersion injection sites.

(a) MoS<sub>2</sub> deposited on flexible PET substrate in semi-continuous mode using a needle array containing 16 needles and (b) MoS<sub>2</sub> deposited on flexible PET substrate in semi-continuous mode using a needle array containing four injection sites. Despite injecting over the same area, the film shown in image b is more uniform than the film shown in image a. Though some dark areas can still be observed for the four injection sites, they are less apparent and produce an overall more uniform film than when four times as many needles are present.

To validate the proof-of-concept R2R film deposition, a number of factors required optimization. Among the most important were the locations of the injection needles, the rate of dispersion injection, and the travel speeds of the substrate and pusher paddles. Regarding the injection needle locations, it was determined that minimizing injection sites led to a more homogeneous and reproducible self-assembled films with less aggregation compared to films prepared with a large array of injection ports (Figure 4.3). Accordingly, optimal positioning for continuous operation was found to be a single row of evenly-spaced needles located opposite of the substrate feeding as depicted in Figure 4.1a. Needles were placed every 20 mm, for example: four injection sites for a substrate width of 100 mm.

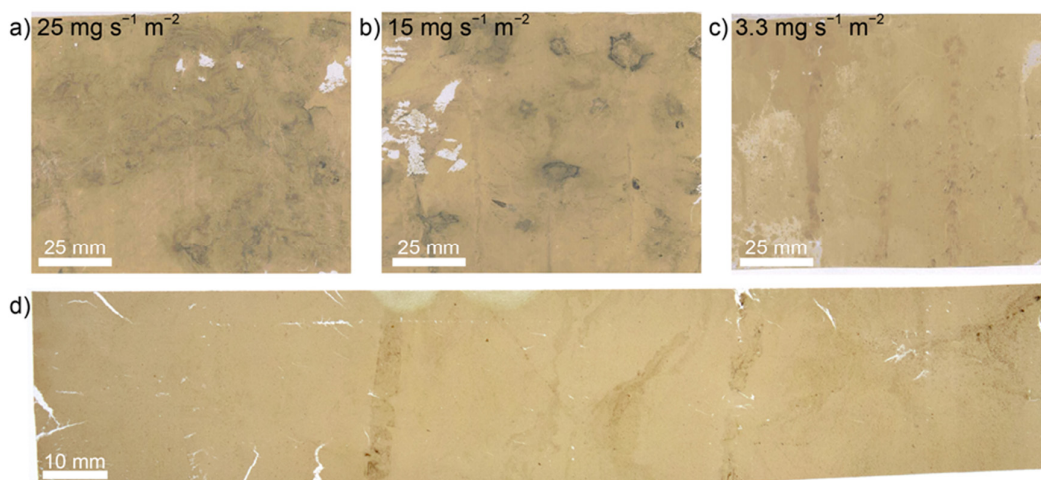


Figure 4.4. Optimization of MoS<sub>2</sub> nanoflake film loading.

(a, b, c) show differences in nanoflake loading rates, respectively, for films deposited in semi-continuous mode. (d) An optimized MoS<sub>2</sub> film deposited in continuous mode.

Table 2. Summary of parameters used in the semi-continuous deposition injection rate study.

A 100 mm by 100 mm liquid-liquid interface was used. Injection rate was controlled via syringe pumps, which could then be translated into flake loading and finally loading rate. For each loading rate similar flake loading per area was observed. Therefore, the large difference in film formation observed in Figure 4.4a-c is solely a result of the nanoflake loading rate.

Dispersion volume injection rate (mL min <sup>-1</sup> )	Dispersion injection duration (s)	Final Nanoflake loading per substrate area (mg m <sup>-2</sup> )	Nanoflake loading rate per substrate area (mg s <sup>-1</sup> m <sup>-2</sup> )
2	13.5	45	3.3
9	2.53	38	15
15	1.88	47	25

Loading rates were also evaluated to estimate the limits of the R2R deposition. Figure 4.4 demonstrates the difference in macroscopic film morphology between films prepared at differing loading rates (using a semi-continuous mode that allows to keep the same substrate feed rate, see Experimental Methods section) with a 1 mg mL<sup>-1</sup> MoS<sub>2</sub> nanoflake dispersion. Despite similar amounts of material being loaded per unit area in each case (about 40 mg m<sup>-2</sup> for each case, see Table 2), slower flake loading rates yield more uniform films (as seen in Figure 4.4c), while faster rates (Figure 4.4a,b) show dark spots indicating regions of aggregated nanoflakes (as compared to the lighter tan-colored regions, which represent a single nanoflake layer, and the white regions which represent gaps in the film). It is supposed that higher deposition rates create turbulence at the liquid-liquid interface making it difficult for the TMD nanoflakes to self-assemble in the expected edge-to-edge fashion, leading to aggregates and gaps in the final film. Regarding the dispersion concentration, ca. 1 mg mL<sup>-1</sup> typically gave the most uniform thin films. Increasing the concentration will cause the TMD nanoflakes to aggregate in the dispersion before injection and lead to poor film formation. On the other hand, reducing the concentration requires either increased loading rates, which has negative effects as discussed above, or that overall deposition be slowed.

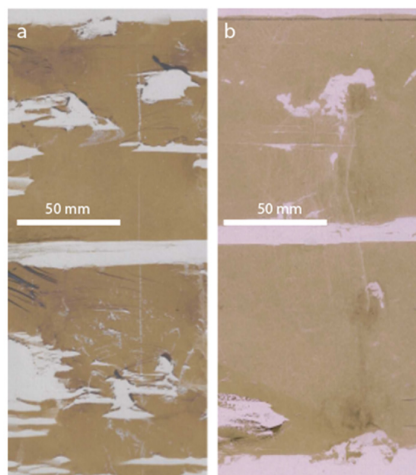


Figure 4.5. Optimizing substrate pre-treatment.

(a) MoS<sub>2</sub> deposited on as-received ITO-coated PET (solaronix) and (b) UV-treated ITO-coated PET. It is clear that the MoS<sub>2</sub> nanoflakes are better able to adhere to the treated substrate resulting in a better film transfer and a uniform final product.

For the optimal film transfer from the liquid-liquid interface to the substrate in continuous mode, the speeds of the paddles and the substrate should be considered. High speeds should be avoided to maintain laminar flow and the most homogeneous films were formed when the substrate withdrawal speed is matched with the pusher paddle speed. Empirically, a moderate speed of  $10 \text{ mm s}^{-1}$  was found to be ideal. While faster rates can likely be achieved by optimizing the liquid handling to avoid turbulence, it should be noted that the volumetric injection rate and/or dispersion concentration will need to be modified in accordance to obtain full nanoflake coverage. In addition to substrate withdrawal rate, the substrate choice is not trivial. The nanoflakes must be able to adhere well to the substrate, which is immersed in the water layer just prior to deposition. As such, hydrophobic substrates are not suitable. In this case, the conductive and flexible ITO-coated PET substrate requires UV-ozone cleaning as a pretreatment to increase the hydrophilicity before use as demonstrated in Figure 4.5. After substrate optimization the films were observed to be remarkably well-adhered to the substrate, resisting scratching and solvent rinsing. Only sonication in *n*-methyl-2-pyrrolidone (NMP), the original exfoliation solvent, was able to remove the nanoflakes from the substrate.

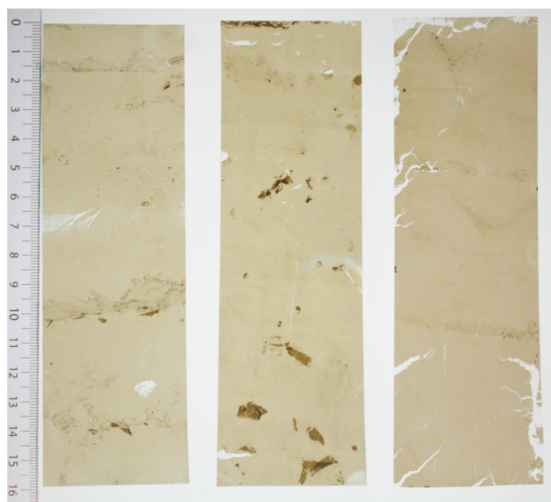


Figure 4.6. Reproducibility of R2R-made films.

Three MoS<sub>2</sub> films on deposited in continuous mode on flexible plastic substrate demonstrate that the R2R system can consistently produce large area thin-films of semiconducting nanoflakes of similar quality.

After exploring the deposition parameter space for continuous-mode deposition, reasonable values were chosen for the R2R deposition: nanoflake loading of  $3.3 \text{ mg s}^{-1} \text{ m}^{-2}$ , at  $10 \text{ mm s}^{-1}$  substrate withdrawal/paddle speed, and a substrate width of 100 mm (equivalent to a mass loading per unit area of  $33 \text{ mg m}^{-2}$ , similar to batch mode operation). These parameters afforded continuous film deposition of MoS<sub>2</sub> nanoflake films as demonstrated in Figure 4.4d where a film with a length ca. 3 times the paddle-to-paddle distance is shown. Figure 4.6 shows repeat depositions illustrating the process reproducibility. While certain film defects can be observed at the edge of the films, these film edge defects could be trimmed off in an industrial system. However, these defects could likely be minimized with additional apparatus modifications which are beyond the scope of this work.

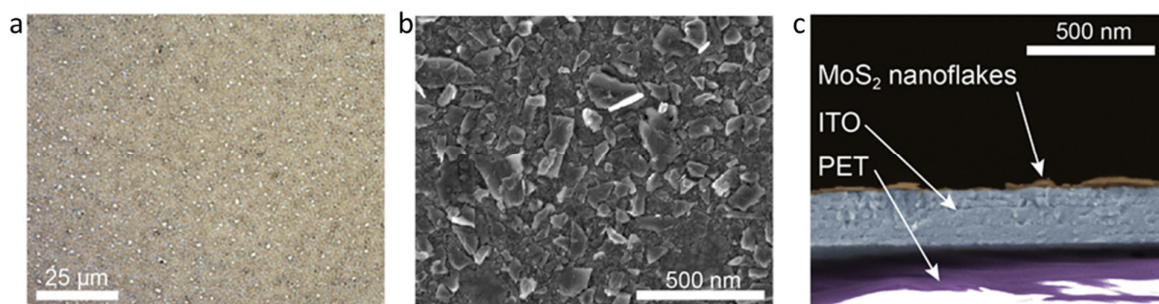


Figure 4.7. Characterization of R2R deposited nanoflake films.

(a) Optical microscopy for a R2R film deposited on FTO-coated glass according to the procedure in the methods section. Scanning electron microscopy for (b) top view and (c) cross-section view of MoS<sub>2</sub> (brown) films deposited via R2R deposition (continuous mode) onto conductive ITO (blue)-coated PET (purple).

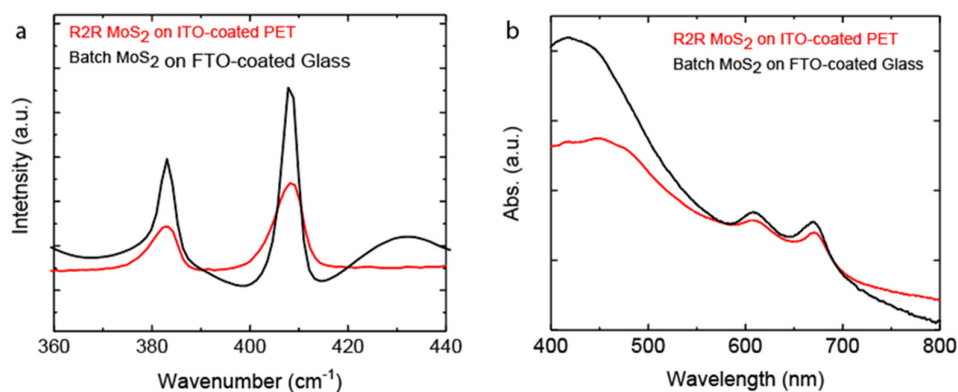


Figure 4.8. Characterization of R2R nanoflake films.

(a) Raman spectroscopy for a R2R (red) and batch (black) film shows the expected MoS<sub>2</sub> vibration modes at 383 cm<sup>-1</sup> and 408 cm<sup>-1</sup> for both deposition methods. (b) UV-Vis spectroscopy for a R2R (red) and batch (black) film gives the expected exciton peaks at 610 nm and 670 nm for both films as well as similar absorbance around these values. No miscellaneous solvent peaks, organic residue, or other impurities are observed.

Visually these large-scale films of MoS<sub>2</sub> nanoflakes appear mostly uniform and complete. Optical microscopy (Figure 4.7a) confirms the completeness of the film and shows no evidence of large agglomerates. Films deposited on conductive ITO-coated PET substrate were examined using scanning electron microscopy (SEM) as shown in top-down and cross-sectional images in Figure 4.7b and c, respectively. Flake-to-flake alignment was observed in the top-down image consistent with previously reported results<sup>65–67,93</sup> and comparable to batch-processed films on rigid substrates (shown for MoS<sub>2</sub> and WSe<sub>2</sub> in Annex Item 11). Importantly, the cross-sectional SEM image shows that the flakes align parallel to the ITO surface. It should be noted that the surface of the flexible conducting substrate is extremely rough compared to its rigid, glass-based counterpart (Figure 4.10), and the final roughness of the film is limited by the substrate roughness.

Finally, UV-Vis measurements and Raman spectroscopy confirm that the R2R thin films of MoS<sub>2</sub> nanoflakes are without residual solvent and retain their expected optical properties for few-layer nanoflakes (Figure 4.8). No measurable difference in spectra is observed between the R2R films and the batch-processed ones. The thickness of the continuously-deposited MoS<sub>2</sub> nanoflakes films was calculated to be ca. 7 nm based on the UV-Vis absorption, which is consistent with the average flake thickness (ca. 9 nm) and the flake coverage (ca. 80%) observed by SEM. These values are similar to MoS<sub>2</sub> films prepared by the batch deposition approach.<sup>93</sup>



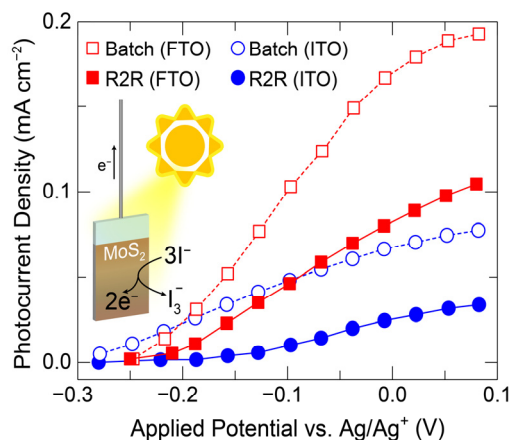


Figure 4.9. PEC characterization of R2R nanoflake films.

Photocurrent density (dark current subtracted) under 1-Sun illumination recorded versus applied potential (vs.  $\text{Ag}/\text{Ag}^+$  in 50 mM TBAP 25 mM LiI in MeCN) for  $\text{MoS}_2$  nanoflake film photoelectrodes deposited on ITO-coated PET (blue circle markers), or FTO-coated glass (red square markers). Filled markers are R2R coated films and open markers represent batch coated films. Inset: Schematic representation of  $\text{MoS}_2$  photoanode and the oxidation reaction occurring under illumination.

Next, to validate the optoelectronic performance of the R2R  $\text{MoS}_2$  films deposited on ITO coated PET, they were employed as photoanodes to explore their photoelectrochemical response in an iodide-based electrolyte. In this case under simulated 1 sun illumination ( $100 \text{ mW cm}^{-2}$ ), photogenerated holes in the  $\text{MoS}_2$  will oxidize iodide to triiodide, and the measurement of the resulting photocurrent in the external circuit as a function of applied potential is an indication of the photoactivity of the film.<sup>197</sup> Figure 4.9 summarizes results for R2R  $\text{MoS}_2$  nanoflake film photoanodes compared to batch-deposited films prepared on flexible ITO-coated PET or rigid fluorine-doped tin oxide (FTO)-coated glass (see Experimental Methods section). Additional current-voltage behavior under dark and intermittent illumination conditions is presented in Annex Item 12. The R2R photoanode prepared on flexible ITO coated PET substrate yielded a photocurrent density of  $40 \mu\text{A cm}^{-2}$  at +0.1 V versus an  $\text{Ag}/\text{Ag}^+$  reference electrode. Notably the R2R-based photoanodes exhibited about 60% of the photocurrent density of the photoanodes prepared via the batch process for both ITO(PET) and FTO(glass) substrates. This is in contrast to a comparison of photoelectrodes prepared by the batch (liquid-liquid self-assembly) technique and a liquid-air interfacial self-assembly technique (also a batch process but with poor flake-substrate alignment), wherein the liquid-air interfacial self-assembled photoelectrode exhibited only 10% of the photocurrent compared to the liquid-liquid self-assembled photoelectrodes.<sup>65</sup> This suggests that the nanoflake self-assembly in the R2R process could still be further improved, but that it is comparable to the batch process. Additional steps towards ameliorated nanoflake PEC performance include material pretreatment, post-film deposition treatments, and the addition of an appropriate catalyst.<sup>65–67</sup> Such strategies have already been shown to significantly increase TMD nanoflake quantum efficiencies and improve overall device performance, but are not considered in this work.

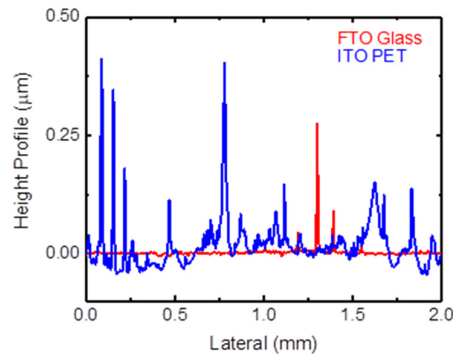


Figure 4.10. Comparison of substrate roughness and conductivity.

Profilometry of blank substrates shows that the conductive, flexible ITO-coated PET substrate is significantly rougher than the conductive, rigid FTO-coated glass substrate. This contributes to the lowered performance of the MoS<sub>2</sub> films coated on the ITO-coated PET substrates compared to those deposited on FTO-coated glass substrates.

Table 3. Substrate sheet-resistivity as measured by a four-point probe.

Notably, the manufacturer, Solaronix, lists the sheet resistivity of the ITO-coated PET as 18 ohm/sq.

Substrate	FTO-Coated Glass	ITO-Coated PET
Sheet Resistivity (ohm/sq)	16	30

Notably, the data in Figure 4.9 also show that the substrate has a large effect on the photocurrent. The performance of the photoanodes prepared on FTO-coated glass is more than double that of those prepared on ITO. As previously mentioned, the ITO-coated PET is significantly rougher than the FTO-coated glass substrate (Figure 4.10). Additionally, the sheet resistance of the ITO-coated PET is greater than that of FTO-coated glass (Table 3), further limiting the performance. Thus, the substrate sheet resistance, substrate roughness, and substrate-to-nanoflake contact in the R2R deposition process are factors to address in future improvements of the R2R 2D TMD nanoflake films.



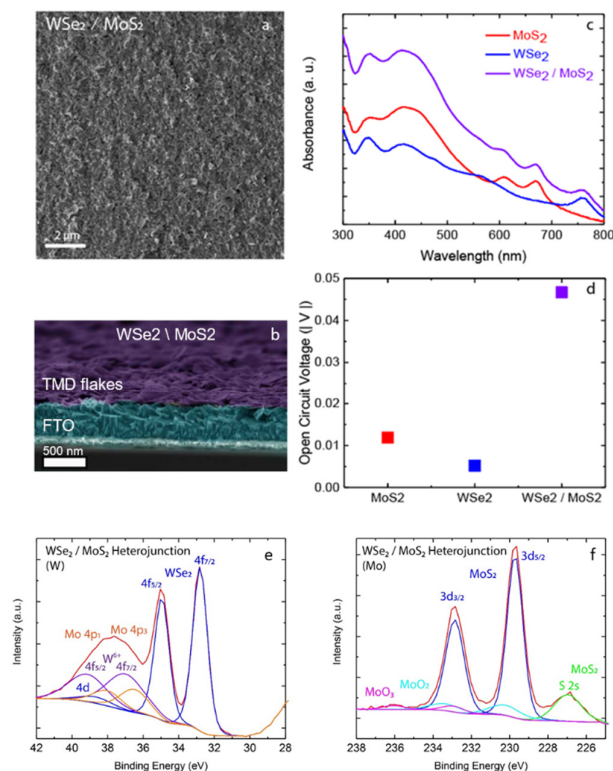


Figure 4.11. Characterization of batch scale WSe<sub>2</sub>/MoS<sub>2</sub> heterojunction film.

(a) Scanning electron microscopy top view and (b) cross-section view of a batch WSe<sub>2</sub>/MoS<sub>2</sub> heterojunction deposited on FTO-coated glass. (c) UV-Vis spectroscopy of the individual films and heterojunction film. (d) Open circuit photopotential of the individual films and the Van der Waals heterojunction in sacrificial conditions (MoS<sub>2</sub>: 25 mM LiI and 50mM TBAP in acetonitrile; WSe<sub>2</sub> and WSe<sub>2</sub>/MoS<sub>2</sub>: 100 mM NBu<sub>4</sub>PF<sub>6</sub> and saturated chloranil in acetonitrile). As in the individual TMD films, SEM images continue to show good flake-to-flake alignment and parallel flake-to-substrate alignment for the heterojunction film. UV-Vis spectroscopy shows that the expected exciton peaks are present for the individual MoS<sub>2</sub> (610 nm and 670 nm) and WSe<sub>2</sub> (760 nm) films as well as in the heterojunction film. As expected, the light absorbance of the heterojunction film is twice that of either of the single films. Open circuit potential for the heterojunction film, however, is not merely additive, but is fundamentally improved. Interfacing these materials allows for electrons and holes to be more efficiently separated in the two materials and for more holes to be stored in the WSe<sub>2</sub>, leading to the greatly improved photovoltage seen here. (e, f) X-ray photoelectron spectroscopy for a batch processed WSe<sub>2</sub>/MoS<sub>2</sub> heterojunction film confirms both material's presence within the same spot. Notably, sputtering was not needed to detect WSe<sub>2</sub> as the MoS<sub>2</sub> layer is extremely thin.

In addition, one well-documented route to improve the performance of 2D TMD-based solar energy conversion devices is employing a van der Waals heterojunction (vdWHJ) between two different TMD nanoflakes.<sup>198</sup> The offset in conduction and valence bands between the two different TMDs provides a thermodynamic driving force for photogenerated charge separation.<sup>199</sup> Mechanically-exfoliated 2D TMD heterojunctions,<sup>200–202</sup> CVD grown heterojunctions,<sup>182</sup> and LPE TMD nanoflake heterojunctions<sup>96,203</sup> have been demonstrated in photovoltaic or photoelectrochemical cells. To provide proof-of-concept that the R2R deposition system is capable of producing vdWHJs with different TMD nanoflake films, the WSe<sub>2</sub>/MoS<sub>2</sub> combination was chosen as it is well demonstrated in the literature.<sup>59,204,205</sup> For referencing purposes, a nanoflake heterojunction film was first prepared using the batch-processing method sequentially (see Experimental Methods). Characterization by SEM, UV-vis spectroscopy, and X-ray photoelectron spectroscopy verify the morphology and composition of the resulting vdWHJ film (see Figure 4.11), and an improved performance of the heterojunction photoelectrode was observed via photopotential measurements (Figure 4.11d).

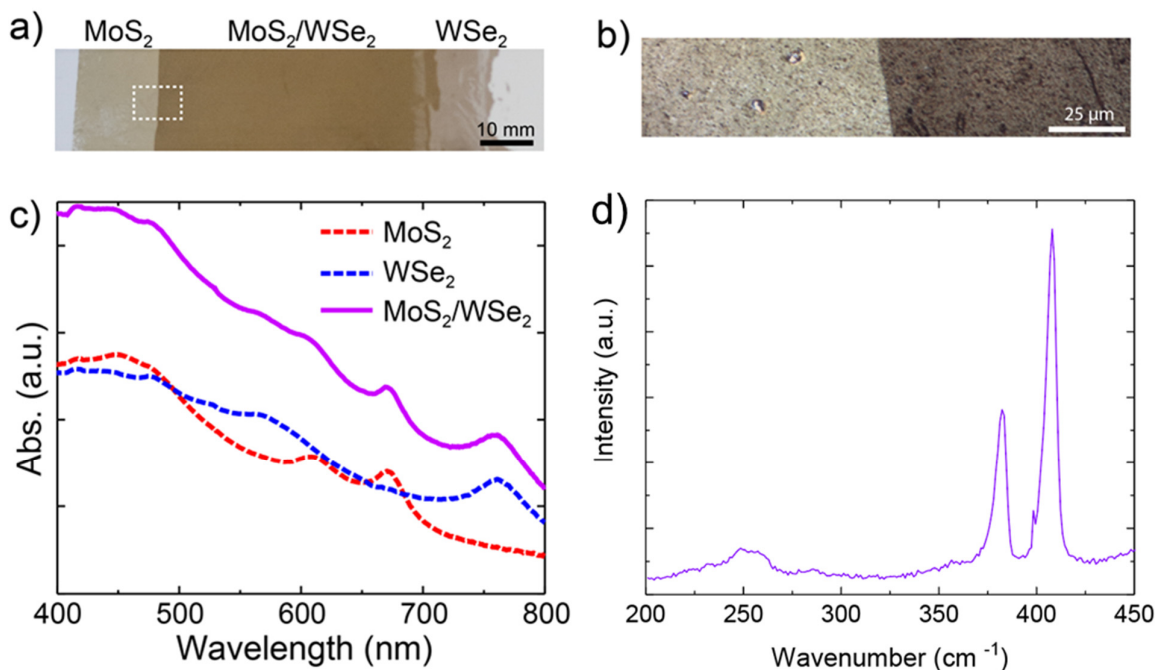


Figure 4.12. Characterization of a R2R MoS<sub>2</sub>/WSe<sub>2</sub> heterojunction film.

(a) Photograph of a R2R-produced MoS<sub>2</sub>/WSe<sub>2</sub> film produced using the R2R deposition apparatus. (b) Optical microscope image of interface highlighted in (a). (c) UV-vis spectra of individual MoS<sub>2</sub> and WSe<sub>2</sub> films compared to the heterojunction film. For MoS<sub>2</sub> excitonic peaks at 670 nm and 610 nm are observed. For WSe<sub>2</sub>, an excitonic peak at 760 nm is observed. The heterojunction film displays all three peaks. (d) Raman spectroscopy for the R2R heterojunction film presents the expected vibrational modes for MoS<sub>2</sub> (383 cm<sup>-1</sup> and 410 cm<sup>-1</sup>) and WSe<sub>2</sub> (250 cm<sup>-1</sup>) as well as confirms that no miscellaneous peaks are present due to residual solvents, organic residue, or other impurities.

Next, the vdWHJ formation with the R2R system was straightforwardly performed by first depositing MoS<sub>2</sub> onto a plastic substrate, allowing the film to dry, and then depositing the WSe<sub>2</sub> on the MoS<sub>2</sub>. It is important to note that this procedure could be performed in a continuous manner by using two R2R units in series with proper film drying between them. Figure 4.12a shows a large area R2R-processed vdWHJ film composed of MoS<sub>2</sub>, WSe<sub>2</sub>, and overlapping heterojunction domains as indicated. Visual inspection indicates a uniform film, absent of aggregates and large cracks. A closer look with optical microscopy highlights a sharp interface between the MoS<sub>2</sub> and MoS<sub>2</sub> / WSe<sub>2</sub> films (Figure 4.12b), verifying that the MoS<sub>2</sub> film remained intact during the second deposition. The UV-vis spectra (Figure 4.12c) show the expected excitonic peaks for both MoS<sub>2</sub> and WSe<sub>2</sub> in the heterojunction film and an overall increase in the absorbance compared to the single component films. A Raman spectrum of the heterojunction film also gives the expected peaks for each material and is notably free of additional impurity or solvent peaks (Figure 4.12d). These results clearly indicate the presence of both TMD materials in the heterojunction while also emphasizing the robustness of the films and the versatility of the R2R deposition method, which can be used for a range of 2D nano-materials to produce thin films of various thicknesses and material configurations.

### 4.3 Conclusions

In summary, this chapter presented a novel approach for producing large area single-flake-layer semiconducting TMD thin films in a continuous manner using a custom-built R2R system. This approach, which employs a liquid-liquid interface known to afford exceptional 2D nanoflake self-assembly, consists of a substrate roll system, deposition bath, and film pusher system that acts as a movable barrier. The batch-deposition protocol was modified to include solvents that are both environmentally friendly and avoid the accumulation of nanoflakes in the system, further supporting the appeal of this system for practical application. Parameters affecting the operation of the system were discussed and optimized settings for homogeneous film formation were identified using  $1 \text{ mg mL}^{-1}$  TMD nanoflake dispersions at loading rates of  $3.3 \text{ mg s}^{-1} \text{ m}^{-2}$  and a  $10 \text{ mm s}^{-1}$  substrate withdrawal/paddle speed. Using  $\text{MoS}_2$  the resulting nanoflake films had a loading of  $33 \text{ mg m}^{-2}$  and a thickness of ca. 7 nm. While reproducible film formation as large as  $80 \text{ cm}^2$  was demonstrated, it is accepted that additional device optimization will be needed for the production of completely defect-free films. The liquid handling and the substrate roughness/adhesion were identified as important factors for further improvement. Remarkably, these R2R TMD nanoflake films showed similar photoactivity in photoelectrochemical tests compared to their batch-scale counterparts. Moreover, the R2R method is highly adaptable and can be used for multiple depositions, heterojunction formation and a variety of layered materials. This presents a crucial advance towards the industrially-scaled production of a promising class of materials for low-cost and high-performance solar energy conversion.

## 4.4 Methods

### *Liquid-assisted exfoliation of 2D TMDs*

For MoS<sub>2</sub>, 500 mg of as received powder (Aldrich; powder < 2 μm, 99%, see Figure S13 for an SEM characterization of the starting powder) was sonicated in 50 mL NMP (Acros Organics; 99+% for spectroscopy) using a Qsonica Model Q700 probe sonicator for 2-12 hours at 50% amplitude (10 s on, 2 s off) while keeping the dispersion at 0.4 °C using a recirculating chiller. The resulting dispersion was centrifuged first at 2000 rpm (Eppendorf Fixed-angle rotor F-35-6-30) for 60 min to remove unexfoliated material, then again at 7830 rpm for 30 min to remove impurities. The pellet was collected and redispersed in 20 mL 10:1 (by volume) tert-butanol:n-butanol (Sigma-Aldrich; ACS reagent > 99.7%) bath sonication for 30 min at 0 °C. For WSe<sub>2</sub> 250 mg was sonicated in 50 mL NMP for 12 hours at 50% amplitude (10 s on, 2s off) at 0.4 °C. The solution was collected and centrifuged at 2000 rpm for 30 min followed by 7830 rpm for 30 min. The pellet was collected and redispersed in 20 mL 10:1 (by volume) tert-butanol:n-butanol via bath sonication for 30 min at 0 °C. Raman and UV-Vis characterization of the as-exfoliated MoS<sub>2</sub> and WSe<sub>2</sub>, before R2R deposition, is presented in Figures S14 and S15, respectively.

### *R2R Deposition*

A liquid/liquid interface was created between deionized water and heptane (Sigma-Aldrich; >99%) in a bath with overall dimensions of 250 mm by 100 mm as shown in Figure 1. The substrate was a 188 μm thick polyethylene terephthalate (PET) film with an 18 ohm sq<sup>-1</sup> indium tin oxide (ITO) coating on one side (Solaronix S.A.) or 100 μm thick polyester films (Folex). Deposition was operated in one of two modes: semi-continuous and continuous. For the semi-continuous deposition, first the paddle belt and substrate feed roll were static. The paddle submerged in the bath together with the back wall of the bath defined an area of liquid-liquid interface of 100 mm by 100 mm for the nanoflake deposition. The TMD dispersion (1 mg mL<sup>-1</sup>) was injected via 4 needles arranged in a square formation supplied by two syringe pumps. The dispersion injection rate and injection time was varied as described in the main text and Table S1, Supporting Information. Once a complete film was formed at the liquid-liquid interface, the injection was stopped and the paddle belt and substrate roll system were switched on (paddle speed and substrate linear speed of 10 mm s<sup>-1</sup>). The self-assembled nanoflake film was then advanced toward the substrate at the opposite end of the bath until the film transfer was complete and the belt and substrate roll system were stopped. This process can be repeated forming a 100 mm by 100 mm film each cycle. For continuous mode operation, a single row of 4 evenly-spaced needles was used (located opposite of the substrate feeding as depicted in Figure 1a), and continuous operation was started by first starting the dispersion (1 mg mL<sup>-1</sup>) injection at ca. 2 mL min<sup>-1</sup> (total) until a complete self-assembled film was formed over the area defined by the static paddle and the back wall of the bath (again 100 mm by 100 mm). Then the paddle belt and substrate roll system were started (at 10 mm s<sup>-1</sup> linear speed) while the injection of the TMD dispersion continued at 2 mL min<sup>-1</sup> (33 μL s<sup>-1</sup>). Slight tension was maintained across the substrate at all times. At this point, the R2R apparatus can be run continuously keeping the same settings.

### *R2R film deposition on FTO-glass*

An FTO-coated glass slide (10mm by 10mm) was attached the plastic substrate and lowered into the water layer prior to film formation and subsequent deposition. The R2R system was then run under normal continuous-mode conditions, the rigid slide being pulled up through the bath with the plastic substrate. The TMD thin film was thus deposited on the FTO-coated glass and surrounding plastic substrate simultaneously.

*Batch-mode electrode fabrication*

A liquid/liquid interface was created between deionized water and heptane (Sigma-Aldrich; >99%). The TMD dispersion ( $1 \text{ mg mL}^{-1}$ ) was injected just below the interface (ca.  $12.5 \text{ cm}^2$ ). Once a complete film was formed the heptane was removed via pipette and then dried with the assistance of light argon gas flow. A slight vacuum removed the water layer through a porous PTFE membrane and fritted glass, depositing the film on the substrate (FTO-coated glass or ITO-coated PET). The film was dried for 1 hour at  $100^\circ\text{C}$ . For heterojunction films  $\text{WSe}_2$  was first deposited in this manner, the film was dried at room temperature before depositing the  $\text{MoS}_2$  using the same procedure.

*Ultraviolet-Visible spectroscopy*

Measurements of solutions were taken using a quartz cuvette and films were analyzed directly in transmission mode using a Shimadzu UV 3600 spectrometer. Spectra were acquired between wavelengths of 800-300 nm using an integrating sphere with step size 0.5 nm and slit width of 8 nm. The thickness of the resulting  $\text{MoS}_2$  films were estimated using the UV-vis spectra and the reported absorption coefficient of  $2.4 \times 10^5 \text{ cm}^{-1}$ .<sup>206</sup>

*Electron microscopy*

Single window silicon nitride support film were used for TEM imaging. The grids were placed on the substrate during the film fabrication process and thus transferring the film to the grid in the exact same manner. TEM was measured using a FEI Talos electron microscope operated at 200 kV. SEM images were acquired using a Zeiss Merlin operated at 2.00 kV, probe current set to 100 pA, working distance of 2.7-2.9 mm, and using an In-Lens detector.

*X-Ray Photoelectron Spectroscopy*

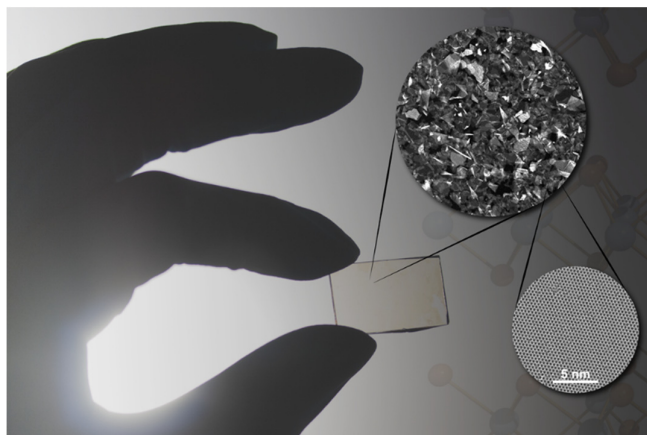
Measurements were carried out using a PHI VersaProbe II (Physical Instruments AG, Germany). Analysis was performed using a monochromatic Al K $\alpha$  X-ray source operated at 50W. The spherical mirror analyzer was set at  $45^\circ$  take-off angle with respect to the sample surface. The pass energy was 46.95 eV yielding a full width at half maximum of 0.91 eV for the Ag 3d 5/2 peak. Curve fitting was performed using CasaXPS software.

*Photoelectrochemical measurements*

Single-layer nanoflakes films deposited on FTO-coated glass or ITO-coated PET substrates were used as photoelectrodes directly. The flexible substrates were fixed to glass substrates to aid with the rigidity of the samples. Silver paste was coated at the top edge of each electrode to improve the electrical contact between the working electrode and the alligator clip. Linear scanning voltammetry (LSV) measurements were obtained using a three-electrode (BioLogic SP-200 potentiostat) system with the TMD thin film as the working electrode a Pt counter electrode and an  $\text{Ag}/\text{AgNO}_3$  (saturated) reference electrode. The active area of the electrode was  $0.26 \text{ cm}^2$ . For  $\text{MoS}_2$  the electrolyte was 25 mM LiI and 50 mM TBAP in acetonitrile. Voltage was applied from  $-0.3 \text{ V}$  to  $0.3 \text{ V}$  (vs  $\text{Ag}/\text{Ag}^+$ ) at a scan rate of  $10 \text{ mV s}^{-1}$ . For  $\text{WSe}_2/\text{MoS}_2$  the electrolyte used was 0.1 M tetra-n-butylammonium hexafluorophosphate and saturated chloranil in acetonitrile. Voltage was applied from  $0.3 \text{ V}$  to  $-0.3 \text{ V}$  (vs  $\text{Ag}/\text{Ag}^+$ ) at a scan rate of  $10 \text{ mV s}^{-1}$ . For all electrodes 1-sun illumination ( $100 \text{ mW cm}^{-2}$ ) with a filtered Xenon lamp was used to provide intermittent illumination (calibration of light source given in a previous study<sup>207</sup>).



## Chapter 5 Conclusions and outlook



A bright future for solution-processed 2D TMDs.

This last section briefly summarizes the work presented in this thesis, addresses ongoing questions raised therein, and suggests possible future avenues to advance the field.

### 5.1 Summary of findings

The exceptional semiconducting properties of exfoliated transition metal dichalcogenide (TMDs) nanosheets have inspired their use in applications such as transistors, photodetectors, biosensors, and photoelectrodes. These two-dimensional (2D) TMDs (ex.,  $\text{MoS}_2$ ,  $\text{MoSe}_2$ ,  $\text{WS}_2$ , and  $\text{WSe}_2$ ) are particularly desirable for their tunable optoelectronic properties and robustness, which are ideal for solar energy conversion. However, scalable routes to produce large-area, high-quality TMD thin films remain a challenge for device implementation on a globally relevant scale.

The work discussed in this thesis aims to address the limitations related to the (1) scalable production of high-performance semiconducting TMD nanosheets and (2) processing them into large-area thin film devices. A novel exfoliation technique was presented which advanced 2D TMD dispersion preparation towards nanosheets with more favorable morphologies, fewer defects, and higher internal quantum yields, thereby achieving benchmark solar energy conversion performance for liquid phase-exfoliated  $\text{MoS}_2$ . This technique was further applied to make composition-tuned alloyed TMDs, which extended the range of optoelectronic properties accessible to solution-processable methods. Lastly, a system for continuous roll-to-roll (R2R) nanoflake film deposition was described when in large volumes of 2D TMD material were processed into large-area thin film devices. The highlights from each chapter are briefly summarized below.

Chapter 2 details the electrochemical pellet intercalation (ECPI) technique for gently exfoliating bulk TMDs to high-performance semiconducting nanoflakes. Using the model material  $\text{MoS}_2$ , improved nanosheet morphology (large lateral dimensions, 1-3 atomic layers) was observed compared to ultrasonicated nanoflakes. Indeed, exceptional optoelectronic performance was found in the form of enhanced photoluminescence, charge carrier mobility (up to  $0.2 \text{ cm}^2 \text{ V}^{-1} \text{ s}^{-1}$  in a multi-sheet device), and photon-to-current efficiency while maintaining high transparency ( $>80\%$ ). Specifically, as a photoanode for iodide oxidation, an internal quantum efficiency up to 90% (at +0.3 V vs Pt) was achieved (compared to only 12% for  $\text{MoS}_2$  nanosheets produced *via* ultrasonication). This impressive behavior was attributed both to improved flake morphology and a lower defect density ( $2.33 \times 10^{13} \text{ cm}^{-2}$ , comparable to monolayer  $\text{MoS}_2$  prepared by vacuum-based techniques) as shown by fluorescence microscopy and high-resolution scanning transmission electron microscopy (STEM). Notably this method was extended to include other TMDs ( $\text{WS}_2$ ,  $\text{WSe}_2$ ), demonstrating versatility and adaptability, which is important when considering the needs of future devices not yet realized.

Building upon this concept, a modified ECPI technique was presented in Chapter 3, further extending it to alloyed TMD nanosheets. Here it was shown that composition-tuned TMD alloys could be achieved by mechanically mixing TMDs prior to pellet formation. High-resolution STEM confirmed mixing at the atomic level yielding results similar to monolayers prepared using energy intensive techniques. It was shown that tunable optoelectronic properties could be obtained as a function of composition. For another degree of tunability both metal-alloyed ( $\text{Mo}_{0.5}\text{W}_{0.5}\text{S}$  and  $\text{Mo}_{0.5}\text{W}_{0.5}\text{Se}$ ) and chalcogenide-alloyed ( $\text{MoSSe}$  and  $\text{WSSe}$ ) nanosheets were demonstrated. Finally, this method was employed to make quaternary ( $\text{Mo}_{0.5}\text{W}_{0.5}\text{SSe}$ ) nanosheets. Ultraviolet photoelectron spectroscopy (UPS) was used to estimate and compare the work functions of the nine materials prepared and highlight differences in the electronic structures. Indeed, the ability to facily tune these materials using a scalable method is an attractive prospect for future large area-devices and one that can likely be pushed beyond what has been shown here.

Finally, Chapter 4 addressed large-area film formation of 2D nanoflakes by presenting a R2R system capable of depositing self-assembled films on flexible substrates. Large-area films up to 100 mm in width were reproducibly printed at  $10\text{ mm s}^{-1}$  with nanoflake loadings of  $35\text{ mg m}^{-2}$  and key printing parameters to afford the required single-flake-layer deposition were identified. Optically uniform coverage on transparent conductive oxide coated flexible plastic substrates was obtained and good flake-substrate alignment was observed. Photoelectrochemical testing verified the optoelectronic activity of the  $\text{MoS}_2$  nanoflake films achieving photocurrent densities for iodide oxidation of  $40\text{ }\mu\text{A cm}^{-2}$  at  $+0.1\text{ V}$  (vs. an  $\text{Ag}/\text{Ag}^+$  reference) under 1-sun illumination. Importantly, large-area  $\text{MoS}_2/\text{WSe}_2$  heterojunction nanoflake films were prepared *via* successive flake layer depositions rendering this method applicable for all of the 2D materials prepared in this thesis as well as additional combinations not considered here, but are of interest elsewhere.

In conclusion, the work presented here advances solution-processing methods for semiconducting TMDs towards processes that yield 2D materials with greatly improved optoelectronic properties and expanded opportunities for tuning these properties. While the devices shown here do not demonstrate record-breaking performances compared to 2D materials prepared by expensive vacuum-based techniques, they push the boundaries beyond what was previously accepted for solution-processed TMD nanosheets. For example, overcoming the size-dependent thickness limit typically observed in other liquid phase exfoliation techniques; approaching 100% photon conversion efficiency which has only been demonstrated in mechanically exfoliated or CVD/MBE prepared monolayers; transforming commercial powders into exfoliated alloyed nanosheets; preparing a meter-long film with controlled nanosheet orientation. These advances motivate further attention be given to these solution-processed materials. Indeed, combining high APCEs and facile continuous tunability with R2R film deposition signals promise for the future of TMD-based, large-area solar conversion devices.



## 5.2 Future work

While this body of work attempted to address ongoing challenges in the field, there remain many more to overcome. Furthermore, the studies presented also raised some additional questions of their own. To this end, the future work discussion will begin with avenues that are directly adjacent to this thesis and will briefly discuss ongoing queries and additional remarks. The second part will take a broader look at possible future directions and themes.

### 5.2.1 Future work related to this thesis

#### *Pellet annealing*

The success of the electrochemical pellet intercalation technique (ECPI) relies heavily on the success of the annealed pellet. If sufficient conductivity is not achieved the process will fail. Notably different materials such as S-based and Se-based TMDs require different annealing conditions. One study that was not done but would be of interest for the future of this method for industrial applications, would be to study the performance of TMD nanosheets as a function of annealing time and/temperature. This may lead to several outcomes including: a change in nanosheet morphology, an increase in method efficiency (ex., if the same results can be achieved at lower temperatures or for less time), and/or an overall better understanding of the role of this crucial step.

In the same domain, such a study for the alloyed materials could lead to a fundamental understanding of the alloying process that takes place during the annealing of mixed powder pellets. While some mechanisms have been proposed,<sup>48</sup> they are few and little has been done to support them. Notably these works typically consider monolayer examples and discussion of bulk alloy formation is challenging to find. Furthermore, the atomic configurations generally predicted by computational studies<sup>46,47</sup> are in stark contrast to what has been observed experimentally as described in this thesis and elsewhere,<sup>44,161–163</sup> yet it does not appear to be discussed in the literature. By controlling all aspects of pellet annealing (ramp time, holding time, cooling time, temperature, pellet mass, etc.) it may be possible to extract more fundamental information as well as more favorable results. Ideally both experimental and computational work would be carried out in tandem.

#### *Doping with ECPI*

It was well-established in this work that ECPI could be used to obtain desirable nanosheet morphology as well as tune the properties of the nanosheets through alloying. An additional extension to this method would be to use ECPI to dope TMD nanosheets. Indeed, many works involving CVD grown TMD monolayers have used other transition metals (ex. Nb to p-type dope MoS<sub>2</sub>) to tune the properties of the materials, for example to create catalytically active sites for the hydrogen evolution reaction (HER) or to obtain ambipolar behavior.<sup>208–213</sup> Given the promising results observed in those works, achieving the same using a scalable approach (i.e., ECPI) would be a powerful tool moving forward.

#### *Use of “green” solvents*

Notably the solvent chosen for liquid exfoliation in this work is N-Methyl-2-pyrrolidone (NMP), which is an excellent solvent for exfoliating nanomaterials, but is also toxic, particularly to the reproductive system.<sup>214</sup> Thus, large scale processing of TMDs (exfoliation, storage, and film fabrication) would be better carried out in less harmful solvents. This poses a particular problem as solvents that are least harmful typically destabilize nanomaterial dispersions (water, ethanol, etc.). As such, it may be necessary to engineer the appropriate solvent. While works have begun to move in this direction,<sup>215</sup> and some have even considered solvents from renewable sources as possible candidates,<sup>216</sup> more could certainly be done in this direction.

*Non-traditional uses of TMD nanosheets*

Typically works that describe TMD-based devices, including this one, are centered around the performance of the TMD. However, many opportunities are likely missed by not using the TMD as a mere component. For example, as a charge transport and/or protective layer in perovskite or organic solar cells or an additive in polymer blends for 3D printed electrodes. The exceptional semiconducting properties of these materials combined with their thinness and robustness means that they can be beneficial to existing device structures. Though some works have tentatively explored this,<sup>158,217–219</sup> the field would likely benefit from further optimization of such devices and additional creativity for future devices.

Furthermore, it was demonstrated in this work that characterization techniques (2D PAINT, high-resolution STEM) and devices (FETs) which have typically been reserved for mechanically exfoliated and CVD-grown single flakes can be applied to solution-processed material so long as the nanosheets are of good quality. Blending the two sectors further will inevitably lead to new fundamental insights, particularly for solution-processed materials.

## 5.2.2 2D TMDs for solar energy conversion on a global scale

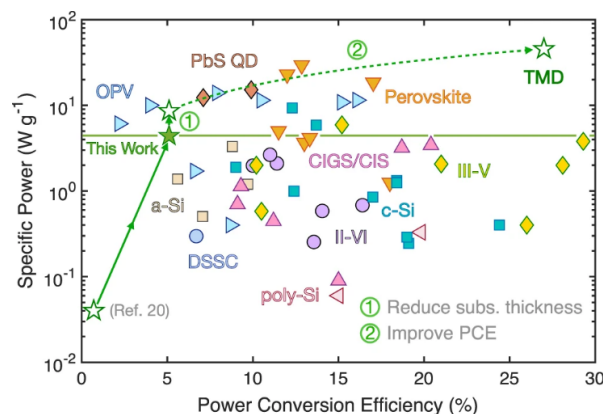


Figure 5.1. Projected performance of TMD-based, flexible solar cells.

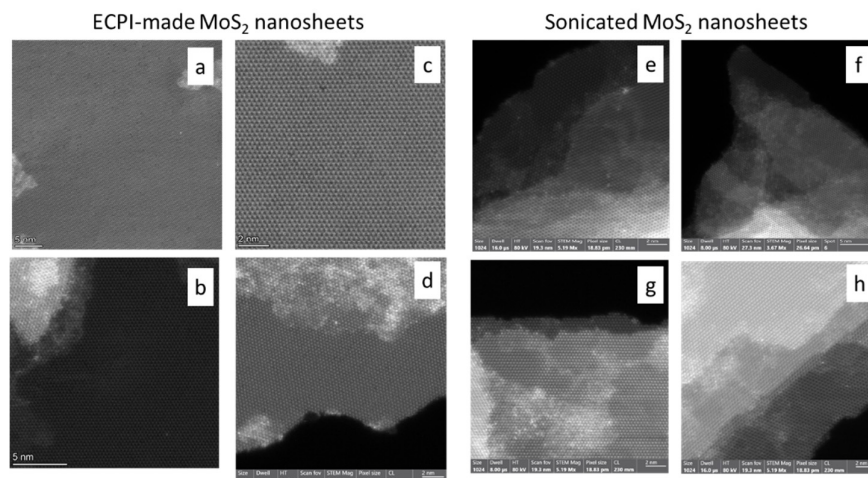
This projection highlights the (1) current state for TMD-based flexible solar cells and (2) projects unprecedented performance with the improvement of the power conversion efficiencies of these materials. Figure reproduced from reference <sup>3</sup>.

This work presented in this thesis focused primarily on TMD-based devices for solar-to-chemical energy conversion applications. However, in the context of solar energy conversion on the global scale, there are other systems where TMD nanomaterials can have a positive impact, namely photovoltaic and photocatalytic. Indeed, the diversification of renewable energy technologies is an effective and necessary strategy for combating climate change globally.

In particular ultrathin, flexible photovoltaic (PV) devices are particularly interesting as large-area devices require little material and they can be easily incorporated into existing structures (i.e., smart windows, solar farms, etc.). In fact, a recently published work showed that TMD-based materials have the potential to outperform nearly all existing flexible and thin solar cell technologies (Figure 5.1).<sup>3</sup> While TMDs have high theoretical limits (ex., ~27%), state-of-the-art typically give power conversion efficiencies (PCE) less than 10% (for 2D single crystals). Thus, bridging this gap is essential towards advancing these technologies. This will require nanomaterials with high quantum efficiencies, high charge mobility, and efficient charge separation. While these phenomena are often studied in single flake devices, similar studies on solution-processed 2D material is scarcer. Indeed, for such technologies to become viable on a global scale, more scalable solutions will likely need to be employed. As hinted to in the previous section, work in general should be carried out to fill the gaps in understanding the fundamental behavior of solution-processed TMD nanosheets. By taking techniques once reserved for single flakes, these lapses can be filled. Such techniques include: small-gated FETs to assess charge mobility across films as a function of gate width and time-resolved PL (TRPL) to study charge life time (and charge separation in a heterojunction), and intensity modulated photovoltage spectroscopy (IMVS) and intensity modulated photocurrent spectroscopy (IMPS) to provide insight into charge carrier dynamics. In amassing more information about what happens inside these solution-processed nanosheets, it will be possible to identify limitations and design additional strategies to help these materials reach their theoretical limits.

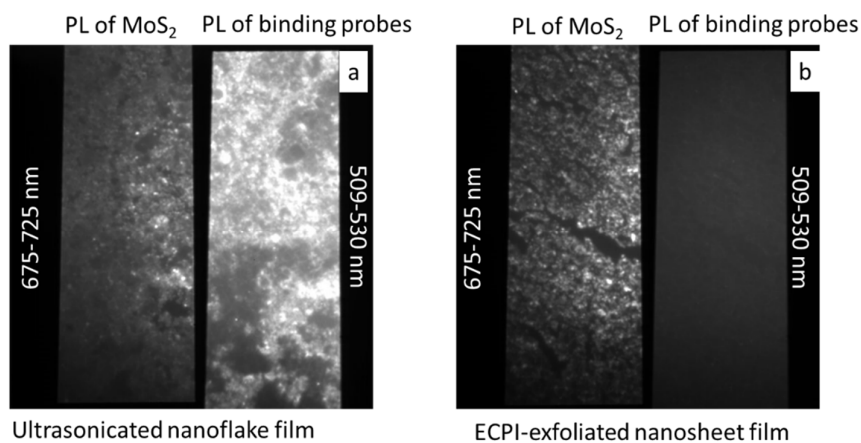
Stepping away from thin film devices, photocatalytic systems are an emerging technology and TMD-based photocatalysts should be considered moving forward as well. Notably these systems have the advantage of being incredibly simple as they are typically comprised of the photocatalyst floating in electrolyte. From this respect, solution-processed TMDs are ideally suited as they are made in solution and can be easily transferred without requiring complicated transfer processes as would be the case for mechanical or CVD-prepared materials. Furthermore, the range of tunable properties shown by TMDs are such that they can be engineered for the desired reaction (ex. HER), including band gap and catalytically active sites. Additionally, similar strategies which have been used to improve the performance of thin films, will likely be transferrable to photocatalytic systems (i.e., vdW HJs, hybrid organic-inorganic, HJ, chemical functionalization, etc.), proving a plethora of initial studies to be done. Lastly, the stability of these materials compared to their organic counterpart would mean longer lifetimes and the potential to be operating under harsher conditions. However, to date very little work can be found in the literature using TMD-based photocatalysts. Future work devoted to this area would likely be of much interest to the field and of much use to a planet seeking alternative sources of energy.

# Annex



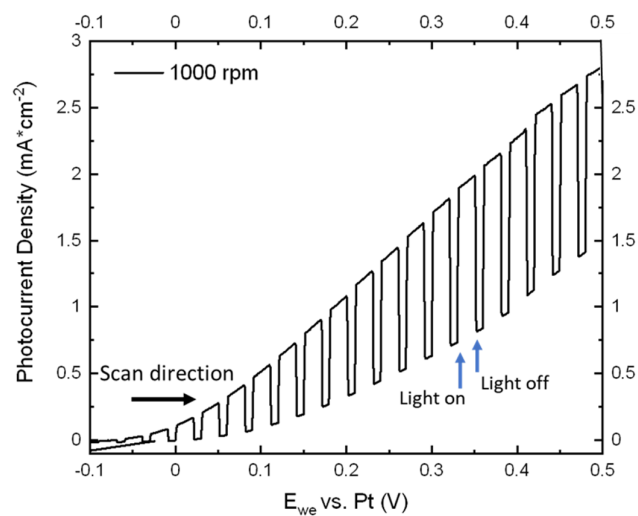
Annex Item 1. Additional high-resolution STEM images for ECPI-made and ultrasonicated MoS<sub>2</sub>.

Images (a-d) display additional high-resolution ADF STEM images for ECPI-made MoS<sub>2</sub> nanosheets, highlighting their clean lattice and homogenous thickness. Images (e-h) display additional high-resolution ADF STEM images for sonicated MoS<sub>2</sub> nanoflakes where edge steps cover the surface, leaving only very small areas of few- or monolayered flake at the perimeter.



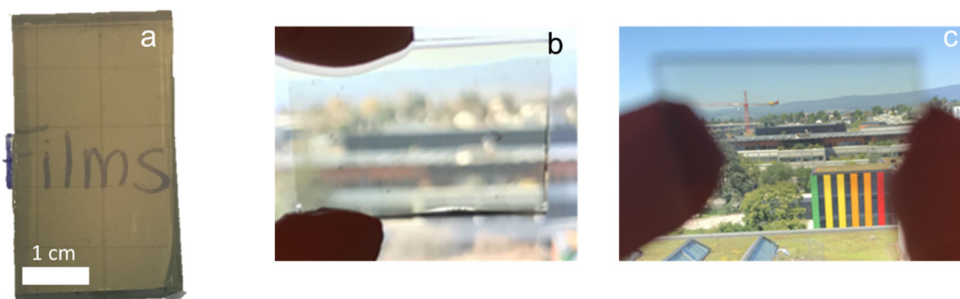
Annex Item 2. Raw images from optical defect mapping experiment (2D PAINT) for sonicated and ECPI-made MoS<sub>2</sub>.

Raw images from optical defect mapping experiment for sonicated nanoflakes (a) and ECPI-made nanosheets (b). The left panels show the unnormalized PL of the MoS<sub>2</sub> material (channel 675-725 nm) while the right panels show the unnormalized PL of the bound probes (channel 509-530 nm). THE ECPI-made MoS<sub>2</sub> has stronger PL (left) with fewer probe binding events (right).



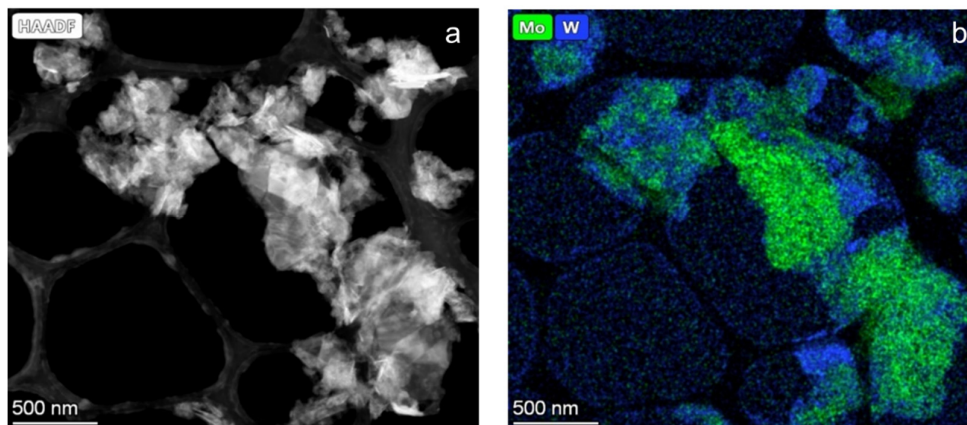
Annex Item 3. Raw LSV for "champion" performing device for ECPI-made  $\text{MoS}_2$  nanosheets.

Raw linear scanning voltammetry (LSV) under intermittent 1-Sun solar illumination in 50 mM LiI, acetonitrile for a "champion" performing device for the ECPI-made  $\text{MoS}_2$  nanoflakes with a photocurrent around 1.2 mA at +0.5 V vs Pt.



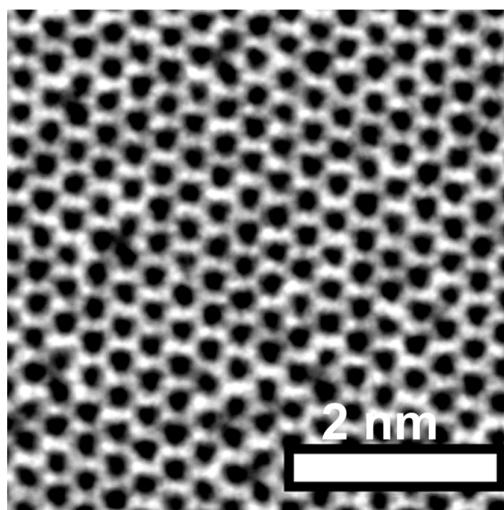
Annex Item 4. Typical batch-scale nanoflake films made *via* LLISA deposition.

Batch-scale films ( $\sim 5 \text{ cm}^2$ ) of (a) ultrasonicated  $\text{MoS}_2$ , (b) ECPI-made  $\text{MoS}_2$ , and (c) ECPI-made  $\text{Mo}_{0.5}\text{W}_{0.5}\text{S}_2$  made *via* Liquid-liquid self-assembly (LLISA) deposition into FTO-coated glass.



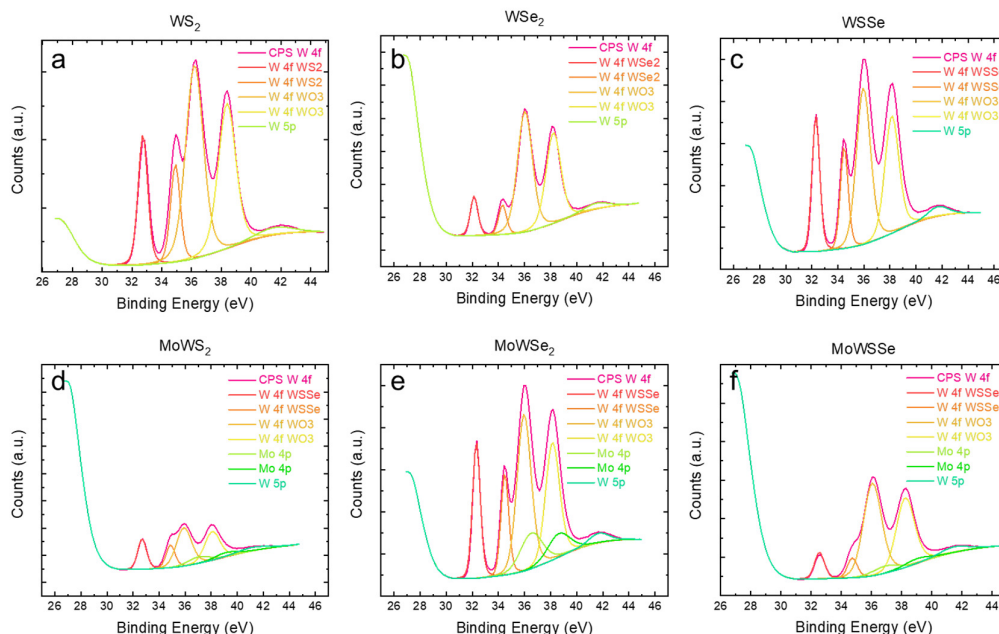
Annex Item 5. STEM EDX of exfoliated nanosheets made from alloyed powders which were not mechanically ground.

STEM (a) HAADF and (b) EDX images for  $\text{Mo}_{0.5}\text{W}_{0.5}\text{S}_2$  nanoflakes made from powders which were mixed but not mechanically ground prior to pellet formation. While some nanosheets show even distribution, indicating alloy formation, others appear to be phase pure. This emphasizes the importance of thorough grinding of the powders before pressing them into pellets.



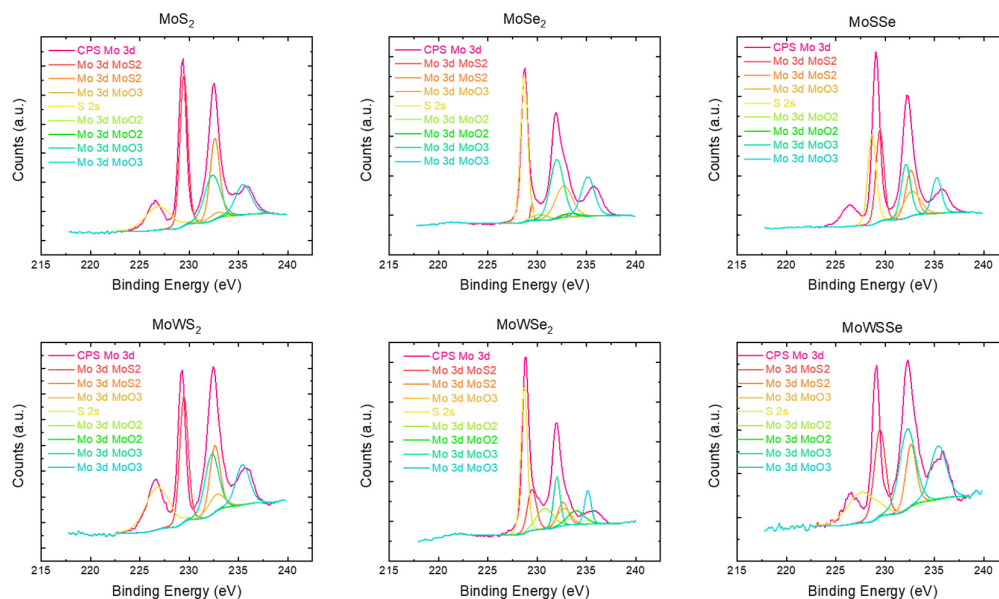
Annex Item 6. iDPC image of a  $\text{Mo}_{0.5}\text{W}_{0.5}\text{S}_2$  nanosheet.

Integrated differential phase contrast detector (iDPC) image of a monolayer region of a  $\text{Mo}_{0.5}\text{W}_{0.5}\text{S}_2$  nanosheet, allowing metal and chalcogen species to be observed. The expected hexagonal arrangement is observed where brightness scales linearly with Z. Brightest spots correspond to the heaviest atom, W, followed by Mo, S<sub>2</sub> columns, and finally S in the case of S vacancies.



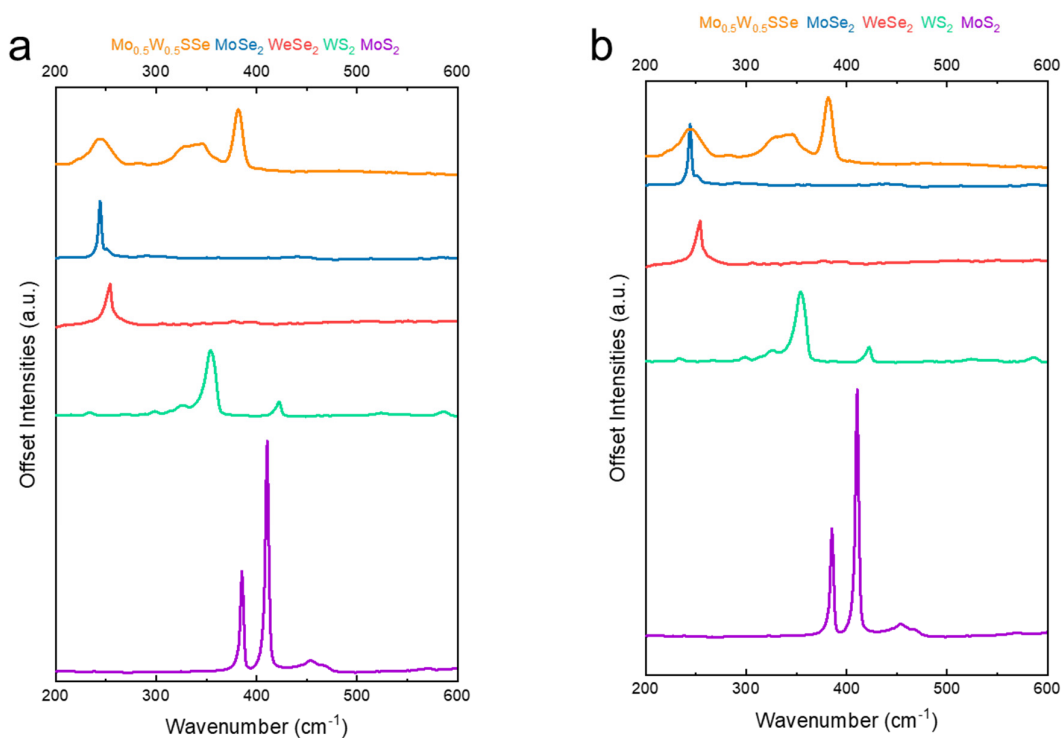
Annex Item 7. Detailed fittings of W4f spectra.

XPS W4f spectra for pure materials (a)  $WS_2$  and (b)  $WSe_2$  yields typical contributions from the  $MX_2$  species as well as  $WO_3$ . Binding energies for the S and Se TMD shift slightly according to the slightly different orbital interactions (2p for S and 3p for Se). W5p can also be observed as a contributing factor for lower binding energies. Similar contributions are observed for the (c) chalcogen alloy,  $WSSe$ ; binding energies are slightly shifted compared to either pure material suggesting different chemical species and interactions. Metal alloyed TMDs (d)  $MoWS_2$  and (e)  $MoWSe_2$  also show contributions from the Mo 4p orbital in addition to the previously discussed contributions. Again, binding energies are unique for these ternary alloys. Finally, (f)  $MoWSSe$  shows contributions from the W4f related to  $MX_2$  and  $WO_3$  as well as W5p and Mo 4p.



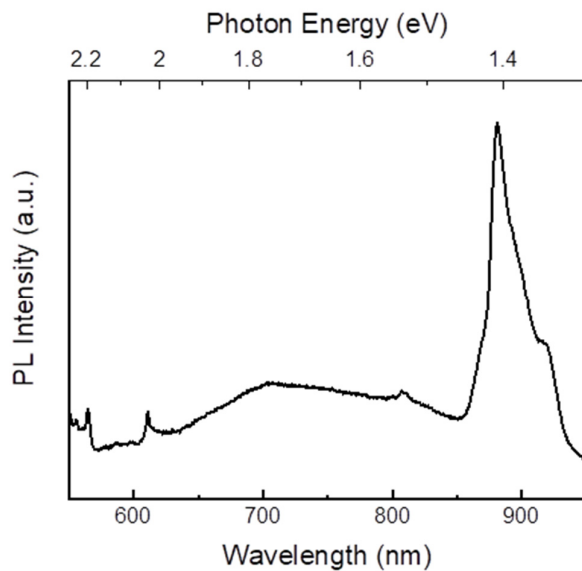
Annex Item 8. Detailed fittings of Mo3d spectra.

XPS Mo3d spectra for pure materials (a)  $MoS_2$  and (b)  $MoSe_2$  yields typical contributions from the  $MX_2$  species as well as  $MoO_x$ . Binding energies for the S and Se TMD shift slightly according to the slightly different orbital interactions (2p for S and 3p for Se) and the S2p is, of course, absent from the  $MoSe_2$  spectra. Similar contributions are observed for the (c) chalcogen alloy,  $MoSSe$ ; binding energies are slightly shifted compared to either pure material, confirming the different chemical nature and interaction. Metal alloyed TMDs (d)  $MoWS_2$  and (e)  $MoWSe_2$  also show the previously discussed contributions and binding energies that are unique for these ternary alloys. Finally, (f)  $MoWSSe$  shows all contributions with shifted binding energies once again. It should be noted that the Mo3d spectra is less well-fitted compared to W4f spectra.



Annex Item 9. Composite of Raman spectra for pure, ternary, and quaternary TMD materials.

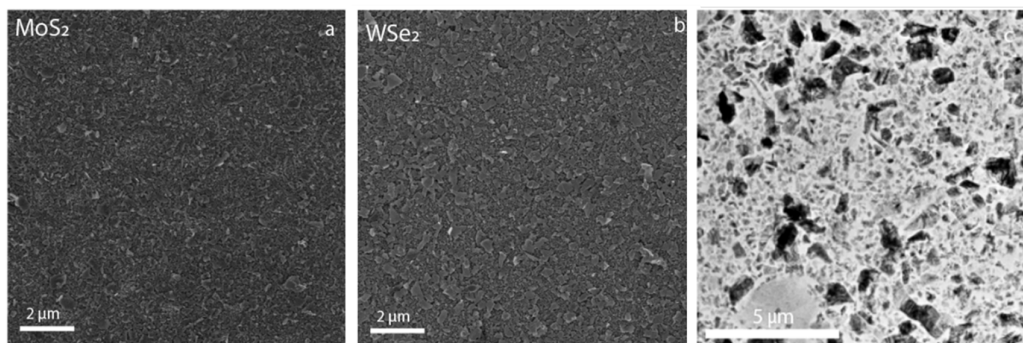
(a) Raman spectra for the quaternary alloy shows distinct signal unique from the pure TMD materials (b) Raman spectra for the quaternary alloy also show unique signals compared to the ternary alloys. This reinforces the notion of a unique quaternary alloy rather than of a material composed of a mixture of various pure or ternary materials.



Annex Item 10. PL of a glass slide.

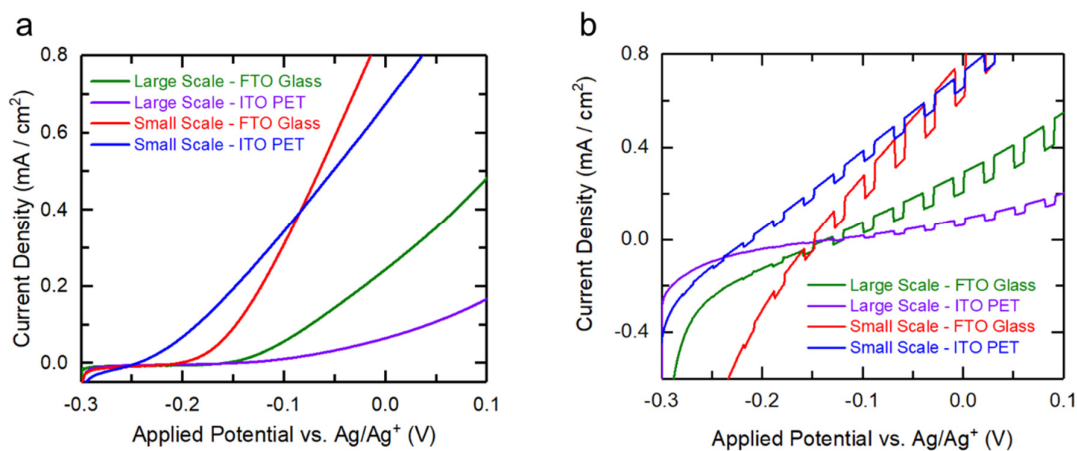
Photoluminescence of a glass slide shows a sharp peak around 900 nm as a result of fluorescing defects within the glass.<sup>172</sup> Owing to the thin nature of the TMD films this peak can always be observed.





Annex Item 11. Electron microscopy of batch-scale LLISA films of ultrasonicated TMD nanoflakes.

Scanning electron microscopy of batch films deposited on FTO-coated glass, MoS<sub>2</sub> (a) and WSe<sub>2</sub> (b). Transmission electron microscopy of a batch film of MoS<sub>2</sub> on a SiNi grid (c), where dark represent thicker flakes, grey represents thinner flakes, and white represents unfilled space. Film coverage is estimated at 80%. Film morphology shows good flake-to-flake alignment and, importantly, no large aggregates. We observe no notable difference between film morphology of the batch and R2R films.



Annex Item 12. Additional PEC characterization of R2R films.

Current-voltage character for R2R and batch films under dark conditions (left) and under chopping, 1-sun illumination (vs. Ag/Ag<sup>+</sup> in 50 mM TBAP 25 mM LiI in MeCN).

# References

- (1) Why silicon is in short supply, affecting everything from cars to consoles. inews.co.uk. <https://inews.co.uk/news/consumer/silicon-shortage-semiconductor-chips-why-cars-consoles-delayed-explained-1229981> (accessed 2022-03-21).
- (2) Lee, Y. N. 2 charts show how much the world depends on Taiwan for semiconductors. CNBC. <https://www.cnn.com/2021/03/16/2-charts-show-how-much-the-world-depends-on-taiwan-for-semiconductors.html> (accessed 2022-03-22).
- (3) Nassiri Nazif, K.; Daus, A.; Hong, J.; Lee, N.; Vaziri, S.; Kumar, A.; Nitta, F.; Chen, M. E.; Kananian, S.; Islam, R.; Kim, K.-H.; Park, J.-H.; Poon, A. S. Y.; Brongersma, M. L.; Pop, E.; Saraswat, K. C. High-Specific-Power Flexible Transition Metal Dichalcogenide Solar Cells. *Nat Commun* **2021**, 12 (1), 7034. <https://doi.org/10.1038/s41467-021-27195-7>.
- (4) Hu, S.; Shaner, M. R.; Beardslee, J. A.; Lichterman, M.; Bruntschwig, B. S.; Lewis, N. S. Amorphous TiO<sub>2</sub> Coatings Stabilize Si, GaAs, and GaP Photoanodes for Efficient Water Oxidation. *Science* **2014**, 344 (6187), 1005–1009. <https://doi.org/10.1126/science.1251428>.
- (5) Seger, B.; Pedersen, T.; Laursen, A. B.; Vesborg, P. C. K.; Hansen, O.; Chorkendorff, I. Using TiO<sub>2</sub> as a Conductive Protective Layer for Photocathodic H<sub>2</sub> Evolution. *J. Am. Chem. Soc.* **2013**, 135 (3), 1057–1064. <https://doi.org/10.1021/ja309523t>.
- (6) Zeng, G.; Pham, T. A.; Vanka, S.; Liu, G.; Song, C.; Cooper, J. K.; Mi, Z.; Ogitsu, T.; Toma, F. M. Development of a Photoelectrochemically Self-Improving Si/GaN Photocathode for Efficient and Durable H<sub>2</sub> Production. *Nat. Mater.* **2021**, 20 (8), 1130–1135. <https://doi.org/10.1038/s41563-021-00965-w>.
- (7) Vanka, S.; Sun, K.; Zeng, G.; Pham, T. A.; Toma, F. M.; Ogitsu, T.; Mi, Z. Long-Term Stability Studies of a Semiconductor Photoelectrode in Three-Electrode Configuration. *J. Mater. Chem. A* **2019**, 7 (48), 27612–27619. <https://doi.org/10.1039/C9TA09926C>.
- (8) Eser, E.; Ramaprasad, K. R.; Volltrauer, H.; Ramos, F.; Gau, S. C.; Vos, R. Long-Term Stability of Amorphous Silicon Solar Cells and Modules. *Solar Cells* **1987**, 21 (1), 25–39. [https://doi.org/10.1016/0379-6787\(87\)90102-5](https://doi.org/10.1016/0379-6787(87)90102-5).
- (9) Frese, K. W.; Madou, M. J.; Morrison, S. R. Investigation of Photoelectrochemical Corrosion of Semiconductors. 1. *J. Phys. Chem.* **1980**, 84 (24), 3172–3178. <https://doi.org/10.1021/j100461a008>.
- (10) Chhowalla, M.; Shin, H. S.; Eda, G.; Li, L.-J.; Loh, K. P.; Zhang, H. The Chemistry of Two-Dimensional Layered Transition Metal Dichalcogenide Nanosheets. *Nature Chemistry* **2013**, 5 (4), 263–275. <https://doi.org/10.1038/nchem.1589>.
- (11) Splendiani, A.; Sun, L.; Zhang, Y.; Li, T.; Kim, J.; Chim, C.-Y.; Galli, G.; Wang, F. Emerging Photoluminescence in Monolayer MoS<sub>2</sub>. *Nano Lett.* **2010**, 10 (4), 1271–1275. <https://doi.org/10.1021/nl903868w>.
- (12) Electrochemistry and Photochemistry of MoS<sub>2</sub> Layer Crystals. I. *Journal of Electroanalytical Chemistry and Interfacial Electrochemistry* **1977**, 81 (1), 97–111. [https://doi.org/10.1016/S0022-0728\(77\)80363-X](https://doi.org/10.1016/S0022-0728(77)80363-X).
- (13) McEvoy, A. J. An Intercalation and Photodeintercalation Reaction of WSe<sub>2</sub>. *Journal of Electroanalytical Chemistry and Interfacial Electrochemistry* **1985**, 195 (1), 207–211. [https://doi.org/10.1016/0022-0728\(85\)80021-8](https://doi.org/10.1016/0022-0728(85)80021-8).
- (14) Chen, J.; Kuriyama, N.; Yuan, H.; Takeshita, H. T.; Sakai, T. Electrochemical Hydrogen Storage in MoS<sub>2</sub> Nanotubes. *J. Am. Chem. Soc.* **2001**, 123 (47), 11813–11814. <https://doi.org/10.1021/ja017121z>.
- (15) Haering, R. R.; Stiles, J. A. R.; Brandt, K. Lithium Molybdenum Disulphide Battery Cathode. US4224390A, September 23, 1980.
- (16) Chaudhry, M. A.; Hill, R. M.; Jonscher, A. K. Electrical Field Effects in Molybdenum Disulphide. *J. Phys. C: Solid State Phys.* **1985**, 18 (8), 1665–1669. <https://doi.org/10.1088/0022-3719/18/8/013>.
- (17) Fivaz, R.; Mooser, E. Mobility of Charge Carriers in Semiconducting Layer Structures. *Phys. Rev.* **1967**, 163 (3), 743–755. <https://doi.org/10.1103/PhysRev.163.743>.
- (18) Akinwande, D.; Huyghebaert, C.; Wang, C.-H.; Serna, M. I.; Goossens, S.; Li, L.-J.; Wong, H.-S. P.; Koppens, F. H. L. Graphene and Two-Dimensional Materials for Silicon Technology. *Nature* **2019**, 573 (7775), 507–518. <https://doi.org/10.1038/s41586-019-1573-9>.
- (19) Bernardi, M.; Palummo, M.; Grossman, J. C. Extraordinary Sunlight Absorption and One Nanometer Thick Photovoltaics Using Two-Dimensional Monolayer Materials. *Nano Lett.* **2013**, 13 (8), 3664–3670. <https://doi.org/10.1021/nl401544y>.
- (20) Yazyev, O. V.; Kis, A. MoS<sub>2</sub> and Semiconductors in the Flatland. *Materials Today* **2015**, 18 (1), 20–30. <https://doi.org/10.1016/j.mat-tod.2014.07.005>.
- (21) Radisavljevic, B.; Radenovic, A.; Brivio, J.; Giacometti, V.; Kis, A. Single-Layer MoS<sub>2</sub> Transistors. *Nature Nanotech* **2011**, 6 (3), 147–150. <https://doi.org/10.1038/nnano.2010.279>.
- (22) Han, B.; Hu, Y. H. MoS<sub>2</sub> as a Co-Catalyst for Photocatalytic Hydrogen Production from Water. *Energy Science & Engineering* **2016**, 4 (5), 285–304. <https://doi.org/10.1002/ese3.128>.
- (23) Jaramillo, T. F.; Jørgensen, K. P.; Bonde, J.; Nielsen, J. H.; Hørch, S.; Chorkendorff, I. Identification of Active Edge Sites for Electrochemical H<sub>2</sub> Evolution from MoS<sub>2</sub> Nanocatalysts. *Science* **2007**, 317 (5834), 100–102. <https://doi.org/10.1126/science.1141483>.
- (24) Kang, Y.; Han, S. An Origin of Unintentional Doping in Transition Metal Dichalcogenides: The Role of Hydrogen Impurities. *Nanoscale* **2017**, 9 (12), 4265–4271. <https://doi.org/10.1039/C6NR08555E>.
- (25) Tan, M. X.; Laibinis, P. E.; Nguyen, S. T.; Kesselman, J. M.; Stanton, C. E.; Lewis, N. S. Principles and Applications of Semiconductor Photoelectrochemistry. In *Progress in Inorganic Chemistry*; Wiley-Blackwell, 2007; pp 21–144. <https://doi.org/10.1002/9780470166420.ch2>.
- (26) McKone, J. R.; Pieterick, A. P.; Gray, H. B.; Lewis, N. S. Hydrogen Evolution from Pt/Ru-Coated p-Type WSe<sub>2</sub> Photocathodes. *J. Am. Chem. Soc.* **2013**, 135 (1), 223–231. <https://doi.org/10.1021/ja308581g>.
- (27) Gusakova et al. Electronic Properties of Bulk and Monolayer TMDs: Theoretical Study Within DFT Framework (GVJ-2e Method). **2017**. <https://doi.org/10.1002/pssa.201700218>.
- (28) Lembke, D.; Allain, A.; Kis, A. Thickness-Dependent Mobility in Two-Dimensional MoS<sub>2</sub> Transistors. *Nanoscale* **2015**, 7 (14), 6255–6260. <https://doi.org/10.1039/C4NR06331G>.
- (29) Bertolazzi, S.; Brivio, J.; Kis, A. Stretching and Breaking of Ultrathin MoS<sub>2</sub>. *ACS Nano* **2011**, 5 (12), 9703–9709. <https://doi.org/10.1021/nn203879f>.

- (30) Mak, K. F.; Lee, C.; Hone, J.; Shan, J.; Heinz, T. F. Atomically Thin  $\text{MoS}_2$ : A New Direct-Gap Semiconductor. *Phys. Rev. Lett.* **2010**, *105* (13), 136805. <https://doi.org/10.1103/PhysRevLett.105.136805>.
- (31) Schlaf, R.; Lang, O.; Pettenkofer, C.; Jaegermann, W. Band Lineup of Layered Semiconductor Heterointerfaces Prepared by van Der Waals Epitaxy: Charge Transfer Correction Term for the Electron Affinity Rule. *Journal of Applied Physics* **1999**, *85* (5), 2732–2753. <https://doi.org/10.1063/1.369590>.
- (32) Cho, H.-H.; Sivula, K. Advancing Operational Stability and Performance of Organic Photoanodes for Solar Water Oxidation. *Trends in Chemistry* **2022**, *4* (2), 93–95. <https://doi.org/10.1016/j.trechm.2021.11.004>.
- (33) Bertolazzi, S.; Gobbi, M.; Zhao, Y.; Backes, C.; Samorì, P. Molecular Chemistry Approaches for Tuning the Properties of Two-Dimensional Transition Metal Dichalcogenides. *Chemical Society Reviews* **2018**, *47* (17), 6845–6888. <https://doi.org/10.1039/C8CS00169C>.
- (34) Mouri, S.; Miyauchi, Y.; Matsuda, K. Tunable Photoluminescence of Monolayer  $\text{MoS}_2$  via Chemical Doping. *Nano Lett.* **2013**, *13* (12), 5944–5948. <https://doi.org/10.1021/nl403036h>.
- (35) Lin, Z.; Carvalho, B. R.; Kahn, E.; Lv, R.; Rao, R.; Terrones, H.; Pimenta, M. A.; Terrones, M. Defect Engineering of Two-Dimensional Transition Metal Dichalcogenides. *2D Mater.* **2016**, *3* (2), 022002. <https://doi.org/10.1088/2053-1583/3/2/022002>.
- (36) Yu, Z.; Pan, Y.; Shen, Y.; Wang, Z.; Ong, Z.-Y.; Xu, T.; Xin, R.; Pan, L.; Wang, B.; Sun, L.; Wang, J.; Zhang, G.; Zhang, Y. W.; Shi, Y.; Wang, X. Towards Intrinsic Charge Transport in Monolayer Molybdenum Disulfide by Defect and Interface Engineering. *Nat Commun* **2014**, *5*, 5290. <https://doi.org/10.1038/ncomms6290>.
- (37) Zhang, M.; Lihter, M.; Chen, T.-H.; Macha, M.; Rayabharam, A.; Banjac, K.; Zhao, Y.; Wang, Z.; Zhang, J.; Comtet, J.; Aluru, N. R.; Lingenfelder, M.; Kis, A.; Radenovic, A. Super-Resolved Optical Mapping of Reactive Sulfur-Vacancies in Two-Dimensional Transition Metal Dichalcogenides. *ACS Nano* **2021**, *15* (4), 7168–7178. <https://doi.org/10.1021/acsnano.1c00373>.
- (38) Li, G.; Zhang, D.; Qiao, Q.; Yu, Y.; Peterson, D.; Zafar, A.; Kumar, R.; Curtarolo, S.; Hunte, F.; Shannon, S.; Zhu, Y.; Yang, W.; Cao, L. All The Catalytic Active Sites of  $\text{MoS}_2$  for Hydrogen Evolution. *J. Am. Chem. Soc.* **2016**, *138* (51), 16632–16638. <https://doi.org/10.1021/jacs.6b05940>.
- (39) Hong, J.; Hu, Z.; Probert, M.; Li, K.; Lv, D.; Yang, X.; Gu, L.; Mao, N.; Feng, Q.; Xie, L.; Zhang, J.; Wu, D.; Zhang, Z.; Jin, C.; Ji, W.; Zhang, X.; Yuan, J.; Zhang, Z. Exploring Atomic Defects in Molybdenum Disulphide Monolayers. *Nat Commun* **2015**, *6* (1), 6293. <https://doi.org/10.1038/ncomms7293>.
- (40) Qiu, H.; Xu, T.; Wang, Z.; Ren, W.; Nan, H.; Ni, Z.; Chen, Q.; Yuan, S.; Miao, F.; Song, F.; Long, G.; Shi, Y.; Sun, L.; Wang, J.; Wang, X. Hopping Transport through Defect-Induced Localized States in Molybdenum Disulphide. *Nat Commun* **2013**, *4* (1), 2642. <https://doi.org/10.1038/ncomms3642>.
- (41) Ippolito, S.; Samorì, P. Defect Engineering Strategies Toward Controlled Functionalization of Solution-Processed Transition Metal Dichalcogenides. *Small Science* **2022**, *2* (4), 2100122. <https://doi.org/10.1002/sssc.202100122>.
- (42) Voiry, D.; Goswami, A.; Kappera, R.; Silva, C. de C. e.; Kaplan, D.; Fujita, T.; Chen, M.; Asefa, T.; Chhowalla, M. Covalent Functionalization of Monolayered Transition Metal Dichalcogenides by Phase Engineering. *Nature Chemistry* **2015**, *7* (1), 45–49. <https://doi.org/10.1038/nchem.2108>.
- (43) Zhou, W.; Zou, X.; Najmaei, S.; Liu, Z.; Shi, Y.; Kong, J.; Lou, J.; Ajayan, P. M.; Yakobson, B. I.; Idrobo, J.-C. Intrinsic Structural Defects in Monolayer Molybdenum Disulfide. *Nano Lett.* **2013**, *13* (6), 2615–2622. <https://doi.org/10.1021/nl4007479>.
- (44) Susarla, S.; Kutana, A.; Hachtel, J. A.; Kochat, V.; Apte, A.; Vajtai, R.; Idrobo, J. C.; Yakobson, B. I.; Tiwary, C. S.; Ajayan, P. M. Quaternary 2D Transition Metal Dichalcogenides (TMDs) with Tunable Bandgap. *Advanced Materials* **2017**, *29* (35), 1702457. <https://doi.org/10.1002/adma.201702457>.
- (45) Song, J.-G.; Ryu, G. H.; Lee, S. J.; Sim, S.; Lee, C. W.; Choi, T.; Jung, H.; Kim, Y.; Lee, Z.; Myoung, J.-M.; Dussarrat, C.; Lansalot-Matras, C.; Park, J.; Choi, H.; Kim, H. Controllable Synthesis of Molybdenum Tungsten Disulfide Alloy for Vertically Composition-Controlled Multilayer. *Nature Communications* **2015**, *6* (1), 7817. <https://doi.org/10.1038/ncomms8817>.
- (46) Gan, L.-Y.; Zhang, Q.; Zhao, Y.-J.; Cheng, Y.; Schwingenschlögl, U. Order-Disorder Phase Transitions in the Two-Dimensional Semiconducting Transition Metal Dichalcogenide Alloys  $\text{Mo}_{1-x}\text{W}_x\text{X}_2$  ( $\text{X} = \text{S}, \text{Se}$  and  $\text{Te}$ ). *Scientific Reports* **2014**, *4* (1), 6691. <https://doi.org/10.1038/srep06691>.
- (47) Kang, J.; Tongay, S.; Li, J.; Wu, J. Monolayer Semiconducting Transition Metal Dichalcogenide Alloys: Stability and Band Bowing. *Journal of Applied Physics* **2013**, *113* (14), 143703. <https://doi.org/10.1063/1.4799126>.
- (48) Bogaert, K.; Liu, S.; Liu, T.; Guo, N.; Zhang, C.; Gradečak, S.; Garaj, S. Two-Dimensional  $\text{Mo}_x\text{W}_{1-x}\text{S}_2$  Graded Alloys: Growth and Optical Properties. *Scientific Reports* **2018**, *8* (1), 12889. <https://doi.org/10.1038/s41598-018-31220-z>.
- (49) Duan, X.; Wang, C.; Fan, Z.; Hao, G.; Kou, L.; Halim, U.; Li, H.; Wu, X.; Wang, Y.; Jiang, J.; Pan, A.; Huang, Y.; Yu, R.; Duan, X. Synthesis of  $\text{WS}_2\text{xSe}_{2-2x}$  Alloy Nanosheets with Composition-Tunable Electronic Properties. *Nano Lett.* **2016**, *16* (1), 264–269. <https://doi.org/10.1021/acs.nanolett.5b03662>.
- (50) Feng, Q.; Zhu, Y.; Hong, J.; Zhang, M.; Duan, W.; Mao, N.; Wu, J.; Xu, H.; Dong, F.; Lin, F.; Jin, C.; Wang, C.; Zhang, J.; Xie, L. Growth of Large-Area 2D  $\text{MoS}_2(1-x)\text{Se}_{2x}$  Semiconductor Alloys. *Advanced Materials* **2014**, *26* (17), 2648–2653. <https://doi.org/10.1002/adma.201306095>.
- (51) Apte, A.; Kochat, V.; Rajak, P.; Krishnamoorthy, A.; Manimunda, P.; Hachtel, J. A.; Idrobo, J. C.; Syed Amanulla, S. A.; Vashishta, P.; Nakano, A.; Kalia, R. K.; Tiwary, C. S.; Ajayan, P. M. Structural Phase Transformation in Strained Monolayer  $\text{MoWSe}_2$  Alloy. *ACS Nano* **2018**, *12* (4), 3468–3476. <https://doi.org/10.1021/acsnano.8b00248>.
- (52) Chaves, A.; Azadani, J. G.; Alsalman, H.; da Costa, D. R.; Frisenda, R.; Chaves, A. J.; Song, S. H.; Kim, Y. D.; He, D.; Zhou, J.; Castellanos-Gomez, A.; Peeters, F. M.; Liu, Z.; Hinkle, C. L.; Oh, S.-H.; Ye, P. D.; Koester, S. J.; Lee, Y. H.; Avouris, P.; Wang, X.; Low, T. Bandgap Engineering of Two-Dimensional Semiconductor Materials. *npj 2D Mater Appl* **2020**, *4* (1), 1–21. <https://doi.org/10.1038/s41699-020-00162-4>.

- (53) Akama, T.; Okita, W.; Nagai, R.; Li, C.; Kaneko, T.; Kato, T. Schottky Solar Cell Using Few-Layered Transition Metal Dichalcogenides toward Large-Scale Fabrication of Semitransparent and Flexible Power Generator. *Scientific Reports* **2017**, *7* (1), 11967. <https://doi.org/10.1038/s41598-017-12287-6>.
- (54) Wang, L.; Tahir, M.; Chen, H.; Sambur, J. B. Probing Charge Carrier Transport and Recombination Pathways in Monolayer MoS<sub>2</sub>/WS<sub>2</sub> Heterojunction Photoelectrodes. *Nano Lett.* **2019**, *19* (12), 9084–9094. <https://doi.org/10.1021/acs.nanolett.9b04209>.
- (55) Cho, A.-J.; Song, M.-K.; Kang, D.-W.; Kwon, J.-Y. Two-Dimensional WSe<sub>2</sub>/MoS<sub>2</sub> p–n Heterojunction-Based Transparent Photovoltaic Cell and Its Performance Enhancement by Fluoropolymer Passivation. *ACS Appl. Mater. Interfaces* **2018**, *10* (42), 35972–35977. <https://doi.org/10.1021/acsami.8b12250>.
- (56) Tsai, M.-L.; Su, S.-H.; Chang, J.-K.; Tsai, D.-S.; Chen, C.-H.; Wu, C.-I.; Li, L.-J.; Chen, L.-J.; He, J.-H. Monolayer MoS<sub>2</sub> Heterojunction Solar Cells. *ACS Nano* **2014**, *8* (8), 8317–8322. <https://doi.org/10.1021/nn502776h>.
- (57) Chen, J.; Bailey, C. S.; Cui, D.; Wang, Y.; Wang, B.; Shi, H.; Cai, Z.; Pop, E.; Zhou, C.; Cronin, S. B. Stacking Independence and Resonant Interlayer Excitation of Monolayer WSe<sub>2</sub>/MoSe<sub>2</sub> Heterostructures for Photocatalytic Energy Conversion. *ACS Appl. Nano Mater.* **2020**, *3* (2), 1175–1181. <https://doi.org/10.1021/acsanm.9b01898>.
- (58) Furchi, M. M.; Höller, F.; Dobusch, L.; Polyushkin, D. K.; Schuler, S.; Mueller, T. Device Physics of van Der Waals Heterojunction Solar Cells. *npj 2D Materials and Applications* **2018**, *2* (1), 3. <https://doi.org/10.1038/s41699-018-0049-3>.
- (59) Xiao, J.; Zhang, Y.; Chen, H.; Xu, N.; Deng, S. Enhanced Performance of a Monolayer MoS<sub>2</sub>/WSe<sub>2</sub> Heterojunction as a Photoelectrochemical Cathode. *Nano-Micro Lett.* **2018**, *10* (4), 60. <https://doi.org/10.1007/s40820-018-0212-6>.
- (60) Hong, X.; Kim, J.; Shi, S.-F.; Zhang, Y.; Jin, C.; Sun, Y.; Tongay, S.; Wu, J.; Zhang, Y.; Wang, F. Ultrafast Charge Transfer in Atomically Thin MoS<sub>2</sub>/WS<sub>2</sub> Heterostructures. *Nature Nanotechnology* **2014**, *9* (9), 682–686. <https://doi.org/10.1038/nnano.2014.167>.
- (61) Yu, X.; Sivula, K. Toward Large-Area Solar Energy Conversion with Semiconducting 2D Transition Metal Dichalcogenides. *ACS Energy Lett.* **2016**, *1* (1), 315–322. <https://doi.org/10.1021/acsenergylett.6b00114>.
- (62) Hernandez, Y.; Nicolosi, V.; Lotya, M.; Blighe, F. M.; Sun, Z.; De, S.; McGovern, I. T.; Holland, B.; Byrne, M.; Gun'ko, Y. K.; Boland, J. J.; Niraj, P.; Duesberg, G.; Krishnamurthy, S.; Goodhue, R.; Hutchison, J.; Scardaci, V.; Ferrari, A. C.; Coleman, J. N. High-Yield Production of Graphene by Liquid-Phase Exfoliation of Graphite. *Nature Nanotechnology* **2008**, *3* (9), 563–568. <https://doi.org/10.1038/nnano.2008.215>.
- (63) Coleman, J. N.; Lotya, M.; O'Neill, A.; Bergin, S. D.; King, P. J.; Khan, U.; Young, K.; Gaucher, A.; De, S.; Smith, R. J.; Shvets, I. V.; Arora, S. K.; Stanton, G.; Kim, H.-Y.; Lee, K.; Kim, G. T.; Duesberg, G. S.; Hallam, T.; Boland, J. J.; Wang, J. J.; Donegan, J. F.; Grunlan, J. C.; Moriarty, G.; Shmeliov, A.; Nicholls, R. J.; Perkins, J. M.; Grieveson, E. M.; Theuvsen, K.; McComb, D. W.; Nellist, P. D.; Nicolosi, V. Two-Dimensional Nanosheets Produced by Liquid Exfoliation of Layered Materials. *Science* **2011**, *331* (6017), 568–571. <https://doi.org/10.1126/science.1194975>.
- (64) O'Neill, A.; Khan, U.; Coleman, J. N. Preparation of High Concentration Dispersions of Exfoliated MoS<sub>2</sub> with Increased Flake Size. *Chem. Mater.* **2012**, *24* (12), 2414–2421. <https://doi.org/10.1021/cm301515z>.
- (65) Yu, X.; Prévot, M. S.; Guijarro, N.; Sivula, K. Self-Assembled 2D WSe<sub>2</sub> Thin Films for Photoelectrochemical Hydrogen Production. *Nature Communications* **2015**, *6*, 7596. <https://doi.org/10.1038/ncomms8596>.
- (66) Yu, X.; Guijarro, N.; Johnson, M.; Sivula, K. Defect Mitigation of Solution-Processed 2D WSe<sub>2</sub> Nanoflakes for Solar-to-Hydrogen Conversion. *Nano Lett.* **2018**, *18* (1), 215–222. <https://doi.org/10.1021/acs.nanolett.7b03948>.
- (67) Yu, X.; Sivula, K. Photogenerated Charge Harvesting and Recombination in Photocathodes of Solvent-Exfoliated WSe<sub>2</sub>. *Chemistry of Materials* **2017**, *29* (16), 6863–6875. <https://doi.org/10.1021/acs.chemmater.7b02018>.
- (68) Amani, M.; Lien, D.-H.; Kiriya, D.; Xiao, J.; Azcatl, A.; Noh, J.; Madhupratyap, S. R.; Addou, R.; Kc, S.; Dubey, M.; Cho, K.; Wallace, R. M.; Lee, S.-C.; He, J.-H.; Ager, J. W.; Zhang, X.; Yablonovitch, E.; Javey, A. Near-Unity Photoluminescence Quantum Yield in MoS<sub>2</sub>. *Science* **2015**, *350* (6264), 1065–1068. <https://doi.org/10.1126/science.aad2114>.
- (69) Nicolosi, V.; Chhowalla, M.; Kanatzidis, M. G.; Strano, M. S.; Coleman, J. N. Liquid Exfoliation of Layered Materials. *Science* **2013**, *340* (6139), 1226419. <https://doi.org/10.1126/science.1226419>.
- (70) Zheng, W.; Lee, L. Y. S. Beyond Sonication: Advanced Exfoliation Methods for Scalable Production of 2D Materials. *Matter* **2022**, *0* (0). <https://doi.org/10.1016/j.matt.2021.12.010>.
- (71) Das, S. K.; Gawas, R.; Chakrabarty, S.; Harini, G.; Patidar, R.; Jasuja, K. An Unexpected Transformation of Organic Solvents into 2D Fluorescent Quantum Dots during Ultrasonication-Assisted Liquid-Phase Exfoliation. *J. Phys. Chem. C* **2019**, *123* (41), 25412–25421. <https://doi.org/10.1021/acs.jpcc.9b03975>.
- (72) Paton, K. R.; Varrla, E.; Backes, C.; Smith, R. J.; Khan, U.; O'Neill, A.; Boland, C.; Lotya, M.; Istrate, O. M.; King, P.; Higgins, T.; Barwich, S.; May, P.; Puczkarski, P.; Ahmed, I.; Moebius, M.; Pettersson, H.; Long, E.; Coelho, J.; O'Brien, S. E.; McGuire, E. K.; Sanchez, B. M.; Duesberg, G. S.; McEvoy, N.; Pennycook, T. J.; Downing, C.; Crossley, A.; Nicolosi, V.; Coleman, J. N. Scalable Production of Large Quantities of Defect-Free Few-Layer Graphene by Shear Exfoliation in Liquids. *Nature Materials* **2014**, *13* (6), 624–630. <https://doi.org/10.1038/nmat3944>.
- (73) Bicca, S.; Barwich, S.; Boland, D.; Harvey, A.; Hanlon, D.; McEvoy, N.; Coleman, J. N. Exfoliation of 2D Materials by High Shear Mixing. *2D Mater.* **2018**, *6* (1), 015008. <https://doi.org/10.1088/2053-1583/aae7e3>.
- (74) Fan, X.; Xu, P.; Zhou, D.; Sun, Y.; Li, Y. C.; Nguyen, M. A. T.; Terrones, M.; Mallouk, T. E. Fast and Efficient Preparation of Exfoliated 2H MoS<sub>2</sub> Nanosheets by Sonication-Assisted Lithium Intercalation and Infrared Laser-Induced 1T to 2H Phase Reversion. *Nano Letters* **2015**, *15* (9), 5956–5960. <https://doi.org/10.1021/acs.nanolett.5b02091>.
- (75) Lukowski, M. A.; Daniel, A. S.; Meng, F.; Forticaux, A.; Li, L.; Jin, S. Enhanced Hydrogen Evolution Catalysis from Chemically Exfoliated Metallic MoS<sub>2</sub> Nanosheets. *Journal of the American Chemical Society* **2013**, *135* (28), 10274–10277. <https://doi.org/10.1021/ja404523s>.
- (76) Chen, W.; Gu, J.; Liu, Q.; Luo, R.; Yao, L.; Sun, B.; Zhang, W.; Su, H.; Chen, B.; Liu, P.; Zhang, D. Quantum Dots of 1T Phase Transitional Metal Dichalcogenides Generated via Electrochemical Li Intercalation. *ACS Nano* **2017**. <https://doi.org/10.1021/acs.nano.7b06364>.

- (77) Ejigu, A.; Kinloch, I. A.; Prestat, E.; Dryfe, R. A. W. A Simple Electrochemical Route to Metallic Phase Trilayer MoS<sub>2</sub>: Evaluation as Electrocatalysts and Supercapacitors. *J. Mater. Chem. A* **2017**, *5* (22), 11316–11330. <https://doi.org/10.1039/C7TA02577G>.
- (78) Lin, Z.; Liu, Y.; Halim, U.; Ding, M.; Liu, Y.; Wang, Y.; Jia, C.; Chen, P.; Duan, X.; Wang, C.; Song, F.; Li, M.; Wan, C.; Huang, Y.; Duan, X. Solution-Processable 2D Semiconductors for High-Performance Large-Area Electronics. *Nature* **2018**, *562* (7726), 254–258. <https://doi.org/10.1038/s41586-018-0574-4>.
- (79) Eda, G.; Yamaguchi, H.; Voiry, D.; Fujita, T.; Chen, M.; Chhowalla, M. Photoluminescence from Chemically Exfoliated MoS<sub>2</sub>. *Nano Lett.* **2011**, *11* (12), 5111–5116. <https://doi.org/10.1021/nl201874w>.
- (80) Li, J.; Song, P.; Zhao, J.; Vaklinova, K.; Zhao, X.; Li, Z.; Qiu, Z.; Wang, Z.; Lin, L.; Zhao, M.; Herng, T. S.; Zuo, Y.; Jonhson, W.; Yu, W.; Hai, X.; Lyu, P.; Xu, H.; Yang, H.; Chen, C.; Pennycook, S. J.; Ding, J.; Teng, J.; Castro Neto, A. H.; Novoselov, K. S.; Lu, J. Printable Two-Dimensional Superconducting Monolayers. *Nature Materials* **2020**, 1–7. <https://doi.org/10.1038/s41563-020-00831-1>.
- (81) Kang, J.; Seo, J.-W. T.; Alducin, D.; Ponce, A.; Yacaman, M. J.; Hersam, M. C. Thickness Sorting of Two-Dimensional Transition Metal Dichalcogenides via Copolymer-Assisted Density Gradient Ultracentrifugation. *Nat Commun* **2014**, *5* (1), 5478. <https://doi.org/10.1038/ncomms6478>.
- (82) Yu, X.; Prévot, M. S.; Sivula, K. Multiflake Thin Film Electronic Devices of Solution Processed 2D MoS<sub>2</sub> Enabled by Sonopolymer Assisted Exfoliation and Surface Modification. *Chem. Mater.* **2014**, *26* (20), 5892–5899. <https://doi.org/10.1021/cm502378g>.
- (83) Wells, R. A.; Johnson, H.; Lhermitte, C. R.; Kinge, S.; Sivula, K. Roll-to-Roll Deposition of Semiconducting 2D Nanoflake Films of Transition Metal Dichalcogenides for Optoelectronic Applications. *ACS Appl. Nano Mater.* **2019**, *2* (12), 7705–7712. <https://doi.org/10.1021/acsanm.9b01774>.
- (84) Arnold, M. S.; Green, A. A.; Hulvat, J. F.; Stupp, S. I.; Hersam, M. C. Sorting Carbon Nanotubes by Electronic Structure Using Density Differentiation. *Nature Nanotech* **2006**, *1* (1), 60–65. <https://doi.org/10.1038/nnano.2006.52>.
- (85) Green, A. A.; Hersam, M. C. Solution Phase Production of Graphene with Controlled Thickness via Density Differentiation. *Nano Lett.* **2009**, *9* (12), 4031–4036. <https://doi.org/10.1021/nl902200b>.
- (86) Deegan, R. D.; Bakajin, O.; Dupont, T. F.; Huber, G.; Nagel, S. R.; Witten, T. A. Capillary Flow as the Cause of Ring Stains from Dried Liquid Drops. *Nature* **1997**, *389* (6653), 827–829. <https://doi.org/10.1038/39827>.
- (87) Kaliyaraj Selva Kumar, A.; Zhang, Y.; Li, D.; Compton, R. G. A Mini-Review: How Reliable Is the Drop Casting Technique? *Electrochemistry Communications* **2020**, *121*, 106867. <https://doi.org/10.1016/j.elecom.2020.106867>.
- (88) Neilson, J.; Avery, M. P.; Derby, B. Tiled Monolayer Films of 2D Molybdenum Disulfide Nanoflakes Assembled at Liquid/Liquid Interfaces. *ACS Appl. Mater. Interfaces* **2020**, *12* (22), 25125–25134. <https://doi.org/10.1021/acsami.0c03794>.
- (89) Hiroaki Tachibana, \*; Yasushi Yamanaka, ‡; Hideki Sakai, ‡; Masahiko Abe, ‡ and; Matsumoto†, M. *Highly Conductive Inorganic–Organic Hybrid Langmuir–Blodgett Films Based on MoS<sub>2</sub>*. ACS Publications. <https://pubs.acs.org/doi/full/10.1021/cm990664b> (accessed 2022-02-08). <https://doi.org/10.1021/cm990664b>.
- (90) Zhang, Y.; Xu, L.; Walker, W. R.; Tittle, C. M.; Backhouse, C. J.; Pope, M. A. Langmuir Films and Uniform, Large Area, Transparent Coatings of Chemically Exfoliated MoS<sub>2</sub> Single Layers. *J. Mater. Chem. C* **2017**, *5* (43), 11275–11287. <https://doi.org/10.1039/C7TC02637D>.
- (91) Blodgett, K. B. *MONOMOLECULAR FILMS OF FATTY ACIDS ON GLASS*. ACS Publications. <https://pubs.acs.org/doi/abs/10.1021/ja01317a513> (accessed 2022-02-08). <https://doi.org/10.1021/ja01317a513>.
- (92) Yoshiaki Taguchi, †; Ryota Kimura, †; Reiko Azumi, ‡; Hiroaki Tachibana, ‡; Naoto Koshizaki, ‡; Masaki Shimomura, ‡; Nobuyuki Momozawa, †; Hideki Sakai, †; Masahiko Abe, †; Mutsuyoshi Matsumoto\*, ‡. *Fabrication of Hybrid Layered Films of MoS<sub>2</sub> and an Amphiphilic Ammonium Cation Using the Langmuir–Blodgett Technique*. ACS Publications. <https://pubs.acs.org/doi/full/10.1021/la980551r> (accessed 2022-02-08). <https://doi.org/10.1021/la980551r>.
- (93) Yu, X.; Rahmanudin, A.; Jeanbourquin, X. A.; Tsokkou, D.; Guijarro, N.; Banerji, N.; Sivula, K. Hybrid Heterojunctions of Solution-Processed Semiconducting 2D Transition Metal Dichalcogenides. *ACS Energy Letters* **2017**, *2* (2), 524–531. <https://doi.org/10.1021/acsenenergylett.6b00707>.
- (94) Tsokkou, D.; Yu, X.; Sivula, K.; Banerji, N. The Role of Excitons and Free Charges in the Excited-State Dynamics of Solution-Processed Few-Layer MoS<sub>2</sub> Nanoflakes. *The Journal of Physical Chemistry C* **2016**, *120* (40), 23286–23292. <https://doi.org/10.1021/acs.jpcc.6b09267>.
- (95) Dotan, H.; Sivula, K.; Grätzel, M.; Rothschild, A.; Warren, S. C. Probing the Photoelectrochemical Properties of Hematite (α-Fe<sub>2</sub>O<sub>3</sub>) Electrodes Using Hydrogen Peroxide as a Hole Scavenger. *Energy Environ. Sci.* **2011**, *4* (3), 958–964. <https://doi.org/10.1039/C0EE00570C>.
- (96) Pesci, F. M.; Sokolikova, M. S.; Grotta, C.; Sherrell, P. C.; Reale, F.; Sharda, K.; Ni, N.; Palczynski, P.; Mattevi, C. MoS<sub>2</sub>/WS<sub>2</sub> Heterojunction for Photoelectrochemical Water Oxidation. *ACS Catal.* **2017**, *7* (8), 4990–4998. <https://doi.org/10.1021/acscatal.7b01517>.
- (97) Wang, F.; Wang, J.; Guo, S.; Zhang, J.; Hu, Z.; Chu, J. Tuning Coupling Behavior of Stacked Heterostructures Based on MoS<sub>2</sub>, WS<sub>2</sub>, and WSe<sub>2</sub>. *Scientific Reports* **2017**, *7* (1), 44712. <https://doi.org/10.1038/srep44712>.
- (98) Gobbi, M.; Orgiu, E.; Samorì, P. When 2D Materials Meet Molecules: Opportunities and Challenges of Hybrid Organic/Inorganic van Der Waals Heterostructures. *Advanced Materials* **2018**, *30* (18), 1706103. <https://doi.org/10.1002/adma.201706103>.
- (99) Bizhani, M.; Thorat, R.; Poston, W.; Wickramasinghe, T.; Aleithan, S. H.; Stinaff, E. Thermal Annealing Effects on Naturally Contacted Monolayer MoS<sub>2</sub>. *physica status solidi (b)* **2021**, *258* (9), 2000426. <https://doi.org/10.1002/pssb.202000426>.
- (100) Kim, H.; Lien, D.-H.; Amani, M.; Ager, J. W.; Javey, A. Highly Stable Near-Unity Photoluminescence Yield in Monolayer MoS<sub>2</sub> by Fluoropolymer Encapsulation and Superacid Treatment. *ACS Nano* **2017**, *11* (5), 5179–5185. <https://doi.org/10.1021/acsnano.7b02521>.
- (101) Le Formal, F.; Tétreault, N.; Cornuz, M.; Moehl, T.; Grätzel, M.; Sivula, K. Passivating Surface States on Water Splitting Hematite Photoanodes with Alumina Overlayers. *Chem. Sci.* **2011**, *2* (4), 737–743. <https://doi.org/10.1039/C0SC00578A>.

- (102) Zhao, Y.; Gali, S. M.; Wang, C.; Pershin, A.; Slassi, A.; Beljonne, D.; Samorì, P. Molecular Functionalization of Chemically Active Defects in WSe<sub>2</sub> for Enhanced Opto-Electronics. *Advanced Functional Materials* n/a (n/a), 2005045. <https://doi.org/10.1002/adfm.202005045>.
- (103) Alzakia, F. I.; Tan, S. C. Liquid-Exfoliated 2D Materials for Optoelectronic Applications. *Advanced Science* **2021**, *8* (11), 2003864. <https://doi.org/10.1002/advs.202003864>.
- (104) Li, J.; Yang, X.; Liu, Y.; Huang, B.; Wu, R.; Zhang, Z.; Zhao, B.; Ma, H.; Dang, W.; Wei, Z.; Wang, K.; Lin, Z.; Yan, X.; Sun, M.; Li, B.; Pan, X.; Luo, J.; Zhang, G.; Liu, Y.; Huang, Y.; Duan, X.; Duan, X. General Synthesis of Two-Dimensional van Der Waals Heterostructure Arrays. *Nature* **2020**, *579* (7799), 368–374. <https://doi.org/10.1038/s41586-020-2098-y>.
- (105) Liang, S.; Cheng, B.; Cui, X.; Miao, F. Van Der Waals Heterostructures for High-Performance Device Applications: Challenges and Opportunities. *Adv. Mater.* **2019**, 1903800. <https://doi.org/10.1002/adma.201903800>.
- (106) Lin, Z.; Huang, Y.; Duan, X. Van Der Waals Thin-Film Electronics. *Nat Electron* **2019**, *2* (9), 378–388. <https://doi.org/10.1038/s41928-019-0301-7>.
- (107) Ricciardulli, A. G.; Blom, P. W. M. Solution-Processable 2D Materials Applied in Light-Emitting Diodes and Solar Cells. *Adv. Mater. Technol.* **2020**, *5* (8), 1900972. <https://doi.org/10.1002/admt.201900972>.
- (108) Ganguly, P.; Harb, M.; Cao, Z.; Cavallo, L.; Breen, A.; Dervin, S.; Dionysiou, D. D.; Pillai, S. C. 2D Nanomaterials for Photocatalytic Hydrogen Production. *ACS Energy Lett.* **2019**, *4* (7), 1687–1709. <https://doi.org/10.1021/acseenergylett.9b00940>.
- (109) Li, C.; Cao, Q.; Wang, F.; Xiao, Y.; Li, Y.; Delaunay, J.-J.; Zhu, H. Engineering Graphene and TMDs Based van Der Waals Heterostructures for Photovoltaic and Photoelectrochemical Solar Energy Conversion. *Chem. Soc. Rev.* **2018**, *47* (13), 4981–5037. <https://doi.org/10.1039/C8CS00067K>.
- (110) Xu, X.; Pan, Y.; Liu, S.; Han, B.; Gu, P.; Li, S.; Xu, W.; Peng, Y.; Han, Z.; Chen, J.; Gao, P.; Ye, Y. Seeded 2D Epitaxy of Large-Area Single-Crystal Films of the van Der Waals Semiconductor 2H MoTe<sub>2</sub>. *Science* **2021**, *372* (6538), 195–200. <https://doi.org/10.1126/science.abf5825>.
- (111) Lee, Y.-H.; Zhang, X.-Q.; Zhang, W.; Chang, M.-T.; Lin, C.-T.; Chang, K.-D.; Yu, Y.-C.; Wang, J. T.-W.; Chang, C.-S.; Li, L.-J.; Lin, T.-W. Synthesis of Large-Area MoS<sub>2</sub> Atomic Layers with Chemical Vapor Deposition. *Advanced Materials* **2012**, *24* (17), 2320–2325. <https://doi.org/10.1002/adma.201104798>.
- (112) Zhan, Y.; Liu, Z.; Najmaei, S.; Ajayan, P. M.; Lou, J. Large-Area Vapor-Phase Growth and Characterization of MoS<sub>2</sub> Atomic Layers on a SiO<sub>2</sub> Substrate. *Small* **2012**, *8* (7), 966–971. <https://doi.org/10.1002/sml.201102654>.
- (113) Fu, D.; Zhao, X.; Zhang, Y.-Y.; Li, L.; Xu, H.; Jang, A.-R.; Yoon, S. I.; Song, P.; Poh, S. M.; Ren, T.; Ding, Z.; Fu, W.; Shin, T. J.; Shin, H. S.; Pantelides, S. T.; Zhou, W.; Loh, K. P. Molecular Beam Epitaxy of Highly Crystalline Monolayer Molybdenum Disulfide on Hexagonal Boron Nitride. *J. Am. Chem. Soc.* **2017**, *139* (27), 9392–9400. <https://doi.org/10.1021/jacs.7b05131>.
- (114) Wang, Q. H.; Kalantar-Zadeh, K.; Kis, A.; Coleman, J. N.; Strano, M. S. Electronics and Optoelectronics of Two-Dimensional Transition Metal Dichalcogenides. *Nature Nanotech* **2012**, *7* (11), 699–712. <https://doi.org/10.1038/nnano.2012.193>.
- (115) Bonneau, P. R.; Wiley, J. B.; Kaner, R. B.; Mansukht, M. F. Metathetical Precursor Route to Molybdenum Disulfide. In *Inorganic Syntheses*; John Wiley & Sons, Ltd, 1995; pp 33–37. <https://doi.org/10.1002/9780470132616.ch8>.
- (116) Backes, C.; Higgins, T. M.; Kelly, A.; Boland, C.; Harvey, A.; Hanlon, D.; Coleman, J. N. Guidelines for Exfoliation, Characterization and Processing of Layered Materials Produced by Liquid Exfoliation. *Chem. Mater.* **2017**, *29* (1), 243–255. <https://doi.org/10.1021/acs.chemmater.6b03335>.
- (117) Forsberg, V.; Zhang, R.; Bäckström, J.; Dahlström, C.; Andres, B.; Norgren, M.; Andersson, M.; Hummelgård, M.; Olin, H. Exfoliated MoS<sub>2</sub> in Water without Additives. *PLoS One* **2016**, *11* (4). <https://doi.org/10.1371/journal.pone.0154522>.
- (118) Varrla, E.; Backes, C.; Paton, K. R.; Harvey, A.; Gholamvand, Z.; McCauley, J.; Coleman, J. N. Large-Scale Production of Size-Controlled MoS<sub>2</sub> Nanosheets by Shear Exfoliation. *Chem. Mater.* **2015**, *27* (3), 1129–1139. <https://doi.org/10.1021/cm5044864>.
- (119) Fan, X.; Xu, P.; Li, Y. C.; Zhou, D.; Sun, Y.; Nguyen, M. A. T.; Terrones, M.; Mallouk, T. E. Controlled Exfoliation of MoS<sub>2</sub> Crystals into Trilayer Nanosheets. *Journal of the American Chemical Society* **2016**, *138* (15), 5143–5149. <https://doi.org/10.1021/jacs.6b01502>.
- (120) Cheng, Y.; Nie, A.; Zhang, Q.; Gan, L.-Y.; Shahbazian-Yassar, R.; Schwingenschlogl, U. Origin of the Phase Transition in Lithiated Molybdenum Disulfide. *ACS Nano* **2014**, *8* (11), 11447–11453. <https://doi.org/10.1021/nn505668c>.
- (121) Er, E.; Hou, H.-L.; Criado, A.; Langer, J.; Möller, M.; Erk, N.; Liz-Marzán, L. M.; Prato, M. High-Yield Preparation of Exfoliated 1T-MoS<sub>2</sub> with SERS Activity. *Chem. Mater.* **2019**, *31* (15), 5725–5734. <https://doi.org/10.1021/acs.chemmater.9b01698>.
- (122) Chou, S. S.; De, M.; Kim, J.; Byun, S.; Dykstra, C.; Yu, J.; Huang, J.; Dravid, V. P. Ligand Conjugation of Chemically Exfoliated MoS<sub>2</sub>. *Journal of the American Chemical Society* **2013**, *135* (12), 4584–4587. <https://doi.org/10.1021/ja310929s>.
- (123) Hu, R.; Huang, Z.; Wang, B.; Qiao, H.; Qi, X. Electrochemical Exfoliation of Molybdenum Disulfide Nanosheets for High-Performance Supercapacitors. *J Mater Sci: Mater Electron* **2021**, *32* (6), 7237–7248. <https://doi.org/10.1007/s10854-021-05432-5>.
- (124) Golub, A. S.; Zubavichus, Ya. V.; Slovokhotov, Yu. L.; Novikov, Yu. N.; Danot, M. Layered Compounds Assembled from Molybdenum Disulfide Single-Layers and Alkylammonium Cations. *Solid State Ionics* **2000**, *128* (1), 151–160. [https://doi.org/10.1016/S0167-2738\(99\)00347-1](https://doi.org/10.1016/S0167-2738(99)00347-1).
- (125) Stepanov, A. A.; Lenenko, N. D.; Golub', A. S.; Pervov, V. S. Synthesis of Layered Metal Dichalcogenides with Organic Cations by Electrochemical Reduction in Suspensions. *Russ J Electrochem* **2013**, *49* (1), 86–90. <https://doi.org/10.1134/S1023193513010138>.
- (126) Wells, R. A.; Zhang, M.; Chen, T.-H.; Boureau, V.; Caretti, M.; Liu, Y.; Yum, J.-H.; Johnson, H.; Kinge, S.; Radenovic, A.; Sivula, K. High Performance Semiconducting Nanosheets via a Scalable Powder-Based Electrochemical Exfoliation Technique. *ACS Nano* **2022**. <https://doi.org/10.1021/acsnano.1c10739>.
- (127) LeBeau, J. M.; Findlay, S. D.; Allen, L. J.; Stemmer, S. Quantitative STEM: Experimental Methods and Applications. *J. Phys.: Conf. Ser.* **2012**, *371*, 012053. <https://doi.org/10.1088/1742-6596/371/1/012053>.
- (128) Powell, C. X-Ray Photoelectron Spectroscopy Database XPS, Version 4.1, NIST Standard Reference Database 20, 1989. <https://doi.org/10.18434/T4T88K>.

- (129) Attanayake, N. H.; Thenuwara, A. C.; Patra, A.; Aulin, Y. V.; Tran, T. M.; Chakraborty, H.; Borguet, E.; Klein, M. L.; Perdew, J. P.; Strongin, D. R. Effect of Intercalated Metals on the Electrocatalytic Activity of 1T-MoS<sub>2</sub> for the Hydrogen Evolution Reaction. *ACS Energy Lett.* **2018**, *3* (1), 7–13. <https://doi.org/10.1021/acseenergylett.7b00865>.
- (130) Velazquez, J. M.; John, J.; Esposito, D. V.; Pieterick, A.; Pala, R.; Sun, G.; Zhou, X.; Huang, Z.; Ardo, S.; Soriaga, M. P.; Brunschwig, B. S.; Lewis, N. S. A Scanning Probe Investigation of the Role of Surface Motifs in the Behavior of P-WSe<sub>2</sub> Photocathodes. *Energy Environ. Sci.* **2016**, *9* (1), 164–175. <https://doi.org/10.1039/C5EE02530C>.
- (131) Castellanos-Gomez, A.; Quereda, J.; Meulen, H. P. van der; Agraït, N.; Rubio-Bollinger, G. Spatially Resolved Optical Absorption Spectroscopy of Single- and Few-Layer MoS<sub>2</sub> by Hyperspectral Imaging. *Nanotechnology* **2016**, *27* (11), 115705. <https://doi.org/10.1088/0957-4484/27/11/115705>.
- (132) Dhakal, K. P.; Duong, D. L.; Lee, J.; Nam, H.; Kim, M.; Kan, M.; Lee, Y. H.; Kim, J. Confocal Absorption Spectral Imaging of MoS<sub>2</sub>: Optical Transitions Depending on the Atomic Thickness of Intrinsic and Chemically Doped MoS<sub>2</sub>. *Nanoscale* **2014**, *6* (21), 13028–13035. <https://doi.org/10.1039/C4NR03703K>.
- (133) Molina-Sánchez, A.; Sangalli, D.; Hummer, K.; Marini, A.; Wirtz, L. Effect of Spin-Orbit Interaction on the Optical Spectra of Single-Layer, Double-Layer, and Bulk MoS<sub>2</sub>. *Phys. Rev. B* **2013**, *88* (4), 045412. <https://doi.org/10.1103/PhysRevB.88.045412>.
- (134) Lazić, I.; Bosch, E. G. T.; Lazar, S. Phase Contrast STEM for Thin Samples: Integrated Differential Phase Contrast. *Ultramicroscopy* **2016**, *160*, 265–280. <https://doi.org/10.1016/j.ultramic.2015.10.011>.
- (135) Lin, J.; Pantelides, S. T.; Zhou, W. Vacancy-Induced Formation and Growth of Inversion Domains in Transition-Metal Dichalcogenide Monolayer. *ACS Nano* **2015**, *9* (5), 5189–5197. <https://doi.org/10.1021/acsnano.5b00554>.
- (136) Vancsó, P.; Magda, G. Z.; Pető, J.; Noh, J.-Y.; Kim, Y.-S.; Hwang, C.; Biró, L. P.; Tapasztó, L. The Intrinsic Defect Structure of Exfoliated MoS<sub>2</sub> Single Layers Revealed by Scanning Tunneling Microscopy. *Sci Rep* **2016**, *6* (1), 29726. <https://doi.org/10.1038/srep29726>.
- (137) Thompson, E. S.; Saveyn, P.; Declercq, M.; Meert, J.; Guida, V.; Eads, C. D.; Robles, E. S. J.; Britton, M. M. Characterisation of Heterogeneity and Spatial Autocorrelation in Phase Separating Mixtures Using Moran's I. *Journal of Colloid and Interface Science* **2018**, *513*, 180–187. <https://doi.org/10.1016/j.jcis.2017.10.115>.
- (138) *Moran's I - File Exchange - MATLAB Central*. <https://www.mathworks.com/matlabcentral/fileexchange/13663-moran-s-i> (accessed 2021-10-19).
- (139) Tsai, H.-S.; Huang, Y.-H.; Tsai, P.-C.; Chen, Y.-J.; Ahn, H.; Lin, S.-Y.; Lu, Y.-J. Ultrafast Exciton Dynamics in Scalable Monolayer MoS<sub>2</sub> Synthesized by Metal Sulfurization. *ACS Omega* **2020**, *5* (19), 10725–10730. <https://doi.org/10.1021/acsomega.0c00187>.
- (140) Makula, P.; Pacia, M.; Macyk, W. How To Correctly Determine the Band Gap Energy of Modified Semiconductor Photocatalysts Based on UV-Vis Spectra. *J. Phys. Chem. Lett.* **2018**, *9* (23), 6814–6817. <https://doi.org/10.1021/acs.jpclett.8b02892>.
- (141) Ardekani, H.; Younts, R.; Yu, Y.; Cao, L.; Gundogdu, K. Reversible Photoluminescence Tuning by Defect Passivation via Laser Irradiation on Aged Monolayer MoS<sub>2</sub>. *ACS Appl. Mater. Interfaces* **2019**, *11* (41), 38240–38246. <https://doi.org/10.1021/acsmi.9b10688>.
- (142) Kam, K. K.; Parkinson, B. A. Detailed Photocurrent Spectroscopy of the Semiconducting Group VIB Transition Metal Dichalcogenides. *J. Phys. Chem.* **1982**, *86* (4), 463–467. <https://doi.org/10.1021/j100393a010>.
- (143) Gurarslan, A.; Yu, Y.; Su, L.; Yu, Y.; Suarez, F.; Yao, S.; Zhu, Y.; Ozturk, M.; Zhang, Y.; Cao, L. Surface-Energy-Assisted Perfect Transfer of Centimeter-Scale Monolayer and Few-Layer MoS<sub>2</sub> Films onto Arbitrary Substrates. *ACS Nano* **2014**, *8* (11), 11522–11528. <https://doi.org/10.1021/nn5057673>.
- (144) Lee, Y.; Yang, J.; Lee, D.; Kim, Y.-H.; Park, J.-H.; Kim, H.; Cho, J. H. Trap-Induced Photoresponse of Solution-Synthesized MoS<sub>2</sub>. *Nanoscale* **2016**, *8* (17), 9193–9200. <https://doi.org/10.1039/C6NR00654J>.
- (145) George, A. S.; Mutlu, Z.; Ionescu, R.; Wu, R. J.; Jeong, J. S.; Bay, H. H.; Chai, Y.; Mkhoyan, K. A.; Ozkan, M.; Ozkan, C. S. Wafer Scale Synthesis and High Resolution Structural Characterization of Atomically Thin MoS<sub>2</sub> Layers. *Advanced Functional Materials* **2014**, *24* (47), 7461–7466. <https://doi.org/10.1002/adfm.201402519>.
- (146) Boschloo, G.; Hagfeldt, A. Characteristics of the Iodide/Triiodide Redox Mediator in Dye-Sensitized Solar Cells. *Acc. Chem. Res.* **2009**, *42* (11), 1819–1826. <https://doi.org/10.1021/ar900138m>.
- (147) Yao, L.; Liu, Y.; Cho, H.-H.; Xia, M.; Sekar, A.; Darwich, B. P.; Wells, R. A.; Yum, J.-H.; Ren, D.; Grätzel, M.; Guijarro, N.; Sivula, K. A Hybrid Bulk-Heterojunction Photoanode for Direct Solar-to-Chemical Conversion. *Energy Environ. Sci.* **2021**, *14* (5), 3141–3151. <https://doi.org/10.1039/D1EE00152C>.
- (148) Yu, W. J.; Vu, Q. A.; Oh, H.; Nam, H. G.; Zhou, H.; Cha, S.; Kim, J.-Y.; Carvalho, A.; Jeong, M.; Choi, H.; Castro Neto, A. H.; Lee, Y. H.; Duan, X. Unusually Efficient Photocurrent Extraction in Monolayer van Der Waals Heterostructure by Tunneling through Discretized Barriers. *Nat Commun* **2016**, *7* (1), 13278. <https://doi.org/10.1038/ncomms13278>.
- (149) Yu, W. J.; Liu, Y.; Zhou, H.; Yin, A.; Li, Z.; Huang, Y.; Duan, X. Highly Efficient Gate-Tunable Photocurrent Generation in Vertical Heterostructures of Layered Materials. *Nature Nanotechnology* **2013**, *8* (12), 952–958. <https://doi.org/10.1038/nnano.2013.219>.
- (150) Britnell, L.; Ribeiro, R. M.; Eckmann, A.; Jalil, R.; Belle, B. D.; Mishchenko, A.; Kim, Y.-J.; Gorbachev, R. V.; Georgiou, T.; Morozov, S. V.; Grigorenko, A. N.; Geim, A. K.; Casiraghi, C.; Neto, A. H. C.; Novoselov, K. S. Strong Light-Matter Interactions in Heterostructures of Atomically Thin Films. *Science* **2013**, *340* (6138), 1311–1314. <https://doi.org/10.1126/science.1235547>.
- (151) Wang, L.; Schmid, M.; Nilsson, Z. N.; Tahir, M.; Chen, H.; Sambur, J. B. Laser Annealing Improves the Photoelectrochemical Activity of Ultrathin MoSe<sub>2</sub> Photoelectrodes. *ACS Appl. Mater. Interfaces* **2019**, *11* (21), 19207–19217. <https://doi.org/10.1021/acsmi.9b04785>.
- (152) Ovesný, M.; Křížek, P.; Borkovec, J.; Švindrych, Z.; Hagen, G. M. ThunderSTORM: A Comprehensive ImageJ Plug-in for PALM and STORM Data Analysis and Super-Resolution Imaging. *Bioinformatics* **2014**, *30* (16), 2389–2390. <https://doi.org/10.1093/bioinformatics/btu202>.
- (153) Hebel, F. *Moran's I*. <https://www.mathworks.com/matlabcentral/fileexchange/13663-moran-s-i> (accessed 2021-10-28).
- (154) *Evolution of Electronic Structure in Atomically Thin Sheets of WS<sub>2</sub> and WSe<sub>2</sub>* | *ACS Nano*. <https://pubs.acs.org/doi/10.1021/nn305275h> (accessed 2020-05-13).

- (155) Mueller, T.; Malic, E. Exciton Physics and Device Application of Two-Dimensional Transition Metal Dichalcogenide Semiconductors. *npj 2D Materials and Applications* **2018**, *2* (1), 1–12. <https://doi.org/10.1038/s41699-018-0074-2>.
- (156) Migliato Marega, G.; Zhao, Y.; Avsar, A.; Wang, Z.; Tripathi, M.; Radenovic, A.; Kis, A. Logic-in-Memory Based on an Atomically Thin Semiconductor. *Nature* **2020**, *587* (7832), 72–77. <https://doi.org/10.1038/s41586-020-2861-0>.
- (157) Lin, L.; Sherrell, P.; Liu, Y.; Lei, W.; Zhang, S.; Zhang, H.; Wallace, G. G.; Chen, J. Engineered 2D Transition Metal Dichalcogenides—A Vision of Viable Hydrogen Evolution Reaction Catalysis. *Advanced Energy Materials* **2020**, *10* (16), 1903870. <https://doi.org/10.1002/aenm.201903870>.
- (158) Liang, M.; Ali, A.; Belaidi, A.; Hossain, M. I.; Ronan, O.; Downing, C.; Tabet, N.; Sanvito, S.; El-Mellouhi, F.; Nicolosi, V. Improving Stability of Organometallic-Halide Perovskite Solar Cells Using Exfoliation Two-Dimensional Molybdenum Chalcogenides. *npj 2D Mater Appl* **2020**, *4* (1), 1–8. <https://doi.org/10.1038/s41699-020-00173-1>.
- (159) Li, N.; Wang, Q.; Shen, C.; Wei, Z.; Yu, H.; Zhao, J.; Lu, X.; Wang, G.; He, C.; Xie, L.; Zhu, J.; Du, L.; Yang, R.; Shi, D.; Zhang, G. Large-Scale Flexible and Transparent Electronics Based on Monolayer Molybdenum Disulfide Field-Effect Transistors. *Nature Electronics* **2020**, 1–7. <https://doi.org/10.1038/s41928-020-00475-8>.
- (160) Sarkar, D.; Liu, W.; Xie, X.; Anselmo, A. C.; Mitragotri, S.; Banerjee, K. MoS<sub>2</sub> Field-Effect Transistor for Next-Generation Label-Free Biosensors. *ACS Nano* **2014**, *8* (4), 3992–4003. <https://doi.org/10.1021/nn5009148>.
- (161) Lin, Y.-C.; Torsi, R.; Geoghegan, D. B.; Robinson, J. A.; Xiao, K. Controllable Thin-Film Approaches for Doping and Alloying Transition Metal Dichalcogenides Monolayers. *Advanced Science* **2021**, *8* (9), 2004249. <https://doi.org/10.1002/adv.202004249>.
- (162) Park, J.; Kim, M. S.; Park, B.; Oh, S. H.; Roy, S.; Kim, J.; Choi, W. Composition-Tunable Synthesis of Large-Scale Mo<sub>1</sub>–XW<sub>x</sub>S<sub>2</sub> Alloys with Enhanced Photoluminescence. *ACS Nano* **2018**. <https://doi.org/10.1021/acsnano.8b03408>.
- (163) Chen, Y.; Xi, J.; Dumcenco, D. O.; Liu, Z.; Suenaga, K.; Wang, D.; Shuai, Z.; Huang, Y.-S.; Xie, L. Tunable Band Gap Photoluminescence from Atomically Thin Transition-Metal Dichalcogenide Alloys. *ACS Nano* **2013**, *7* (5), 4610–4616. <https://doi.org/10.1021/nn401420h>.
- (164) Dumcenco, D. O.; Kobayashi, H.; Liu, Z.; Huang, Y.-S.; Suenaga, K. Visualization and Quantification of Transition Metal Atomic Mixing in Mo 1–x W x S 2 Single Layers. *Nature Communications* **2013**, *4* (1), 1351. <https://doi.org/10.1038/ncomms2351>.
- (165) Bhoyate, S.; Kim, J.; Lee, E.; Park, B.; Lee, E.; Park, J.; Oh, S. H.; Kim, J.; Choi, W. Mixed Phase 2D Mo<sub>0.5</sub>W<sub>0.5</sub>S<sub>2</sub> Alloy as a Multi-Functional Electrocatalyst for a High-Performance Cathode in Li–S Batteries. *J. Mater. Chem. A* **2020**, *8* (25), 12436–12445. <https://doi.org/10.1039/D0TA04354K>.
- (166) Xi, J.; Zhao, T.; Wang, D.; Shuai, Z. Tunable Electronic Properties of Two-Dimensional Transition Metal Dichalcogenide Alloys: A First-Principles Prediction. *J. Phys. Chem. Lett.* **2014**, *5* (2), 285–291. <https://doi.org/10.1021/jz402375s>.
- (167) Tan, W.; Wei, Z.; Liu, X.; Liu, J.; Fang, X.; Fang, D.; Wang, X.; Wang, D.; Tang, J.; Fan, X. Ordered and Disordered Phases in Mo<sub>1</sub>–xW<sub>x</sub>S<sub>2</sub> Monolayer. *Sci Rep* **2017**, *7* (1), 15124. <https://doi.org/10.1038/s41598-017-15286-9>.
- (168) Chen, Y.; Dumcenco, D. O.; Zhu, Y.; Zhang, X.; Mao, N.; Feng, Q.; Zhang, M.; Zhang, J.; Tan, P.-H.; Huang, Y.-S.; Xie, L. Composition-Dependent Raman Modes of Mo<sub>1</sub>–xW<sub>x</sub>S<sub>2</sub> Monolayer Alloys. *Nanoscale* **2014**, *6* (5), 2833–2839. <https://doi.org/10.1039/C3NR05630A>.
- (169) Chen, F.; Wang, L.; Ji, X. Evolution of Two-Dimensional Mo<sub>1</sub>–XW<sub>x</sub>S<sub>2</sub> Alloy-Based Vertical Heterostructures with Various Composition Ranges via Manipulating the Mo/W Precursors. *J. Phys. Chem. C* **2018**, *122* (49), 28337–28346. <https://doi.org/10.1021/acs.jpcc.8b09002>.
- (170) Deng, Q.; Li, X.; Si, H.; Hong, J.; Wang, S.; Feng, Q.; Hu, C.-X.; Wang, S.; Zhang, H.-L.; Suenaga, K.; Xu, H. Strong Band Bowing Effects and Distinctive Optoelectronic Properties of 2H and 1T' Phase-Tunable Mo<sub>x</sub>Re<sub>1–x</sub>S<sub>2</sub> Alloys. *Advanced Functional Materials* **2020**, *30* (34), 2003264. <https://doi.org/10.1002/adfm.202003264>.
- (171) Cullen, C. P.; Hartwig, O.; Coileáin, C. Ó.; McManus, J. B.; Peters, L.; Ilhan, C.; Duesberg, G. S.; McEvoy, N. Synthesis and Thermal Stability of TMD Thin Films: A Comprehensive XPS and Raman Study. 72.
- (172) Rabouw, F. T.; Cogan, N. M. B.; Berends, A. C.; Stam, W. van der; Vanmaekelbergh, D.; Koenderink, A. F.; Krauss, T. D.; Donega, C. de M. Non-Blinking Single-Photon Emitters in Silica. *Sci Rep* **2016**, *6* (1), 21187. <https://doi.org/10.1038/srep21187>.
- (173) Yücelen, E.; Lazić, I.; Bosch, E. G. T. Phase Contrast Scanning Transmission Electron Microscopy Imaging of Light and Heavy Atoms at the Limit of Contrast and Resolution. *Sci Rep* **2018**, *8* (1), 2676. <https://doi.org/10.1038/s41598-018-20377-2>.
- (174) Markeev, P. A.; Najafidehaghani, E.; Gan, Z.; Soththwes, K.; George, A.; Turchanin, A.; de Jong, M. P. Energy-Level Alignment at Interfaces between Transition-Metal Dichalcogenide Monolayers and Metal Electrodes Studied with Kelvin Probe Force Microscopy. *J. Phys. Chem. C* **2021**, *125* (24), 13551–13559. <https://doi.org/10.1021/acs.jpcc.1c01612>.
- (175) Jariwala, D.; Sangwan, V. K.; Lauhon, L. J.; Marks, T. J.; Hersam, M. C. Emerging Device Applications for Semiconducting Two-Dimensional Transition Metal Dichalcogenides. *ACS Nano* **2014**, *8* (2), 1102–1120. <https://doi.org/10.1021/nn500064s>.
- (176) Shim, J.; Park, H.-Y.; Kang, D.-H.; Kim, J.-O.; Jo, S.-H.; Park, Y.; Park, J.-H. Electronic and Optoelectronic Devices Based on Two-Dimensional Materials: From Fabrication to Application. *Advanced Electronic Materials* **2017**, *3* (4), 1600364. <https://doi.org/10.1002/aenm.201600364>.
- (177) Barua, S.; Dutta, H. S.; Gogoi, S.; Devi, R.; Khan, R. Nanostructured MoS<sub>2</sub>-Based Advanced Biosensors: A Review. *ACS Appl. Nano Mater.* **2018**, *1* (1), 2–25. <https://doi.org/10.1021/acsnm.7b00157>.
- (178) Mao, S.; Chang, J.; Pu, H.; Lu, G.; He, Q.; Zhang, H.; Chen, J. Two-Dimensional Nanomaterial-Based Field-Effect Transistors for Chemical and Biological Sensing. *Chem. Soc. Rev.* **2017**, *46* (22), 6872–6904. <https://doi.org/10.1039/C6CS00827E>.
- (179) Bie, Y.-Q.; Grosso, G.; Heuck, M.; Furchi, M. M.; Cao, Y.; Zheng, J.; Bunandar, D.; Navarro-Moratalla, E.; Zhou, L.; Efetov, D. K.; Taniguchi, T.; Watanabe, K.; Kong, J.; Englund, D.; Jarillo-Herrero, P. A MoTe<sub>2</sub>-Based Light-Emitting Diode and Photodetector for Silicon Photonic Integrated Circuits. *Nature Nanotechnology* **2017**, *12* (12), 1124–1129. <https://doi.org/10.1038/nnano.2017.209>.
- (180) Huo, N.; Konstantatos, G. Recent Progress and Future Prospects of 2D-Based Photodetectors. *Advanced Materials* **2018**, *30* (51), 1801164. <https://doi.org/10.1002/adma.201801164>.



- (181) Lu, Y.; Chen, T.; Ryu, G. H.; Huang, H.; Sheng, Y.; Chang, R.-J.; Warner, J. H. Self-Limiting Growth of High-Quality 2D Monolayer MoS<sub>2</sub> by Direct Sulfurization Using Precursor-Soluble Substrates for Advanced Field-Effect Transistors and Photodetectors. *ACS Appl. Nano Mater.* **2019**, *2* (1), 369–378. <https://doi.org/10.1021/acsnm.8b01955>.
- (182) Sherrell, P. C.; Palczynski, P.; Sokolikova, M. S.; Reale, F.; Pesci, F. M.; Och, M.; Mattevi, C. Large-Area CVD MoS<sub>2</sub>/WS<sub>2</sub> Heterojunctions as a Photoelectrocatalyst for Salt-Water Oxidation. *ACS Appl. Energy Mater.* **2019**. <https://doi.org/10.1021/acsaem.9b01008>.
- (183) Park, G.-H.; Nielsch, K.; Thomas, A. 2D Transition Metal Dichalcogenide Thin Films Obtained by Chemical Gas Phase Deposition Techniques. *Advanced Materials Interfaces* **2019**, *6* (3), 1800688. <https://doi.org/10.1002/admi.201800688>.
- (184) Lim, Y. R.; Han, J. K.; Kim, S. K.; Lee, Y. B.; Yoon, Y.; Kim, S. J.; Min, B. K.; Kim, Y.; Jeon, C.; Won, S.; Kim, J.-H.; Song, W.; Myung, S.; Lee, S. S.; An, K.-S.; Lim, J. Roll-to-Roll Production of Layer-Controlled Molybdenum Disulfide: A Platform for 2D Semiconductor-Based Industrial Applications. *Advanced Materials* **2018**, *30* (5), 1705270. <https://doi.org/10.1002/adma.201705270>.
- (185) Anenburg, M. Molybdenum and Rhenium Disulfide Synthesis via High-Pressure Carbonate Melt. *CrystEngComm* **2019**, *21* (30), 4513–4518. <https://doi.org/10.1039/C9CE00188C>.
- (186) Yu, H.; Liao, M.; Zhao, W.; Liu, G.; Zhou, X. J.; Wei, Z.; Xu, X.; Liu, K.; Hu, Z.; Deng, K.; Zhou, S.; Shi, J.-A.; Gu, L.; Shen, C.; Zhang, T.; Du, L.; Xie, L.; Zhu, J.; Chen, W.; Yang, R.; Shi, D.; Zhang, G. Wafer-Scale Growth and Transfer of Highly-Oriented Monolayer MoS<sub>2</sub> Continuous Films. *ACS Nano* **2017**, *11* (12), 12001–12007. <https://doi.org/10.1021/acsnano.7b03819>.
- (187) Gao, Y.; Liu, Z.; Sun, D.-M.; Huang, L.; Ma, L.-P.; Yin, L.-C.; Ma, T.; Zhang, Z.; Ma, X.-L.; Peng, L.-M.; Cheng, H.-M.; Ren, W. Large-Area Synthesis of High-Quality and Uniform Monolayer WS<sub>2</sub> on Reusable Au Foils. *Nature Communications* **2015**, *6* (1). <https://doi.org/10.1038/ncomms9569>.
- (188) Ahn, C.; Lee, J.; Kim, H.-U.; Bark, H.; Jeon, M.; Ryu, G. H.; Lee, Z.; Yeom, G. Y.; Kim, K.; Jung, J.; Kim, Y.; Lee, C.; Kim, T. Low-Temperature Synthesis of Large-Scale Molybdenum Disulfide Thin Films Directly on a Plastic Substrate Using Plasma-Enhanced Chemical Vapor Deposition. *Advanced Materials* **2015**, *27* (35), 5223–5229. <https://doi.org/10.1002/adma.201501678>.
- (189) Mattinen, M.; Hatanpää, T.; Sarnet, T.; Mizohata, K.; Meinander, K.; King, P. J.; Khriachtchev, L.; Räisänen, J.; Ritala, M.; Leskelä, M. Atomic Layer Deposition of Crystalline MoS<sub>2</sub> Thin Films: New Molybdenum Precursor for Low-Temperature Film Growth. *Advanced Materials Interfaces* **2017**, *4* (18), 1700123. <https://doi.org/10.1002/admi.201700123>.
- (190) Liu, N.; Kim, P.; Kim, J. H.; Ye, J. H.; Kim, S.; Lee, C. J. Large-Area Atomically Thin MoS<sub>2</sub> Nanosheets Prepared Using Electrochemical Exfoliation. *ACS Nano* **2014**, *8* (7), 6902–6910. <https://doi.org/10.1021/nn5016242>.
- (191) Zhang, X.; Lai, Z.; Tan, C.; Zhang, H. Solution-Processed Two-Dimensional MoS<sub>2</sub> Nanosheets: Preparation, Hybridization, and Applications. *Angewandte Chemie International Edition* **2016**, *55* (31), 8816–8838. <https://doi.org/10.1002/anie.201509933>.
- (192) Ippolito, S.; Ciesielski, A.; Samori, P. Tailoring the Physicochemical Properties of Solution-Processed Transition Metal Dichalcogenides via Molecular Approaches. *Chemical Communications* **2019**, *55* (61), 8900–8914. <https://doi.org/10.1039/C9CC03845K>.
- (193) Mastria, R.; Scarfiello, R.; Altamura, D.; Giannini, C.; Liscio, A.; Kovtun, A.; Bianco, G. V.; Bruno, G.; Grillo, V.; Tavabi, A. H.; Dunin-Borkowski, R. E.; Nobile, C.; Cola, A.; Cozzoli, P. D.; Gambino, S.; Rizzo, A. In-Plane Aligned Colloidal 2D WS<sub>2</sub> Nanoflakes for Solution-Processable Thin Films with High Planar Conductivity. *Scientific Reports* **2019**, *9* (1). <https://doi.org/10.1038/s41598-019-45192-1>.
- (194) McManus, D.; Vranic, S.; Withers, F.; Sanchez-Romaguera, V.; Macucci, M.; Yang, H.; Sorrentino, R.; Parvez, K.; Son, S.-K.; Iannaccone, G.; Kostarelou, K.; Fiori, G.; Casiraghi, C. Water-Based and Biocompatible 2D Crystal Inks for All-Inkjet-Printed Heterostructures. *Nature Nanotechnology* **2017**, *12* (4), 343–350. <https://doi.org/10.1038/nnano.2016.281>.
- (195) Burgués-Ceballos, I.; Stella, M.; Lacharmoise, P.; Martínez-Ferrero, E. Towards Industrialization of Polymer Solar Cells: Material Processing for Upscaling. *J. Mater. Chem. A* **2014**, *2* (42), 17711–17722. <https://doi.org/10.1039/C4TA03780D>.
- (196) Parchine, M.; McGrath, J.; Bardosova, M.; Pemble, M. E. Large Area 2D and 3D Colloidal Photonic Crystals Fabricated by a Roll-to-Roll Langmuir–Blodgett Method. *Langmuir* **2016**, *32* (23), 5862–5869. <https://doi.org/10.1021/acs.langmuir.6b01242>.
- (197) Fornarini, L.; Stirpe, F.; Scrosati, B.; Razzini, G. Electrochemical Solar Cells with Layer-Type Semiconductor Anodes. Performance of n-MoS<sub>2</sub> Cells. *Solar Energy Materials* **1981**, *5* (1), 107–114. [https://doi.org/10.1016/0165-1633\(81\)90063-0](https://doi.org/10.1016/0165-1633(81)90063-0).
- (198) Liu, Y.; Weiss, N. O.; Duan, X.; Cheng, H.-C.; Huang, Y.; Duan, X. Van Der Waals Heterostructures and Devices. *Nature Reviews Materials* **2016**, *1* (9), 16042. <https://doi.org/10.1038/natrevmats.2016.42>.
- (199) Ceballos, F.; Bellus, M. Z.; Chiu, H.-Y.; Zhao, H. Ultrafast Charge Separation and Indirect Exciton Formation in a MoS<sub>2</sub>–MoSe<sub>2</sub> van Der Waals Heterostructure. *ACS Nano* **2014**, *8* (12), 12717–12724. <https://doi.org/10.1021/nn505736z>.
- (200) Furchi, M. M.; Pospischil, A.; Libisch, F.; Burgdörfer, J.; Mueller, T. Photovoltaic Effect in an Electrically Tunable van Der Waals Heterojunction. *Nano Lett.* **2014**, *14* (8), 4785–4791. <https://doi.org/10.1021/nl501962c>.
- (201) Lee, C.-H.; Lee, G.-H.; Zande, A. M. van der; Chen, W.; Li, Y.; Han, M.; Cui, X.; Arefe, G.; Nuckolls, C.; Heinz, T. F.; Guo, J.; Hone, J.; Kim, P. Atomically Thin p–n Junctions with van Der Waals Heterointerfaces. *Nature Nanotechnology* **2014**, *9* (9), 676–681. <https://doi.org/10.1038/nnano.2014.150>.
- (202) Pezeshki, A.; Shokouh, S. H. H.; Nazari, T.; Oh, K.; Im, S. Electric and Photovoltaic Behavior of a Few-Layer  $\alpha$ -MoTe<sub>2</sub>/MoS<sub>2</sub> Dichalcogenide Heterojunction. *Advanced Materials* **2016**, *28* (16), 3216–3222. <https://doi.org/10.1002/adma.201504090>.
- (203) Patel, A. B.; Machhi, H. K.; Chauhan, P.; Narayan, S.; Dixit, V.; Soni, S. S.; Jha, P. K.; Solanki, G. K.; Patel, K. D.; Pathak, V. M. Electrophoretically Deposited MoSe<sub>2</sub>/WSe<sub>2</sub> Heterojunction from Ultrasonically Exfoliated Nanocrystals for Enhanced Electrochemical Photoreponse. *ACS Appl. Mater. Interfaces* **2019**, *11* (4), 4093–4102. <https://doi.org/10.1021/acsaami.8b18177>.
- (204) Doan, M.-H.; Jin, Y.; Adhikari, S.; Lee, S.; Zhao, J.; Lim, S. C.; Lee, Y. H. Charge Transport in MoS<sub>2</sub>/WSe<sub>2</sub> van Der Waals Heterostructure with Tunable Inversion Layer. *ACS Nano* **2017**, *11* (4), 3832–3840. <https://doi.org/10.1021/acsnano.7b00021>.
- (205) Li, M.-Y.; Shi, Y.; Cheng, C.-C.; Lu, L.-S.; Lin, Y.-C.; Tang, H.-L.; Tsai, M.-L.; Chu, C.-W.; Wei, K.-H.; He, J.-H.; Chang, W.-H.; Suenaga, K.; Li, L.-J. Epitaxial Growth of a Monolayer WSe<sub>2</sub>-MoS<sub>2</sub> Lateral p–n Junction with an Atomically Sharp Interface. *Science* **2015**, *349* (6247), 524–528. <https://doi.org/10.1126/science.aab4097>.
- (206) Beal, A. R.; Hughes, H. P. Kramers-Kronig Analysis of the Reflectivity Spectra of 2H-MoS<sub>2</sub>, 2H-MoSe<sub>2</sub> and 2H-MoTe<sub>2</sub>. *Journal of Physics C: Solid State Physics* **1979**, *12* (5), 881–890. <https://doi.org/10.1088/0022-3719/12/5/017>.

- (207) Prévot, M. S.; Guijarro, N.; Sivula, K. Enhancing the Performance of a Robust Sol–Gel-Processed p-Type Delafossite CuFeO<sub>2</sub> Photocathode for Solar Water Reduction. *ChemSusChem* **2015**, *8* (8), 1359–1367. <https://doi.org/10.1002/cssc.201403146>.
- (208) Laskar, M. R.; Nath, D. N.; Ma, L.; Lee, E. W.; Lee, C. H.; Kent, T.; Yang, Z.; Mishra, R.; Roldan, M. A.; Idrobo, J.-C.; Pantelides, S. T.; Pennycook, S. J.; Myers, R. C.; Wu, Y.; Rajan, S. P-Type Doping of MoS<sub>2</sub> Thin Films Using Nb. *Appl. Phys. Lett.* **2014**, *104* (9), 092104. <https://doi.org/10.1063/1.4867197>.
- (209) Li, M.; Yao, J.; Wu, X.; Zhang, S.; Xing, B.; Niu, X.; Yan, X.; Yu, Y.; Liu, Y.; Wang, Y. P-Type Doping in Large-Area Monolayer MoS<sub>2</sub> by Chemical Vapor Deposition. *ACS Appl. Mater. Interfaces* **2020**, *12* (5), 6276–6282. <https://doi.org/10.1021/acsami.9b19864>.
- (210) Suh, J.; Tan, T. L.; Zhao, W.; Park, J.; Lin, D.-Y.; Park, T.-E.; Kim, J.; Jin, C.; Saigal, N.; Ghosh, S.; Wong, Z. M.; Chen, Y.; Wang, F.; Walukiewicz, W.; Eda, G.; Wu, J. Reconfiguring Crystal and Electronic Structures of MoS<sub>2</sub> by Substitutional Doping. *Nature Communications* **2018**, *9* (1), 199. <https://doi.org/10.1038/s41467-017-02631-9>.
- (211) Lin, D.-Y.; Jheng, J.-J.; Ko, T.-S.; Hsu, H.-P.; Lin, C.-F. Doping with Nb Enhances the Photoresponsivity of WSe<sub>2</sub> Thin Sheets. *AIP Advances* **2018**, *8* (5), 055011. <https://doi.org/10.1063/1.5024570>.
- (212) Xu, E. Z.; Liu, H. M.; Park, K.; Li, Z.; Losovyj, Y.; Starr, M.; Werbiński, M.; Fertig, H. A.; Zhang, S. X. P-Type Transition-Metal Doping of Large-Area MoS<sub>2</sub> Thin Films Grown by Chemical Vapor Deposition. *Nanoscale* **2017**, *9* (10), 3576–3584. <https://doi.org/10.1039/C6NR09495C>.
- (213) Qin, Z.; Loh, L.; Wang, J.; Xu, X.; Zhang, Q.; Haas, B.; Alvarez, C.; Okuno, H.; Yong, J. Z.; Schultz, T.; Koch, N.; Dan, J.; Pennycook, S. J.; Zeng, D.; Bosman, M.; Eda, G. Growth of Nb-Doped Monolayer WS<sub>2</sub> by Liquid-Phase Precursor Mixing. *ACS Nano* **2019**, *13* (9), 10768–10775. <https://doi.org/10.1021/acsnano.9b05574>.
- (214) Safety Data Sheet. 6.
- (215) Paolucci, V.; D'Olimpio, G.; Lozzi, L.; Mio, A. M.; Ottaviano, L.; Nardone, M.; Nicotra, G.; Le-Cornec, P.; Cantalini, C.; Politano, A. Sustainable Liquid-Phase Exfoliation of Layered Materials with Nontoxic Polarclean Solvent. *ACS Sustainable Chem. Eng.* **2020**, *8* (51), 18830–18840. <https://doi.org/10.1021/acssuschemeng.0c04191>.
- (216) O. Komarova, A.; R. Dick, G.; S. Luterbacher, J. Diformylxylose as a New Polar Aprotic Solvent Produced from Renewable Biomass. *Green Chemistry* **2021**, *23* (13), 4790–4799. <https://doi.org/10.1039/D1GC00641J>.
- (217) Huang, P.; Wang, Z.; Liu, Y.; Zhang, K.; Yuan, L.; Zhou, Y.; Song, B.; Li, Y. Water-Soluble 2D Transition Metal Dichalcogenides as the Hole-Transport Layer for Highly Efficient and Stable p–i–n Perovskite Solar Cells. *ACS Appl. Mater. Interfaces* **2017**, *9* (30), 25323–25331. <https://doi.org/10.1021/acsami.7b06403>.
- (218) Gusmão, R.; Sofer, Z.; Marvan, P.; Pumera, M. MoS<sub>2</sub> Versatile Spray-Coating of 3D Electrodes for the Hydrogen Evolution Reaction. *Nanoscale* **2019**, *11* (20), 9888–9895. <https://doi.org/10.1039/C9NR01876J>.
- (219) *2D MoS<sub>2</sub>/carbon/poly(lactic acid) filament for 3D printing: Photo and electrochemical energy conversion and storage* | Elsevier Enhanced Reader. <https://reader.elsevier.com/reader/sd/pii/S2352940721003644?token=C5B37F78CFC6CC0F859EB139C6AFFC72DBF9BB93F96B5C1831923EBD4D9B507E01B8EEECB312E5D78EE69487DFB0A35A&originRegion=eu-west-1&originCreation=20220413201856> (accessed 2022-04-13). <https://doi.org/10.1016/j.apmt.2021.101301>.

# CV Rebekah Wells

Graduate Research Assistant

+41 21 693 76 69 | [Rebekah.Wells@epfl.ch](mailto:Rebekah.Wells@epfl.ch)

Google Scholar ID : iwfphiAAAAAJ

h-index : 7

Orcid ID : 0000-0002-5785-3392

École Polytechnique Fédérale de Lausanne

Station 6, Bâtiment CH

CH-1015, Lausanne, Switzerland

Experienced physical chemist with a passion for interdisciplinary science and cross-field collaborations. My works focus on novel nanomaterials with emphasis on harnessing their unique optoelectronic properties for solar energy applications. I am trained in a variety of spectroscopic and microscopic techniques to bring together fundamental understanding with real-world performances. My biggest asset is my resourceful nature – both in the lab with innovative solutions and in forming collaborations of researchers with diverse backgrounds and expertise.

## Education

**Ph.D. in Chemistry and chemical engineering (EPFL, Lausanne)**

September 2017 - Present

Anticipated graduation: Spring 2022

**Bachelor of Science in Chemistry (University of North Carolina, Chapel Hill)**

August 2012 - May 2016

*Highest Honors and distinction. 3.7/4.0*

*Thesis:* Phosphorene: Synthesis and controlled oxidation using selective environmental parameters

**Exchange year (Université Joseph Fourier, Grenoble)**

September 2014 – June 2015

## Professional Experience

*École Polytechnique Fédérale de Lausanne (EPFL), Lausanne*

September 2017 - Present

Laboratory for molecular engineering of optoelectronic nanomaterials (head: Prof. Kevin Sivula)

### **Graduate Research Assistant, Chemistry and Chemical Engineering**

Developed innovative methods for scalable production of pristine 2D TMD materials. Extensively characterized their morphology and optoelectronic properties with emphasis on photovoltaic and electrochemical device performance.

*University of North Carolina, Chapel Hill, North Carolina*

August 2013 – May 2016

The Warren Lab (head: Prof. Scott Warren)

### **Undergraduate Research Assistant, Chemistry & Applied Physical Sciences**

Characterized the then novel 2D material phosphorene, special focus on optoelectronic properties and scalable production. Studied oxidation and degradation mechanisms in response to varying environmental factors.

*Duke University, Durham, North Carolina*

August 2011 – August 2012

The Jinks-Robertson Lab (head: Prof. Sue Jinks-Robertson)

### **Research Intern, Molecular Genetics and Microbiology**

## Teaching Experience

- General chemistry for medical students (French) **EPFL**
- Intro to chemistry (French/English), Intro to chemical engineering lab (French/English) **EPFL**
- Supervision of Masters thesis projects (2) **EPFL**
- Course translations (French/English) for intro to chemistry **EPFL**
- Teaching assistant for general chemistry I&II (English) **UNC**

## Selected Publications

---

**RA Wells**, M Zhang, TH Cheng, V Boureau, MC Caretti, Y Liu, JH Liu, H Johnson, S Kinge, A Radenovic, K Sivula. High performance semiconducting nanosheets via a scalable powder-based electrochemical exfoliation technique. *ACS Nano*. **(2022)**

**RA Wells**, H Johnson, CR Lhermitte, S Kinge, K Sivula. Roll-to-Roll Deposition of Semiconducting 2D Nanoflake Films of Transition Metal Dichalcogenides for Optoelectronic Applications. *ACS Applied Nano Materials* 2 (12), 7705-7712. **(2019)** \*ACS Editors' Choice, Cover Art awarded

KL Kuntz, **RA Wells**, J Hu, T Yang, B Dong, H Guo, AH Woomer, et al, SC Warren. Control of surface and edge oxidation on phosphorene. *ACS applied materials & interfaces* 9 (10), 9126-9135. **(2017)**

AH Woomer, TW Farnsworth, J Hu, **RA Wells**, CL Donley, SC Warren. Phosphorene: synthesis, scale-up, and quantitative optical spectroscopy. *ACS nano* 9 (9), 8869-8884. **(2015)** \*ACS Nano Most Read

## Conferences & Seminars

---

*European Materials Research Society, oral presentation* (June 2022)

- Exploring the optoelectronic properties of high-performing 2D TMDs exfoliated via solution-processable routes (Young Researcher Award)
- Engineering 2D TMD nanoflake films for solar energy conversion applications (Honorarium speaker)
- Roll-to-roll deposition of 2D TMD nanoflake films for large area solar energy conversion

*Materials Research Society, oral presentation* (May 2022)

- Engineering solution-processable 2D TMD nanoflakes for photoelectrochemical applications (best student presentation awarded)
- From powder to large-area films—A solution-processable route for production of pristine and alloyed 2D TMDs for optoelectronic applications (MRS Graduate Student Gold Award)

*Electrochemical Society (PRiME), oral presentation + poster presentation* (October 2020)

- Roll-to-roll deposition of 2D nanoflake films of TMDs for optoelectronic applications
- Exploring the optoelectronic properties of solution processed 2D TMD nanoflakes Exfoliated via large molecule electrointercalation

*European Materials Research Society, oral presentation* (May 2019)

- The roll-to-roll deposition of 2D nanoflake films of TMDs for optoelectronic applications

## Patent Record

---

Solution-based deposition method for preparing semiconducting thin films via dispersed particle self-assembly at a liquid-liquid interface, **2019** | *Patent pending*

Solution-based deposition method for preparing semiconducting thin films via dispersed particle self-assembly at a liquid-liquid interface, **2018** | (WO2020025146 (A1))

Two dimensional materials produced by the liquid exfoliation of black phosphorous, **2016** | (WO2016018988 (A1))

## Awards and Honors

---

- MRS Graduate Student Award Gold, 2022
- MRS Best Student Presentation award, 2022
- E-MRS Young Researcher Award, 2022
- E-MRS Women in Renewable Energy (WiRE) Honorarium speaker, 2022
- RSC young researcher development grant, 2022
- Swiss Academy of Sciences (SCNAT) Chemistry Travel Award, 2020
- Highest Honors in Chemistry, 2016
- Graduation with distinction, 2016
- Jason D. Altom Memorial Award for Undergraduate Research, 2015
- Lottie & Marvin Boykin Scholarship, 2014
- Pearl L. Cavin Initial Scholarship, 2014
- Herring Study Abroad Scholar, 2014-2015
- William I. Witkin Scholarship, 2014
- Carrie Largent Research Fellowship, 2014
- Dean's List (5 terms), 2012-2014 & 2015-2016

## Languages

---

English, native speaker

French, Advanced written and oral competency

## Technical Specialties & Interests

---

*Instrumental Techniques:* Transmission electron microscopy (JEOL 100CX II, FEI TALOS F200X) – scanning, EDX, and high resolution, Scanning electron microscopy (Carl Zeiss Merlin FESEM), Atomic force microscopy, UV-vis-NIR, Raman spectroscopy, Photoluminescence spectroscopy, Optical spectroscopy, Photoelectrochemical testing, Thin film fabrication

*Software:* Solidworks, Blender, Origin Lab, EC Lab, Image J, Mac OSX, Windows, Latex, Microsoft Office, Matlab (basics), Python (basics)

## Extracurricular & Volunteer Activities

---

PhD Student Representative, EDCH Doctoral School October 2020 – January 2022  
Liaison between EDCH doctoral students and the EPFL administration at all levels (section – school)  
Event planner, social media organizer, student coordinator, and mental health advocate

Sponsor Relations Coordinator, Club Montagne, EPFL September 2019 – December 2021  
Maintain working relationships with club sponsors, identify new partnerships, and negotiate deals and promotions for club members



